Conference Proceedings of the Society for Experimental Mechanics Series

Nikolaos Dervilis *Editor*

Special Topics in Structural Dynamics & Experimental Techniques, Volume 5

Proceedings of the 37th IMAC, A Conference and Exposition on Structural Dynamics 2019

SEM

Springer

Conference Proceedings of the Society for Experimental Mechanics Series

Series Editor

Kristin B. Zimmerman, Ph.D.
Society for Experimental Mechanics, Inc.,
Bethel, CT, USA

More information about this series at http://www.springer.com/series/8922

Nikolaos Dervilis
Editor

Special Topics in Structural Dynamics & Experimental Techniques, Volume 5

Proceedings of the 37th IMAC, A Conference and Exposition on Structural Dynamics 2019

Springer

Editor
Nikolaos Dervilis
University of Sheffield
Sheffield, UK

ISSN 2191-5644 ISSN 2191-5652 (electronic)
Conference Proceedings of the Society for Experimental Mechanics Series
ISBN 978-3-030-12242-3 ISBN 978-3-030-12243-0 (eBook)
https://doi.org/10.1007/978-3-030-12243-0

This Springer imprint is published by the registered company Springer Nature Switzerland AG
The registered company address is: Gewerbestrasse 11, 6330 Cham, Switzerland

Preface

Special Topics in Structural Dynamics & Experimental Techniques represents one of eight volumes of technical papers presented at the 37th IMAC, A Conference and Exposition on Structural Dynamics, organized by the Society for Experimental Mechanics and held in Orlando, Florida, January 28–31, 2019. The full proceedings also include volumes on Nonlinear Structures & Systems; Dynamics of Civil Structures; Model Validation and Uncertainty Quantification; Dynamics of Coupled Structures; Rotating Machinery, Optical Methods & Scanning LDV Methods; Sensors and Instrumentation, Aircraft/Aerospace, Energy Harvesting & Dynamic Environments Testing; and Topics in Modal Analysis & Testing.

Each collection presents early findings from experimental and computational investigations on an important area within structural dynamics. Special Topics in Structural Dynamics represents papers on enabling technologies for general dynamics and both modal analysis measurements, system identification, and damage detection.

The organizers would like to thank the authors, presenters, session organizers, and session chairs for their participation in this track.

University of Sheffield, Sheffield, UK Nikolaos Dervilis

Contents

Chapter 1
A Step Towards Testing of Foot Prostheses Using Real-Time Substructuring (RTS)

Christina Insam, Andreas Bartl, and Daniel J. Rixen

Abstract Despite extensive research in prostheses development, amputees still have to cope with severe limits. Tasks, such as climbing stairs and running or walking on soft ground are demanding and represent obstacles in everyday life. Design verification of new devices helps to accelerate the development. However, current test procedures do not include the dynamic interaction between a prosthesis and the human. Real-time Substructuring (RTS) enables investigation of the dynamic behavior of a system, here human and prosthesis, by splitting it into numerically simulated components and one physical component. As this test imitates real dynamic conditions, foot prostheses can be improved during the development stage. In this preliminary study, a one-dimensional mass-spring-mass system is investigated. The upper mass, representing the human being, is simulated numerically on the computer. It is coupled virtually to a prosthesis, represented here as a spring-mass system, which is mounted on a Stewart Platform. Both systems exchange displacement and force information. The upper mass tries to follow a periodic desired trajectory, which is influenced by the coupling. This paper describes the experimental setup and the effect of delay compensation. In addition, it is shown how the accuracy and stability of the RTS simulation depends on the problem description, i.e. how much the system is governed by the mechanical properties of the numerical part. Although we are specifically considering the application of RTS to prosthetics, the current research tackles generic problems that will also help to enhance other applications involving contact, e.g. the docking of satellites.

Keywords Real-time substructuring · Testing of prosthetic feet · Stewart platform · Real-time hybrid testing with contact · Force compensation

1.1 Introduction

Testing of foot prostheses is an expedient step in the development of foot prostheses. The aim of prostheses is, in general, to emulate the behavior of the missing body part. Despite great advances in the design of foot prostheses, they need to be improved further to enable amputees to resume a normal everyday life. Walking on uneven and soft ground is one of the challenging situations for patients because a healthy human foot can balance actively in this situation. Testing procedures during the early development stage help to accelerate prosthesis development and improvement [1]. Currently, there are different methods for testing foot prostheses: one approach is that the force and position data are taken from gait analysis laboratories and incorporated on test benches [2]. Another method for validating the newly developed design is via finite element modeling [1]. Moreover, prostheses are also evaluated via in-vivo testing. Patients are asked to wear the device and give feedback. The results from these tests are important, as they give a response on how well the amputees cope with the prosthesis in everyday life. However, even though this represents valuable feedback for prostheses developers, it is not without difficulties as it is not reproducible and unsafe for the amputees [1, 2]. The main advantage of robot-driven test benches is that they can also mimic potentially dangerous situations, such as tripping, in a safe and reproducible environment. Therefore, it would be advantageous to combine the advantages of all mentioned methods; a promising approach is the use of Real-Time Substructuring.

Real-Time Substructuring (RTS) or Real-Time Hybrid Testing is a method for investigating the dynamic behavior of complex mechanical systems. The mechanical system is split into two parts (or substructures) and each of the parts is analyzed—one is analyzed in a numerical simulation, the other is investigated on the test bench which is driven by an actuator. Both simulations are coupled in real-time in order to assess the dynamic behavior of the whole system [3, 4].

C. Insam (✉) · A. Bartl · D. J. Rixen
Chair of Applied Mechanics, Faculty of Mechanical Engineering, Technical University of Munich, Garching, Germany
e-mail: christina.insam@tum.de; andreas.bartl@tum.de; rixen@tum.de

N. Dervilis (ed.), *Special Topics in Structural Dynamics & Experimental Techniques, Volume 5*, Conference Proceedings of the Society for Experimental Mechanics Series, https://doi.org/10.1007/978-3-030-12243-0_1

Fig. 1.1 Stewart Platform used for the RTS simulation

This method was established and extensively used for earthquake engineering [5] but is nowadays also used in diverse fields, e.g. for the simulation of wind turbine blades [6] or spacecraft parachute deployment [7]. The applicability of the RTS method in biomechanics has also been proven by Herrmann et al. [8]. They tested the dislocation of artificial hip and knee joints under physiological conditions.

The idea of testing foot prostheses using the RTS method was also proposed in [9]. The human is modeled in a multibody simulation which is solved numerically. The prosthesis is mounted on the test bench and force as well as displacement values are exchanged in real-time between the two systems. In [9] it is assumed that stability problems occur due to the highly nonlinear system properties and the discontinuity due to contact. Extensive research on stability problems due to delay and unknown dynamics of the transfer system (actuator and controller, force sensor) have been conducted over the last decades, e.g. by Horiuchi et al. [10], Darby et al. [11], Bonnet [12], and Bartl et al. [13]. Furthermore, Boge and Ma [14] addressed contact issues for their application satellite docking. In general, time delay of the transfer system brings negative damping into the simulated system. Therefore, they actively balance the energy input and output so that the total energy does not increase and the system remains stable.

In this paper, we present the experimental setup for testing foot prostheses using RTS. The presented experimental setup is tested in an RTS simulation, where a mass-spring-mass system that can move in vertical direction serves as the mechanical system being tested. The effects of delay compensation using polynomial extrapolation [10] are investigated.

Section 1.2 introduces the test bench and the coupling problem. The mechanical system as well as the required force compensation are presented and derived in Sect. 1.3. Section 1.4 presents the results of the experiments. It also highlights issues regarding contact problems for the stability and accuracy of RTS simulations. Finally, a brief summary and outlook are given in Sect. 1.5.

1.2 Experimental Setup

A Stewart Platform, shown in Fig. 1.1, is used as an actuator for the RTS simulations. Stewart Platforms are six DOFs manipulators with parallel kinematics. Therefore, they offer the benefits of high stiffness and accuracy making them suitable for use, for example, in milling machines and driving simulators [15]. The Stewart Platform used in this investigation, is driven by six electric motors and is position-controlled by a decentralized cascade controller (PPI) [15]. For parallel robots, the inverse kinematics can be directly calculated using kinematic relationships in contrast to serial robots, where Newton-Raphson iterations or similar methods need to be used. Thus, the desired displacement command for the Tool Center Point

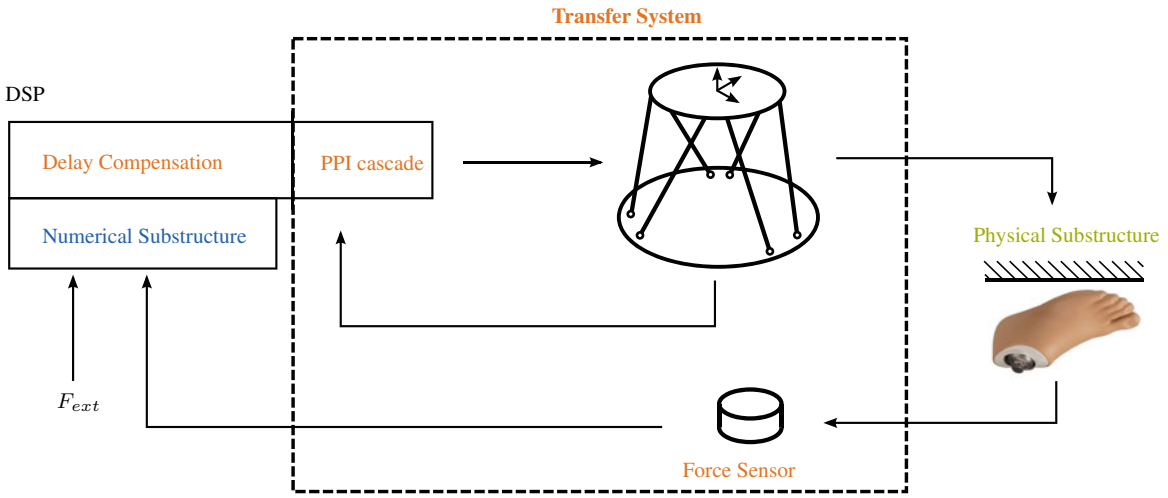

Fig. 1.2 Control loop for RTS testing using a Stewart Platform [16]

(center of upper platform) can be converted to a displacement command of each leg. Additionally, there is a velocity feed-forward in the control loop of the position-control that improves the controlled behavior of the Stewart Platform. The sample time of the controller is set to 1 ms.

The whole RTS simulation consists of a virtual and an experimental part as well as of a transfer system that imposes the desired displacement command. If the transfer system was ideal, i.e. it did not have any time delay or its own dynamics, the coupling of the virtual and experimental part would be perfect and the RTS simulation could perfectly imitate the dynamic behavior of the mechanical system [4]. The control loop for the RTS simulation is depicted in Fig. 1.2. The numerical model of the virtual part (blue), which is needed for the RTS simulation, is implemented in a Simulink Model. The real-time execution is done using a dSpace MicroLabBox as a Digital Signal Processor (DSP). The behavior of the numerical substructure is solved using a time integration scheme. The behavior depends on the current state as well as the loading and possible external forces F_{ext}. The calculated displacement at the interface between the virtual and physical substructure is sent to the transfer system (orange). The transfer system includes the Stewart Platform as an actuator with its inner control loop (position control) and a potential outer control loop for delay compensation. The Stewart Platform executes the desired displacement originating from the numerical substructure. The physical substructure (green), which is connected to a force sensor and mounted on the actuator, is being moved by this displacement. The force at the interface of the physical substructure is measured by a six DOFs force-torque sensor and fed back to the DSP. The next numerical simulation is performed on the numerical substructure and, depending on the new loading, updates the displacement command for the Stewart Platform.

1.3 Problem Description

In order to test foot prostheses with the experimental setup described in Sect. 1.2, the feasibility of the proposed idea must be validated. In addition, there are several research questions that must be solved to obtain a running and reliable RTS simulation. Therefore, the first simulations are done with the simple mechanical system described in Sect. 1.3.1. In Sect. 1.3.2, the force compensation of gravitational forces is derived. Finally, this section summarizes the delay compensation technique of [10] in Sect. 1.3.3.

1.3.1 Mechanical System

The system that we investigate is a mass-spring-mass system as depicted in Fig. 1.3a. The system consists of two masses, the upper mass m_V and the lower mass m_E. Following the later application $m_V \gg m_E$ is set. The spring stiffness of the massless spring is set to be k_E. Indices V and E imply the substructure to which the part belongs; mass m_V is simulated

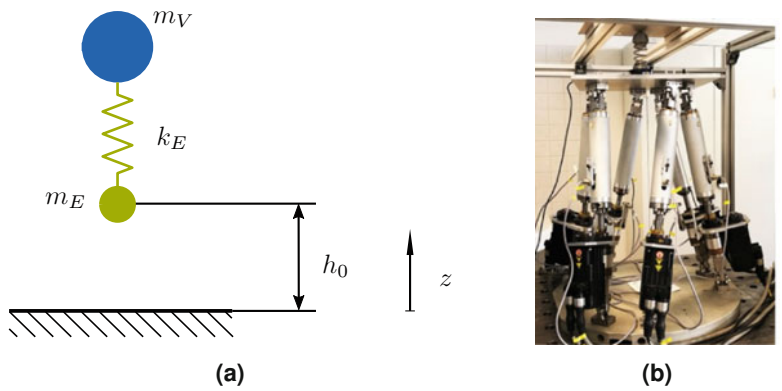

Fig. 1.3 Description and realization of the mechanical system. (**a**) Overall system for RTS simulation. (**b**) Experimental setup with mass m_E and spring (stiffness k_E)

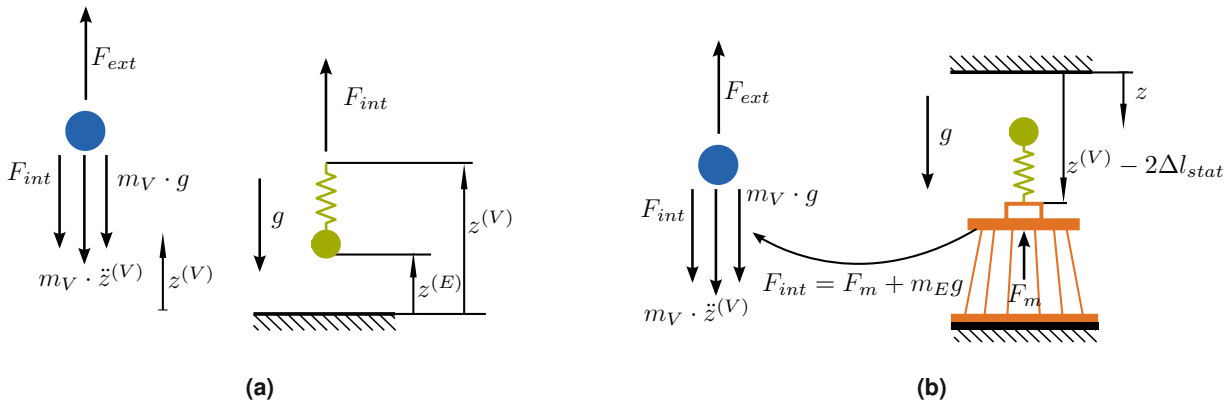

Fig. 1.4 Comparison of the dynamic behavior between validation simulation and measurement in the experimental setup. The RTS simulation consists of the numerical substructure (blue), the physical substructure (green) and the transfer system (orange). (**a**) Forces and displacements in the reference system. (**b**) Forces and displacements in the experimental setup

numerically (blue), whereas mass m_E and the spring (stiffness k_E) are tested on the test bench (green). Gravity acts in the negative $z-$direction and the height of mass m_E at time zero, i.e. when the simulation begins, is h_0. The behavior of the spring is linear over the range used in the experiments. The spring has an undeformed spring length of l_0. Furthermore, it is assumed, that the real system does not include any damping. The test bench realization is shown in Fig. 1.3b. The experimental substructure is connected to the Tool Center Point of the Stewart Platform by a force sensor and can be brought into contact by the actuator.

1.3.2 Compensation of Gravity Effects

The test setup is shown in Fig. 1.3b. The device under test that is mounted on its platform can be brought into contact with a ceiling but not with the ground. We could have inverted the Stewart Platform, however, the construction effort that would have been required prevented us from doing so. Consequently, the dynamic behavior of the system changes because the effect of gravity differs in the experimental setup and in the reference model, which must be included and compensated for in the RTS simulation.

The considerations are visualized in Fig. 1.4, where Fig. 1.4a shows the reference model and Fig. 1.4b shows the experimental realization. The position $z^{(V)}$ stands for the position of mass m_V and hence the position of the interface. Likewise, the position of mass m_E is denoted by $z^{(E)}$. The numerical simulation consists of the mass m_V (blue) which is under the following loads: the inertia force $m_V \cdot \ddot{z}^{(V)}$, the gravitational force $m_V \cdot g$, the force at the interface F_{int} and a (time-dependent) external force F_{ext}. As the mass m_E and its corresponding accelerations $\ddot{z}^{(E)}$ are in the same range as the noise of the force sensor, the inertia forces of mass m_E are henceforth assumed to be negligible. In addition, it is assumed that

there is no delay in the transfer system (orange). In the real-time experiments, the force offset is set when the experimental part is already mounted on the test bench. Hence, the measured force is $F_m = 0\ N$ if the mass m_E is not in contact. However, the force that acts at the interface of the reference system is $F_{int} = m_E \cdot g$. Since the interface force F_{int} acts on the numerical part and is thus required for a correct RTS simulation, the measured force must be corrected by

$$F_{int} = F_m + m_E \cdot g. \tag{1.1}$$

In other words, the difference between the measured forces and the interface forces in the reference system is $2m_E g$, which results from the different orientation of the gravitational force. However, due to setting the offset of the force sensor when the mass m_E is already mounted, we only have to compensate $m_E g$ according to Eq. (1.1).

1.3.3 Delay Compensation

The delay and dynamics of the transfer system can lead to instability and inaccuracy of the RTS simulation, as they bring negative damping into the system. To compensate, there are a lot of different delay compensation techniques. For the experiments presented in Sect. 1.4, we used a polynomial extrapolation as published in [10]. The formulation is

$$z'(t) = \sum_{i=0}^{2} a_i \cdot z(t - i \cdot \tau) \qquad \text{with } a_0 = 3,\ \ a_1 = -1 \ \text{ and } a_2 = 3,$$

if a polynomial of degree $n = 2$ is used and the time delay of the transfer system is τ. Here, the position value that is calculated by the numerical simulation at the current time t is z and the command that is sent to the actuator is z'. z' is an extrapolated value that depends on the value of z in the past.

1.4 Experiment

This section presents the experiments performed and results obtained with the mechanical system presented in Sect. 1.3. Firstly, the load case is described with the corresponding simulation parameters in Sect. 1.4.1 and then the results are shown in Sect. 1.4.2.

1.4.1 Loading Condition and Simulation Parameters

The aim of our research is to carry out a RTS simulation of a human walking with a prosthesis. A major question is how a human being stabilizes its body so that it does not fall, even if there are disturbances. One approach used in robotics for stabilizing bipeds is to use a planned trajectory and track this trajectory with a controller [17]. Using this approach, we prescribed a desired trajectory z_d (and $\dot{z}_d$) for the mass m_V in the numerical substructure. A PD controller (parameters K_p and K_d) attempts to follow this trajectory by adding an external force, if the desired motion is not tracked:

$$F_{ext} = (m_V + m_E) \cdot g + K_p \cdot (z_d - z^{(V)}) + K_d \cdot (\dot{z}_d - \dot{z}^{(V)}).$$

The first term corresponds to the static external force for holding the system in the air. Hence, the external force F_{ext} that acts on the system as displayed in Fig. 1.4 is the force that is required to keep mass m_V on the desired trajectory. The higher the values K_p and K_d, the faster the controller that tries to hold mass m_V on the desired trajectory z_d. Even small deviations from the trajectory are adjusted in a short period. If the parameters of the PD controller are reduced, the ability of the mass to follow its desired trajectory is reduced as well. Returning to the aim of testing a prosthesis using the RTS approach, this is similar to the case where the forces coming from a badly designed prosthesis are so large compared to the equilibrating forces, that the patient needs for example to tension a muscle much more than usual or tilt the hip. The dynamic behavior of the mechanical system is more relevant in this case and not dominated by the properties of the PD controller.

Table 1.1 Simulation parameters

Parameter	Value	Parameter	Value
m_V	9.62 kg	f_d	0.25 Hz and 1 Hz
m_E	0.38 kg	Δz_{max}	0.005 m
k_E	10,000 N/m	K_p	$2 \cdot 10^6$ kg/s^2 and 10^4 kg/s^2
h_0	0.01 m	K_d	500 kg/s and 50 kg/s
τ	10 ms		

The trajectory is chosen to be of sinusoidal shape

$$z_d(t) = h_0 + l_0 + \Delta l_{stat} - \frac{h_0 + \Delta z_{max}}{2} + \frac{h_0 + \Delta z_{max}}{2} \cdot \cos(2\pi f_d t)$$
$$= z_0^{(V)} - \frac{h_0 + \Delta z_{max}}{2} + \frac{h_0 + \Delta z_{max}}{2} \cos(2\pi f_d t),$$

starting at the initial position $z^{(V)}(t = 0) = z_0^{(V)}$ and using $\Delta l_{stat} = \frac{m_E \cdot g}{k_E}$. Here, the initial height of mass m_E is $z^{(E)}(t = 0) = h_0$, the frequency of the cosine is f_d and the maximum deflection of the spring is Δz_{max} (neglecting the static sag Δl_{stat} due to the weight $m_E \cdot g$). The velocity at time zero is $\dot{z}_{d,0}^{(V)} = 0$.

In the numerical simulation, Heun's method (*ode2* in Simulink) was used as a time integration scheme and the sample time was taken to be 1 ms. The properties of the mechanical system and the parameters for the RTS simulation were chosen as follows:

All results were compared to the validation simulation, where the reference mass-spring-mass system was simulated fully numerical by solving the differential equation with Simulink and an explicit Runge-Kutta time integration scheme (*ode45*). The contact was considered according to the penalization method, i.e. a spring acts as the mass m_E penetrates the ground. The spring constant was defined as $k = 10^9$ N/m. The solver returned the positions and velocities of both masses, i.e. $z^{(V)}$, $z^{(E)}$, $\dot{z}^{(V)}$ and respectively $\dot{z}^{(E)}$. Consequently, the interface force F_{int} can be calculated using the spring constant k_E,

$$F_{int} = k_E \cdot \left(z^{(V)} - z^{(E)} - l_0 \right). \tag{1.2}$$

1.4.2 Results

The first experiments included a sinusoidal trajectory with $f_d = 0.25$ Hz and $f_d = 1$ Hz. Preliminary experiments revealed that the delay of the Stewart Platform is $\tau \approx 10$ ms for this kind and amplitude of excitation. K_p and K_d were chosen to be $K_p = 2 \cdot 10^6$ kg/s^2 and $K_d = 500$ kg/s, respectively, which means that the controller that keeps the upper mass on the desired trajectory z_d has a strong influence. All other parameters were taken from Table 1.1. The results are shown in Fig. 1.5. Each figure includes the validation simulation of the reference system (dashed line) and the measured solution from our RTS simulation (solid line). Figure 1.5a and b shows the displacement of mass m_V for an excitation of $f_d = 0.25$ Hz and $f_d = 1$ Hz. Figure 1.5c and d shows the interface force that was measured and adjusted as given in Eq. (1.1) compared to the interface force from the validation simulation, see Eq. (1.2). Due to numerical oscillation and rounding errors, the interface force of the validation simulation oscillates when there is no contact between m_E and the ground.

The results in Fig. 1.5 show that the results from the RTS experiment closely correspond to the results from the validation simulation. As the parameters K_p and K_d are quite high, the system dynamics are dominated by this controller that keeps m_V on the desired trajectory. Nevertheless, these first results show that our implementation is correct and that the experimental setup (introduced in Sect. 1.2) can be used for RTS simulations. Similar experiments were also conducted using a delay compensation. Nevertheless, the results are not improved because the results without delay compensation already sufficiently emulate the system dynamics.

So far, we have analyzed the feasibility of RTS experiments with the experimental setup. However, in the case of prostheses testing, we assume that the human will not control its desired trajectory as closely as the controller in the first experiments. Rather it will behave like a floating system. Hence, we have reduced the parameters to $K_p = 10^4$ kg/s^2 and $K_d = 50$ kg/s, respectively and performed similar tests. The prescribed trajectory had a frequency of $f_d = 0.25$ Hz. The

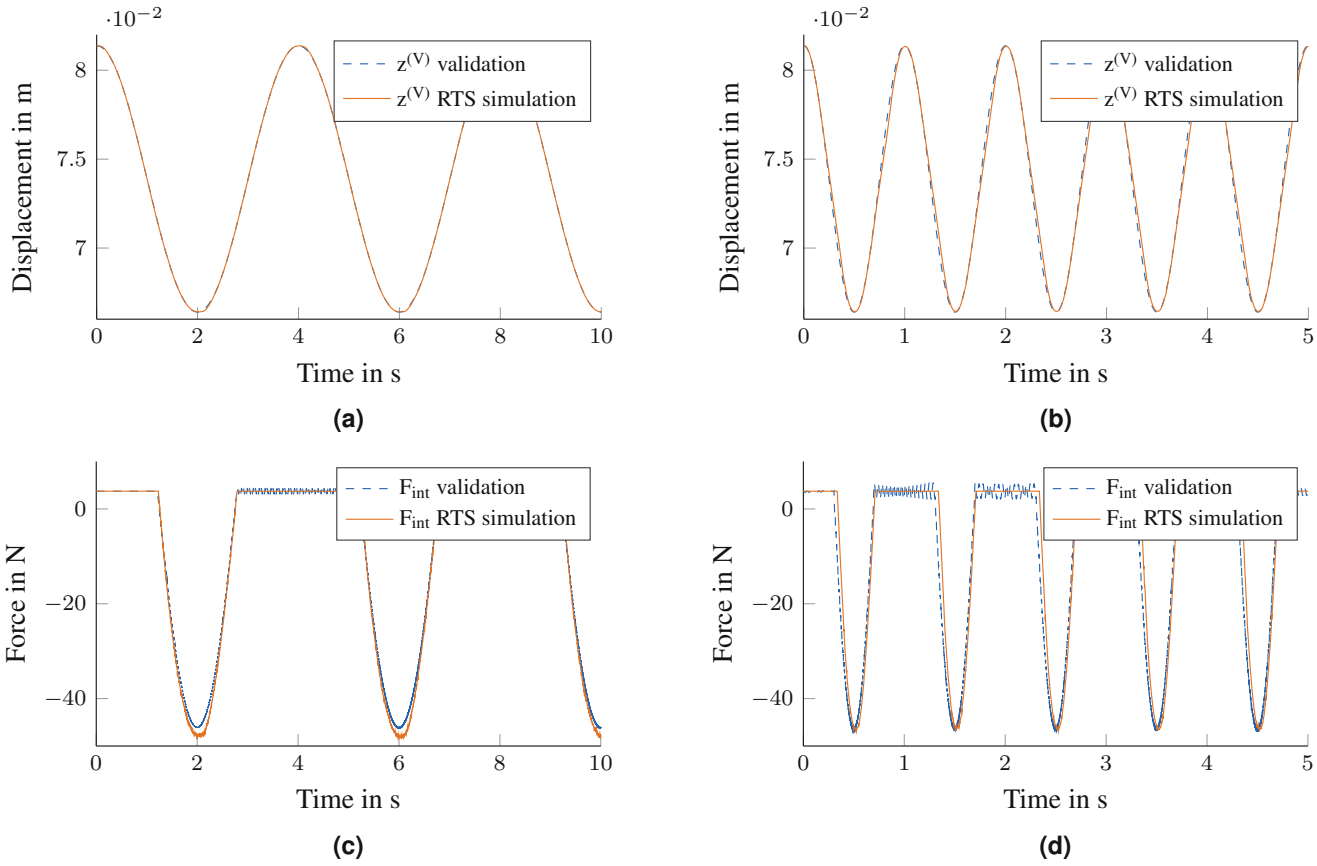

Fig. 1.5 Comparison of displacements and forces at the interface between validation simulation (dashed line) and real-time hybrid test (solid line). Experiments were conducted without delay compensation at 0.25 Hz and 1 Hz. (**a**) Displacement 0.25 Hz. (**b**) Displacement 1 Hz. (**c**) Interface force 0.25 Hz. (**d**) Interface force 1 Hz

experiments were conducted without and with a delay compensation as introduced in Sect. 1.3.3 with a polynomial of degree $n = 2$. The system dynamics are now much more influenced by contact problems and delay of the transfer system, as can be seen in Fig. 1.6. Figure 1.6a and b shows the displacement at the interface ($z^{(V)}$) without and respectively with delay compensation. Figure 1.6c and d shows the corresponding forces at the interface F_{int}.

Previously, the PD controller had higher values for K_p and K_d. This helped to stabilize the whole mechanical system, as the dynamics that are taken into account through the transfer system and the contact forces were suppressed. Now, the results show that coupling during contact makes the RTS simulation unstable. The displacement at the interface oscillates around the desired position with increasing amplitude. This effect is smaller, if we use the polynomial extrapolation as delay compensation (Fig. 1.6b and d). As the influence of the transfer system and the contact is increased (parameters K_p and K_d reduced), stability problems that can occur during RTS simulation with contact become clearly apparent. Furthermore, the accuracy of the dynamic analysis is reduced.

1.5 Conclusions

We have presented the experimental setup for RTS tests using a Stewart Platform. Ongoing research aims to test foot prostheses using this approach. First experiments show the applicability of this kind of actuator for real-time tests. The experimental setup differs from the reference model in respect of its orientation to external forces. This paper describes the relation between measured forces and interface forces that are required for a correct RTS simulation. As a first step towards testing of foot prostheses, we assume a simplified system for RTS simulations. The mechanical system investigated in this paper, is a mass-spring-mass system that moves in the vertical direction and is brought into contact with the ground. The upper mass is controlled by a PD controller (parameters K_p and K_d) so that it follows a desired, defined trajectory.

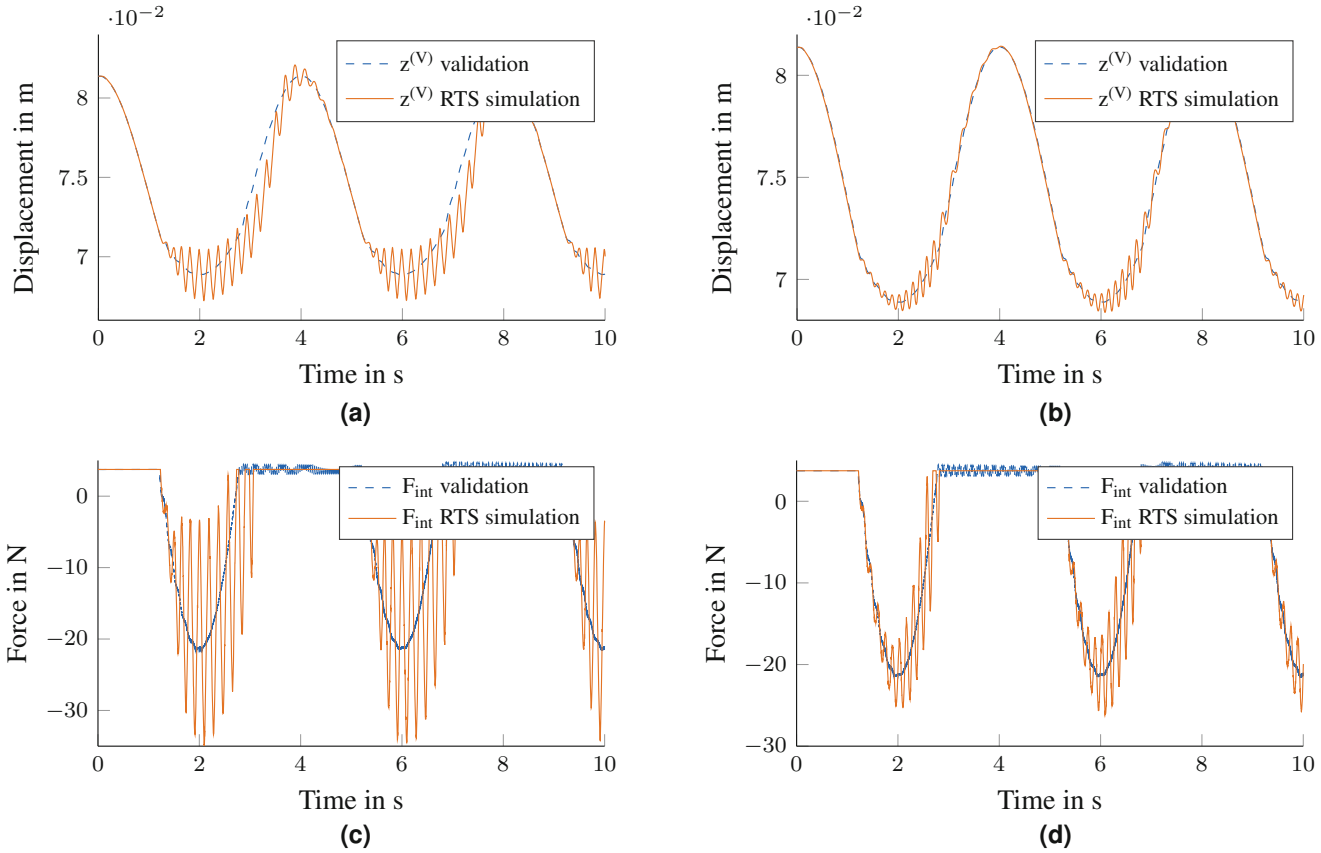

Fig. 1.6 Comparison of displacements and forces at the interface between validation simulation (dashed line) and real-time hybrid test (solid line) with smaller controller values for K_p and K_d. Experiments were conducted with a trajectory of frequency 0.25 Hz without and with delay compensation. (**a**) Displacement 0.25 Hz. (**b**) Displacement 0.25 Hz with delay compensation. (**c**) Interface Force 0.25 Hz. (**d**) Interface Force 0.25 Hz with delay compensation

Depending on the parameters of the PD controller, the dynamic behavior of the mechanical system is dominated by the PD controller or by the dynamics through coupling, i.e. the dynamics of the transfer system and forces when the device under test comes into contact. Experiments were conducted with different values for K_p and K_d as well as with delay compensation. The technique adopted for delay compensation is a polynomial extrapolation with degree $n = 2$. Results show that the influence of the coupling dynamics causes the RTS simulation to become unstable. The accuracy improves when using the delay compensation, although the system is still unstable in the RTS simulation. These preliminary results reveal the main obstacles that will also occur in the RTS simulation of a human walking with a prostheses. Hence, we need to improve the current test setup to obtain more accurate results even for those systems where the numerical part is floating.

References

1. Tryggvason, H., Starker, F., Lecompte, C., Jónsdóttir, F.: Modeling and simulation in the design process of a prosthetic foot. In: Proceedings of the 58th SIMS, pp. 398–404 (2016). https://doi.org/10.3384/ecp17138398
2. Marinelli, C.: Design, development and engineering of a bench for testing lower limb prosthesis, with focus on high-technological solutions. PhD thesis (2016)
3. Nakashima, M., Masaoka, N.: Real-time on-line test for MDOF systems. Earthq. Eng. Struct. Dyn. **28**(4), 393–420 (1999). https://doi.org/10.1002/(SICI)1096-9845(199904)28:4<393::AIDEQE823>3.0.CO;2-C
4. Bonnet, P.A., Lim, C.N., Williams, M.S., Blakeborough, A., Neild, S.A., Stoten, D.P., Taylor, C.A.: Real-time hybrid experiments with Newmark integration, MCSmd outer-loop control and multi-tasking strategies. Earthq. Eng. Struct. Dyn. **36**, 119–141 (2007). https://doi.org/10.1002/eqe.arXiv:1403.5481
5. Blakeborough, A., Williams, M.S., Darby, A.P., Williams, D.M.: The development of real-time substructure testing. Philos. Trans. R. Soc. Lond. A Math. Phys. Eng. Sci. **359**(1786), 1869–1891 (2001)

6. Bosse, D., Radner, D., Schelenz, R., Jacobs, G.: Analysis and application of hardware in the loop wind loads for full scale nacelle ground testing. DEWI Mag. **43**, 65–70 (2013)
7. Harris, M.J., Christenson, R.E.: Experimental test of spacecraft parachute deployment using real-time hybrid substructuring. In: Sensors and Instrumentation, Aircraft/Aerospace and Energy Harvesting, Conference Proceedings of the Society for Experimental Mechanics Series, vol. 8, pp. 67–70 (2018)
8. Herrmann, S., Kluess, D., Kaehler, M., Grawe, R., Rachholz, R., Souffrant, R., Zierath, J., Bader, R., Woernle, C.: A novel approach for dynamic testing of total hip dislocation under physiological conditions. PLoS One **10**(12), 1–24 (2015). https://doi.org/10.1371/journal.pone.0145798
9. Yang, Z., Iravani, P., Plummer, A., Pan, M.: Investigation of hardware-in-the-loop walking/running test with spring mass system. In: Towards Autonomous Robotic Systems, pp. 126–133 (2017). https://doi.org/10.1007/978-3-319-64107-2
10. Horiuchi, T., Inoue, M., Konno, T., Namita, Y.: Real-time hybrid experimental system with actuator delay compensation and its application to a piping system with energy absorber. Earthq. Eng. Struct. Dyn. **28**(10), 1121–1141 (1999). https://doi.org/10.1002/(SICI)1096-9845(199910)28:10<1121::AIDEQE858>3.0.CO;2-O
11. Darby, A.P., Williams, M.S., Blakeborough, A.: Stability and delay compensation for real-time substructure testing. J. Eng. Mech. **128**(12), 1276–1284 (2002). https://doi.org/10.1061/(ASCE)0733-9399(2002)128:12(1276)
12. Bonnet, P.A.: The development of multi-axis real-time substructure testing. PhD thesis, University of Oxford (2006)
13. Bartl, A., Mayet, J., Rixen, D.J.: Adaptive feedforward compensation for real time hybrid testing with harmonic excitation. In: Proceedings of the 11th International Conference on Engineering Vibration September (2015)
14. Boge, T., Ma, O.: Using advanced industrial robotics for spacecraft rendezvous and docking simulation. In: Proceedings – IEEE International Conference on Robotics and Automation (2011). https://doi.org/10.1109/ICRA.2011.5980583
15. Riebe, S., Ulbrich, H.: Experiments on linear and nonlinear control of a multi-DOF parallel mechanism. In: Proceedings of the ASME 2003 International Design Engineering Technical Conferences and Computers and Information in Engineering Conference (DETC) (2003)
16. Ottobock Foot Prosthesis, Duderstadt. http://www.ottobock.de. Accessed 04 Mar 2018
17. Wittmann, R., Hildebrandt, A.C., Ewald, A., Buschmann, T.: An estimation model for footstep modifications of biped robots. In: IEEE International Conference on Intelligent Robots and Systems, pp. 2572–2578 (2014). https://doi.org/10.1109/IROS.2014.6942913

Chapter 2
Augmented Reality for Interactive Robot Control

Levi Manring, John Pederson, Dillon Potts, Beth Boardman, David Mascarenas, Troy Harden, and Alessandro Cattaneo

Abstract Robots are widely used to support mission-critical, high-risk and complex operations. Human supervision and remote robot control are often required to operate robots in unpredictable and changing scenarios. Often, robots are controlled remotely by technicians via joystick interfaces which require training and experience to operate. To improve robot usage and practicality, we propose using augmented reality (AR) to create a more intuitive, less training-intensive means of controlling robots than traditional joystick control. AR is a creative platform for developing robot control systems, because AR combines the real world (the environment around the user, the physical robot, etc.) with the digital world (holograms, digital displays, etc.); it can even interpret physical gestures, such as pinching two fingers.

In this research, a Microsoft Hololens headset is used to create an AR environment to control a Yaskawa Motoman SIA5D robot. The control process begins with the user placing an interactable holographic robot in 3D space. The user can then select between two control methods: manual control and automatic control. In manual control, the user can move the end effector of the holographic robot and the physical robot will respond immediately. In automatic control, the user can move the end effector of the holographic robot to a desired location, view a holographic preview of the motion, and select execute if the motion plan is satisfactory. In this preview mode, the user is able to preview both the motion of the robot and the torques experienced by the joints of the manipulator. This gives the user additional feedback on the planned motion. In this project we succeeded in creating an AR control system that makes controlling a robotic manipulator intuitive and effective.

Keywords Augmented reality · Microsoft Hololens · Robotic arm · Force feedback · Motion planning

2.1 Introduction

Augmented reality (AR) is an emerging field that offers new tools for human-based control and interaction with complex systems. AR combines the sensory experience of a user with information from a digital system; this contrasts with virtual reality, which seeks to eliminate the user's perception of the real world. Physical-digital interaction allows for intuitive control of digital systems with sensory feedback that can be more easily interpreted by the user. Intuitive AR systems are used in applications such as virtual surgery training and robotic tele-operation. AR is particularly advantageous for robotic control where direct human control is needed; because conditions and objectives are unpredictable or rapidly changing, decisions must be made by an operator in real time.

Current robotic control is difficult because of non-intuitive controls (e.g. moving a joystick to the right to rotate a gripper) and a lack of force feedback, since haptic feedback interfaces are still niche products. Without force feedback, it is difficult for an operator to have a sense of how much force a robot is exerting on an object; this often leads to over- or under-applying

L. Manring
Department of Mechanical Engineering and Materials Science, Pratt School of Engineering, Duke University, Durham, NC, USA

J. Pederson
Department of Mechanical Engineering, The Fu Foundation School of Engineering and Applied Science, Columbia University, New York, NY, USA

D. Potts
Department of Mechanical Engineering, Ira A. Fulton College, Brigham Young University, Provo, UT, USA

B. Boardman · T. Harden · A. Cattaneo (✉)
Engineering Technology and Design Division, Los Alamos National Laboratory, Los Alamos, NM, USA
e-mail: cattaneo@lanl.gov

D. Mascarenas
Engineering Institute, Los Alamos National Laboratory, Los Alamos, NM, USA

N. Dervilis (ed.), *Special Topics in Structural Dynamics & Experimental Techniques, Volume 5*, Conference Proceedings of the Society for Experimental Mechanics Series, https://doi.org/10.1007/978-3-030-12243-0_2

forces, which can be detrimental in delicate operations. These two limitations require human operators to have extensive training and experience. By implementing AR robotic control, the amount of training required to operate robots will be reduced, and operators will be able to control applied forces more accurately. Improving human-robot control will allow for a wider utilization of robots in many fields where real-time operator control is necessary.

2.2 Background

Augmented reality (AR) is emerging as a technology that is able to connect people to a growing number of tools in a more user-friendly manner. As a result, AR applications are growing in complexity and in scope, which can be seen in the following published applications.

There are multiple AR mediums, and in [1] touch-screen devices are used to implement AR as a feature in a game that encourages exercise in young people. The authors developed their research game using Unity3D, the Vuforia AR library, and OpenGL to create an interactive AR world game-space on touch-screen devices. Ref. [2] uses spatial AR. This involves projecting AR from a projector (as opposed to the classic uses of touchscreen devices, computers, and glasses). This research sought to develop a control method to control the position and orientation of such a projector to be used for an even wider workspace. The advantage of the system proposed in this work lies in its understanding of kinematic control without knowing the exact kinematic specifications of a projector pan/tilt mount (such as an ad hoc assembly). In [3], the authors propose an AR system that generates pattern identifications by analyzing infrared optical markers projected in actual space measured by an infrared camera. For this system, the operator gives commands by projecting markers on a position on a screen. AR applications continue to be developed to assist in the daily activities of people affected by adverse health conditions [4]. This paper proposes a unique application for AR to assist people affected by paralysis in performing daily tasks. The authors use a BMI (brain-machine interface) to measure the brain-waves of the user be means of electroencephalography. They also use gaze-selection via pupil tracking. The BMI enables to denote either a “command” state or a “rest” state based on the brain activity of the user, and the gaze-selection is used to denote direction and goals for the robotic arm. The researchers found that across the board, AR assisted the user in selection and movement of obstacles using the robotic arm. The researchers propose in future work the importance of changing the interface medium from a computer screen to wearable AR glasses.

As research in the field of robotics continues to grow, AR is being used more often to reduce the complexity of controlling robots. In [5], the authors propose a mixed reality human-robot interface to assist operators in tele-operation for remote maintenance tasks. In this system, visual inspection and corrective task execution are two phases activated by the operator. For the second phase, a virtual robot helps the operator visualize the movement of the robotic arm before the task is executed. This allows the user to create/refine path movements in advance of completing them. However, this system also requires that the obstacles in the environment are known about a priori. Part of their interest in future work is to input depth sensors to detect objects in the surroundings. In [6], the authors seek to perform something similar to [5] by overlaying a computer graphic/hologram on top of the actual robot that is updated based on user input. The purpose of this graphic is to account for the time delay between when the user sends a command and when the physical robot responds. The graphic will move immediately, the actual robot will follow the graphic, and they will eventually meet. In addition, digital handles are projected over the real robotic hand which can be selected and moved to rotate the robotic arm. Another AR-based system to facilitate programming robots and planning trajectories is presented in [7]. This research incorporates robot dynamics into task-optimized executable robot paths that are also collision free. A method for assisting in robot end-effector planning using AR is presented in [8]. The authors implement a trajectory optimization scheme to assist in end-effector location and angle. This research also considers the system dynamics of the robot while checking for collision detection and simulating the torque and velocity of each robot joint. If the torque/velocity are outside the designated limits, that joint is highlighted as one that has a high probability of deviating from a planned trajectory. The package Roboop is used for robot kinematics and dynamics modeling (this package is no longer available). The authors are able to demonstrate an increased performance in a trajectory that is obtained by incorporating robot dynamics versus one that only considers kinematics.

There has been a significant amount of work in the area of providing force-feedback to the user using AR. In [9], the authors employ the principle of reverse electrovibration using AR, where a weak electrical signal is injected anywhere on the user body to create an oscillating electrical field around the user’s fingers. Using this principle, the user can have a perception of texture that is physically not present. The work of the authors resulted in a device, REVEL, that allows tactile textures to be modified in real time. One of the primary benefits of this system is that it allows tactile feedback without the use of gloves, since it only requires the user to wear a small tactile passive signal generator that can be attached anywhere on the user’s body. The research presented in [10] seeks to overcome the issues with time delay as it influences tele-operated systems. The authors propose a virtual model which can estimate the real-time force feedback and give visual information using AR to

the operator, which reduces the effects of time delay. In [11], the authors present an interesting method for training surgeons using force feedback in combination with AR. This gives the trainee information on collision detection and location. The motivation of this research is to reduce the risks associated with training new surgeons in an actual surgery. A method for providing haptic feedback in an AR setting is presented in [12]. The goal of this research is to enable AR users to have feedback on roughness and friction of surfaces. This paper presents a novel method of using an ungrounded haptic stylus with actuators to overlay texture vibration and friction forces when the user touches an object, which allows the virtual and real worlds to mix.

These AR methods have also been extended to control multiple robots, as shown in [13], where a method for implementing AR for single-user control of four Mindstorms NXT robots is presented. In particular, the authors use Point-and-Go and path planning as two methods to reduce mission completion times as compared to typical joystick control methods. They use a Probabilistic Roadmap Planner as their path planner for the robots to provide a higher level of automation than the Point-and-Go method. This resulted in significantly lower mission completion times and a strong preference by test users for the path-planning AR method. In [14], the authors seek to use ROS and Unity to simulate multiple UAVs to easily verify and develop flight control and navigation algorithms. They also present a layout of the system level structure that is very useful for reconstructing similar applications (including Windows, Ubuntu, ROS, and Unity connections and how it works together). The authors also discuss Unity Socket, which uses TCP/IP to exchange data between ROS and Unity3D.

There are a number of publications that detail the connection between ROS and Unity3D as a means for implementing AR in robotic systems. In [15], the authors seek to reduce the costs of developing real robots and eliminate some of the cost of performing real-world human-robot interaction experiments. They present a modified virtual reality system named SIGVerse 3.0 which includes a connection mechanism to bind Unity to the ROS environment, enabling users to develop robot software in ROS and place a virtual robot model into Unity applications. In addition, this paper includes a helpful table of functions and limitations of related systems which show the compatibility and usefulness of different platforms, showing that their new version of SIGVerse is preferable. In [16], the authors cover the main advantages of different software for visualization and robotic control, particularly using ROS and Unity3D. ROS is based on message passing while Unity3D is tied to a rendering loop where commands are made/updated each frame. Because of this difference, interaction between the two programs is difficult. ROSbridge is used to connect ROS with the outside world. ROSbridge uses WebSocket protocol to communicate JSON (JavaScript Object Notation) strings. The process of communicating between ROS and Unity3D involves transmitting JSON-encoded messages through a WebSocket. In [17], a system is presented for simulating executing the task of monitoring an industrial process, with a particular focus on shortening optimization time for a robot and make the final commissioning more efficient (this is related to the expensive process of tuning and calibrating a one-of-a-kind robot). One of the key parts of their implementation is the use of ROSbridge, which establishes a connection between Unity3D and ROS which allows for invoking ROS services.

Our application of AR is a unique system that allows the user to control a robot by means of holograms projected by a Microsoft Hololens AR headset and provides the user torque feedback that can assist in robot operation.

2.3 Methodology

2.3.1 Overview

To implement robotic control with augmented reality, a Microsoft Hololens headset, used to create an AR environment, communicates with a controllable robotic arm, the Yaskawa Motoman SIA5D. The layout of this system can be seen in Fig. 2.1. The Hololens is a Windows 10 based device that creates and modifies the AR environment. A Unity development environment, which utilizes C# in a .NET framework and scripting backend, creates the AR scene. The Hololens projects holograms into the real-world view of the user. Users interact with the holograms through hand motions. Hand motions, known as gestures, are used to make selections and move holograms. One example of a gesture is the ability to “click”, which occurs when the user moves thumb and index finger from an open position to a closed position. To interface with the SIA5D Motoman robot, we used the conventional Robot Operating System (ROS) (version indigo). The Hololens sends and receives information from the robotic arm using the ROS. The communication between the Hololens and ROS is done via a ROSbridge websocket.

Fig. 2.1 The transmitting/reception layout connecting the Hololens to the SIA5D robot

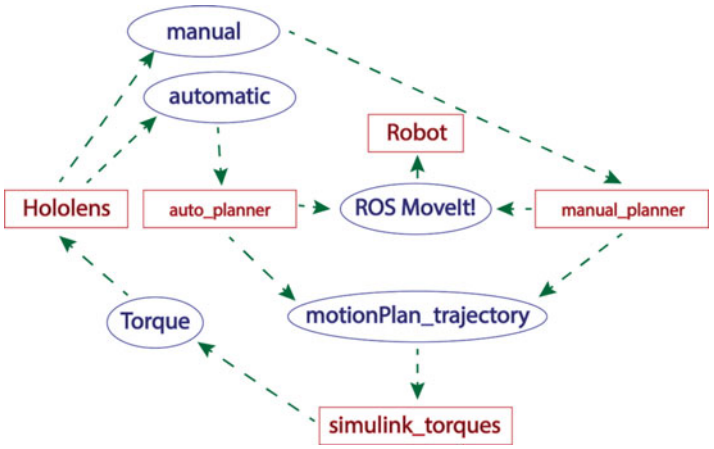

Fig. 2.2 A diagram of the ROS nodes and topics used in this application

2.3.2 System Layout and ROS

The framework of our system can be best understood after a brief discussion of how ROS works. ROS provides a useful framework for communicating with the robot using categories called nodes, topics, publishers, and subscribers. Nodes represent any entity involved in the robot's operation; examples include sensors, processors, and motors. Topics are entities that act as channels to pass information between nodes. Publishers are a type of node that publish information to topics, and subscribers are nodes that subscribe to topics. For node A to pass information to another node B, it must publish that information to a topic, and node B must subscribe to that topic.

One particularly useful feature of ROS is that it is simple to go from simulation of the robot in RViz (a visualization library in ROS) to actual control of the physical robot. The system implemented in this paper is laid out in Fig. 2.2, where the blue ovals denote topics and the red rectangles indicate nodes in ROS.

In Fig. 2.2, the Hololens node publishes desired robotic arm position information to the two robot control topics: manual and automatic depending on whether the user chooses to use manual or automatic mode. Auto_planner and manual_planner each subscribe to the automatic and manual topics, respectively. These nodes calculate and publish a motion plan to the motionPlan_trajectory topic. The simulink_torques node subscribes to the motionPlan_trajectory node and calculates a prediction for the torque exerted on the robot based on the motion plan in the motionPlan_trajectory topic. The torque calculations are then combined with the motion plan information and published to the Torque topic. The Hololens node uses the information stored in the Torque topic to preview motion plans and torque values graphically with holograms. Then the user has the option of allowing the robot to execute the plan. Pressing the "Execute" button in the user interface sends a message over the execute topic, as well as the robot's current joint states over the automatic topic; the Hololens receives the information via the websocket connection and moves the robot according to the joint states specified.

The simulink_torques node is an implementation of the Robotics System Toolbox (RST) from Mathworks that calculates the inverse dynamics (particularly joint torques) based on the motion plan. The Hololens node subscribes to the simulink_torques topic so that the user can gain additional information about the expected loadings on the robot manipulator.

2.3.3 Unity

To coordinate the holograms, user interface, and C# scripts that make up our application, we used the popular game engine Unity. Unity allows the user to place, modify, and manipulate two and three-dimensional objects, including text boxes, buttons, and CAD models in a virtual environment. In addition, scripts written in the C# programming language can be attached to such objects; their methods can be used to move and change objects, get system properties, and even communicate with websockets which are a means of two-way, message-based communication over a local network.

Unity packages add additional functionality to the editor itself. For our application, we used the ROS and HoloToolkit packages. ROS is a free library designed to improve communication between Unity and ROS; it includes scripts for communication over a websocket via ROSbridge, as well as an importer for Universal Robot Description Format (URDF) files. The HoloToolkit enables gesture recognition functionality to be used in Unity programs. To produce our application environment, we first imported the necessary packages and the URDF of our SIA5 robot into the Unity environment. We then wrote and compiled several scripts that coordinated all aspects of the application; these tasks included communicating with ROSbridge websockets, dragging and moving the robot's virtual end effector, and animating the robot's joints. We also added physical joints with rotation limits to the 3D robot model, in order to ensure that the virtual robot would only animate valid robot positions.

2.3.4 Control Modes

The AR robotic control system we implemented has multiple options for control. For this application, we have created two control modes: manual and automatic. In each mode, the motion planner library within MoveIt! is used to plan the robot trajectory. The MoveIt! library works by loading a robot package, which is created by importing a URDF file for the SIA5D robot and designating groups of joints and end effectors. The user can get a trajectory by designating a goal pose or by specifying a set of joint states to reach. The motion planning library will plan the trajectory while avoiding self-collisions but will not execute the trajectory unless given a command to execute. The implementation of MoveIt! with the robot is done using C++ code to create nodes that call this library.

2.3.5 Manual Control

When manual control is selected, the user moves the holographic robot in 3D space by clicking and dragging the virtual end effector with their hand. At a predetermined update rate, the robotic arm follows the motion of the holographic robot, making for near-real-time robot motion control. In ROS, this means that as soon as soon as the manual_planner node calculates the motion plan, the motion plan is executed. The user can move the holographic end effector by pinching their fingers over the holographic end effector and moving it where desired. The physical end effector then follows the motion of the holographic end effector.

2.3.6 Automatic Control

In automatic control, the user moves the robot using the hologram's virtual end effector in the same manner as manual control. However, the robotic arm does not automatically move to the position specified by the holographic arm; it instead waits for further user input. The Hololens can preview the motion plan by having the holographic arm follow the proposed path. If the user is satisfied with the motion plan, they can execute it; if not, they can move the arm to a new position and try again, or switch to manual control. In ROS, the motion plan is saved to a .bag file so that it can be executed when the user desires.

2.3.7 Connections

Much of the difficulties encountered in building our application lay in the various communications and connections between each component of the project. The Hololens communicates with the ROS environment to exchange information about user-selected end-effector positions and robot joint states; it does this through an intermediary websocket called ROSbridge. Both positions and states must be published to ROS topics in order for the path-planning algorithms to use them; thus, the C# scripts first format this information according to the JSON string-based file format and then add the topic to which it will be published. The Hololens must then send the resulting formatted string to the ROSbridge websocket server, which runs on the Linux system running ROS; using the Windows.Networking.Sockets library, the Hololens connects to the websocket as a client and sends the JSON-formatted string messages to it. Once received, ROSbridge parses the messages and publishes their information to the ROS topics specified in the JSON formatted strings. The motion planning algorithm nodes (auto_planner and manual_planner) then subscribe to these ROS topics, process the information to create a motion plan, and publish the plan over the motionPlan_trajectory and ROS MoveIt! topics; the MoveIt! node subscribes to the latter topic and moves the robotic arm according to the motion plan.

Receiving information on the Hololens (such as the motion plan and torque information) works much the same way as transmitting in reverse, except for a few differences on the ROSbridge server. For the Hololens to subscribe to the motionPlan_trajectory and Torque topics (which contain information about the motion plan and joint torques, respectively), it must tell ROSbridge to subscribe to those particular topics. Then, whenever a message is published on those topics, ROSbridge will format the message into a JSON string and send it to the Hololens client. The Hololens then uses the information to relay motion plan previews and torque information to the user. The various ROS components (including the path-planning algorithms, torque simulators, and robotic controllers) communicate internally with each other via ROS topics, as mentioned above.

2.3.8 Torque Simulation in ROS

One of the primary features of AR we have implemented is the ability to employ additional user feedback. One common disadvantage of conventional robot control implementations is that force/torque feedback is difficult to provide and if this feedback is available, it is difficult to give a meaningful output to the user. This means that the user is "running blind" when it comes to understanding the loading that a manipulator is undergoing.

In ROS, we can extract the motion plan for a robot trajectory in the form of waypoints and timestamps, which is effectively a time-series for each joint of the robot. Using Mathworks RST, we can import this time-series and use an inverse dynamics solver to compute the torques for each joint. For this application, we used Simulink as our primary platform because it is easier to deploy with ROS than Matlab alone. Simulink has blocks for publishing and subscribing to topics in ROS and has the ability to be deployed as a standalone application as a node in ROS as seen in Fig. 2.3.

In Fig. 2.3, the red block describes the subscription to the motion plan calculated by the MoveIt! library. The blue block calculates the inverse dynamics of the system of ordinary differential forcing equations with the state variables (position, velocity, and acceleration) along with mass and inertia information for the joints. Finally, the simulink_torques node sends the torque information back to the Hololens in the green publishing block.

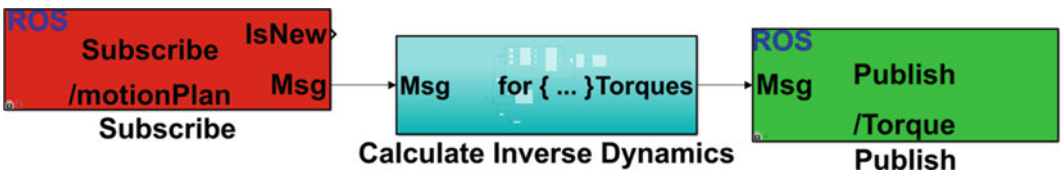

Fig. 2.3 The Simulink diagram for the simulink_torques node

Fig. 2.4 A screenshot of the Hololens application in action. *Left:* The physical robotic arm has just moved to the position of the holographic arm. Notice the overlay of the hologram onto the physical robotic arm. *Right:* The hologram "Preview Motion Plan" operation, providing torque feedback via color media

2.4 Results

The final result of our project was a Hololens application and Linux terminal backend that can successfully control a SIA5D robotic arm. Designed for intuitive user control, the application features a holographic button interface that follows the user, manual and automatic control modes, motion plan previewing, torque simulation, and visual feedback.

To use the application, the ROS scripts and nodes are first initialized and run on the Linux machine. Next, the ROSbridge websocket is launched in the Linux terminal. Our application is then run on the Hololens. In the user's field of view, a single holographic button labeled "Open Menu" will appear. When clicked, a menu containing buttons for manual control, automatic control, and holographic arm initialization will appear. When the user clicks the initialization button, a holographic model of the robotic arm appears. The user then drags the hologram until it is superimposed on the physical robot.

Once the hologram has been superimposed on the robotic arm, the user selects either manual or automatic control with the appropriate buttons. For both manual and automatic control, the user drags the virtual end effector to move the holographic arm. In manual control, the joint angles of the holographic arm are transmitted to the motion planner once a second, and the robotic arm moves to mimic the hologram accordingly. This creates a near-real-time remote manipulation of the robotic arm. In automatic control, the robot moves to the position of the holographic arm only when the "Execute" button is selected by the user. In addition, automatic control has a "Preview Motion Plan" button, which when selected, displays a preview of the calculated motion plan by moving the holographic arm accordingly. Unfortunately, there was a slight issue with exactly mimicking the motion plan due to a disparity between the joint angles of the Unity model and those of the real robot. This issue only raised its head in the "Preview Motion Plan" operation, but the simulated torques for the joints were displayed through changes of color, varying from blue to red (low to high torque) and then black if the joint torque exceeds some maximum torque value (Fig. 2.4).

2.5 Conclusion

Using the above connections, interfaces, simulations, and algorithms, we were successful in controlling the SIA5D robotic arm using the Hololens. Both manual and automatic modes work as described, and the torque state algorithms, based on the robotic arm's specifications, are able to predict joint torques. While all of the aforementioned connections (e.g. websockets, ROSbridge, publishers and subscribers, MoveIt!) have been employed in previous academic and industrial work, our intuitive robotic control interface is the first application, to our knowledge, to combine all of them in a seamless pipeline from Hololens to robotic motion. This integration will help pave the way for future applications of augmented reality to practical, industrial, and other applications.

2.6 Future Work

Expanding the options and capabilities of our control modes would improve the user experience, as well as make our project more usable in a wide variety of environments and applications. For example, the ability to manipulate all of the robot linkages, instead of just the end effector, would allow for much more precise control of joint positions and robot poses, as well as adding greater obstacle avoidance capabilities.

Implementing a mesh-based obstacle avoidance functionality would aid in maneuvering the robotic arm in tight spaces, as well as areas with several obstacles to the robotic arm's motion. One of the Hololens' core attributes is the ability to detect its surroundings; by using several cameras mounted around the headset, the Hololens can generate a 2D mesh of its environment—essentially creating a map of all visible obstacles around it. One could envision feeding this mesh into the motion planning algorithm, thus giving the application the ability to plan the path of the robotic arm around any visible obstacles.

Reducing the time delay involved in our near-real-time manual control would also aid the user experience. Due to the large number of connections, algorithms, and interfacing involved, the delay between the user dragging the holographic arm and the robotic arm reaching the corresponding pose is approximately one second. This could be potentially be reduced by using lower-level interfaces with the Yaskawa Motoman robot controller itself; field programmable gate arrays (FPGA's), for example, could potentially speed up communications by eliminating the overhead of ROS.

Acknowledgements We would like to acknowledge the 2018 Dynamics Summer School at the Los Alamos National Laboratory for sponsoring this project as well as James Riback and Anita Jaramillo for their contributions to this project.

References

1. Kim, S.L., Suk, H.J., Kang, J.H., Jung, J.M., Laine, T.H., Westlin, J.: Using unity 3D to facilitate mobile augmented reality game development. In: 2014 IEEE World Forum on Internet of Things (WF-IoT), pp. 21–26. IEEE, Hoboken (2014)
2. Lee, A., Lee, J.-H., Kim, J.: Data-driven kinematic control for robotic spatial augmented reality system with loose kinematic specifications. ETRI J. **38**(2), 337–346 (2016)
3. Kuriya, R., Tsujimura, T., Izumi, K.: Augmented reality robot navigation using infrared marker. In: Robot and Human Interactive Communication (RO-MAN), 2015 24th IEEE International Symposium on, pp. 450–455. IEEE, Hoboken (2015)
4. Zeng, H., Wang, Y., Wu, C., Song, A., Liu, J., Ji, P., Xu, B., Zhu, L., Li, H., Wen, P.: Closed-loop hybrid gaze brain-machine interface based robotic arm control with augmented reality feedback. Front. Neurorobot. **11**, 60 (2017)
5. Yew, A.W.W., Ong, S.K., Nee, A.Y.C.: Immersive augmented reality environment for the teleoperation of maintenance robots. Procedia CIRP. **61**, 305–310 (2017)
6. Hashimoto, S., Ishida, A., Inami, M., Igarashi, T.: Touchme: an augmented reality based remote robot manipulation. In: 21st International Conference on Artificial Reality and Telexistence, Proceedings of ICAT2011. Osaka University, Osaka (2011)
7. Fang, H.C., Ong, S.K., Nee, A.Y.C.: Interactive robot trajectory planning and simulation using augmented reality. Robot. Comput. Integr. Manuf. **28**(2), 227–237 (2012)
8. Fang, H.C., Ong, S.K., Nee, A.Y.C.: Orientation planning of robot end-effector using augmented reality. Int. J. Adv. Manuf. Technol. **67**(9–12), 2033–2049 (2013)
9. Bau, O., Poupyrev, I.: REVEL. ACM Trans. Graph. **31**(4), 1–11 (2012)
10. Zhao, Z., Huang, P., Lu, Z., Liu, Z.: Augmented reality for enhancing tele-robotic system with force feedback. Robot. Auton. Syst. **96**, 93–101 (2017)
11. Chen, R.-J., Lin, H.-W., Chang, Y.-H., Wu, C.-T., Lee, S.-T.: Development of an augmented reality force feedback virtual surgery training platform. Int J. Autom. Smart Technol. **1**(1), 41–51 (2011)
12. Culbertson, H., Kuchenbecker, K.J.: Ungrounded haptic augmented reality system for displaying roughness and friction. IEEE-ASME Trans. Mech. **22**(4), 1839–1849 (2017)
13. Lee, S., Lucas, N.P., Darin Ellis, R., Pandya, A.: Development and human factors analysis of an augmented reality interface for multi-robot tele-operation and control. In: Unmanned Systems Technology XIV, vol. 8387, p. 83870N. International Society for Optics and Photonics, Baltimore, Maryland (2012)
14. Hu, Y., Meng, W.: Rosunitysim: Development and experimentation of a real-time simulator for multi-unmanned aerial vehicle local planning. Simulation. **92**(10), 931–944 (2016)
15. Mizuchi, Y., Inamura, T.: Cloud-based multimodal human-robot interaction simulator utilizing ros and unity frameworks. In: System Integration (SII), 2017 IEEE/SICE International Symposium on, pp. 948–955. IEEE, Hoboken (2017)
16. Codd-Downey, R., Mojiri Forooshani, P., Speers, A., Wang, H., Jenkin, M.: From ROS to unity: leveraging robot and virtual environment middleware for immersive teleoperation. In: Information and Automation (ICIA), 2014 IEEE International Conference on, pp. 932–936. IEEE, Hoboken (2014)
17. Sita, E., Horvath, C.M., Thomessen, T., Korondi, P., Pipe, A.G.: ROS-Unity3D based system for monitoring of an industrial robotic process. In: 2017 IEEE/SICE International Symposium on System Integration (SII). IEEE, Hoboken (2018)

Chapter 3
Optimizing Logarithmic Decrement Damping Estimation via Uncertainty Analysis

Jared A. Little and Brian P. Mann

Abstract The logarithmic decrement method is perhaps the most common technique for estimating the damping ratio of linear systems with viscous damping. The approach directly relates the damping ratio to two samples collected from peaks of a recorded free oscillation. These peaks are separated by one or more oscillation periods and are inherently influenced by experimental uncertainty. Literature on the method indicates that improved estimates are sometimes obtained with more periods between samples. However, it is unknown when improvements can be expected for a given data set because there is a trade-off between the chosen number of periods and measurement noise. A guideline for selecting the number of periods which minimizes uncertainty in estimated damping is desired.

In this work, an analytical expression is derived for the optimal number of periods between peaks. This expression, obtained from an uncertainty analysis of the logarithmic decrement equation, is shown to be a function of only one system parameter: the damping ratio. This suggests that for linear systems with viscous damping there is a unique, damping-dependent period choice which guarantees minimum uncertainty in the estimated damping ratio. This result is used to obtain an optimal amplitude ratio which offers a simple, accurate, and easy to implement guideline for selecting a second sample. The derived expressions are applied to a set of numerical systems to confirm their validity.

Keywords Logarithmic decrement · Uncertainty analysis · Optimization · System identification · Damping

3.1 Introduction

The logarithmic decrement method is a fundamental technique in the field of vibrations. It is used to estimate viscous damping in single degree-of-freedom linear oscillators or in small oscillations about equilibria of nonlinear systems. The method's satisfying analytical derivation and seemingly simple implementation lend to its widespread use and ubiquity in vibrations textbooks [1]. Satisfaction with the technique quickly wanes when put into practice, however, since the approach requires unguided choices which greatly influence accuracy. Specifically, the method's derivation permits any number of periods between samples. However, the number of response periods between measurements can greatly influence accuracy in the presence of experimental noise. Nevertheless, little guidance is currently provided for this choice, as the approach has been the subject of very little additional research since its inception.

One previous work attempted to address the problem of period choice through uncertainty analyses incorporating amplitude and temporal uncertainties [2]. The primary contribution of that work was a numerically generated graphical guideline for selecting an effective number of periods for a range of damping ratios. The work presented in this study employs a similar approach, but with significant extensions, to identify appropriate choices which minimize uncertainty in the estimated damping. The result is an analytical expression for the optimal number of periods and a corresponding optimal amplitude ratio, which is simple to teach and implement.

The remainder of this work is organized as follows. First, the uncertainty analysis and subsequent optimization performed on the logarithmic decrement equation are described resulting in expressions for the optimal number of periods and corresponding amplitude ratio. This is followed by a numerical study verifying the findings of the optimization. Finally, the implications of the discoveries are discussed.

J. A. Little (✉) · B. P. Mann
Department of Mechanical Engineering and Materials Science, Pratt School of Engineering, Duke University, Durham, NC, USA
e-mail: jal87@duke.edu

N. Dervilis (ed.), *Special Topics in Structural Dynamics & Experimental Techniques, Volume 5*, Conference Proceedings of the Society for Experimental Mechanics Series, https://doi.org/10.1007/978-3-030-12243-0_3

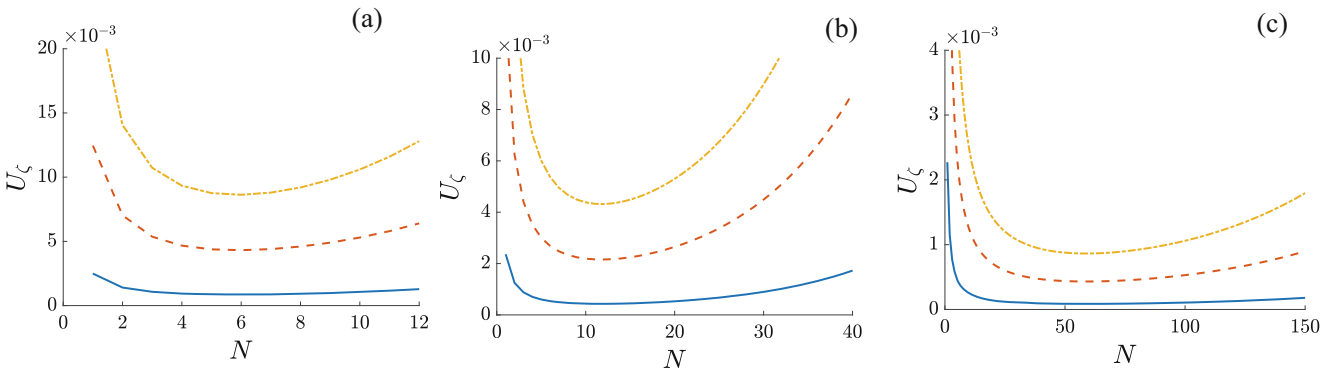

Fig. 3.1 Uncertainty in damping ratio U_ζ versus N for $U_x = 0.01$ (blue solid), $U_x = 0.05$ (red dashed), and $U_x = 0.1$ (yellow dot-dashed) for nominal damping of (**a**) $\zeta = 0.030$, (**b**) $\zeta = 0.015$, and (**c**) $\zeta = 0.003$

3.2 Analysis

The logarithmic decrement method assumes motion of the system takes the form of an unforced linear oscillator with exponential decay. Subsequently, the observed damping ratio is directly related to two samples collected at response peaks by

$$\zeta(\delta) = \frac{\delta}{\sqrt{(2\pi)^2 + \delta^2}} \tag{3.1}$$

where $\delta = \frac{1}{N}\ln(x_0/x_N)$ is the logarithmic decrement, x_0 is the magnitude of the first sample, and x_N is the magnitude of the sample N periods later. Applying uncertainty propagation to Eq. (3.1) [3], uncertainty in estimated damping U_ζ is related to uncertainty in the measurements U_x by

$$U_\zeta^2 = \left[\left(\frac{\partial\zeta}{\partial x_0}\right)^2 + \left(\frac{\partial\zeta}{\partial x_N}\right)^2\right] U_x^2 \tag{3.2}$$

where U_x affects both measurements equally and is the cumulative result of experimental uncertainties including noise and temporal misalignment of the samples relative to the oscillation period. Plots of U_ζ for various damping cases and U_x levels across a range of N, such as those in Fig. 3.1, clearly show the limited benefit of increases in N. Also apparent is a minimum uncertainty that occurs at different N for each damping ratio. The optimal number of periods $\tilde{N}$ is found by setting the derivative of U_ζ with respect to N to zero and solving for N leading to the following expression

$$\tilde{N}(\zeta) = \frac{\sqrt{1-\zeta^2}}{2\pi\zeta}\left[\frac{2+W_0(2/e^2)}{2}\right] \tag{3.3}$$

where $W_0(2/e^2)$ is a constant found by evaluating the principal branch of the Lambert W function at $2/e^2$. Equation (3.3) provides the number of periods corresponding to the lowest uncertainty in estimated damping and is a function of only the damping ratio. This expression is plotted in Fig. 3.2, where both the continuous function and the function rounded to the nearest integer, as would be used in practice, are shown. Figure 3.2b shows that for higher damping, the optimal number of periods drops to 0, signifying the method is not practical for these systems.

Although $\tilde{N}$ is now known, its dependence on ζ makes implementation difficult. However, by identifying that the damping-dependent term in Eq. (3.3) is equal to $1/\delta$, the amplitude ratio of minimum uncertainty $x_{\tilde{N}}/x_0$ (i.e. the ratio of amplitudes observed when $N = \tilde{N}$) can be derived. This provides the optimal amplitude of the second sample relative to the first and is found to be

$$\frac{x_{\tilde{N}}}{x_0} = e^{-\left[\frac{2+W_0(2/e^2)}{2}\right]} \approx 0.3299 \tag{3.4}$$

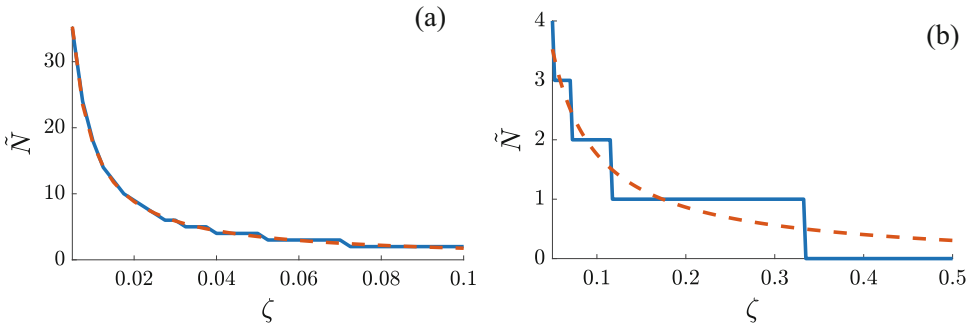

Fig. 3.2 Continuous (orange dashed) and nearest integer (blue solid) $\tilde{N}$ as a function of damping ratio for ranges (**a**) $0.005 < \zeta < 0.1$ and (b) $0.05 < \zeta < 0.5$

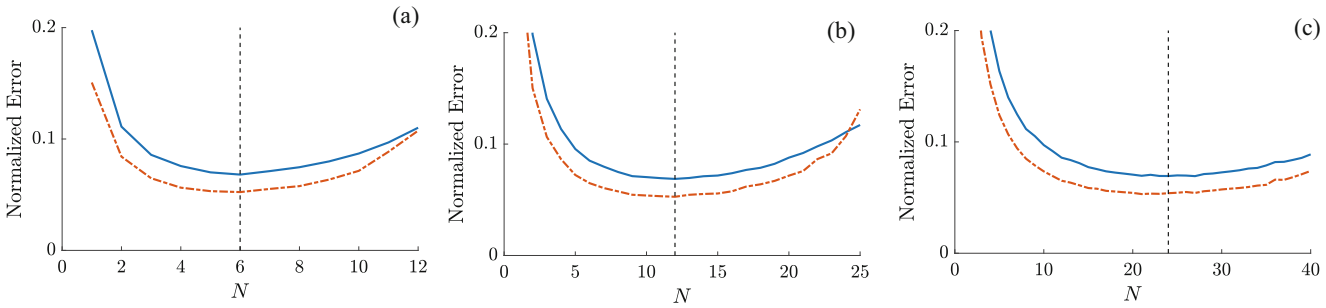

Fig. 3.3 Normalized average error (blue solid) and standard deviation of error (orange dot-dashed) of damping estimates versus N for systems where (**a**) $\zeta = 0.03$, (**b**) $\zeta = 0.015$, and (**c**) $\zeta = 0.0075$ with predicted $\tilde{N}$ (vertical dashed black) for comparison

This result offers an elegant guideline for identifying a second sample as it indicates that, for all systems where the original assumptions of the method hold, there is a constant amplitude ratio guaranteeing minimum uncertainty in estimated damping.

3.3 Results

The optimization performed in the previous section successfully identified the minimum of the uncertainty expression. To determine if the findings accurately reflect experimental conditions, a set of numerical studies were performed. The free vibration response of a linear oscillator was simulated for multiple damping ratios. For each simulated response, Gaussian noise was added 10,000 times and damping was estimated using logarithmic decrement over a range of N. The numerous estimates allowed for an average error and standard deviation of the error to be calculated for each N. Three cases are presented in Fig. 3.3. It is clear from these plots that both average estimation error and its standard deviation are minimized when damping is estimated using the $\tilde{N}$ value derived in this work, suggesting the findings are valid.

3.4 Conclusion

The uncertainty analysis and subsequent optimization performed in this work has provided an analytical expression, supported by numerical examples, for the optimal number of periods between samples. This result led to the discovery of a constant optimal amplitude ratio offering a straightforward guideline for obtaining best possible estimates when applying logarithmic decrement. The implications of these findings on the use of logarithmic decrement are numerous. For example, the damping ratios where the method is ineffective are now known. Additionally, since the non-zero minimum uncertainty is a function of uncertainty in the data, the findings of this work can be used in conjunction with other signal analysis methods (e.g. smoothing, filtering, etc.) to further reduce uncertainty in the estimates obtained. By optimally balancing the trade-off

between increased N and measurement error, experimenters can estimate damping with confidence in their results. Thus, the satisfying simplicity of the method is no longer lost in its difficulty of experimental application.

References

1. Meirovitch, L.: Fundamentals of Vibrations. Waveland Press, Long Grove (2010)
2. Tweten, D.J., Ballard, Z., Mann, B.P.: Minimizing error in the logarithmic decrement method through uncertainty propagation. J. Sound Vib. **333**(13), 2804–2811 (2014)
3. Hughes, I., Hase, T.: Measurements and Their Uncertainties: A Practical Guide to Modern Error Analysis. Oxford University Press, Oxford (2010)

Chapter 4
A Simplified Current Blocking Piezoelectric Shunt Circuit for Multimodal Vibration Mitigation

Ghislain Raze, Andy Jadoul, Valery Broun, and Gaetan Kerschen

Abstract This paper presents a novel arrangement of a current blocking shunt circuit for the mitigation of multiple structural resonances. The number of required electrical components is reduced compared to the previous versions of this circuit proposed in the literature. This paper also proposes a tuning methodology for the electrical parameters of this circuit based on the evaluation of the electromechanical coupling between the electrical circuit and the structure. Effective mitigation performance can be expected with little knowledge of the host structure. A comparison with the solutions in the literature demonstrates the efficiency of the proposed approach.

Keywords Piezoelectric absorber · Multimodal damping · Passive control · Two-port network

4.1 Introduction

Piezoelectric shunt damping terms a mean by which a piezoelectric transducer mechanically connected to a host structure is used to mitigate the vibratory amplitude of this structure. Thanks to the direct piezoelectric effect, a part of the mechanical energy of the vibrating structure is transformed into electrical energy by the transducer. This energy can efficiently be dissipated with the help of a shunt circuit, usually composed of an inductor and a resistor arranged either in series [1] or in parallel [2]. Hence, piezoelectric shunt damping can be used to mitigate the vibratory amplitude of a resonance of a structure.

One of the advantage of piezoelectric shunt damping is the possibility to passively control multiple structural modes if the electrical circuit is properly designed. A number of ad-hoc circuits aimed at multiple mode shunt damping can be found in the literature. The current blocking shunt circuit proposed by Wu [3] and the current flowing shunt circuit proposed by Behrens et al. [4] are well-known examples of such circuits. The former is efficient but requires a large number of electrical components to be implemented. The latter requires less electrical components but it has been shown by Cigada et al. [5] that tuning this circuit results from a tradeoff between damping performance and tuning easiness.

The purpose of this paper is to present a new simplified current blocking shunt circuit for the mitigation of multiple structural resonances and to provide and associated tuning methodology. This circuit does not suffer from the same tradeoffs as the current flowing shunt circuit, and generally requires less electrical components than the arrangements of the current blocking circuit proposed in the literature.

4.2 Simplified Current Blocking Shunt Circuit

A new arrangement for the current blocking circuit is presented in Fig. 4.1. This circuit consists in a periodic repetition of a current blocking filter (parallel LC circuit) and a shunt branch (series RL or parallel RL branch, generically represented as $Z_{s,i}$, $i = 1, \ldots, N$ in Fig. 4.1). Each branch is tuned to a specific resonance frequency. The impedance of a shunt branch generally decreases with increasing frequency of the structural mode it is tuned to. At a given frequency, the branches tuned to a higher structural frequency appear nearly as a short circuit compared to the branch of interest. To prevent current from bypassing this branch, the access to the lower-impedance branches is forbidden by a current blocking filter. At the

G. Raze (✉) · G. Kerschen
Department of Aerospace and Mechanical Engineering, University of Liege, Liège, Belgium
e-mail: G.Raze@uliege.be

A. Jadoul · V. Broun
Departement Ingenieur Industriel, Haute Ecole de la Province de Liege, Liège, Belgium

N. Dervilis (ed.), *Special Topics in Structural Dynamics & Experimental Techniques, Volume 5*, Conference Proceedings of the Society for Experimental Mechanics Series, https://doi.org/10.1007/978-3-030-12243-0_4

frequency of interest, this filter has an infinitely high impedance which rapidly decreases away from this frequency. If the shunt branches are arranged in ascending order of structural frequencies they are tuned to, this shunt circuit can act like a classical single-mode shunt circuit at multiple resonance frequencies.

Compared to the original current blocking shunt circuit and its modified version proposed by Wu [3], the simplified current blocking shunt circuit has the advantage of requiring a number of electrical components that grows linearly with respect to the number of modes to be controlled (whereas this growth is quadratic in [3]).

4.3 Tuning Methodology

This section proposes a tuning methodology that is based on the knowledge of the electromechanical coupling between the piezoelectric transducer and the structure (through the resonance frequencies when the electrodes of the piezoelectric transducer are short-circuited and open-circuited) and the electrical parameters (including the piezoelectric capacitance at constant strain). For each shunt branch, an optimal impedance is computed from the single-mode shunt formulas available in the literature (in this paper, the formulas in [6] are used for series RL shunt circuits and the formulas in [2] are used for parallel RL shunt circuits).

The methodology is divided into several steps in which each shunt branch and its associated current blocking filter are tuned. Since the impedance of the current blocking filter is very high at the frequency of interest, the electrical elements placed after it (to its right in Fig. 4.1) may be neglected, i.e. approximated as a short circuit. This way, thanks to the current blocking filters, the shunt branches and associated current blocking filters can be tuned sequentially in ascending order. At a given step of the methodology, there are no other unknowns than the ones related to the structural mode of interest. The capacitance of the filter is left as a degree of freedom in the design. The inductance of the filter is simply determined by requiring that the resonance frequency of the filter be equal to the considered structural resonance frequency. Finally, the resistance and inductance of the shunt branch are tuned according to the method explained hereafter.

The tuning problem of a shunt branch can be modelled in a general way by abstracting the surrounding electrical network as a two-port network. One port is connected to the shunt branch and the other is connected to the piezoelectric transducer. To simplify the problem, the electrical characteristics of the piezoelectric transducer and of the two-port network are first reduced to an RLC circuit. The capacitance of this reduced circuit is used to assess the electromechanical coupling between the shunt branch and the structure, based on the electromechanical coupling of the piezoelectric transducer and the structure. An optimal impedance can then be computed using single-mode shunt formulas from the literature. The resistance and inductance of the shunt branch are finally determined by requiring that their combination with the resistance and inductance of the reduced circuit be an impedance equal to the optimal impedance.

The proposed tuning methodology is simple and requires the knowledge of a limited number of parameters of the electromechanical system. These parameters are relatively easy to obtain either numerically or experimentally. It yields satisfactory performance without the need for costly numerical optimization algorithms. Figure 4.2 illustrates this statement with a two-degree-of-freedom spring mass system to which a piezoelectric transducer is attached. This piezoelectric transducer is then connected to a current blocking shunt circuit. The filter capacitance is chosen in each case equal to the piezoelectric capacitance at constant strain. The amplitudes of the two structural modes are reduced using either series or parallel shunt branches. An improvement in performance can be observed with the new tuning methodology, especially on mode 2.

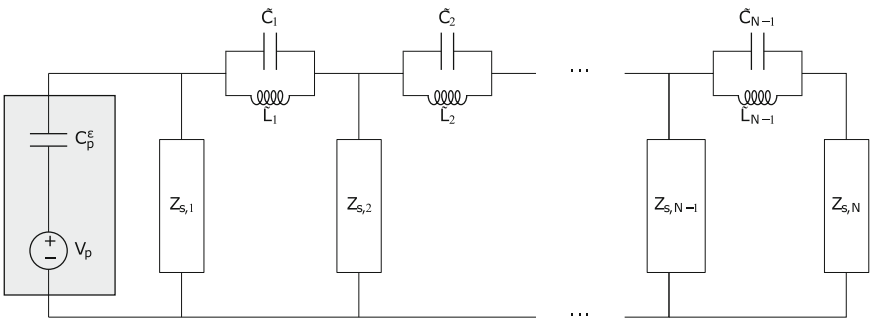

Fig. 4.1 A simplified current blocking shunt circuit to control N structural frequencies

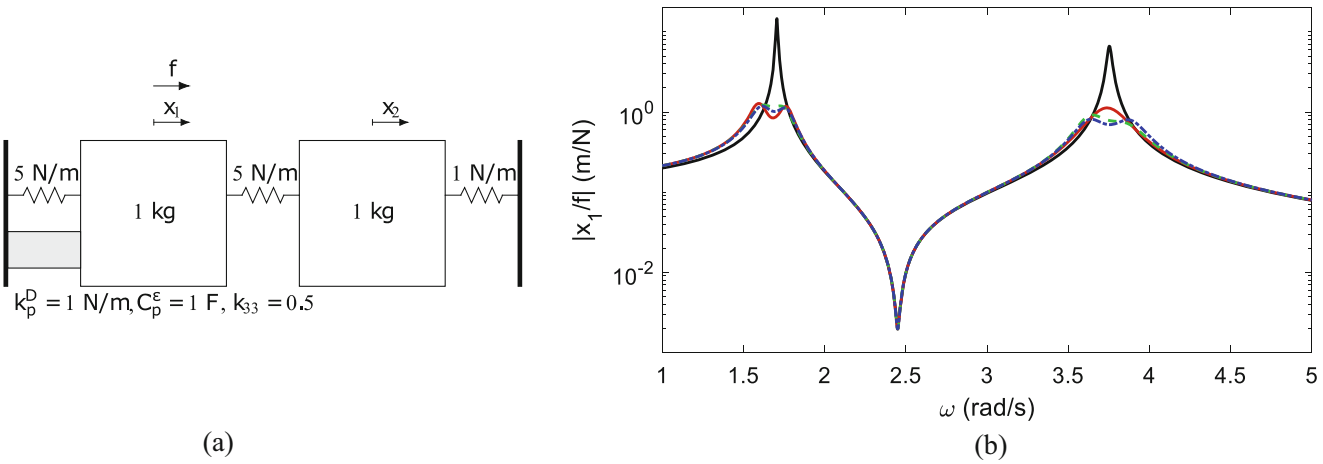

(a) (b)

Fig. 4.2 Considered two-degree-of-freedom system (**a**) and corresponding frequency response function (**b**): open-circuit piezoelectric transducer (-), Wu's modified current blocking circuit [3] (–), simplified current blocking circuit with parallel RL shunt branches (– –) and simplified current blocking shunt circuit with series RL shunt branches (-·-)

4.4 Conclusion

This paper presented a simplified current blocking shunt circuit able to mitigate the vibratory amplitude of multiple resonance frequencies. This new arrangement results in a reduced number of electrical components compared to previous arrangements in the literature. Thanks to the proposed tuning methodology, a near-optimal design can be obtained with limited knowledge of the electromechanical system.

Acknowledgements The authors G. Raze and G. Kerschen would like to acknowledge the financial support of the SPW (WALInnov grant 1610122).

References

1. Hagood, N.W., von Flotow, A.: Damping of structural vibrations with piezoelectric materials and passive electrical networks. J. Sound Vib. **146**(2), 243–268 (1991)
2. Wu, S.-Y.: Piezoelectric shunts with a parallel R-L circuit for structural damping and vibration control. In: Smart Structures and Materials 1996: Passive Damping and Isolation, 2720, pp. 259–279. SPIE Press, Bellingham, WA (1996)
3. Wu, S.-Y.: Method for multiple-mode shunt damping of structural vibration using a single PZT transducer. In: Smart Structures and Materials 1998: Passive Damping and Isolation, vol. 3327, pp. 159–169. SPIE Press, Bellingham, WA (1998)
4. Behrens, S., Fleming, A.J., Moheimani, S.O.R.: Multiple mode current flowing passive piezoelectric shunt controller. J. Sound Vib. **266**(5), 929–942 (2003)
5. Ciagada, A., Manzoni, S., Redaelli, M., Vanali, M.: Optimization of the current flowing technique aimed at semi-passive multi-modal vibration reduction. J. Vib. Control. **18**(2), 298–312 (2012)
6. Soltani, P., Kerschen, G., Trondeau, G., Deraemaeker, A.: Piezoelectric vibration damping using resonant shunt circuits: an exact solution. Smart Mater. Struct. **23**(12), 125014 (2014)

Chapter 5
Using the SEREP Idea for the Projection of Modal Coordinates to Different Finite Element Meshes

Wolfgang Witteveen, Pöchacker Stefan, and Florian Pichler

Abstract Reduced order modelling is of crucial importance for the dynamics of complex Finite Element structures. Thereby the overall deformation state is approximated by a superposition of weighted trial vectors, commonly called modes. The weighting factors ('modal coordinates') are obtained by numerical time integration of the reduced order model. In case of complex systems, the time integration normally dominates the overall simulation time. A multibody simulation of a flexible crankshaft interacting with pistons, con rods, fly wheel, hydrodynamic bearings and furthers for instance, takes at least several hours of CPU time. The modal coordinates can then be used for modal stress recovery in order to predict the fatigue lifetime. If a variant of the flexible body with small changes needs to be investigated, a new numerical time integration is necessary. In this paper a method is proposed where the modal coordinates of a flexible body will be projected unto another mode base. This will be done by using the key idea of the SEREP method where the modal coordinates are computed via the Pseudo-Inverse. One academic and one industrial example demonstrate that the time integration of the variant can totally be skipped without remarkable loss of accuracy, as long as the differences between the two flexible bodies are small enough.

Keywords Model reduction · Modal stress recovery · SEREP

5.1 Introduction

Efficient multibody simulation normally utilizes model reduction for the dynamics of Finite Element (FE) structures. Thereby the overall deformation state is approximated by a superposition of weighted trial vectors, commonly called modes. The weighting factors ('modal coordinates') are the remaining degrees of freedom (dof) for the time integration. The number of modal coordinates is normally significant smaller than the number of nodal dof of the FE structure. In case of an FE mesh of a 6-cylinder crankshaft, which can be used for stress based fatigue life prediction, more than 10^7 dof are common. Model reduction reduces the problem size to maximal several hundred modes (=dof) which is suitable for efficient multibody simulation. The result of the time integration are the modal scaling factors at each time. These modal scaling factors can then be used for efficient stress recovery which is based on so called "modal stress shapes", see [1, 2] for more details. The idea of modal stress recovery offers a very efficient possibility for fatigue life prediction when a channel based fatigue life software is used [3]. Figure 5.1 contains a typical flow of a mode based fatigue life prediction.

In case of complex systems, the time integration inside the multibody simulation software is the most time consuming task. In case of a 6-cylinder crank drive with (elasto-) hydrodynamic main bearings a run up simulation needs more than 50 h CPU time. A small change in the FE model, like another notch radius, results in a new FE computation, a new multibody simulation and a new fatigue life prediction. In order to accelerate an evaluation of a variant according to Fig. 5.1 a new method is proposed below. Thereby the modal coordinates of the variant are computed based on the modal coordinates of the original FE model without performing the expensive time integration.

W. Witteveen (✉) · P. Stefan · F. Pichler
Degree Program Mechanical Engineering, Upper Austria University of Applied Sciences, Wels, Austria
e-mail: wolfgang.witteveen@fh-wels.at

N. Dervilis (ed.), *Special Topics in Structural Dynamics & Experimental Techniques, Volume 5*, Conference Proceedings of the Society for Experimental Mechanics Series, https://doi.org/10.1007/978-3-030-12243-0_5

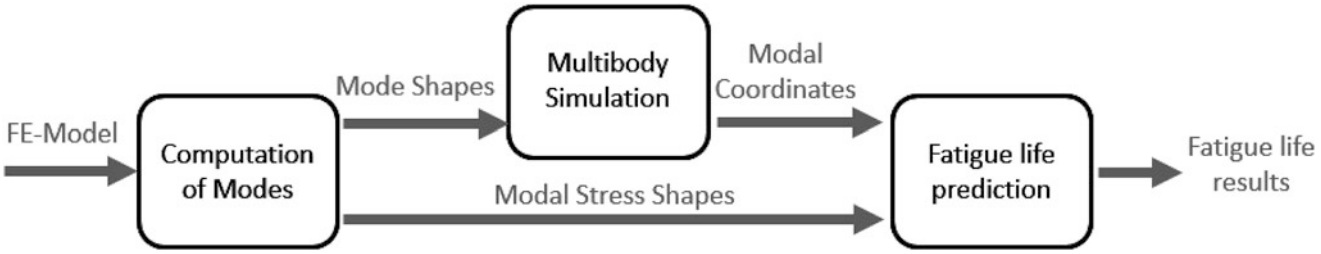

Fig. 5.1 Typical flow of mode based fatigue life prediction

5.2 Theory

The translational (and maybe rotational) degrees of freedom of the involved Finite Element models are collected in the vectors $\mathbf{x}$ and $\mathbf{y}$:

$$\mathbf{x} = \begin{bmatrix} \mathbf{x}_C \\ \mathbf{x}_R \end{bmatrix} \qquad \mathbf{y} = \begin{bmatrix} \mathbf{y}_C \\ \mathbf{y}_R \end{bmatrix} \tag{5.1}$$

The $(n_x\ x\ 1)$ vector $\mathbf{x}$ holds the degrees of freedom (dof) of the original model for which a numerical simulation has been performed. The $(n_y\ x\ 1)$ vector $\mathbf{y}$ holds the dof of a model which is a variant of the original one. Both vectors are used to describe the nodal deflection of either the original or the variant at one particular time instant. We assume that a coincident set of dof exist in both models. This set is collected into the $(n_C\ x\ 1)$ vectors $\mathbf{x}_C$ and $\mathbf{y}_C$. The subscript R denotes the remaining degrees of freedom. In reality, the dof vectors of the original and the variant will not have the former structure and need to be rearranged in order to appear like it is stated in (5.1).

If it is assumed that model order reduction via projection is performed the nodal displacements are approximated by a set of modes. This can be written as

$$\mathbf{x} = \boldsymbol{\Phi}_x\ \mathbf{q}_x \qquad \mathbf{y} = \boldsymbol{\Phi}_y\ \mathbf{q}_y \tag{5.2}$$

where the $(n_x\ x\ r_x)$ matrix $\boldsymbol{\Phi}_x$ contains in its columns the r_x modes which are used to approximate the deformation of the original. The according modal coordinates are stored in the $(r_x\ x\ 1)$ vector $\mathbf{q}_x$. The $(n_y\ x\ r_y)$ mode matrix of the variant is called $\boldsymbol{\Phi}_y$ and its modal coordinates are collected in the $(r_y\ x\ 1)$ vector $\mathbf{q}_y$. Using the subdivision introduced in (5.1), the equations given in (5.2) can be rearranged in the form of

$$\begin{bmatrix} \mathbf{x}_C \\ \mathbf{x}_R \end{bmatrix} = \begin{bmatrix} \boldsymbol{\Phi}_{x,C} \\ \boldsymbol{\Phi}_{x,R} \end{bmatrix} \mathbf{q}_x \qquad \begin{bmatrix} \mathbf{y}_C \\ \mathbf{y}_R \end{bmatrix} = \begin{bmatrix} \boldsymbol{\Phi}_{y,C} \\ \boldsymbol{\Phi}_{y,R} \end{bmatrix} \mathbf{q}_y \tag{5.3}$$

where the $(n_C\ x\ r_x)$ matrix $\boldsymbol{\Phi}_{x,C}$ holds the partition of $\boldsymbol{\Phi}_x$ which is associated with the dof collected in $\mathbf{x}_C$. Very similar a $(n_C\ x\ r_y)$ matrix $\boldsymbol{\Phi}_{y,C}$ can be given for the FE model holding the variant.

The basic idea of the presented approach is that local modifications will just minimally change the global deformation state during the numerical time integration. Therefore, the computation of $\mathbf{q}_y$ is based on the assumption

$$\mathbf{x}_C \approx \mathbf{y}_C \tag{5.4}$$

In the spirit of the SEREP method [4], the pseudo inverse is applied to the first line of the right equation in (5.3) in order to compute the modal coordinates of the variant based on its nodal deformation:

$$\mathbf{q}_y = \boldsymbol{\Phi}_{y,C}{}^{\dagger} \mathbf{y}_C \tag{5.5}$$

The nodal deformation $\mathbf{y}_C$ is a known quantity because of the assumption in (5.4). The insertion of the according line of the left equation in (5.3) into expression (5.5)) delivers

$$\mathbf{q}_y = \boldsymbol{\Phi}_{y,C}{}^{\dagger} \boldsymbol{\Phi}_{x,C} \mathbf{q}_x \tag{5.6}$$

which holds an equation for the computation of $\mathbf{q}_y$ based on $\mathbf{q}_x$ using the assumption (5.4).

Four obvious requirements can be stated for a successful application of the proposed approach:

- The first requirement is the validity of Eq. (5.4). If the structural modifications of the variant are not minor and local enough, a full numerical simulation would lead to modal coordinates $\mathbf{q}_y$ which differ from the ones computed by Eq. (5.6).
- The second one is, that the number of coincident dof n_C should be significant higher as the number of modes r_x and r_y.
- It is recommended that the location of the dof inside $\mathbf{x}_C$ is uniformly distributed over the entire structure. A local concentration should be avoided.
- Finally, the mode base $\mathbf{\Phi}_y$ needs to be of sufficient quality, so that the occurring deformations can be represented.

5.3 Academic Example: Cantiliver Beam

The first example is of academic nature and deals with a circular cantilever beam having two different cross sections, see Fig. 5.2. Consequently, there is a notch at the boundary of those two sections. In the FE model, which is called "original", no radius is modelled in the notch. In the "variant" model, a small radius is regarded. This can be seen in Fig. 5.2 as well.

The cantilever is loaded on the tip with a time varying load. The FE Modell has been created in ABAQUS [5] and imported via the "*mnf*—interface" into the multibody simulation software MSC.ADAMS [6]. As it can be read in the according manuals, the mnf file contains the so called Craig/Bampton [7] modes. The modal stresses and the modal coordinates have been imported into the fatigue life software FEMFAT [8] and the safety factor against fatigue failure has been computed. Three different result distributions are depicted in Fig. 5.3.

The outer left and the middle picture contain the results when the modal coordinates have been computed based on time integration within MSC.ADAMS. The outer left picture holds the result of the original (no radius) and the middle picture holds the result of the variant with a radius in the notch. The outer right picture holds again the distribution of the safety factor against fatigue failure of the FE model with the notch radius. In contrast to the middle picture, the modal coordinates have been computed based on the modal coordinates of the original using the projection (5.6) instead of a full time integration. It can be seen, that the results are almost the same.

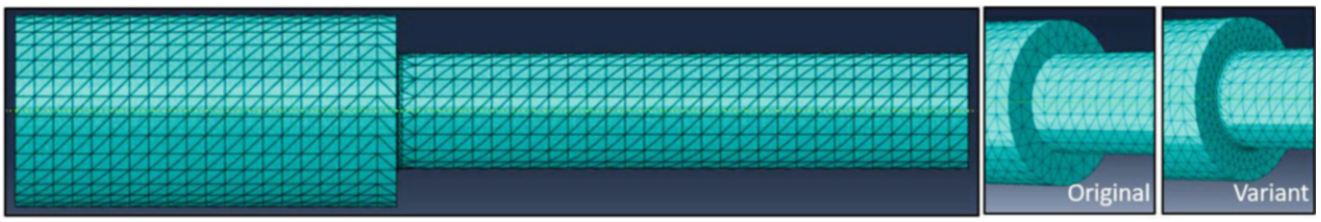

Fig. 5.2 Circular cantilever beam

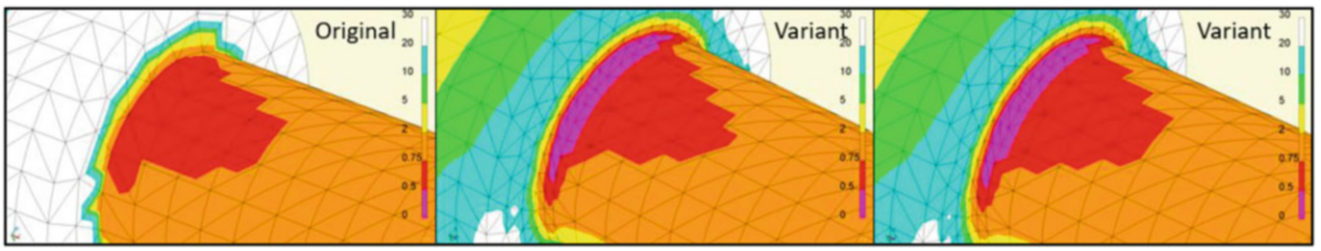

Fig. 5.3 Cantilever beam—Distribution of safety factor against fatigue failure

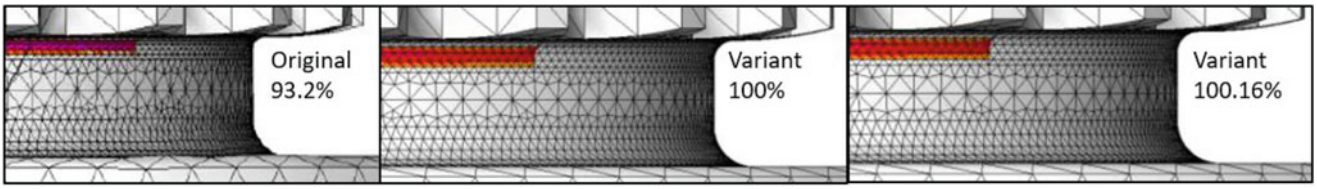

Fig. 5.4 Crankshaft (Detail)—Distribution of safety factor against fatigue failure

5.4 Industrial Example: Crankshaft

The second example is of industrial nature. It deals with modal stress based computation of the safety factor against fatigue failure of a 6-cylinder crankshaft. The overall process is dominated by the multibody simulation of the entire crank drive, which needs more than 60 h CPU time. It is a common scenario in the development of a crankshaft that the safety factor against fatigue failure of many variants needs to be evaluated. The changes in those variants are very small like a different shape of a particular notch.

Figure 5.4 contains again three pictures of a detail of the crankshaft. The outer left one holds a small part of the original crankshaft with a notch radius of 0.6 mm. The middle picture holds the result for a variant where the radius has been modified to 1 mm. That picture is kind of a reference because the modal coordinates have been determined using a full time integration. The normalized result of this computation is 100%. The outer right picture contains the result when the modal coordinates have been computed by means of the modal coordinates of the original, which needs a couple of minutes CPU time. The normalized result is 100.16% and almost identical but a significant amount of time has be saved.

5.5 Conclusion

A method has been presented which allows the computation of the modal coordinates of a variant based on the modal coordinates of the original without performing a time integration. The underlying projection will deliver suitable results when the global deformation state of the variant can be approximated with the one of the original FE model. In case of complex multibody simulation models a significant amount of time can be saved.

References

1. Schwertassek, R., Dombrowski, S.V., Wallrapp, O.: Modal representation of stress in flexible multibody simulation. Nonlinear Dyn. **20**, 381–399 (1999)
2. Tobias, C., Berhard, P.: Stress recovery with Krylov-subspaces in reduced elastic multibody systems. Multibody Sys. Dyn. **25**, 377–393 (2011)
3. Fischer, P., Witteveen, W., Schabasser, M.: Integrated MBS-FE-durability analysis of truck frame components by modal stresses. In: 15th ADAMS Users Conference (2000)
4. Callahan, J., Avitabile, P., Riemer, R.: System equivalent reduction expansion process (SEREP). In: Proceedings of the 7th International Modal Analysis Conference, pp. 29–37. Society of Experimental Mechanics, Bethel, CT (1989)
5. https://www.3ds.com/de/produkte-und-services/simulia/produkte/abaqus
6. http://www.mscsoftware.com
7. Bampton, M.C.C., Craig, R.R.: Coupling of substructures for dynamic analyses. AIAA J. **6**(7), 1313–1319 (1968)
8. http://www.femfat.com

Chapter 6
Identification System for Structural Health Monitoring in Buildings

Jesús Morales-Valdez, Luis Alvarez-Icaza, José Alberto Escobar, and Héctor Guerrero

Abstract A novel real time system identification method for structural health monitoring in a multi-story buildings is presented. The goal is to identify structural parameters in order to improve damage detection methods. Here, structural dynamics is modeled by means of a wave equation with Kelvin damping, that relates the stiffness loss with reduction of shear wave velocity propagation of seismic movements in structural elements. The identification system requires only acceleration signals and is based on the least squares method with forgetting factor. Moreover, a new parameterization is presented based on linear integral filters, which eliminates constant disturbances and attenuate measurement noise. The experimental results through an RC building, validate the feasibility of the proposed method.

Keywords Parameter estimation · Linear integral filters · Wave propagation · Damage detection · Structural health monitoring

6.1 Introduction

The aging and degradation of the infrastructures, especially multi-story buildings impose a major concern on their safety and reliability. On this point, structural health monitoring (SHM) provides solution to the problem by evaluating the integrity of the infrastructures to determine their current health state at the earliest possible stage. Most methods for structural health monitoring in civil engineering are based on modal analysis, that studies changes in natural frequencies and modal shape. An extensive review of these methods can be found in [1, 2], while [3, 4] present a review of these methods with emphasis on structural engineering applications. Following this line, a comparative study between different methods of damage detection is presented in [5].

Wave propagation methods are an alternative approach that allow studying local characteristics of buildings. Under this idea, works like those of [6–9] present different methods for structural health monitoring and discuss the advantages and limitations of this approach. One of them is that these methods are developed in the frequency domain and consequently are not suitable for real-time applications.

In this article, the work of [7, 8] on wave propagation is extend, by transforming information processing from an offline to a real-time solution. This change allows a more timely damage assessment. In addition, to eliminate bias in acceleration measurements linear integral filters (LIF) are introduced designed to work in the bandwidth of interest of the acceleration spectrum. Subsequently, a fault detection threshold is designed based on the difference between the identified structural parameters and a set of reference values. This article is organized as follows: section II describes the used model, while section III describes the developed damage detection scheme. Finally, experimental results are described in section IV and conclusions are presented in section V.

J. Morales-Valdez (✉)
Automatic Control, Cátedras CONACYT-CINVESTAV, Gustavo A. Madero, CDMX, Mexico
e-mail: jesus.morales@conacyt.mx

L. Alvarez-Icaza · J. Alberto Escobar · H. Guerrero
Instituto de Ingeniería, Universidad Nacional Autónoma de México, México City, Mexico

N. Dervilis (ed.), *Special Topics in Structural Dynamics & Experimental Techniques, Volume 5*, Conference Proceedings of the Society for Experimental Mechanics Series, https://doi.org/10.1007/978-3-030-12243-0_6

Fig. 6.1 Shear building

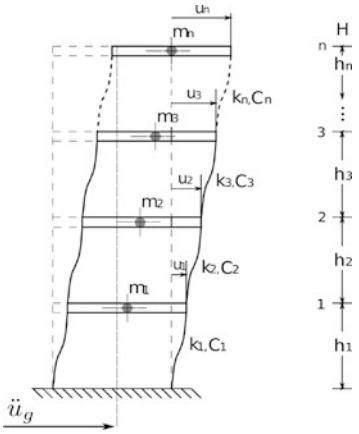

6.2 Mathematical Model

Let the multi-story building shown in Fig. 6.1, whose dynamics is modeled by a one dimensional wave equation with Kelvin damping [10].

$$\beta^2 \frac{\partial^2 u}{\partial y^2} + \eta^2 \frac{\partial^2 \dot{u}}{\partial y^2} = \frac{\partial^2 u}{\partial t^2} \tag{6.1}$$

where β is the shear wave velocity of movement propagation and η is a constant proportional to the damping force. The initial and boundary conditions for this model (6.1) are:

$$u(y,0) = 0 \qquad 0 \le y \le H \tag{6.2a}$$

$$\dot{u}(y,0) = 0 \qquad 0 \le y \le H \tag{6.2b}$$

$$u(0,t) = u_g \qquad 0 < t \tag{6.2c}$$

$$\mu \dot{u}(H,t) = 0 \qquad 0 < t \tag{6.2d}$$

where μ is the shear module. Note that the building is initially at rest according to (6.2a) y (6.2b). Only the base of the structure is excited during a seismic activity, see (6.2c). Moreover, the building is stress free at the roof, according to (6.2d), and finally, the model (6.1), allows to treat the shear building model as an elastic shear beam and therefore the effects of wave propagation can be studied.

6.2.1 Semidiscretization

In order to create an online identification system, the continuous model is discretized in points that coincide with the instrumented floors. Therefore, different shear wave velocities of propagation and damping coefficients are produced. For the points 1 to $n-1$ a centered second-order approximation is used while a first-order *backward* approximation is used for the n point, generating

$$\ddot{u} = \beta_M^2 \Lambda u + \eta_M^2 \Lambda \dot{u} + b\ddot{u}_g \tag{6.3}$$

where β_M^2 and η_M^2 arematrices $\in \mathcal{R}^{p\times p}$, with $p = n+1$, which are defined as follows

$$\beta_M^2 = \begin{bmatrix} 0 & 0 & 0 & \cdots & 0 \\ 0 & \beta_1^2 & 0 & \cdots & 0 \\ 0 & 0 & \beta_2^2 & \cdots & 0 \\ \vdots & \vdots & \vdots & \ddots & \vdots \\ 0 & 0 & \cdots & 0 & \beta_n^2 \end{bmatrix} \qquad \eta_M^2 = \begin{bmatrix} 0 & 0 & 0 & \cdots & 0 \\ 0 & \eta_1^2 & 0 & \cdots & 0 \\ 0 & 0 & \eta_2^2 & \cdots & 0 \\ \vdots & \vdots & \vdots & \ddots & \vdots \\ 0 & 0 & \cdots & 0 & \eta_n^2 \end{bmatrix} \tag{6.4}$$

Elements of matrices in (6.4) are related to the properties of each floor. An important advantage of (6.3) is that the solution of the system does not require any coordinate transformation. Matrix distribution Λ is given by

$$\Lambda = \frac{1}{\Delta h^2}\begin{bmatrix} 0 & 0 & 0 & 0 & \cdots & 0 \\ 1 & -2 & 1 & 0 & \cdots & 0 \\ 0 & 1 & -2 & 1 & \cdots & 0 \\ \vdots & \vdots & \vdots & \ddots & \ddots & \vdots \\ 0 & 0 & \cdots & 1 & -2 & 1 \\ 0 & 0 & \cdots & 0 & 1 & -1 \end{bmatrix}, \qquad b = \begin{bmatrix} 1 \\ 0 \\ 0 \\ \vdots \\ 0 \\ 0 \end{bmatrix} \tag{6.5}$$

$$u = [u_0, u_1, u_2, \ldots, u_n]^T, \ \dot{u} = [\dot{u}_0, \dot{u}_1, \dot{u}_2, \ldots, \dot{u}_n]^T, \\ \ddot{u} = [\ddot{u}_0, \ddot{u}_1, \ddot{u}_2, \ldots, \ddot{u}_n]^T \tag{6.6}$$

and $\Delta h = H/(n+1)$ for uniformly spaced floors. Considering that the acceleration in the boundary condition is measurable and equivalent to the seismic excitation, $\ddot{u}_0 = \ddot{u}_g$. The entries u_0 and $\dot{u}_0 \in \mathcal{R}^+$ within vectors u and $\dot{u} \in \mathcal{R}^{p\times 1}$ in (6.6) describe the displacement and velocity of the ground, respectively. While the remaining floors u_i and $\dot{u}_i$ with $i = 1, 2, \ldots, n$ represent the respective measurements in each floor. Finally $\ddot{u} \in \mathcal{R}^{p\times 1}$ is the absolute acceleration vector.

6.3 Identification System

Assuming that in a real building parameters β_M^2 y η_M^2 are unknown, in this section an identification system is designed to estimate them in real time.

Let the discretized equation (6.3) be rewritten as[1]

$$z = \beta_M^2 \Lambda u + \eta_M^2 \Lambda \dot{u}, \qquad \text{with} \qquad z = (\ddot{u} - b\ddot{u}_g) \tag{6.7}$$

redefining

$$\beta_M^2 \Lambda u = \psi \beta_V^2 = \psi \Theta_\beta \tag{6.8}$$

$$\eta_M^2 \Lambda \dot{u} = \dot{\psi} \eta_V^2 = \dot{\psi} \Theta_\eta \tag{6.9}$$

the elements of the matrices β_M^2 y η_M^2 are used to build the vectors β_V^2 y $\eta_V^2 \ \in \mathcal{R}^{p\times 1}$. Hence, Λu y $\Lambda \dot{u}$ are now matrices with dimension $\mathcal{R}^{p\times p}$. For ease of notation, they are renamed as ψ y $\dot{\psi}$ and defined by

$$\Theta_\beta = \begin{bmatrix} 0 & \beta_1^2 & \beta_2^2 & \beta_3^2 & \ldots & \beta_{n-1}^2 & \beta_n^2 \end{bmatrix}^T \tag{6.10}$$

$$\psi = \frac{1}{\Delta h^2}\begin{bmatrix} 0 & 0 & 0 & 0 & 0 & \cdots & 0 \\ u_0 & -2u_1 & u_2 & 0 & 0 & \cdots & 0 \\ 0 & u_1 & -2u_2 & u_3 & 0 & \cdots & 0 \\ 0 & 0 & u_2 & -2u_3 & u_4 & \cdots & 0 \\ \vdots & \vdots & \vdots & \vdots & \ddots & \ddots & \vdots \\ 0 & 0 & 0 & \cdots & u_{n-2} & -2u_{n-1} & u_n \\ 0 & 0 & 0 & \cdots & 0 & u_{n-1} & -u_n \end{bmatrix} \tag{6.11}$$

$$\Theta_\eta = \begin{bmatrix} 0 & \eta_1^2 & \eta_2^2 & \eta_3^2 & \ldots & \eta_{n-1}^2 & \eta_n^2 \end{bmatrix}^T \tag{6.12}$$

[1] This identification system was first used in [10].

$$\dot{\psi} = \frac{1}{\Delta h^2}\begin{bmatrix} 0 & 0 & 0 & 0 & 0 & \cdots & 0 \\ \dot{u}_0 & -2\dot{u}_1 & \dot{u}_2 & 0 & 0 & \cdots & 0 \\ 0 & \dot{u}_1 & -2\dot{u}_2 & \dot{u}_3 & 0 & \cdots & 0 \\ 0 & 0 & \dot{u}_2 & -2\dot{u}_3 & \dot{u}_4 & \cdots & 0 \\ \vdots & \vdots & \vdots & \vdots & \ddots & \ddots & \vdots \\ 0 & 0 & 0 & \cdots & \dot{u}_{n-2} & -2\dot{u}_{n-1} & \dot{u}_n \\ 0 & 0 & 0 & \cdots & 0 & \dot{u}_{n-1} & -\dot{u}_n \end{bmatrix} \tag{6.13}$$

where, Θ_β, $\Theta_\eta \in \mathcal{R}^{p\times 1}$. Therefore, (6.7) is now expressed as

$$z = \psi\Theta_\beta + \dot{\psi}\Theta_\eta \tag{6.14}$$

using the Laplace transform, (6.14) is rewritten in the frequency domain as

$$Z(s) = \Psi(s)\Theta_\beta + s\Psi(s)\Theta_\eta \tag{6.15}$$

In order to use only acceleration measurements and to attenuate low and high frequency measurement noise, (6.15) is first derived three times with respect to time

$$\begin{aligned} s^3 Z(s) =& s^3\Psi(s)\Theta_\beta + s^4\Psi(s)\Theta_\eta \\ =& s\mathcal{L}[\ddot{\psi}]\Psi(s)\Theta_\beta + s^2\mathcal{L}[\ddot{\psi}]\Psi(s)\Theta_\eta \end{aligned} \tag{6.16}$$

subsequently, the resulting expression is integrated five times over finite time intervals by using LIF and defined by [11]

$$I_q\{\varphi(t)\} = \frac{1}{\delta^q}\int_{t-\delta}^{t}\int_{\tau_1-\delta}^{\tau_1}\cdots\int_{\tau_{q-1}-\delta}^{\tau_{q-1}}\varphi(\tau_q)d\tau_q\cdots d\tau_1 \tag{6.17}$$

where, q is the number of integrals over finite time intervals of the signal $\varphi(t)$. On the other hand, the integration time $\delta \in \mathcal{R}^+$ is defined by the size of the moving window

$$\delta = \overline{n}T_s \tag{6.18}$$

where T_s is the sampling time and $\overline{n} > 0$ is a scale factor that determines the time of the integration window, which is selected according to the system bandwidth. Applying the operator $I_5[\cdot]$ to (6.16), yield

$$\Xi(t) = \Upsilon_\beta(t)\Theta_\beta + \Upsilon_\eta(t)\Theta_\eta \tag{6.19}$$

where

$$\Xi(t) = \frac{\vartheta}{\delta^3}I_2\left\{\sum_{j=0}^{3}\binom{3}{j}(-1)^j z(t-j\delta)\right\} \tag{6.20}$$

$$\Upsilon_\beta(t) = \frac{\vartheta}{\delta}I_4\left\{\sum_{j=0}^{1}\binom{1}{j}(-1)^j \ddot{\psi}(t-j\delta)\right\} \tag{6.21}$$

$$\Upsilon_\eta(t) = \frac{\vartheta}{\delta^2}I_3\left\{\sum_{j=0}^{2}\binom{2}{j}(-1)^j \ddot{\psi}(t-j\delta)\right\} \tag{6.22}$$

where, $\Xi \in R^{p\times 1}$, Υ_β y $\Upsilon_\eta \in \mathcal{R}^{p\times p}$, $\binom{n}{j}$ is the binomial coefficient and finally $\vartheta \in \mathcal{R}^+$ is a degree of freedom that allows to normalize the amplitude of the filtered signals. A way to parameterize (6.19) is

$$\Xi(t) = \Upsilon(t)\Theta \tag{6.23}$$

where, $\Theta = [\Theta_\beta^T, \Theta_\eta^T]^T \in \mathcal{R}^{2p\times 1}$ is the vector contained real parameters and $\Upsilon = [\Upsilon_\beta, \Upsilon_\eta] \in \mathcal{R}^{p\times 2p}$ is the regressor formed by filtered acceleration signals. The vector of estimated parameters $\hat{\Theta} = [\hat{\Theta}_\beta^T, \hat{\Theta}_\eta^T]^T$ is obtanied using the least squares algorithm with forgetting factor given by

$$\dot{P} = \alpha P - \frac{P\Upsilon^T\Upsilon P}{m^2} \tag{6.24}$$

$$\dot{\hat{\Theta}} = P\Upsilon^T\varepsilon \tag{6.25}$$

where α is the forgetting factor, P is the covariance matrix, that fulfills $P = P^T > 0 \in \mathcal{R}^{2p\times 2p}$, $P(0) > 0$, $1 > \alpha \geq 0 \in \mathcal{R}^+$, $m^2 = 1 + \left\|\Upsilon\Upsilon^T\right\|$ satisfies that $\Upsilon/m \in \mathcal{L}_\infty$, ensuring that the normalized estimation error tends to zero.

$$\hat{\Xi} = \Upsilon\hat{\Theta} \tag{6.26}$$

6.3.1 Parameter Projection

Using the parameter projection in (6.27) and (6.28), positive estimates are guaranteed $\forall\, t > 0$

$$\hat{\Theta}_{\beta i+}(t) = \hat{\Theta}_{\beta i}(t) + (\varsigma_1 - \hat{\Theta}_{\beta i}(t))\frac{1 - \tanh(\chi_1\hat{\Theta}_{\beta i}(t))}{2} \tag{6.27}$$

$$\hat{\Theta}_{\eta i+}(t) = \hat{\Theta}_{\eta i}(t) + (\varsigma_2 - \hat{\Theta}_{\eta i}(t))\frac{1 - \tanh(\chi_2\hat{\Theta}_{\eta i}(t))}{2} \tag{6.28}$$

where $\hat{\Theta}_{\beta i+}(t)$, $\hat{\Theta}_{\eta i+}(t)$ are the projected estimates of $\Theta_{\beta i}$, $\Theta_{\eta i}$, $i = 0, 1, 2, \ldots, n$; $\varsigma_1 = \varsigma_2 = 0.0001$, are the lower bounds for the estimated parameters, $\chi_1 = \chi_2 = 500$ are parameters that allow us to approximate the sign function. For simplicity it will be used $\hat{\Theta}_{\beta i} = \hat{\Theta}_{\beta i+}$, in the same way $\hat{\Theta}_{\eta i} = \hat{\Theta}_{\eta i+}$.

6.4 Experimental Results

In order to evaluate the performance of the proposed identification system, fourteen experiments were carried out using a reduced scale four story building, made with prefabricated elements of reinforced concrete. The building has a total height of 4.8 m and 1.1 m of inter story separation between floors. The plan dimensions of the models are 3.3 × 3.3 m, while the columns of 20 × 20 cm, respectively, as shown in Fig. 6.2. The tests were conducted on a shaking table located at the Engineering Institute-UNAM in November of 2014. Experiments here were carried out with a sampling time of 0.004 s.

The excitation used was white noise with an amplitude of 20 gal for this first nine experiments and later, the México city 1985 earthquake ground motion, measured at Secretaría de Comunicaciones y Transportes (SCT) station was used with intensity of 50, 100, 150 and 200%. It is important to note that after the first test, braces were placed on each floor, one on each direction X and Y, with the intention of emulating the stiffness loss and the damping increase for damage detection purposes. Details about this can be found in Table 6.1, where braces are represented by / or X for one or two directions, respectively.

As a first step, the identification algorithm proposed in Sect. 6.3 is used to characterized the non-damage building to obtain a priori information in the first test. The algorithm recovers the structural response of the building by identifying the reference structural parameters, when the base of the building was excited with white noise signal. Taking into account that the sampling time is $Ts = 0.004$, linear integral filters ware designed with parameters $\alpha = 0.001$ y $P(0) = 10^5 * I_{12\times 12}$, $\overline{n} = 3$.[2] Figure 6.3 shows the evolution of the identified shear wave velocities, while the damping coefficients can be observed in Fig. 6.4. Table 6.2 presents the identified values. Note that the results presented in this article were obtained using parameters with null initial conditions β_i and η_i.

[2]We recommend to use a cutoff frequency with twice the maximum system frequency, to achieve correct filtering.

Fig. 6.2 Reduced scale four story building

Table 6.1 Test, seismic motion and configuration

Test	Seismic motion	Configuration
1	W.N	–
2	W.N	/
3	W.N	X
4	W.N	X/
5	W.N	XX
6	W.N	XX/
7	W.N	XXX
8	W.N	XXX/
9	W.N	XXXX
10	SCT	XXXX
11	SCT	XXXX
12	SCT	XXXX
13	SCT	XXXX
14	W.N	XXXX

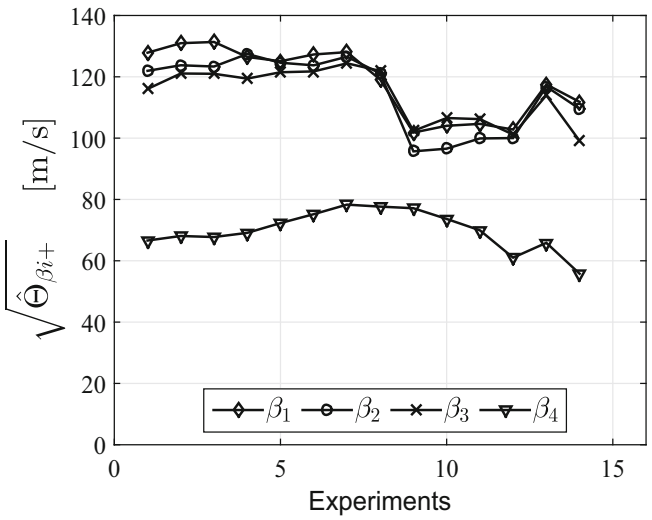

Fig. 6.3 Evolution of identified shear wave velocities

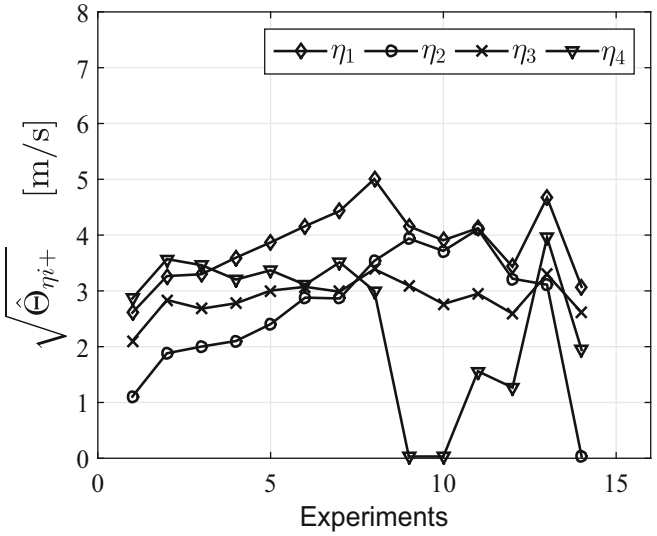

Fig. 6.4 Evolution of the identified damping coefficients

Table 6.2 Identified parameters

Test	$\hat{\beta}_1$	$\hat{\beta}_2$	$\hat{\beta}_3$	$\hat{\beta}_4$	$\hat{\eta}_1$	$\hat{\eta}_2$	$\hat{\eta}_3$	$\hat{\eta}_4$
1	127.8579	121.9503	116.0387	66.6027	2.6093	1.1057	2.1024	2.8654
2	130.9619	123.7639	121.0735	68.0818	3.2655	1.8818	2.8367	3.57
3	131.3605	123.3517	120.9795	67.7428	3.2979	2.0018	2.6808	3.4609
4	126.4719	127.445	119.4149	69.1046	3.596	2.102	2.7783	3.2034
5	125.0793	124.5846	121.4854	72.2954	3.8694	2.4045	3.0049	3.3686
6	127.2826	123.7431	121.7589	75.1921	4.1606	2.8789	3.072	3.1095
7	128.048	126.5449	124.3976	78.3134	4.4322	2.8642	2.9851	3.5129
8	119.0913	121.0934	121.925	77.6625	5.0035	3.5371	3.3900	3.0002
9	101.8139	95.6892	102.3522	77.14	4.1603	3.9379	3.0951	0.0316
10	104.0239	96.5586	106.5534	73.6479	3.908	3.7158	2.7639	0.0316
11	104.6514	99.8957	106.2007	69.9366	4.1238	4.1033	2.9492	1.5588
12	102.7971	100.0221	101.1571	61.0179	3.4323	3.2186	2.5914	1.2681
13	117.5019	116.8022	113.9647	65.8576	4.6709	3.1104	3.2959	3.9572
14	111.8243	109.5613	99.1158	55.7881	3.0724	0.0316	2.6104	1.9437

Table 6.3 Comparison between the actual vibration frequencies and their estimated

f_{r_i} [Hz]	$\hat{f}$ [Hz]	$\Delta\hat{f}/f_{r_i}$ (%)
5.49	4.93	10.20
18.9	17.66	6.56
33.7	36.81	−9.22
46.4	48.77	−5.11

It is important to note that for this experiment the real parameters are unknown and cannot be compared directly with the estimated values. Consequently, the algorithm performance is validated by comparing the vibration frequencies calculated from the estimated parameters with respect to those obtained from the frequency scan of a Chirp signal. Table 6.3 contains a summary of the previous comparison. Note that the calculated frequencies are enough close to the reference values provided by the Chirp, even though they do not exactly match them. This confirms the satisfactory performance of the algorithm, since the estimation error between the real and estimated frequencies is around of 10% approximately, in the worst case.

Note that damping ratio increased during the first nine experiments, and then along with shear wave velocity decreased significantly when seismic loading is used. This could be used as a damage indicator. Considering that floors without braces are damaged, the presented algorithm is enough sensitivity to retrieve information about damage. In practice, this algorithm can help to improve structural health monitoring, while reducing time assessment.

6.5 Conclusion

A real time system identification algorithm has been presented for multi-story buildings capable to estimate parameters as shear wave velocity and Kelvin damping in order to assess structural safety. The main objective of the proposed algorithm is to complement methods based on the wave propagation approach that are traditionally developed in the frequency domain and that are not useful for real-time applications. The introduction of linear integral filters eliminates noise and bias in acceleration measurements. Real-time implementation helps to overcome the problem of data storage and allows carrying out an early evaluation. Experimental results confirm that the proposed method is promising for applications in practice.

Acknowledgements This research was carried out with the support of UNAM-PAPIIT IN104218 grant.

References

1. Doebling, S.W., Farrar, C., Prime, M.B.: A summary review of vibration-based damage identification methods. Shock Vib. Dig. 30(2), 1–34 (1998)
2. Sohn, H., Farrar, C.R., Hemez, F.M., Shunk Devin, D., Stinemates Daniel, W., Nadler Brett, R., Czarnecki Jerry, J.: A review of structural health monitoring literature: 1996–2001. Los Alamos National Laboratory Report, LA-13976-MS, pp. 1–331 (2003)
3. Carden, E.P., Fanning, P.: Vibration based condition monitoring: a review. Struct. Health Monit. 3, 355–377 (2004)
4. Kong, X., Cai, C.S., Hu, J.: The state-of-the-art on framework of vibration-based structural damage identification for decision making. Appl. Sci. 7(5), 497–510 (2017)
5. Das, S., Saha, P., Patro, S.K.: Vibration-based damage detection techniques used for health monitoring of structures: a review. J. Civil Struct. Health Monit. 6(3), 477–507 (2016)
6. Trifunac, M.D., Ivanović, S.S., Todorovska, M.I.: Wave propagation in a seven-story reinforced concrete building: III. Damage detection via changes in wavenumbers. Soil Dyn. Earthq. Eng. 23(1), 65–75 (2003)
7. Todorovska, M.I., Rahmani, M.T.: System identification of building by wave travel time analysis and leyered shear beam models-spatial resolution and accuracy. Struct. Control Health Monit. 20(5), 686–702 (2012)
8. Rahmani, M., Todorovska, M.I.: 1D System identification of a 54-story steel frame building by seismic interferometry. Earthq. Eng. Struct. Dyn. 43(4), 627–640 (2014)
9. Morales-Valdez, J., Alvarez-Icaza, L., Sanchez-Sesma, F.J.: Shear building stiffness estimation by wave traveling time analysis. Struct. Control Health Monit. 25(1), e2045 (2018)
10. Morales-Valdez, J., Alvarez-Icaza, L., Concha, A.: On-line adaptive observer for buildings based on wave propagation approach. J. Vib. Control 24(16), 3758–3778 (2017). https://doi.org/10.1177/1077546317711309
11. Garnier, H., Mensier, M., Richard, A.: Continuous-time model identification from sampled data: implementation issues and performance evaluation. Int. J. Control 76(13), 1337–1357 (2010)

Chapter 7
Experimental and Numerical Study of the Second Order Moment of the First Passage Time of a Steel Strip Subjected to Forced and Parametric Excitations

E. Delhez, H. Vanvinckenroye, V. Denoël, and J.-C. Golinval

Abstract The first passage time is the time required for a stochastic process to leave a subdomain of the state space for the first time when starting from a given initial state in this subdomain. Analytical studies of the first passage time of a linear Mathieu oscillator subjected to forced and parametric excitations defined as δ-correlated Brownian noises highlighted the existence of three behavioral regimes for the average first passage time. The current work describes the design and outcomes of an experimental study demonstrating the practical existence of these regimes for the second order moment of the first passage time. On the one hand, tests are carried out on an experimental set-up consisting in a pre-stressed strip subjected to forced and parametric stochastic excitations. On the other hand, a finite element model of the structure is built, updated and used to address the same problem using a numerical approach. Both the experimental tests and the numerical simulations produce mean square first passage time maps that provide evidence for the existence of the three foreseen behavioral regimes. The good match of the first passage time maps confirms the accuracy of the finite element model updating as well as the relevance of the theoretical model for this type of problem.

Keywords Structural dynamics · First passage time · Stochastic Mathieu equation · Parametric oscillator · Modal analysis

7.1 Introduction

The first passage time refers to the time required for a dynamical system to reach a target energy level for the first time, departing from a known initial state. The theory of first passage time addresses the problem of the determination of the statistics of the first passage time of the response of a dynamical system under stochastic input. It has emerged as an efficient alternative to the classical stability theories. In structural dynamics, this theory can be applied to problems involving parametric or aero-elastic excitations for instance. Closed form expressions of the first and second order moments of the first passage time have been recently derived for single-degree-of-freedom linear systems described by the Mathieu equation

$$z'' + 2\xi z' + [1 + u(\tau)]\, z = w(\tau)\,, \tag{7.1}$$

where $z(\tau)$ is the dependent state variable, τ is a dimensionless time and ξ is the damping coefficient of the system [1, 2]. The system is subjected to a forced excitation $w(\tau)$ and to a parametric excitation $u(\tau)$ which induces variation in time of the system stiffness. The Hamiltonian of this system is defined by

$$H = \frac{z^2}{2} + \frac{\left[z'\right]^2}{2}. \tag{7.2}$$

The analytical study of this system subjected to forced and parametric excitations defined as δ-correlated Brownian noises characterized by constant power spectral densities S_w and S_u has suggested the existence of three behavioral regimes for the

E. Delhez (✉) · J.-C. Golinval
Department of Aerospace and Mechanical Engineering, University of Liège, Liège, Belgium

H. Vanvinckenroye · V. Denoël
Department of Urban and Environmental Engineering, University of Liège, Liège, Belgium

N. Dervilis (ed.), *Special Topics in Structural Dynamics & Experimental Techniques, Volume 5*, Conference Proceedings of the Society for Experimental Mechanics Series, https://doi.org/10.1007/978-3-030-12243-0_7

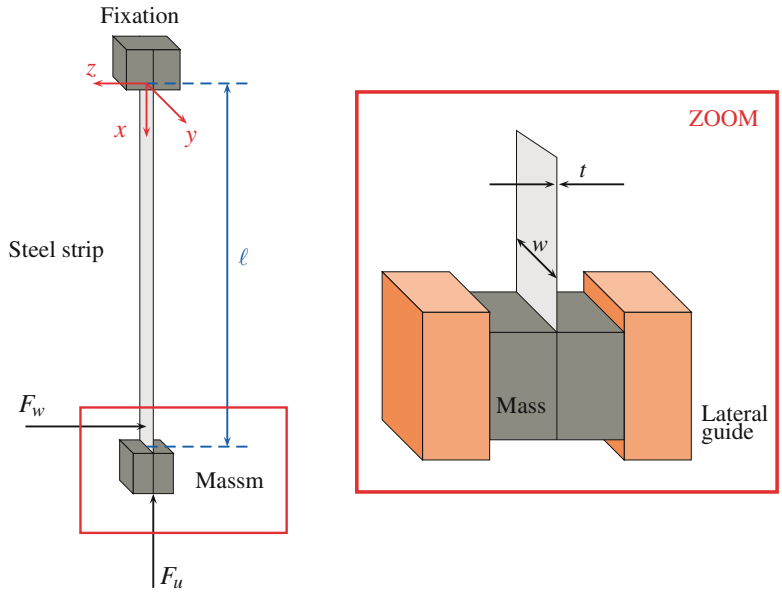

Fig. 7.1 Schematic view of the experimental set-up

first passage time of such systems. The existence of these regimes for the average first passage time have been demonstrated experimentally in [3]. This paper focuses on the study of the second order moment of the first passage time.

7.2 Experimental Set-Up Description

The experimental set-up is represented in a schematic way in Fig. 7.1. It consists in a vertical strip pre-stressed by a mass $m = 1.816\,\text{kg}$. The strip is characterized by a length $\ell = 0.501\,\text{m}$, a width $w = 25\,\text{mm}$ and a thickness $t = 0.4\,\text{mm}$. The structure is made of steel (Young's modulus $E = 206\,\text{GPa}$ and density $\rho = 7767\,\text{kg/m}^3$). It is clamped at its top end. A lateral guide at the bottom end constrains the strip to move only in the vertical direction. The forced and parametric excitations F_w and F_u are applied by means of two shakers. The first shaker is mounted horizontally and is used to excite the strip out of its plane. This force constitutes the forced excitation. The second shaker is mounted vertically at the bottom of the structure. This force modifies the pre-stress load of the strip, giving rise to the parametric excitation. A picture of the physical prototype of the structure with the two shakers is given in Fig. 7.2. Using an appropriate scaling [3], this problem can be cast into a dimensionless format similar to Eq. (7.1).

7.3 Numerical Modelling

The strip itself is modelled in MATLAB using Bernoulli beam elements. Stiffness in rotation about the y-axis is experimentally identified and introduced at both extremities of the strip to reflect the actual boundary conditions. The horizontal shaker, the stinger and the impedance head glued to the strip are modeled by a spring-mass system. The influence of the impedance head is also taken into account by increasing the stiffness of the finite elements in contact with the transducer. The different parameters of the model are tuned to minimize (in a least square sense) the difference between the natural frequencies obtained with the numerical model and those identified experimentally with the "Least Square Complex Exponential" and "Least Square Frequency Domain" methods [3].

Fig. 7.2 Experimental set-up

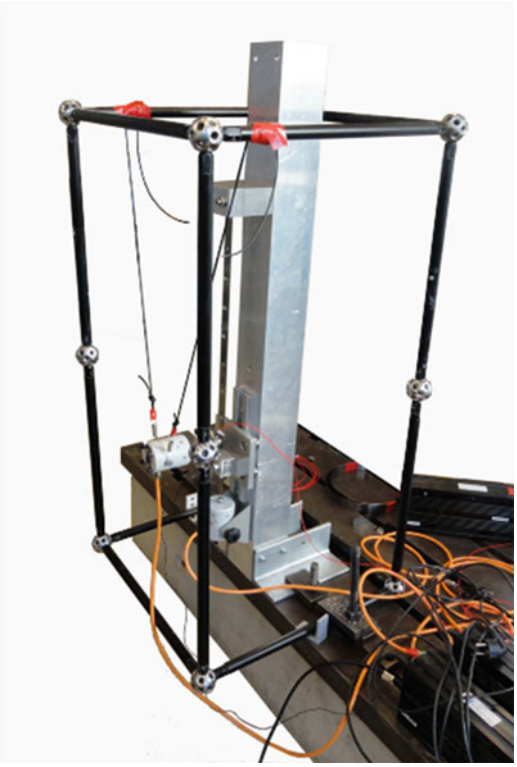

7.4 Model Reduction

In order to fit into the particular framework under which the analytical results have been derived, the multi-degree-of-freedom equation of motion is reduced to a set of single-degree-of-freedom equations of motion by re-writing it in the modal basis. The coupling between these equations come from the parametric excitation. The dynamics of the structure at a single point can therefore be described by a unique single-degree-of-freedom equation when the parametric excitation is kept sufficiently small in amplitude and when the forced and parametric excitations are defined as narrow-band processes exciting only one bending mode of the structure. This work aiming at the experimental validation of a single-degree-of-freedom model, narrow-band excitations are therefore considered.

7.5 Experimental Study

The forced excitation F_w is defined as a narrow-band process of constant power spectral density $\tilde{S}_w = 5 \cdot 10^{-3}$ N^2/Hz on the frequency interval $[0.87f_0;\ 1.13f_0] = [34;\ 44]$ Hz. The parametric excitation F_u is defined as a narrow-band process of constant power spectral density constant power spectral density $\tilde{S}_u = 5 \cdot 10^{-3}$ N^2/Hz on the frequency interval $[0.77f_0;\ 2.57f_0] = [30;\ 100]$ Hz. The definition of these excitations ensures that only one mode of the structure is excited. The equivalent dimensionless parameters corresponding to the dimensionless Mathieu Eq. (7.1) are $S_w = 2.5 \cdot 10^{-10}$, $S_u = 1.8 \cdot 10^{-4}$ and $a = 8\xi/S_u = 132$.

The results are summarized with a first passage time map, representing the contours of equal mean square first passage times as a function of the reduced initial energy and the reduced energy increase in the considered system (Fig. 7.3). The Hamiltonian H of the system is defined by Eq. (7.2).

Figure 7.3(a) shows the influence of the narrow-bandedness of the excitations: even if the behavior is qualitatively the same, quantitative differences are observed between the curves. Figure 7.3(b) compares the maps obtained experimentally and numerically (by Monte Carlo simulations of the system subjected to the narrow-band excitations of the experiment). The good match between the first passage time maps confirms the accuracy of the finite element model updating as well as the relevance of the theoretical model for this type of problem. The three foreseen behavioral regimes are also observed. For small initial levels of energy and sufficiently large energy increments, the first passage time is independent from the initial

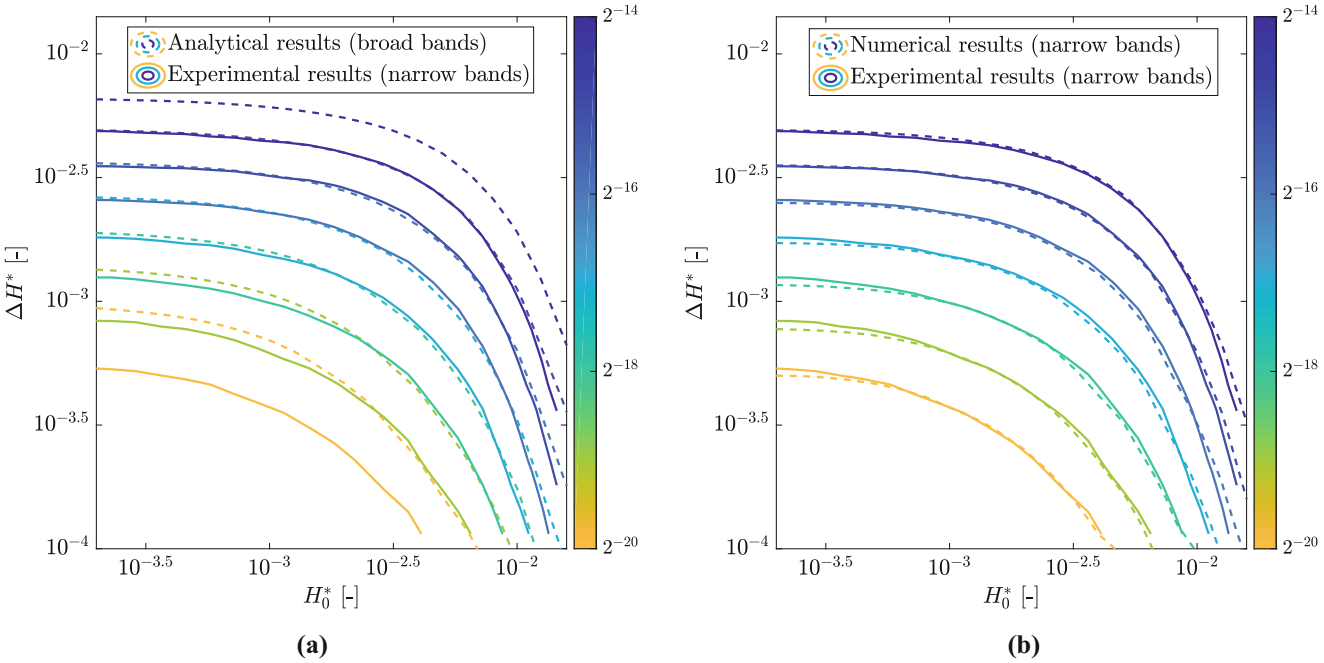

Fig. 7.3 Reduced mean square first passage time $U_2 S_u^2/32$ as a function of $H_0^* = H_0 S_u/2S_w$ and $\Delta H^* = \Delta H S_u/2S_w$. Comparison of the maps obtained experimentally and numerically for narrow-band excitations (F_u on $[0.77\, f_0; 2.57\, f_0]$ and F_w on $[0.87\, f_0; 1.13\, f_0]$) and analytically for broadband excitations ($a = 132$, $S_w = 2.5 \cdot 10^{-10}$, $S_u = 1.8 \cdot 10^{-4}$)

level of energy. This is referred to as the *additive* regime. For large initial levels of energy, the curves show similar slope, which corresponds to the *multiplicative* regime. For small energy increment, in the *incubation* regime, the mean square first passage time scales linearly with the energy increment.

References

1. Vanvinckenroye, H., Denoël, V.: Average first-passage time of a quasi-Hamiltonian Mathieu oscillator with parametric and forcing excitations. J. Sound Vib. **406**, 328–345 (2017)
2. Vanvinckenroye, H., Denoël, V.: Second-order moment of the first passage time of a quasi-Hamiltonian oscillator with stochastic parametric and forcing excitations. J. Sound Vib. **427**, 178–187 (2018)
3. Delhez E., Vanvinckenroye H., Golinval J.-C., Denoël V.: Numerical and experimental study of first passage time of a steel strip subjected to forced and parametric excitations. In: Proceedings of the 28th International Conference on Noise and Vibration Engineering (2018)

Chapter 8
Three-Dimensional Mechanical Metamaterial for Vibration Suppression

Brittany C. Essink and Daniel J. Inman

Abstract Decades of research have been conducted on vibration suppression, cancellation, and absorption methods. Recently, distributed arrays of resonators have been implemented in host structures creating devices termed mechanical metamaterials, also known in the literature as metastructures. The benefit of using mechanical metamaterials as opposed to traditional added absorbers is the structure is initially designed including the absorbers instead of adding them after creation, saving time and weight. Additionally, these structures remain capable of bearing loads without adding additional mass. Where past research has focused on designing and optimizing metastructures based on single degree of freedom excitations, the research presented in this paper focuses on a device capable of vibration suppression under excitation in three directions; longitudinal, transverse, and torsional. This accommodation is necessary for these devices to be implemented in non-laboratory settings to account for excitation from multiple directions.

This paper presents experimental data and a preliminary finite element model for a three-dimensional mechanical metamaterial vibration suppression system. Experimental results compare the structure with blocked absorbers to free absorbers to demonstrate vibration reduction bandwidths of 358 Hz in the longitudinal direction, 24 Hz in the transverse direction, and a frequency shift of 40 Hz in the torsional direction. These promising results show that a metastructure can be effectively designed to suppress vibrations in all three directions of excitation with further motivation to explore optimization of the absorber system for maximum suppression bandwidth.

Keywords Mechanical metamaterial · Metastructure · Multidirectional excitation · Vibration supression

8.1 Introduction

Methods of suppressing and canceling vibration have been widely investigated by scientists and engineers alike. The majority of these suppression methods can be either classified as active or passive vibration systems. Active systems require energy input into the system and control of an actuator to suppress the vibrations whereas passive systems will operate without any additional energy input or control system. Historically, one of the most investigated vibration systems is a tuned mass damper, or TMD. This simple 1DOF system can be added to an existing structure and tuned through the structural and forcing parameters to suppress the vibration of the host structure.

More recently, this TMD concept has been expanded upon and compounded to create a distributed array of tuned mass absorbers throughout a system. This concept is called a mechanical metamaterial, also known as a metastructure. The efficacy of these metastructures for vibration reduction using a chiral design has been demonstrated by Zhu et al. [1]. Other researchers such as Sun et al. and Pai et al. have focused on the traditional tuned mass damper system to achieve broadband absorption in both vibration and acoustics [2, 3].

Previous work in the metastructure field used distributed absorber designs for axial vibration suppression. Hobeck et al. [4] investigated preliminary modeling and experiments for the passive axial metastructure system while Reichl and Inman [5] delved into both passive and active axial suppression including tuning the dampers separately for varying suppression effects. Oftentimes, vibrations are restricted to unidirectional excitation which is achievable in a lab setting but is not often the type of excitation experienced by a structure in the field. The work of Drouard et al. [6] added suppression of torsional vibration to the original axial design for a 2D structure. The research presented in this paper builds upon these works and incorporates the transverse degree of freedom for a metastructure capable of suppression in three dimensions. This paper includes a brief description of the preliminary finite element modeling for this structure, with a main focus on the experimental results.

B. C. Essink (✉) · D. J. Inman
Department of Aerospace Engineering, University of Michigan, Ann Arbor, MI, USA
e-mail: essinkb@umich.edu

N. Dervilis (ed.), *Special Topics in Structural Dynamics & Experimental Techniques, Volume 5*, Conference Proceedings of the Society for Experimental Mechanics Series, https://doi.org/10.1007/978-3-030-12243-0_8

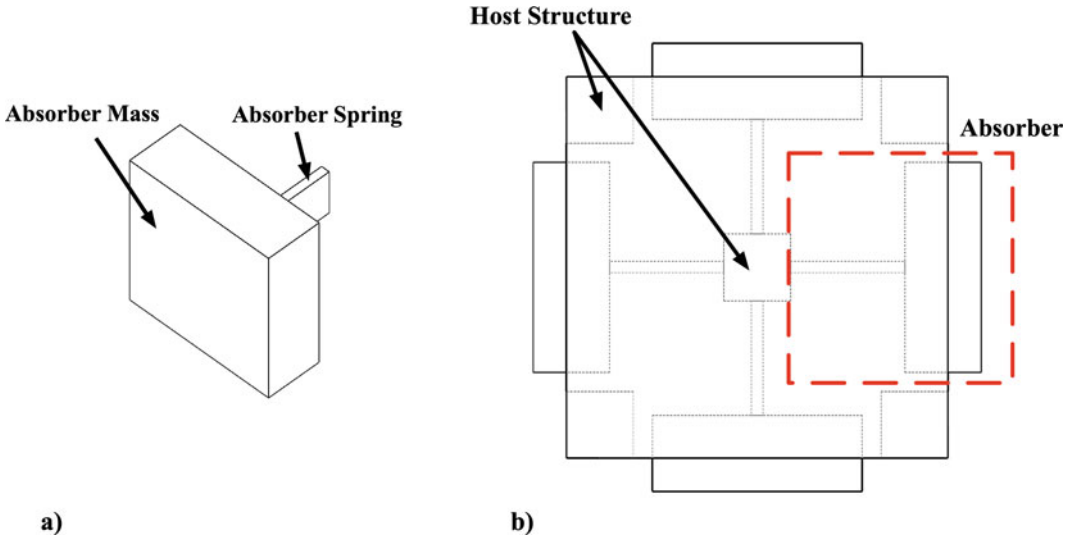

Fig. 8.1 (**a**) Single absorber (**b**) Top down view of full structure

The current research used a 3D printer to create the metastructure. This type of rapid prototyping provides multiple benefits over traditional machining. Using traditional machining for this particular system would require the main beam to be fabricated separately and the absorbers attached later. With additive manufacturing techniques, the absorbers and main beam can be created as a single structure. While this structure is printed out of a stiff polymer material, additional damping can be incorporated using materials with higher viscoelastic effects. With the advances in additive manufacturing, metal printers could also be used to incorporate absorbers into commonly seen structures in the aerospace and automotive industries.

8.2 Modeling Strategies

A finite element model of the structure was developed using the commercial software ANSYS. There were two components considered in the design of the structural model. First was the determination of the natural frequencies of the entire structure with the absorbers blocked from moving. The second part of the design was completed by modeling the individual absorbers. These absorbers were then tuned to match the first natural frequencies of each respective excitation direction for the blocked beam. By tuning the absorbers to the natural frequency of the entire assembly, it is possible to eliminate or significantly reduce vibration of the structure when the absorbers are free to vibrate. After creating the tuned absorbers, the full structure was modeled in ANSYS and all three excitation tests were conducted. Using the blocked and free absorber conditions enables the comparison of the change in frequency response due to only absorber dynamics instead of mass loading effects. The design consists of an array of 8 absorbers on each side of the structure with a square cross section for a total of 64 absorbers. Figure 8.1a shows a schematic of a single absorber. Each absorber is attached to a middle rod on the main structure as shown in the top down view of the full structure in Fig. 8.1b.

8.3 Experimental Analysis

The metastructure was fabricated using a Stratasys Objet Connex 500 printer. Both the host beam and the absorbers were printed using the stiffest printer material called VeroWhite. The specimen was tested using a Team Corporation Tensor 18kN 6DOF test system located at the Army Research Laboratory on the Aberdeen Proving Grounds.

The 6DOF system has 12 electrodynamic shakers for multi-axis testing. Each shaker can be controlled individually for a wide range of testing scenarios. Excitation in the longitudinal direction was achieved by exciting the shakers in only the Z direction. The transverse excitation was measured by exciting the structure only in the X direction. The torsional excitation was achieved by exciting opposing Y direction shakers on each side of the table to create the twisting motion. All tests were sine sweep excitations from 20 to 1000 Hz.

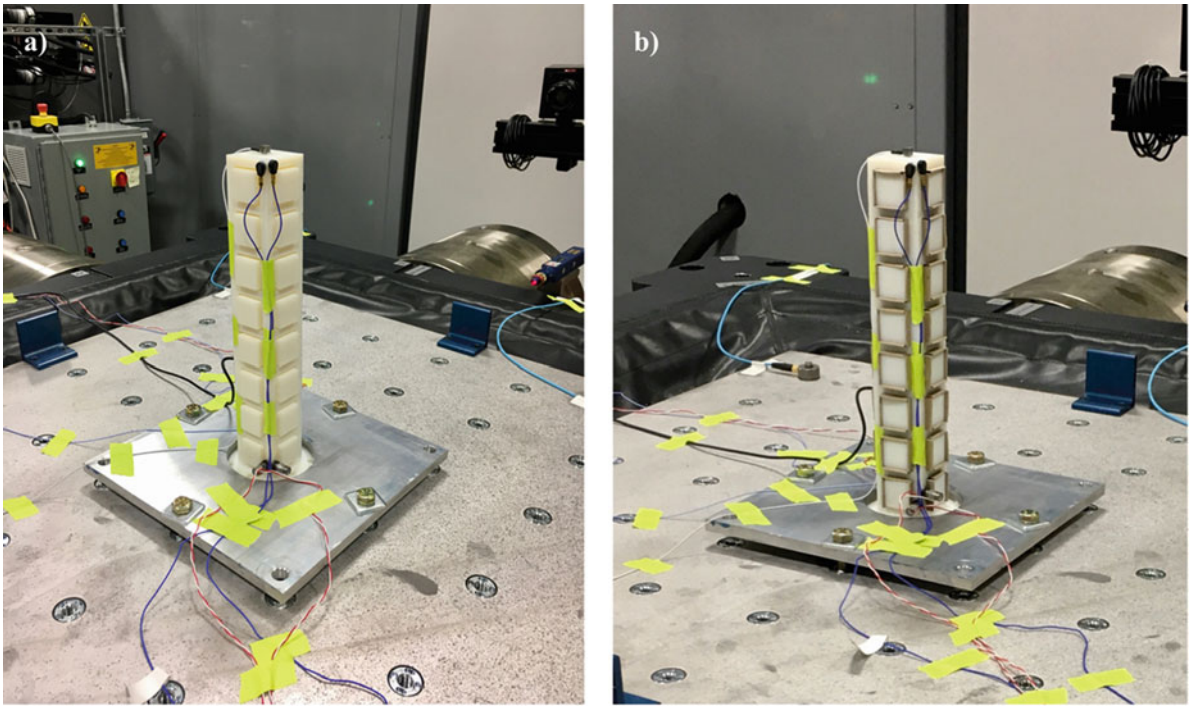

Fig. 8.2 (**a**) Free absorber test configuration (**b**) blocked absorber test configuration

Figure 8.2 shows the shaker setup for both the free and blocked absorber experiments. The base of the beam was clamped to the shaker table using an accessory plate and accelerometers were attached to the beam using wax. Torsional base and tip measurements were taken using four accelerometers attached at the tip and four accelerometers at the base. Longitudinal and transverse measurements were taken using the base accelerometers and a triaxial accelerometer at the top center of the beam.

The metastructure with free absorbers was excited using sine sweeps in the three excitation directions. These tests were repeated using the blocked absorber configuration shown in Fig. 8.2b. The blocked configuration was achieved by adding small cardboard inserts between the absorbers and the main structure. These inserts added a negligible amount of mass to the total system while preventing the absorbers from vibrating during excitation.

8.4 Results

Results of the free and blocked longitudinal sine sweeps are compared in Fig. 8.3. For the blocked test of the absorber system, there is a single resonance peak at approximately 672 Hz. When the absorbers are free to vibrate, the absorber system eliminates the vibration at and around the blocked natural frequency between 428 Hz and 786 Hz for a bandwidth of 358 Hz. Additionally, the global vibration amplitude of the free configuration is reduced compared to the blocked case.

Figure 8.4 compares the free and blocked frequency responses for the structure excited in the transverse direction. The results show a similar trend to the longitudinal results, with a single resonance peak for the blocked system which is eliminated for the free absorber case. The blocked case single peak is located at approximately 69 Hz. The vibration is reduced between approximately 56 Hz and 79 Hz for a bandwidth of 23 Hz in the transverse direction. Similar to the longitudinal response, the global vibration of the structure is reduced for the free absorber case.

The torsional blocked and free response results are compared in Fig. 8.5. Both the blocked and the free configurations show a single resonance peak, however the free absorbers drastically reduced vibration at the blocked resonance frequency and shifted it approximately 40 Hz higher. At the new free absorber resonance, the global displacement is lower compared to the blocked case.

A comparison between finite element and experimental results for both blocked and free responses are listed in Table 8.1. While the trends for the expected peaks match quite well for all three excitation directions, there are some disparities

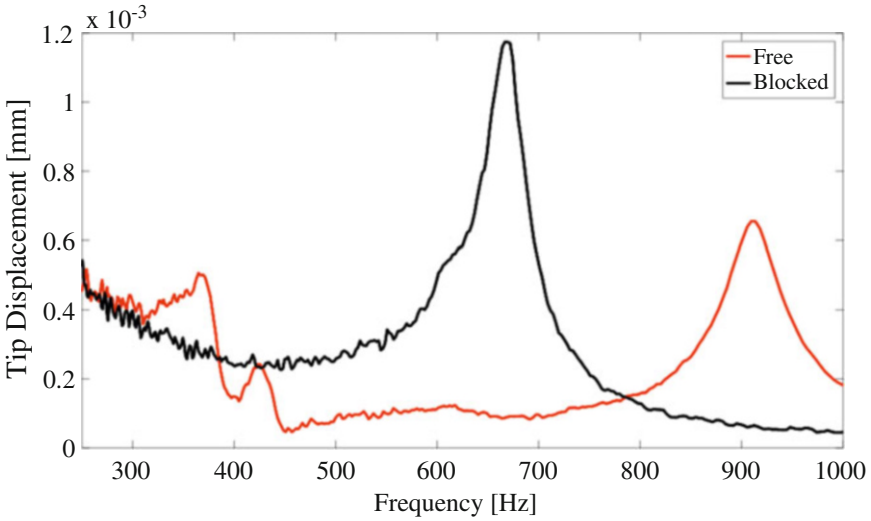

Fig. 8.3 Longitudinal tip displacement for free and blocked configurations

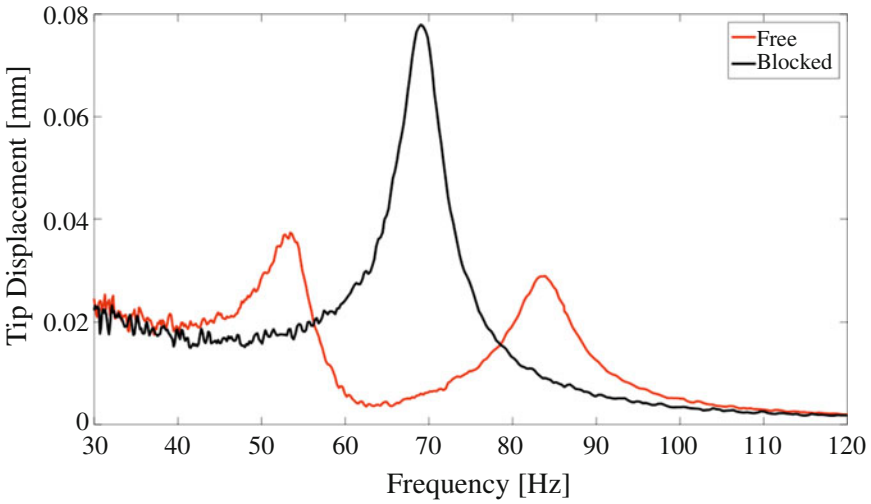

Fig. 8.4 Transverse tip displacement for free and blocked configurations

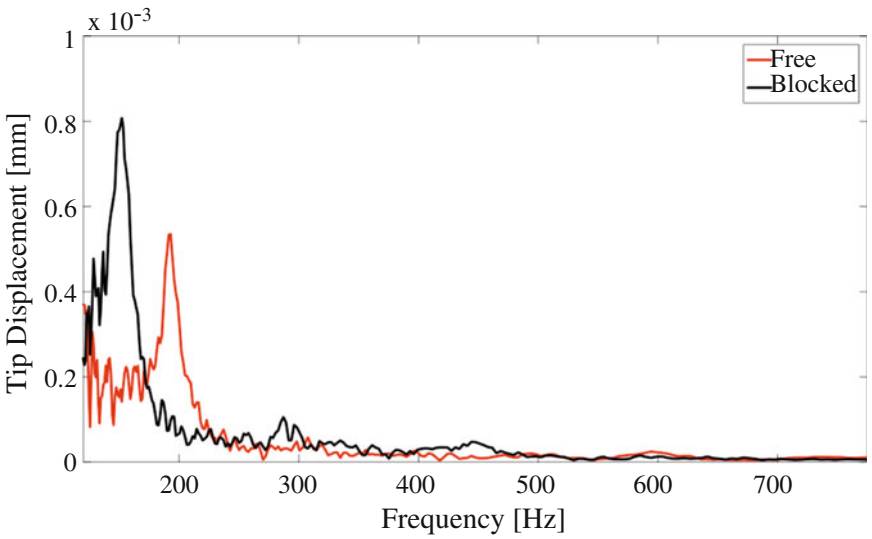

Fig. 8.5 Torsional tip displacement for free and blocked configurations

Table 8.1 Finite element natural frequencies compared to experimental data

Blocked absorbers	ANSYS model		Experimental data	
Longitudinal peak [Hz]	634		672	
Transverse peak [Hz]	66		69	
Torsional peak [Hz]	140		152	
Free absorbers	**ANSYS model**		**Experimental data**	
Longitudinal peaks [Hz]	355	805	370	914
Transverse peaks [Hz]	56	92	54	84
Torsional peaks [Hz]	192		193	

Table 8.2 Measured bandwidths and peak shifts for the mechanical metamaterial beam

	Experimental data
Longitudinal blocked beam frequency [Hz]	672
Longitudinal suppression band [Hz]	358
Longitudinal peak gaps [Hz]	240
Transverse blocked beam frequency [Hz]	69
Transverse suppression band [Hz]	23
Transverse peak gaps [Hz]	15
Torsional blocked beam frequency [Hz]	152
Torsional frequency shift [Hz]	40

between predicted and measured results, notably for the second split peaks in the free absorber system. This difference is most likely due to having chosen a single value for each of the material properties of VeroWhite. In reality, the manufacturer's website provides a range for material density and the material modulus and damping properties are frequency dependent due to the viscoelastic nature of the material [7]. With a more accurate material model, the discrepancies between predicted and experimental values are expected to decrease.

A summary of the experimental results is provided in Table 8.2. This summary lists the peak frequency from the respective directions of excitation for the blocked absorber structure. The suppression band for the both the longitudinal and transverse responses for the free absorbers are listed and the peak gaps detail the full gap between the peaks of free configuration peaks. For the torsional case, the peak frequency of the blocked configuration and the shift away from the blocked frequency are presented.

8.5 Conclusion

This research presents initial modeling and experimental results of an investigation focused on passive vibration suppression in three-dimensional excitation. Finite element modeling methods were presented and successfully applied to the three-dimensional metastructure design. The measured and predicted frequency response of the structure was shown to virtually eliminate vibration at the desired design frequency while creating frequency suppression bands of 358 Hz in the longitudinal direction, 24 Hz in the transverse direction, and shifting the torsional frequency by 40 Hz. Additionally, the global vibration was reduced in all directions when the absorbers were free to vibrate.

Results of this research demonstrate that a metastructure can be effectively designed to suppress vibrations in all three directions of excitation. Further increases to design bandwidth can be made by optimizing the absorbers for each degree of freedom of vibration.

Acknowledgements Special thanks to Dr. Robert Haynes and Dr. Todd Henry at the Army Research Lab on the Aberdeen Proving Grounds for helping us test and validate our mechanical metamaterial on the 6DOF test system located at their facilities. Additional thanks to Dr. Mulugeta Haile for hosting and facilitating the visit.

References

1. Zhu, R., Liu, X.N., Hu, G.K., Sun, C.T., Huang, G.L.: A chiral elastic metamaterial beam for broadband vibration suppression. J. Sound Vib. **333**, 2759–2773 (2014)
2. Sun, H., Du, X., Pai, P.F.: Theory of metamaterial beam for broadband vibration absorption. J. Intell. Mater. Syst. Struct. **21**, 1085–1101 (2010)
3. Pai, P.F., Peng, H., Jiang, S.: Acoustic metamaterial beams based on multi-frequency vibration absorbers. Int. J. Mech. Sci. **79**, 195–205 (2014)
4. Hobeck, J.D., Laurent, C.M.V., Inman, D.J.: 3D printing of metastructures for passive broadband vibration suppression. In: 20th International Conference on Composite Materials, pp. 19–24 (2015)
5. Reichl, K.K., Inman, D.J.: Active metastructures for light-weight vibration suppression (2018)
6. Drouard, S., Hobeck, J.D., Inman, D.J.: ICAM Report (2015)
7. Reichl, K.K., Inman, D.J.: Dynamic modulus properties of Objet Connex 3D Printer digital materials. In: Topics in Modal Analysis & Testing, vol. 10, pp. 191–196. Springer, New York (2016)

Chapter 9
Model Reduction of Self-Repeating Structures with Applications to Metamaterial Modeling

Ryan Romeo and Ryan Schultz

Abstract The dynamic behavior of metamaterials and metastructures is often modeled using finite elements; however, these models can become quite large and therefore computationally expensive to simulate. Traditionally, large models are made smaller using any of the array of model reduction methods, such as Guyan or Craig-Bampton reduction. The regularized nature of metamaterials makes them excellent candidates for reduced-order modeling because the system is essentially comprised of a repeating pattern of unit cell components. These unit cell components can be reduced and then assembled to form a reduced-order system-level model with equivalent dynamics. The process is demonstrated using a finite element model of a 1-D axially vibrating metamaterial bar using Guyan, SEREP, and Craig-Bampton reduction methods. The process is shown to provide substantial reduction in the time needed to simulate the dynamic response of a representative metamaterial while maintaining the dynamics of the system and resonators.

Keywords Metamaterials · Self-repeating structures · Reduced-order model · Component mode synthesis · Finite elements

9.1 Introduction

Capturing the small and large-scale features of structures often results in a finite element model (FEM) that is large and therefore time consuming to run. To combat this, reduced-order modeling (ROM) techniques are used to condense the number of degrees of freedom and create a nearly dynamically equivalent FEM with fewer elements [1]. In this paper, a technique is proposed to take advantage of the nature of self-repeating structures—objects whose models can be divided into a number of identical groups of elements—and reduce the computational expense for obtaining a reduced-order model. One such type of structure seeing recent attention is metamaterials.

Metamaterials are structures which have a number of attached parasitic masses, called metaresonators. These resonators behave as tuned mass dampers, where they absorb kinetic energy from the vibrational response of the parent structure when it resonates near the natural frequencies of the attached masses, therefore decreasing the central structure's resonance response at those frequencies [2]. Metamaterials are typically designed to have a pattern of metaresonators attached along a homogeneous structure; as such, they often have self-repeating geometries.

The process presented here seeks to reduce the time to obtain a reduced-order model for self-repeating structures such as metamaterials. Because these structures can be grouped into identical sets of elements, called unit cells, it should be possible to take one of these unit cell element groups, apply a reduction, and then combine the result with copies of itself to make a full-sized assembly. Because this assembly is comprised of a copies of the ROM of a single unit cell, the overall computational time is greatly reduced compared to the computational time of running the original, full FEM.

R. Romeo
College of Engineering, University of Georgia, Athens, GA, USA
e-mail: rromeo@uga.edu

R. Schultz (✉)
Structural Dynamics Department, Sandia National Laboratories, Albuquerque, NM, USA
e-mail: rschult@sandia.gov

N. Dervilis (ed.), *Special Topics in Structural Dynamics & Experimental Techniques, Volume 5*, Conference Proceedings of the Society for Experimental Mechanics Series, https://doi.org/10.1007/978-3-030-12243-0_9

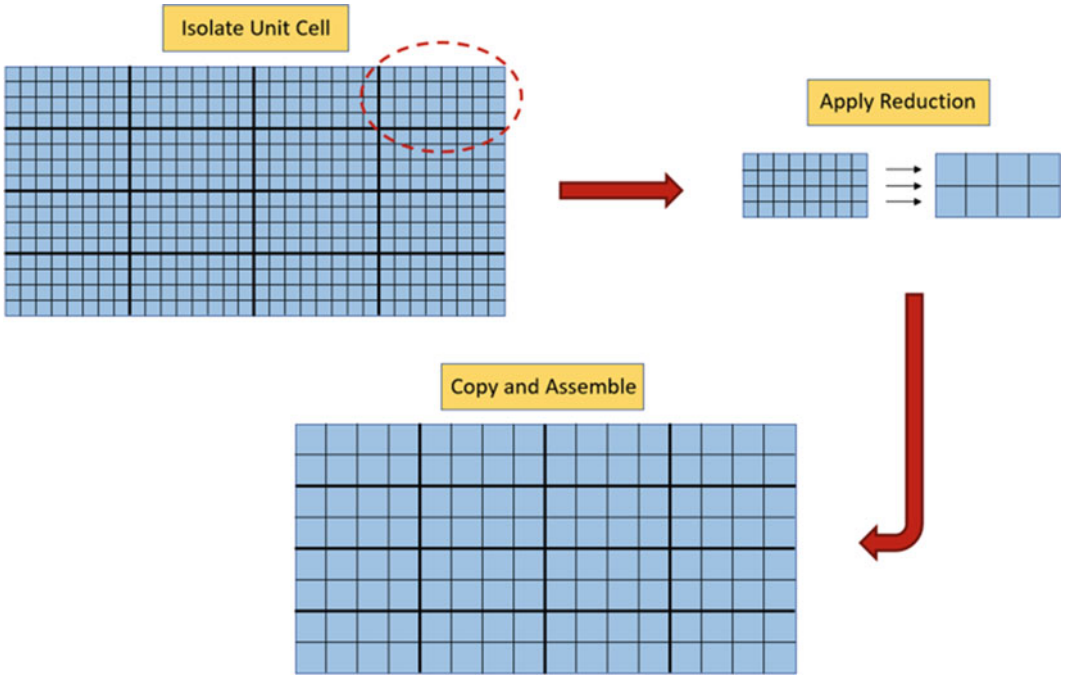

Fig. 9.1 Visualization of the reduction process for self-repeating structures

9.2 Reduced-Order Modeling Techniques Applied to Self-Repeating Structures

Modern finite element models can become quite large (e.g., millions of degrees of freedom) when trying to achieve an accurate representation of a physical object. Model reduction significantly expedites the time to obtain a solution; however, for considerably large FEMs, the reduction itself can also become quite computationally expensive. The process described herein seeks to reduce the time spent in the reduction step by only reducing a single unit cell, further decreasing the overall solution time.

9.2.1 Fundamental Process

The first step in the process is to divide the metamaterial finite element model into m identical groups of elements. One such group is then chosen to become the unit cell, or copy cell. The unit cell is then isolated from the rest of the model via its system property (i.e., mass and stiffness) matrices. A model reduction method is applied to these unit cell matrices, resulting in a ROM for the unit cell. Finally, the ROM cell is copied *m-1* times to form the reduced, full-size assembly. A depiction of this process is provided in Fig. 9.1. System-level boundary conditions should not be applied to the model until the reduced, copied assembly has been obtained.

9.2.2 Reduced-Order Modeling Techniques

Three types of model reduction techniques will be explored in this paper: Guyan condensation, System Equivalent Reduction Expansion Process (SEREP), and Craig-Bampton Reduction (CBR). Generally, a reduction method takes the full n-set of finite element degrees of freedom and splits them into two subsets—the a-set (active) and d-set (deleted)—written as

$$x_n = \begin{Bmatrix} x_a \\ x_d \end{Bmatrix}. \tag{9.1}$$

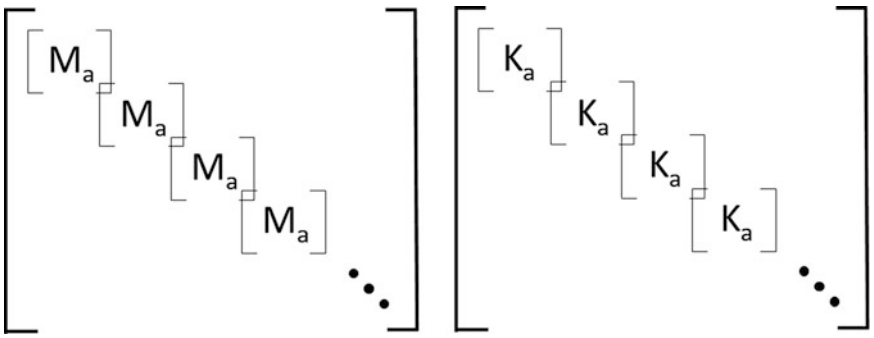

Fig. 9.2 Depiction of the assembly of the reduced M and K matrices

The active set, x_a, contains those degrees of freedom which are determined necessary to accurately represent the dynamics of the system, whereas the deleted set, x_d, contains those DOF to be disregarded. The active set DOFs remain in the ROM. Next, a transformation matrix, $T_{n,a}$, is sought which directly relates the n-set DOFs with those in the a-set:

$$x_n = T_{n,a} x_a. \tag{9.2}$$

The reduced mass and stiffness matrices, M_a and K_a, are then obtained by

$$M_a = T_{n,a}^T M_n T_{n,a}, \tag{9.3}$$

$$K_a = T_{n,a}^T K_n T_{n,a}, \tag{9.4}$$

where M_n and K_n are the mass and stiffness matrices from the original finite element model, respectively.

In the technique presented, the reduced matrices are obtained for the unit cell and assembled to its copies using the same principle for assembling finite element model matrices; an example is shown in Fig. 9.2. Specifically, the M and K sets of reduced matrices and their respective copies are assembled to form two system-level block diagonal matrices. The main diagonal entries corresponding to the DOF connections between two connecting cells are added together, and the associated off-diagonal terms are changed accordingly. In the diagram, this is shown as the corners of each matrix overlapping.

9.2.2.1 Guyan Reduction

Guyan reduction, also known as Guyan or static condensation, is one of the oldest and most well-known model reduction techniques. It involves manipulating the static force equation such that the degrees of freedom are rearranged according to the active and deleted sets [3], expressed as

$$F_n = K_n x_n, \tag{9.5}$$

$$\begin{Bmatrix} F_a \\ F_d \end{Bmatrix} = \begin{bmatrix} K_{aa} & K_{ad} \\ K_{da} & K_{dd} \end{bmatrix} \begin{Bmatrix} x_a \\ x_d \end{Bmatrix}. \tag{9.6}$$

Here, K_{aa} contains the stiffnesses at and between all active degrees of freedom, K_{ad} and K_{da} contain the stiffness connections between active and deleted sets $\left(K_{ad} = K_{da}^T\right)$, K_{dd} contains the stiffnesses and connections between all deleted degrees of freedom, and F_a and F_d contain the external forces acting on the active and deleted DOFs, respectively. Next, the lower partition is taken and F_d is assumed zero (i.e., no forces act on a deleted DOF), yielding:

$$K_{da} x_a + K_{dd} x_d = 0,$$

$$x_d = -K_{dd}^{-1} K_{da} x_a. \tag{9.7}$$

Substituting Eq. (9.7) into the top partition of Eq. (9.6) leads to

$$F_a = \left(K_{aa} - K_{ad} K_{dd}^{-1} K_{da}\right) x_a, \tag{9.8}$$

where the system is now reduced in that its static equilibrium is expressed only by the active DOFs—the set of relevant DOFs has been *condensed* to exclude the deleted set. Thus, Eq. (9.7) can be used to satisfy Eq. (9.2) and determine the Guyan transformation matrix, T_G:

$$\begin{Bmatrix} x_a \\ x_d \end{Bmatrix} = \begin{bmatrix} I_{aa} \\ -K_{dd}^{-1} K_{da} \end{bmatrix} x_a = T_G x_a, \tag{9.9}$$

where I_{aa} is the Identity matrix with dimensions a by a. The reduced mass and stiffness matrices can then be determined according to Eqs. (9.3) and (9.4).

It should be noted that the traditional Guyan reduction technique presented above does not account for mass-inertial effects on the system resulting from the deleted DOFs; thus, an improved Guyan reduction has been developed to combat this for situations where such considerations are critical [4]. The improved Guyan transformation, T_G^*, is defined as

$$T_G^* = T_G + \begin{bmatrix} 0 & 0 \\ 0 & K_{dd}^{-1} \end{bmatrix} M_n T_G M_a^{-1} K_a, \tag{9.10}$$

where M_n is the n-set mass matrix partitioned according to K_n in Eq. (9.6), and M_a and K_a are the traditional Guyan-condensed mass and stiffness matrices.

9.2.2.2 System Equivalent Reduction Expansion Process

The SEREP transformation operates using a modal space projection between the reduced a-set and the full n-set [4]. The modes of the FEM are computed, and the mode shapes, U_n, are partitioned based on the active and deleted DOFs:

$$x_n = U_n p, \tag{9.11}$$

$$\begin{Bmatrix} x_a \\ x_d \end{Bmatrix} = \begin{bmatrix} U_a \\ U_d \end{bmatrix} p, \tag{9.12}$$

where U_a and U_d are the sets of mode shapes corresponding to the active and deleted DOFs and p is the corresponding set of modal-space degrees of freedom. The top partition of Eq. (9.12) can be manipulated and then inserted into Eq. (9.11) to obtain the SEREP transformation matrix as in Eq. (9.2):

$$\begin{aligned} p &= U_a^{\dagger} x_a, \\ x_n &= U_n U_a^{\dagger} x_a = T_S x_a. \end{aligned} \tag{9.13}$$

Note that because U_a is not necessarily square, the generalized inverse is taken, denoted by $\circ^{\dagger}$.

9.2.2.3 Craig-Bampton Reduction

Craig-Bampton Reduction is not a traditional model reduction method; rather, it is a component-mode synthesis (CMS) technique which can act as a reduction method [5]. As a result, it is implemented using CMS, rather than the previously mentioned procedure. The method begins by first identifying the components that will be connected. For each component, the set of n degrees of freedom is split into two sets—the i-set (interior) and the b-set (boundary):

$$x_{CB}^{(s)} = \begin{Bmatrix} x_i^{(s)} \\ x_b^{(s)} \end{Bmatrix}, \tag{9.14}$$

where x_{CB} is the Craig-Bampton partitioned set of DOFs, x_i and x_b represent the interior and boundary DOF sets, and $\circ^{(s)}$ denotes that the associated variable differs based on the component (substructure) it represents. The boundary set contains the DOFs which will overlap with those of another component to connect them together, and the interior set contains the remaining DOFs. Similarly to Eq. (9.6), the original mass and stiffness matrices can then be rearranged according to Eq. (9.14):

$$\widehat{M}_{CB}^{(s)} = \begin{bmatrix} \widehat{M}_{ii}^{(s)} & \widehat{M}_{ib}^{(s)} \\ \widehat{M}_{bi}^{(s)} & \widehat{M}_{bb}^{(s)} \end{bmatrix}, \tag{9.15}$$

$$\widehat{K}_{CB}^{(s)} = \begin{bmatrix} \widehat{K}_{ii}^{(s)} & \widehat{K}_{ib}^{(s)} \\ \widehat{K}_{bi}^{(s)} & \widehat{K}_{bb}^{(s)} \end{bmatrix}. \tag{9.16}$$

The constraint modes, $\widehat{\Psi}_{ib}^{(s)}$, of each component are computed next. The constraint modes are the resulting static deformation of the given component when one of the b-set degrees of freedom is subjected to a unit displacement while the remaining coordinates in the boundary set are restrained and the DOFs in the i-set are left unforced. This is given as

$$\widehat{\Psi}_{ib}^{(s)} = -\widehat{K}_{ii}^{-1}\widehat{K}_{ib}. \tag{9.17}$$

Now the fixed-interface modes, $\widehat{\Phi}_{ii}$, of each component are determined. These are the mode shapes that result from solving the eigenvalue problem for each component while restraining the boundary DOFs, x_b, written as

$$\left[\widehat{K}_{ii}^{(s)} - \omega_{(s)}^2 \widehat{M}_{ii}^{(s)}\right]\left\{\widehat{\Phi}_{ii}^{(s)}\right\} = 0, \tag{9.18}$$

noting that here the resulting eigenvalues, ω^2, are not pertinent to the ROM and can be disregarded.

It is at this point when the reduction can be implemented; this occurs by choosing the desired modes that contain the relevant dynamic information pertinent to the analysis which the reduced model should contain. The columns of $\widehat{\Phi}_{ii}$ contain the i number of interior modes of the given component. The modes desired to be used can be chosen by removing the corresponding columns from $\widehat{\Phi}_{ii}$ and using them to form $\widehat{\Phi}_{ia}$, where a is the number of reduced-set modes. Now, the Craig-Bampton transformation matrix, $\widehat{T}_{CB}$, is assembled for each component as

$$\widehat{T}_{CB}^{(s)} = \begin{bmatrix} \widehat{\Phi}_{ia}^{(s)} & \widehat{\Psi}_{ib}^{(s)} \\ 0 & I_{bb} \end{bmatrix}, \tag{9.19}$$

where I_{bb} is the b by b Identity matrix. Using Eqs. (9.3) and (9.4), the componentwise mass and stiffness matrices can be transformed into CB coordinates:

$$M_{CB}^{(s)} = \widehat{T}_{CB}^{(s)^T}\widehat{M}_{CB}^{(s)}\widehat{T}_{CB}^{(s)}, \tag{9.20}$$

$$K_{CB}^{(s)} = \widehat{T}_{CB}^{(s)^T}\widehat{K}_{CB}^{(s)}\widehat{T}_{CB}^{(s)}. \tag{9.21}$$

Next, the Component Coupling Matrix, S, is formed. This is a Boolean matrix that relates the physical-space coordinates, x_{CB}, and the generalized coordinate space used for the CB transformation, η_{CB}, by the relationship $x_{CB} = S \cdot \eta_{CB}$. An example is provided for a 3-component bar of 1-D elements:

$$\begin{Bmatrix} x_a^{(1)} \\ x_{b,R}^{(1)} \\ x_a^{(2)} \\ x_{b,L}^{(2)} \\ x_{b,R}^{(2)} \\ x_a^{(3)} \\ x_{b,L}^{(3)} \end{Bmatrix} = \begin{bmatrix} 1\,0\,0\,0\,0 \\ 0\,0\,0\,1\,0 \\ 0\,1\,0\,0\,0 \\ 0\,0\,0\,1\,0 \\ 0\,0\,0\,0\,1 \\ 0\,0\,1\,0\,0 \\ 0\,0\,0\,0\,1 \end{bmatrix} \begin{Bmatrix} \eta_{CB}^{(1)} \\ \eta_{CB}^{(2)} \\ \eta_{CB}^{(3)} \\ u_b^{(1)} \\ u_b^{(2)} \end{Bmatrix}.$$

Here, L and R denote the left and right boundary DOF sets, $\eta_{CB}^{(j)}$ contains the CB-transformed interior degrees of freedom of the j'th component, and $u_b^{(k)}$ is the set of boundary DOFs in CB coordinates contained in the k'th interface between substructures.

The reduced mass and stiffness matrices in Craig-Bampton space for the full assembly are formed by creating a block diagonal of the component matrices:

$$\overline{M} = \begin{bmatrix} M_{CB}^{(1)} & \cdots & 0 \\ \vdots & \ddots & \vdots \\ 0 & \cdots & M_{CB}^{(m)} \end{bmatrix}, \tag{9.22}$$

$$\overline{K} = \begin{bmatrix} K_{CB}^{(1)} & \cdots & 0 \\ \vdots & \ddots & \vdots \\ 0 & \cdots & K_{CB}^{(m)} \end{bmatrix}, \tag{9.23}$$

where m is the total number of components. The reduced physical-space system matrices are then

$$M = S^T \overline{M}\, S, \tag{9.24}$$

$$K = S^T \overline{K}\, S, \tag{9.25}$$

and the eigenanalysis of the reduced assembly can be performed:

$$\left[K - \omega_j^2 M\right] \{U_j\} = 0. \tag{9.26}$$

Now, $\overline{U}_{CB}$ is defined as the set of mode shapes in reduced physical coordinates and is found by horizontally concatenating U_j for all j modes. These ROM shapes can be dissected into

$$\overline{U}_{CB} = \begin{Bmatrix} U_a^{(1)} \\ U_a^{(2)} \\ \vdots \\ U_a^{(m)} \\ U_b \end{Bmatrix}, \tag{9.27}$$

where $U_a^{(j)}$ contains a modes of the j'th component's reduced set of interior DOFs and U_b contains a modes for the boundary set degrees of freedom among all components. Finally, the expanded mode shapes, U_{CB}, are determined by performing the following operations with the reduced mode shapes:

$$U_{CB} = \begin{bmatrix} \widehat{\Phi}_{ia}^{(1)} U_a^{(1)} + \widehat{\Psi}_{ib}^{(1)} U_b^{(1)} \\ U_b^{(1)} \\ \vdots \\ \widehat{\Phi}_{ia}^{(m)} U_a^{(m)} + \widehat{\Psi}_{ib}^{(m)} U_b^{(m)} \\ U_b^{(m)} \end{bmatrix}, \tag{9.28}$$

where the superscript of U_b denotes the component by which its rows should be used (e.g., if the superscript is 2, then the rows of U_b corresponding to the boundary degrees of freedom of the second component should are to be taken). It should be noted that the majority of boundary DOFs will be included in two different subscripted U_b partitions due to the overlapping of interface degrees of freedom between conjoined components.

9.3 Results from Finite Element Analysis

To demonstrate the validity and examine the effectiveness of the unit cell reduction technique, a simple finite element model of a metamaterial structure is created. Frequency response functions (FRFs) of the FEM and ROMs are generated to compare reduction accuracy, and the frequency response assurance criterion (FRAC) is used to quantify the accuracy. The FRAC between two given FRF curves is computed as

$$FRAC = \frac{\left| H_{ROM} H_{FEM}^{*T} \right|^2}{\left| H_{ROM} H_{ROM}^{*T} \right| \cdot \left| H_{FEM} H_{FEM}^{*T} \right|}, \tag{9.29}$$

where H_{ROM} and H_{FEM} are the discrete transfer functions for the ROM and FEM and $\circ^{*T}$ denotes the Hermitian transpose [6]. The FRAC ranges from 0 (no resemblance) to 1 (perfect match). For all presented cases, the FRF represents the response at the right end (5001st DOF) due to an input force at the left end (1st DOF), and the FRF magnitudes are presented in terms of acceleration/force with units of $\frac{m/s^2}{N}$.

9.3.1 Model Description

The finite element model is developed using MATLAB and is formulated as a 1-dimensional axially vibrating bar. The bar is divided into 5000 elements—to obtain many modes and a large DOF count for demonstrating the effects of the reduction—and a total of 10 resonators are attached to the bar to simulate the dynamic response of metamaterials. The bar is divided into 10 identical groups of 500 elements each, and one metaresonator is attached to the central DOF in each cell, each having a mass of 0.5% of the bar's total mass. Springs are attached to the left and right-most ends of the model, and their spring constants are varied to approximate free and fixed conditions (e.g., a spring stiffness near zero leads to an effectively free boundary condition). The metaresonators are implemented so that they have the same natural frequency of 20 kHz. The bar is 15.24 cm in length, has a solid square cross section with side lengths of 1.27 cm, and has an elastic modulus of $2.9 \cdot 10^5$ psi (ABS plastic). A diagram depicting a sparser FEM of the same configuration is provided in Fig. 9.3. Additionally, the first five mode shapes of the bar are plotted in Fig. 9.4, and the FRF of the FEM is shown in Fig. 9.5. Both are for fixed-free boundary conditions.

It can be clearly seen from the FRF that there exists a dramatic lack of response in the region near 20 kHz, demonstrating the unique characteristic of metamaterial structures. The metaresonators act similarly to tuned mass dampers in that they absorb the kinetic energy of the parent structure's vibrational response at frequencies near their natural frequency, and if that natural frequency is near to a resonant frequency of the structure, the resonance peak is split.

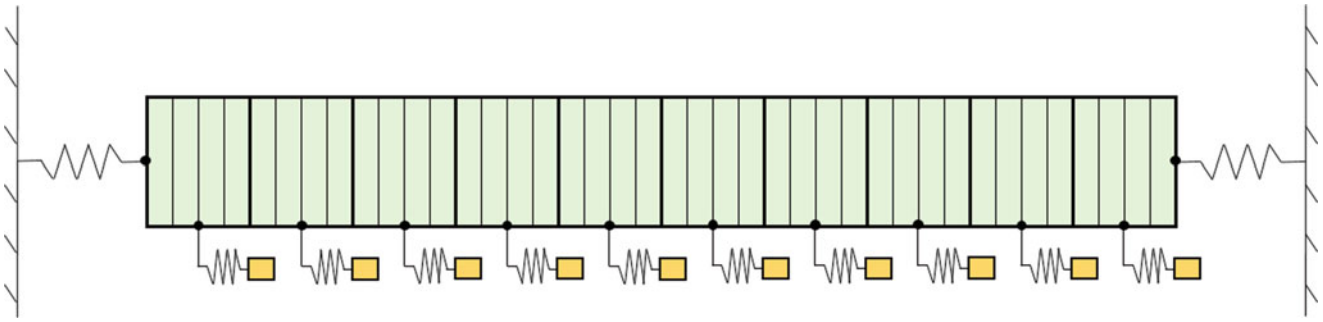

Fig. 9.3 Diagram similar to the finite element model used for analysis

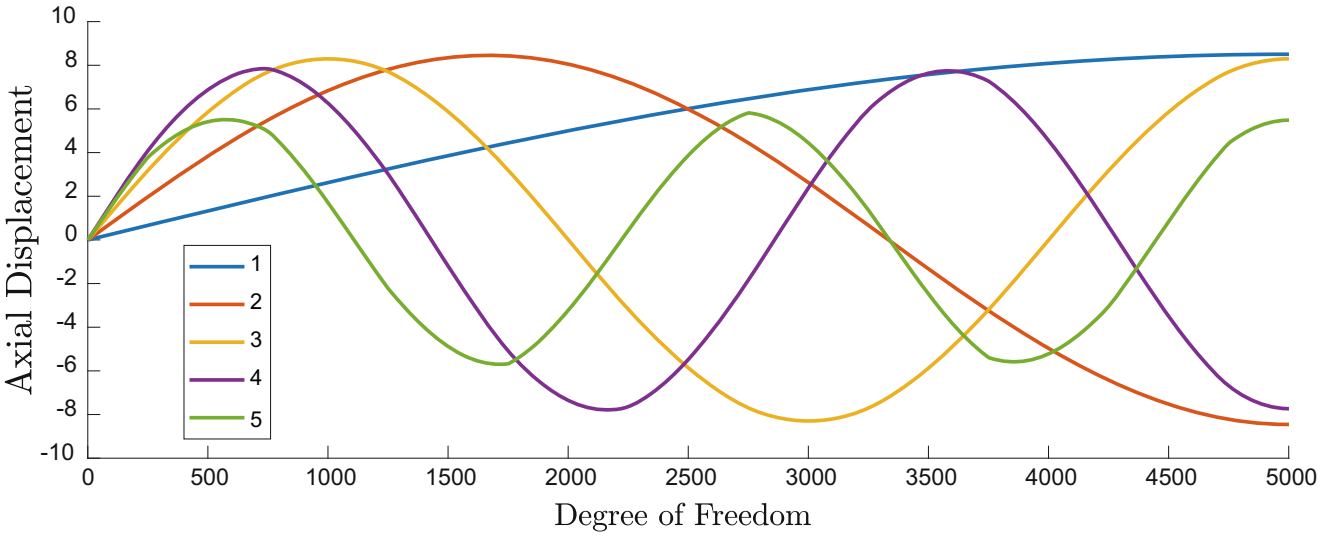

Fig. 9.4 Plot of the first 5 mass-normalized mode shapes of the FEM under fixed-free conditions. The first 5 natural frequencies are 4.37, 8.71, 12.91, 16.62, 18.72 kHz

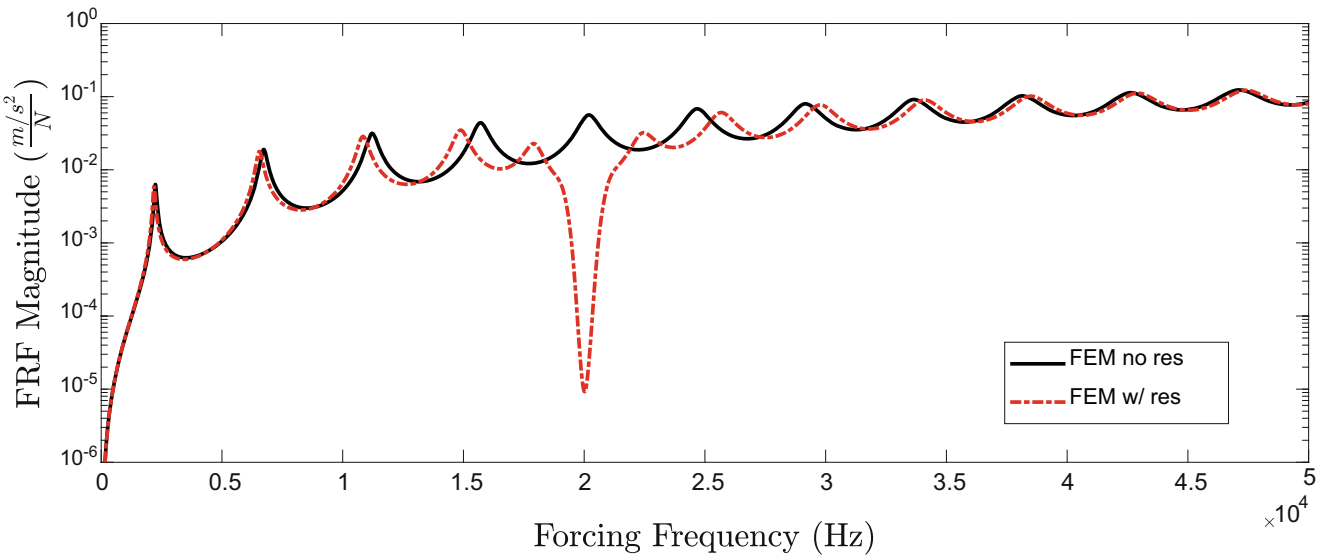

Fig. 9.5 Plot of the FRF (left-end input, right-end output) of the metamaterial FEM for fixed-free conditions with and without the metaresonators attached

Table 9.1 Comparison of cell B.C.'s effects on the FRF prior to assembly when the FEM has free-free conditions

Left B.C. (cell)	Right B.C. (cell)	SEREP FRAC	Guyan FRAC	Impr. Guyan FRAC
Free	Free	0.9505	0.4458	0.6330
Fixed	Free	0.0082	0.0078	0.0682
Fixed	Fixed	0.0174	0.0118	0.0159

Table 9.2 Comparison of cell B.C.'s effects on the FRF prior to assembly when the FEM has fixed-free conditions

Left B.C. (cell)	Right B.C. (cell)	SEREP FRAC	Guyan FRAC	Impr. Guyan FRAC
Free	Free	0.9533	0.7081	0.7564
Fixed	Free	0.0198	0.1910	0.0327
Fixed	Fixed	0.2221	0.0131	0.1872

Table 9.3 Comparison of cell B.C.'s effects on the FRF prior to assembly when the FEM has fixed-fixed conditions

Left B.C. (cell)	Right B.C. (cell)	SEREP FRAC	Guyan FRAC	Impr. Guyan FRAC
Free	Free	0.8763	0.6654	0.6677
Fixed	Free	0.0345	0.0270	0.3531
Fixed	Fixed	0.3263	0.1169	0.1059

9.3.2 Cell-Level Boundary Conditions

As discussed earlier, the Craig-Bampton method requires determination of the fixed-interface modes prior to synthesizing the components/cells to form the reduced assembly. This can be interpreted as the unit cell and its copies having fixed boundary conditions at the active DOFs. When using Guyan or SEREP reduction in performing the technique presented here, it is not initially apparent what, if any, boundary conditions should be assumed on the unit cell prior to copying and assembling. Apropos, a study is conducted pertaining to the effects of the unit cell's boundary conditions before being combined to the system-level reduced space, and the results are presented in Tables 9.1, 9.2 and 9.3. Implementation of the boundary conditions is accomplished by attaching springs to left and right-end DOFs at the component level. A spring constant of 10^{-12} N/m is used to simulate a free condition, whereas a stiffness of 10^{12} N/m is used to simulate a fixed condition. For each run, the same DOFs were used as the active sets for the SEREP and Guyan reductions, in which 96% of the original FEM DOFs were deleted.

For each scenario, it is apparent that using free-free conditions on the cells provides the most accurate FRF in the reduced assembly. That is, the entries in the cell-level stiffness matrices pertaining to the left and right ends of the cell should not be adjusted to increase their rigidity. When using cell B.C.'s that are free-free, SEREP has great accuracy for system-level B.C.'s of free-free and fixed-free, but its accuracy noticeably suffers when reducing a fixed-fixed FEM. On the other hand, Guyan is best (though still lackluster) in reducing FEMs with fixed-free conditions, and suffers accuracy when the assembly B.C.'s are set otherwise. Succinctly put, both methods are best-suited for the model reduction of FEMs with fixed-free conditions at the system level.

9.3.3 Variance in Reduction Percentage

To demonstrate the accuracy of each reduction method, FRF overlays are presented to visually compare the dynamic responses of the reduced-order models as the number of DOFs included in the active set decreases (i.e. the model is further reduced). The plots of the reduced models are named in reference to their cost savings quantified by *percent reduction*—the percentage of cell DOFs that were removed in the reduction process. Each graph also contains the FRF of the original FEM. In addition, a table is presented for each method to provide the FRACs associated with each curve.

Figure 9.6 provides examples of the DOF selections for the reduction techniques used. For the Guyan and SEREP methods, the a-set DOFs must at minimum include the boundary nodes as well as the central DOF. Inclusion of more degrees of freedom in the reduced set requires selection of DOFs symmetrically about the center. It should be noted that the center DOF must be included even if the resonator is attached eccentrically (i.e., attached to the center DOF); the node where the resonator attaches is not as pertinent in this case. For Craig-Bampton reduction, only the boundary nodes are selected; the quality of the reduction is determined by the number of modes chosen to use at the component level (see Eq. 9.19). For

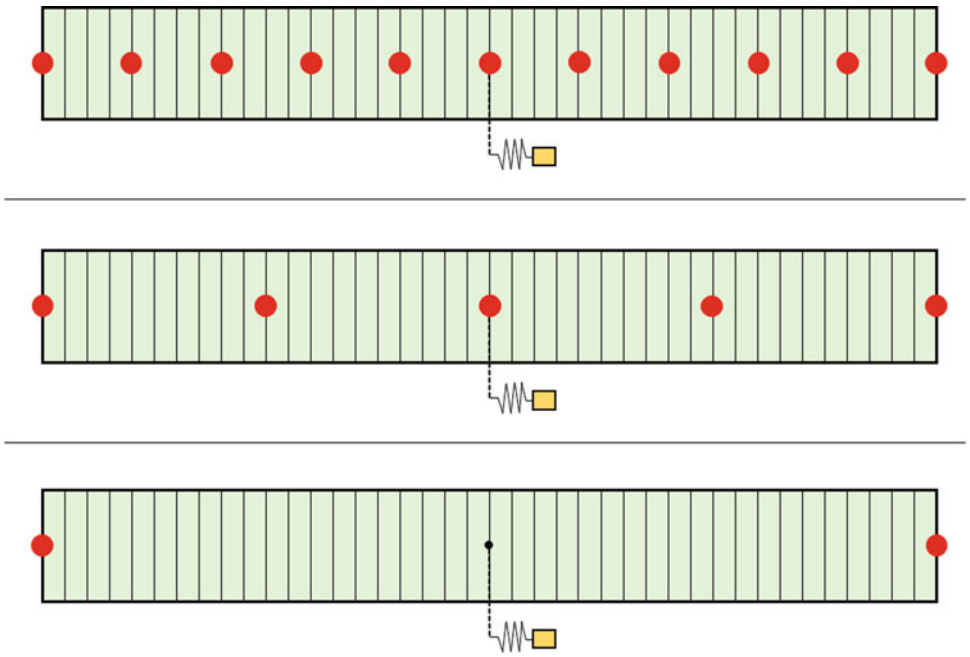

Fig. 9.6 Diagram to provide examples of the a-set DOF selection pattern for the different reduction methods. (Top and center) A pattern which is symmetric about the center of the bar should be chosen for Guyan and SEREP. (Bottom) Only the interface DOFs are chosen for Craig-Bampton

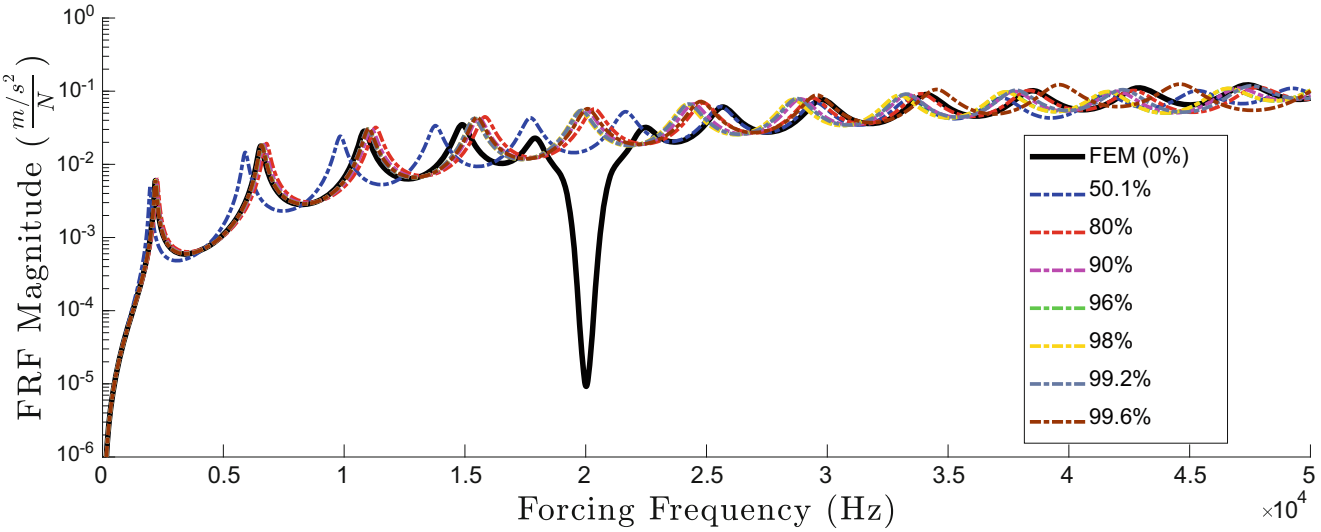

Fig. 9.7 FRF overlays between the FEM and the Guyan ROM with varying percent reduction

the model presented here, there are three unique component/boundary types used: left-end, where the boundary set includes the right-most DOF; right-end, where the boundary set includes the left-most DOF; and interior, where the b-set includes both the left and right-most nodes.

The frequency responses of the traditional and improved Guyan reduction methods are compared in Figs. 9.7, 9.8, and Table 9.4. It can be seen from Fig. 9.7 that the standard Guyan condensation is overall ineffective for reduction of the metamaterial FEM. Most notably, the technique entirely neglects effects due to the metaresonators and predicts a response as though the resonators were not attached to the bar. This is due to the fact that the DOFs of the resonators where the masses reside must be included in the deleted set for the technique to operate properly. As a result, the masses of the resonators (and therefore their dynamic effects on the bar) are excluded in the Guyan condensation.

Figure 9.8 shows that the improved Guyan method does account for the metaresonators quite well as a result of the augmented transformation matrix accounting for mass-inertial effects of the metaresonators. However, the improved

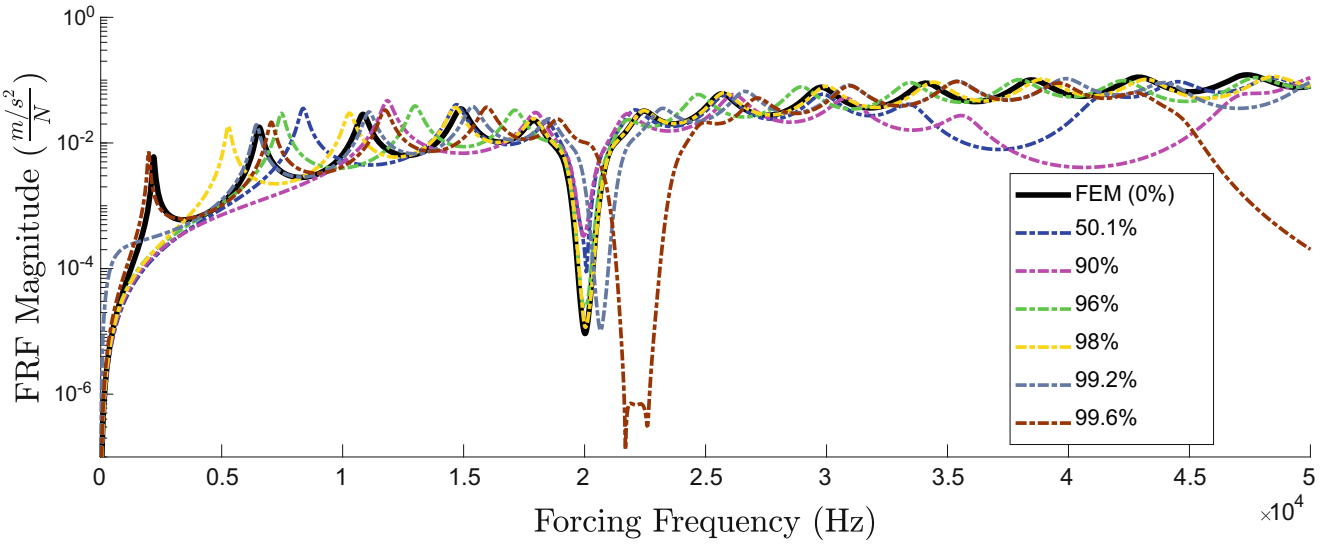

Fig. 9.8 FRF overlays comparing the FEM and improved Guyan ROM with varying percent reduction

Table 9.4 FRACs from Guyan condensation in relation to percent reduction

Percent reduction	Guyan FRAC	Impr. Guyan FRAC
50.1%	0.5745	0.5085
90%	0.7666	0.1824
96%	0.7081	0.7564
98%	0.6995	0.8791
99.2%	0.7122	0.6051
99.6%	0.3850	0.3326

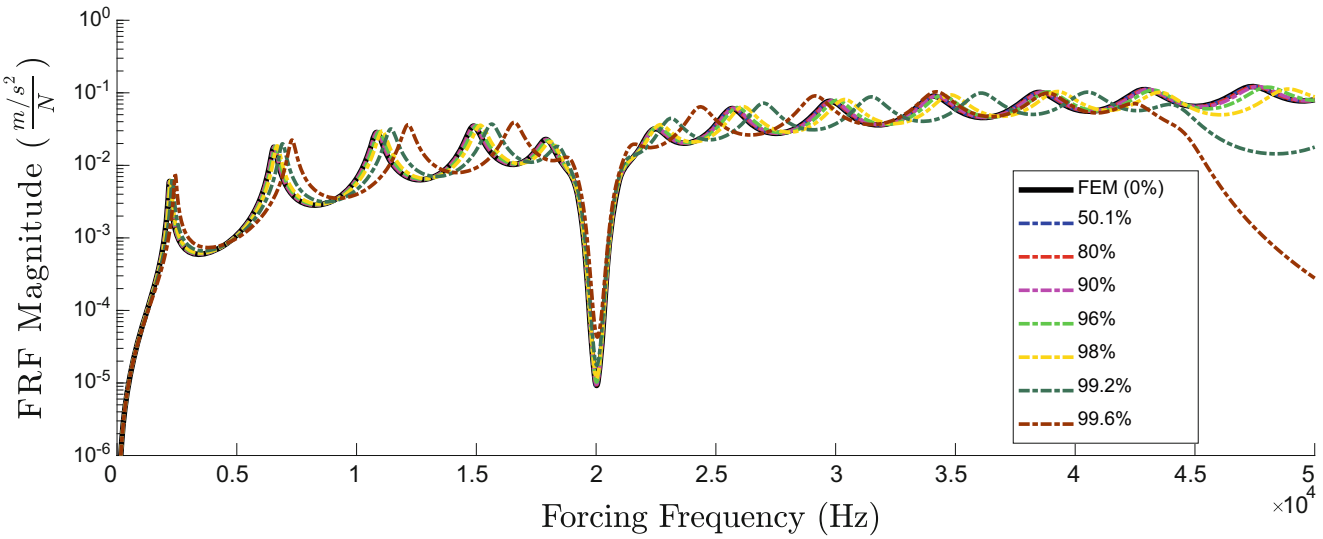

Fig. 9.9 FRF overlays comparing the FEM and SEREP ROM with varying percent reduction

technique comes with an interesting caveat: the results do not improve by including more DOFs in the active set. Rather, there appears to be a strong preference to certain a-set DOF distributions over others, regardless of the number of DOF retained. This is interesting because it is generally expected for lesser degrees of reduction to be more accurate than higher degrees. Also of note is that most of the ROM FRFs do not capture the first peak as in the FEM FRF.

The results from the SEREP ROM are shown in Fig. 9.9. Overall, SEREP has good accuracy for reduction percentages of 96% and below. Considerable deviations from the finite element response only occur beyond 99% reduction. Interestingly,

Table 9.5 FRACs from the SEREP technique in relation to percent reduction

Percent reduction	SEREP FRAC
50.1%	0.9998
80%	0.9984
90%	0.9931
96%	0.8198
98%	0.6110
99.2%	0.4821
99.6%	0.4399

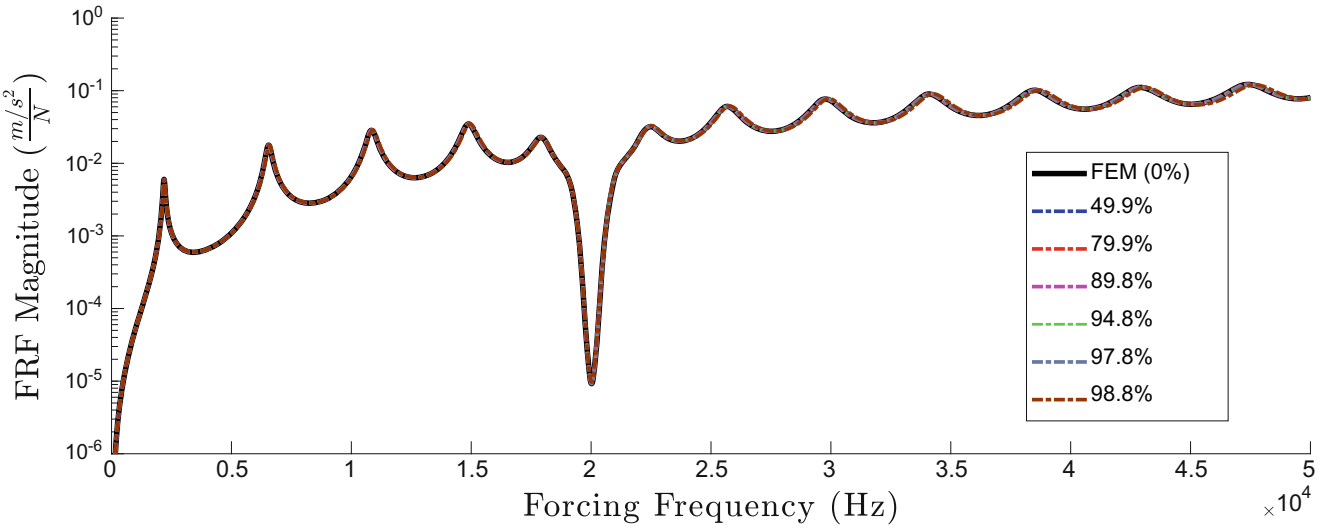

Fig. 9.10 FRF overlays comparing the FEM and Craig-Bampton ROM with varying percent reduction

Table 9.6 FRACs from the Craig-Bampton method in relation to percent reduction

Percent reduction	CBR FRAC
49.9%	1.0
79.9%	1.0
89.8%	0.9999
94.8%	0.9997
97.8%	0.9978
98.8%	0.9882

the SEREP ROM is extremely sensitive to the DOFs selected for the reduced set. For the model used here, the set of active DOFs is required to be symmetric about the location where the resonator attaches to the cell to obtain a reasonable solution. It can be seen from Table 9.5 that SEREP offers exceptional accuracy for up to 90% reduction. However, the authors believe this is an oddity particular to this model, as this issue is not usually present when using the SEREP technique. It is likely due to the nature of the mode shapes of the unit cells being symmetric, thereby creating numerical issues with non-symmetric active DOF selection. In general, SEREP is more sensitive to the modes in U_a than the DOF locations/distributions.

The results of the analysis pertaining to the Craig-Bampton method are shown in Fig. 9.10. It can be seen that CBR provides excellent accuracy in the dynamic response of the metamaterial bar even for considerably large reduction percentages. The FRAC values shown in Table 9.6 show that even at nearly a 99% reduction, the accuracy of the frequency response suffers less than 1.2% error.

The primary reason why the solution accuracies begin to suffer for high percent reductions is due to the number of degrees of freedom in the cells being too few to accurately contain information on a sufficient number of modes. Single-mode FRF plots (i.e., plotting the resonant response of one mode at a time) are presented in Fig. 9.11 to demonstrate the phenomenon using the SEREP method. The left plot represents the 90% reduced-order SEREP model. It can be seen that each single-mode FRF curve lines up appreciably well their corresponding resonance peaks in the FRF of the FEM. On the right plot, however, it can be seen that, at 99.6% reduction, SEREP does not contain sufficient information to accurately describe each resonance

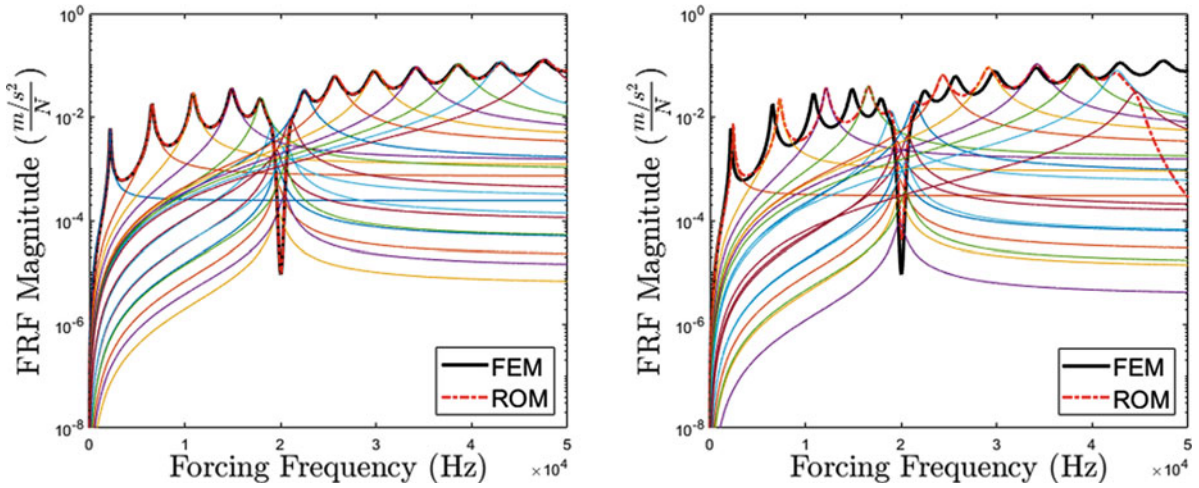

Fig. 9.11 Single-mode FRF overlays of (left) 90% reduction and (right) 99.6% reduction. The SEREP technique is used for both plots

peak, and the solution accuracy suffers as a result. To improve results, more or better a-set DOF and modes would need to be selected. As SEREP is a modal filter of sorts, the choice of modes in the U_a matrix must be similar to the modes important to the response in order to accurately reduce the model.

9.3.4 Discussion of the Reduction Techniques

Numerous commercial finite element packages allow for reduced-order modeling using standard Guyan condensation and/or Craig-Bampton reduction. CBR provides an excellent means for model reduction and boasts the highest accuracy for this FEM. Considerably large degree of freedom reductions of nearly 99% can be applied and still yield excellent agreement with the original finite element model. However, Craig-Bampton reduction is notably more difficult to implement than typical model reduction techniques.

From the analysis presented here, it has been shown that Guyan reduction is inadequate for the reduction of this metamaterial model, because it entirely disregards the mass effects from the metaresonators. This may be due to the metaresonators being modeled as a simple spring-mass. Using the improved Guyan technique rectifies the issue; however, the accuracy of the improved solution is volatile depending on the amount of reduction applied. Despite these flaws, Guyan condensation is less arduous to implement than the Craig-Bampton method, and can lead to respectable accuracies under the proper conditions.

Less ubiquitous than its counterparts presented here, the SEREP technique is the fastest and least difficult method to implement for the presented model. The method is able to produce highly accurate reduced-order models of reduction percentages up to 90%. However, the selection of a-set degrees of freedom and modes in the U_a matrix is perhaps most critical for SEREP and can be a hindrance to obtaining an acceptable solution.

9.4 Conclusions

A finite element model of a simple metamaterial axial bar was developed to demonstrate how model reduction techniques can be used to reduce the computational cost of simulating metamaterial dynamics. The cost savings comes from taking advantage of the self-repeating structure of many metamaterials, where the system is comprised of multiple identical unit cells. Reduction of the unit cell can be performed with any of the various model reductions methods.

However, as shown in this work, the accuracy of the assembled system is affected by the reduction method as well as each methods' nuances. Interestingly, for the model used here, traditional Guyan reduction was ineffective because the static condensation does not account for the resonator mass effects, while Improved Guyan yielded better results. In general, Craig-Bampton or SEREP reduction methods provided good matches to the full FEM FRFs, although SEREP was sensitive to the choice of a-set DOF and modes.

The next step in this work will be to implement this ROM method on a three-dimensional model of a more geometrically complicated metamaterial. Lessons learned from this work, in terms of reduction methods and sensitivities, will be useful for developing the ROMs of the 3-D model. Likely, the main challenge with implementing this ROM method to a self-repeating three-dimensional model will be in the bookkeeping—keeping track of the cell-level interface DOF and making proper connections between the reduced cell DOF during the system assembly process.

References

1. Nonis, C., Thibault, L., Marinone, T., Avitabile, P.: Development of full space system model modes from expansion of reduced order component modal information. In: Topics in Modal Analysis, vol. 7. Springer, New York (2014)
2. Matlack, K.H., Bauhofer, A., Krödel, S., Palermo, A., Daraio, C.: Composite 3D-printed metastructures for low-frequency and broadband vibration absorption. Proc. Natl. Acad. Sci. U. S. A. **113**(30), 8386–8390 (2016)
3. Guyan, R.J.: Reudction of stiffness and mass matrices. AIAA J. **3**(2), 380 (1965)
4. Avitabile, P.: Model reduction and model expansion and their applications Part 1—Theory. Modal Analysis and Controls Laboratory, University of Massachusetts Lowell, Lowell, MA (2005)
5. Craig, R.R., Kurdila, A.J.: Fundamentals of Structural Dynamics. Wiley, Hoboken, NJ (2006)
6. Avitabile, P.: Test-Analysis Correlation-Updating Considerations. Modal Analysis and Controls Laboratory, University of Massachusetts Lowell, Lowell, MA (2001)

Chapter 10
Imager-Based Techniques for Analyzing Metallic Melt Pools for Additive Manufacturing

Cedric Hayes, Caleb Schelle, Greg Taylor, Bridget Martinez, Garrett Kenyon, Thomas Lienert, Yongchao Yang, and David Mascareñas

Abstract Presented is a vision-based algorithm for extracting physical properties from melt pools. The bandwidth requirements for traditional high speed video are too high for real time analysis so silicon retinas are used. This method of imaging has a very fine temporal resolution, high dynamic range, and low bandwidth requirements. The ability to monitor melt pools in real time would improve the quality of laser printed parts and welds because it would allow automatic control systems to recognize and correct imperfections during the printing and welding processes. By measuring the change of intensity within a melt pool then applying blind source separation techniques, spatiotemporal data can be extracted. First a circular membrane model is evaluated to validate the technique. Then the separation technique is performed with a traditional camera on gallium pools of different depths and various lighting conditions. Finally, silicon retina data is used to show that the technique can be applied for this type of imager.

Keywords Additive manufacturing · Event-based imaging · Melt pool depth · Blind source separation · Modal analysis

10.1 Introduction

Additive manufacturing is a rapidly growing industry, but there are still many nuances that have to be addressed. Small errors in the building process can go undetected and cause the print to fail. Furthermore, as the industry moves forward, there is an increased demand for online additive manufacturing because it allows for remote monitoring and control of the manufacturing process. Finding an imaging technique that requires low bandwidth and a fast full field response will go a long way to making that a possibility.

Melt pool depth is a crucial feature of metallic additive manufacturing because it influences the structure and material properties of the printed part. If the pool is too deep, it re-melts the previous layer, changing the microstructure in an unpredictable fashion; however, a shallow pool will create an inconsistent and thinner layer. There are several methods that can be used to control the depth of melt pools, and this paper will focus on analyzing pool oscillations and their correlation to melt pool depth.

C. Hayes
New Mexico Institute of Mining and Technology, Silver City, NM, USA

C. Schelle
Los Alamos National Laboratory (LANL), MSC 932, Los Alamos, NM, USA

G. Taylor
New Mexico State University, Las Cruces, NM, USA

B. Martinez
LANL, Los Alamos National Laboratory MS T001, Los Alamos, NM, USA

G. Kenyon
LANL, Los Alamos National Laboratory MS B256, Los Alamos, NM, USA

T. Lienert
Los Alamos National Laboratory, Los Alamos, NM, USA

Y. Yang
Argonne National Laboratory, Lemont, IL, USA

D. Mascareñas (✉)
Engineering Institute, Los Alamos National Laboratory, Los Alamos, NM, USA
e-mail: dmascarenas@lanl.gov

N. Dervilis (ed.), *Special Topics in Structural Dynamics & Experimental Techniques, Volume 5*, Conference Proceedings of the Society for Experimental Mechanics Series, https://doi.org/10.1007/978-3-030-12243-0_10

Traditionally, data for modal analysis is captured with accelerometers, strain gages, laser Doppler vibrometers, or digital image correlation. These methods are generally insufficient when they are applied to analyze liquid pools; sensors that require contact with the surface, such as accelerometers, cannot be affixed to a liquid pool, and a speckle pattern cannot be applied to the pool for DIC. Video imaging is ideal because it is low cost, easily accessible, and provides a full-field method of sensing, where each pixel acts as a sensor. Implementing video imaging in online additive manufacturing systems is feasible and could provide a robust solution to the challenge of monitoring melt pool depth.

The objective of this study is to improve video-based modal analysis techniques in a way that leads to a correlation between a melt pool's depth and modal features. The new technique will not require any surface preparation or sensors to be mounted and will utilize an event-based imager to extract data from the experiment for analysis. The collected data was treated as a blind source separation problem and was solved with principal component analysis and a complexity pursuit algorithm.

10.2 Background

10.2.1 Additive Manufacturing Melt Pools

Additive manufacturing and laser welding share many similarities, and in both processes, it is difficult to monitor the internal geometry of the melt pool during the automated production of parts. Maximum pool depth is one of the most important features in these processes and there is significant interest in being able to control weld penetration remotely. There have been studies in the past that treated melt pools as thin membranes and examined the correlation between pool oscillations and the resulting ripple formation in the weld [1]. It has also been shown that there is a relation between the natural frequency of oscillations and the diameter of the melt pool. Consequently, there may be a relation between oscillations and pool depth [2].

10.2.2 Phase and Intensity Based Imaging

Phase-based imaging has been used with great success in extracting the mode shapes from videos of solid structures. Phase-based imaging is a technique that tracks changes in phase, in the spatial frequency domain, between consecutive frames [3]. By applying Gabor filters to the Fourier transform of an image, phases of similar spatial scale and orientation can be analyzed together and time histories that are related to an objects position can be extracted [4, 5].

Intensity-based imaging is a more straightforward technique that may prove helpful when looking at out-of-plane motion, such as an oscillating melt pool. In intensity-based imaging, the measurement comes from the changes in light intensity as the waves propagate. The time history associated with this motion assumes an object with a stationary border and changing interior intensity, as opposed to the phase-based technique that assumes a translating border and constant interior intensity.

10.2.3 Blind Source Separation

Blind source separation (BSS) is a group of processes that decompose time histories of combined signals at different measurement locations into the most likely original signals. These methods can be applied to the separation of modes from spatiotemporal measurements. One of these BSS methods, complexity pursuit, has been used previously for phase-based separation [5]. While no BSS technique is perfect, this method has shown to be practical for modal decomposition.

10.2.4 Event-Based Imagers

Most traditional imager data is redundant because each frame captures the entire picture even if only several pixels change. To analyze this data in an efficient manner, it must be reduced to a form that contains the most relevant information. To do this we use principal component analysis (PCA), a statistical method used to reduce the dimensionality of a problem [6]. The process creates orthogonal axes along the largest spreads of data. By creating a new coordinate system about the data

that maximizes variance, the most prominent features are defined, and those become the principal components. This process eliminates unnecessary data from our videos and helps set up the code to extract modal information.

Event-based imagers, such as the silicon retina, capture images using a different method than traditional imagers. The silicon retina's pixels all act independently, only collecting light intensity changes. Traditional imagers are frame-based, and capture images using every pixel in the frame over a discrete time step. Event-based imagers however, have pixels that record independently of one another and capture a time history of events caused by changes in light intensity on each pixel. This technique is advantageous because it requires significantly less bandwidth [7].

Inter-spike intervals are the intervals between the events that are recorded by event based imagers. When an individual pixel detects a positive change in light (brighter), it fires and records a 1 and then resets. When a pixel detects a negative change in light, it records a −1 and then resets. This series of data can then be analyzed to extract the natural frequencies associated with potential mode shapes of the melt pool.

10.3 Finite Element Model of Melt Pool

Based on a paper by Kotecki et al. the melt pool was modeled as a thin circular membrane, analogous to a drum head [1]. Due to the complexity of the components inside melt pools, including Marangoni forces, convection currents, vapor forces from the carrier gas, and Lorenz forces, CFD methods would be necessary to model the pool and the resources required would extend beyond the scope of our research. The membrane model has flaws: it does not conserve volume, include heat flux, or account for Marangoni flows. Additionally, the membrane model uses pinned edge boundary conditions instead of the mixed boundary conditions that are expected on the edges of a liquid pool. Despite these flaws, the membrane model represented the motion of a melt pool accurately enough to inform us what mode shapes and frequencies to expect from a physical pool. Ultimately, a more refined, reduced-order model would better simulate the motion of a physical pool and it could be used to assess the validity of the modes we extracted from the recordings.

10.4 Experimental Model

Gallium was used to represent the melt pools that are created during additive manufacturing because its low melting temperature made it easier to work with than any other metal. The pools of gallium were contained in round bottomed holes that were drilled into a Teflon test fixture. The geometries the holes are listed in Table 10.1. Figure 10.1 shows one of the Teflon test fixtures with four holes drilled into it using a ball-nosed bit. Figure 10.2 depicts how the fixture is bolted to a single axis shaker so that the axis of pool depth is parallel to the axis of excitation. The fixture was excited with two different methods: a hammer and a Gaussian distributed noise signal to look at how the pools respond to impacts and random vibration. A high speed camera and silicon retina (DVS240) were mounted above the fixture so that all pools are visible during the experiment. The data was processed to extract modal features including shape, frequency, and damping ratio.

Currently there are not any direct methods for the analysis of silicon retina data in the purely sparse form. We decided to convert it into a full field data structure like a traditional camera. To do this we followed a simple algorithm. First, for a small interval of time all the sparse data points were summed on a spatial frame, with positive polarity adding and negative subtracting. Then that frame was recorded. Finally, a portion of that frame, 95–99% depending on the frame rate, would be passed on to the next frame. This was done because otherwise noise and other undesirable signals would propagate through the entire time history. Once the silicon retina data is converted, it can be processed using the PCA-CP algorithm.

Table 10.1 Dimensions of the holes in the Teflon fixture

Fixture	Hole 1 depth (in)	Hole 2 depth (in)	Hole 3 depth (in)	Hole 4 depth (in)	Hole width (in)
1 (0.254″)	0.249	0.244	0.247	0.254	0.5
2 (0.362″)	0.362	0.362	0.381	0.354	0.5
3 (0.187″)	0.185	0.193	0.185	0.187	0.5
4 (Various)	0.248	0.205	0.372	0.337	0.5

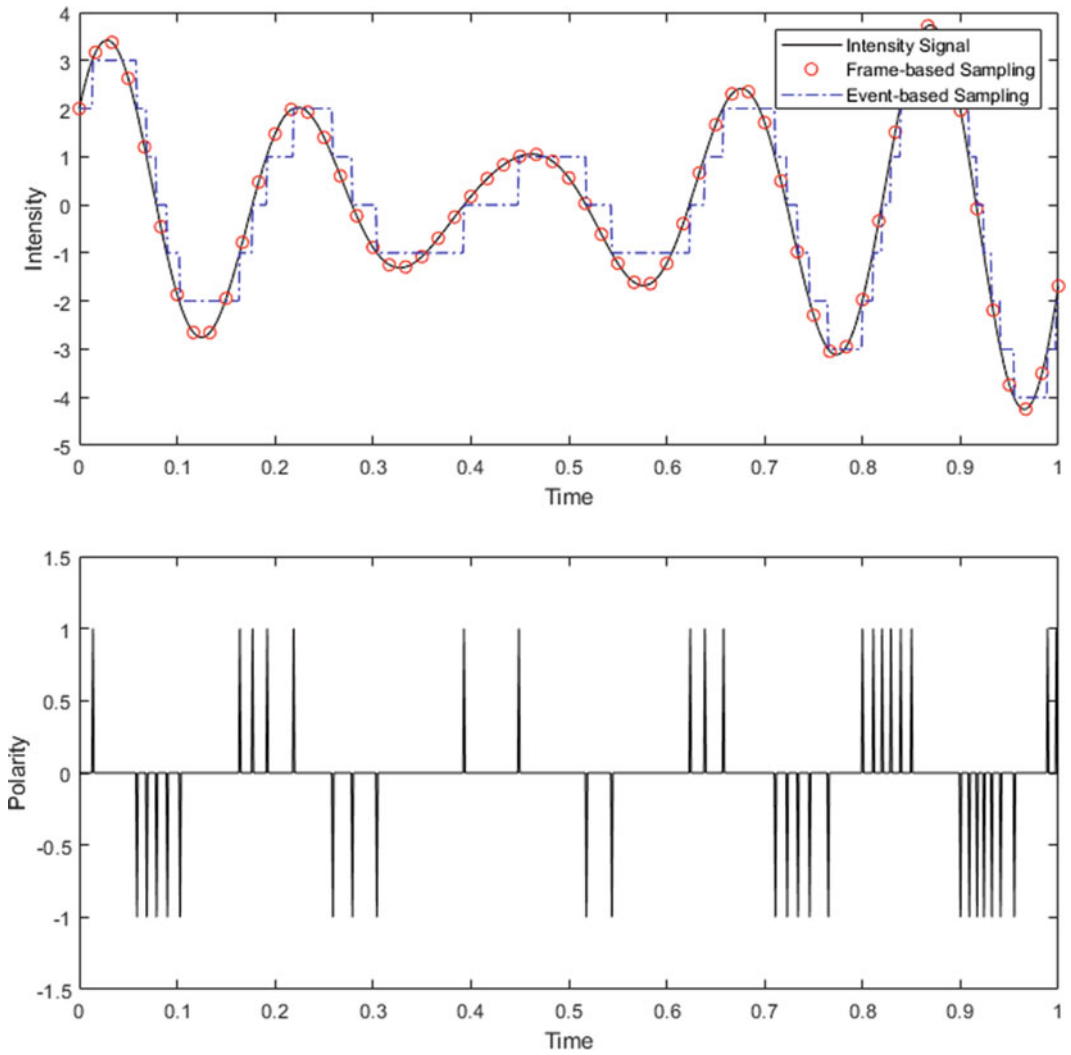

Fig. 10.1 Example of a single pixel's time history where +1 indicates a positive change in light intensity and −1 indicates a negative change in light intensity

10.5 Results

As shown in Fig. 10.3, the blind source separation of mode shapes appeared to be reasonable. The mode shapes of thin membranes are Bessel functions which have been used for most models. However, in our cases we do not see any of the first order. We also see that they all appear to have the same orientation. This is likely due to the origin of the light source causing brighter spots when the angle is directed towards the lens. Although these may not contain the actual displacement mode shapes, there is still frequency information embedded within the system.

The Modal Assurance Criterion (MAC) matrix is used to check the orthogonality between modes. A score of 0 is desirable off the diagonal because it indicates a lack of linear consistency between mode shapes. The Principal Component Analysis-Complexity Pursuit (PCA-CP) method focuses purely on PCA reduced time history data; so, if the MAC matrix is orthogonal, the method has enough time history and principal components to create a reliable interpretation of the data. Figure 10.4 shows a MAC matrix for the first 25 modes extracted and shows the extracted modes are highly dissimilar from one another.

Figure 10.5 shows three spectrograms of different depth pools to determine if there was a trend indicating depth as a function of frequency. The spectrogram on the left is the least deep and appears to have the lowest characteristic frequency. The other two pools' characteristic frequencies increase slightly with depth. However, this trend runs contrary to what would be expected in a system like this. Further investigation is required to determine which step is producing this error.

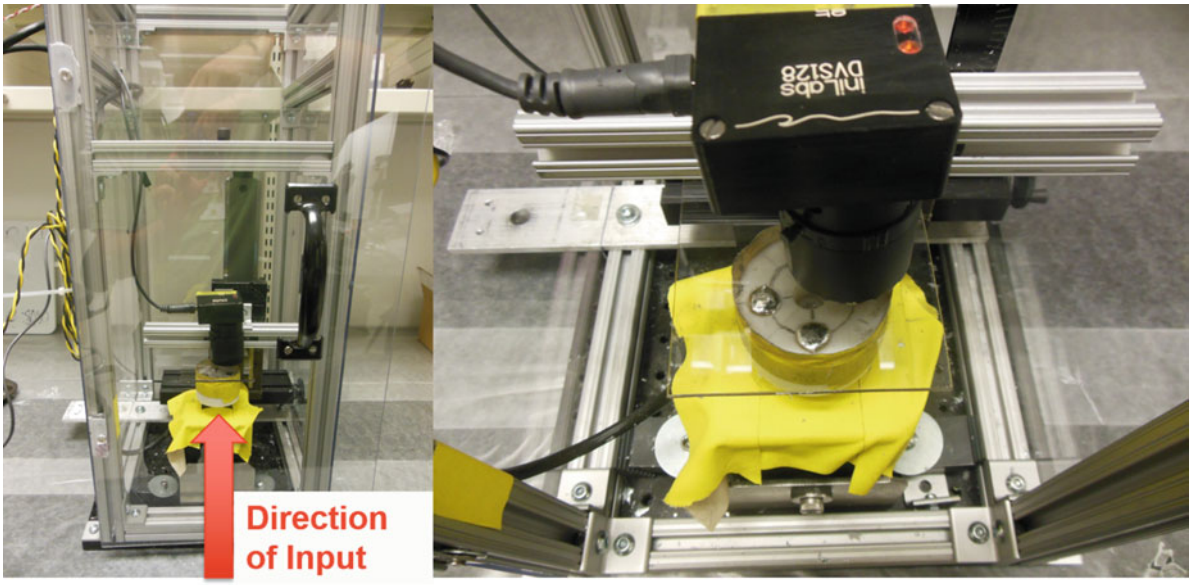

Fig. 10.2 (**a**, **left**) Experimental set up. (**b**, **right**) Close up of silicon retina looking at melt pools

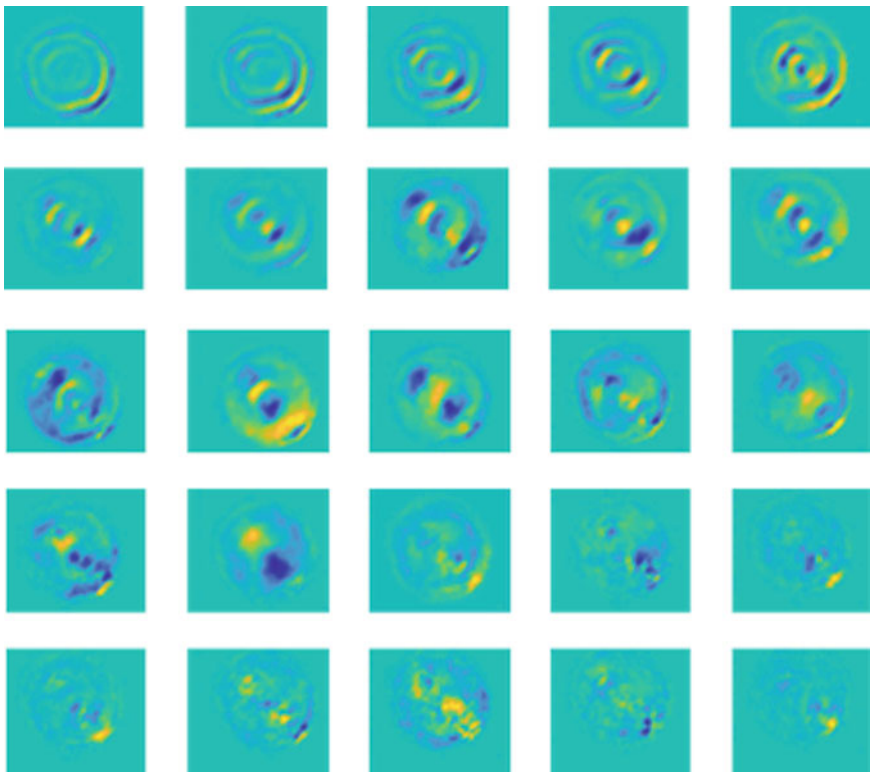

Fig. 10.3 Mode shapes for the first 25 modes

10.6 Conclusion

This study's research showed that extraction of structural dynamics from melt pools is possible using event-based imagers such as the silicon retina and using blind source separation techniques. These techniques have extracted modal information (shapes, frequencies, and damping ratios) from complicated systems, suggesting further research would provide more promising results. The intensity-based extraction technique worked but using intensity values as a form of measurement

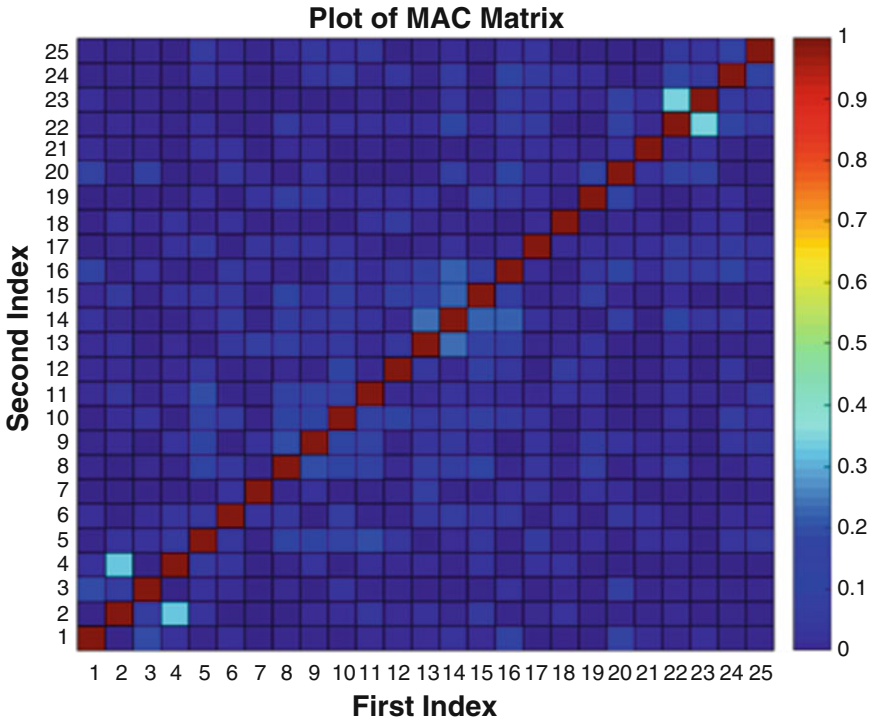

Fig. 10.4 Modal Assurance Criterion matrix for the 25 modes in Fig. 10.3

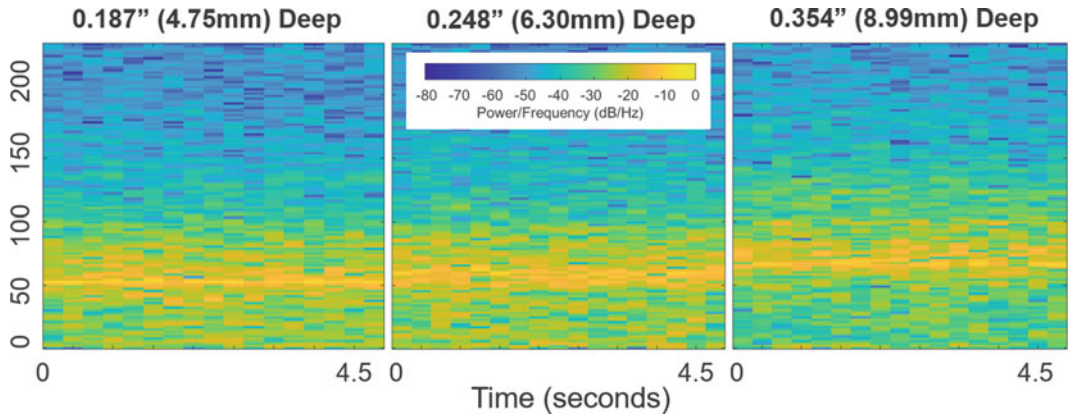

Fig. 10.5 Spectrogram of three pools of different depths

should be studied more to assess its validity. It remains unclear if the information being extracted is physically representative of modes in the pool. There are several factors that could be at work. Either the algorithm is not working on the correct priors (a highly nonlinear system, horizontal translation is dynamically important), or the method for blind source separation is not robust enough and other, more expensive, techniques need to be tried such as a deep neural network.

Acknowledgments This work was completed as a part of the 2018 Los Alamos National Laboratory Dynamic Summer School. Los Alamos National Laboratory is operated by Los Alamos National Security LLC, for the National Nuclear Security Administration of the U.S. Department of Energy, under DOE Contract DE-AC52-06NA25396.

References

1. Kotecki, D.J., Cheever, D.L., Howden, D.G.: Mechanism of ripple formation during weld solidification. Weld. J. **51**(8), 386–391 (1972)
2. Xiao, Y.H., den Ouden, G.: A study of GTA weld pool oscillation. Weld. J. **69**(8), 289–293 (1990)
3. Wadhwa, N., Rubinstein, M., Durand, F., Freeman, W.: Phase-based video motion processing. ACM Trans. Graph. (Proceedings SIGGRAPH). **32**(4), (2013). http://people.csail.mit.edu/nwadhwa/phase-video/
4. Yang, Y., Dorn, C., Mancini, T., Talken, Z., Kenyon, G., Farrar, C., Mascareñas, D.: Blind identification of full-field vibration modes from video. Mech. Syst. Signal Process. **85**, 567–590 (2017)
5. Dorn, C.J., Mancini, T.D., Talken, Z.R., Yang, Y., Kenyon, G., Farrar, C., Mascareñas, D.: Automated extraction of mode shapes using motion magnified video. In: Topics in Modal Analysis & Testing, vol. 10 (2016)
6. Yang, Y., Dorn, C., Mancini, T., Talken, Z., Theiler, J., Kenyon, G., Farrar, C., Mascareñas, D.: Reference-free detection of minute, non-visible, damage using full-field, high-resolution mode shapes output-only identified from digital videos of structures. Struct. Health Monitor. **17**(3), 1–18 (2017)
7. Dorn, C., Dasari, S., Yang, Y., Farrar, C., Kenyon, G., Welch, P., Mascareñas, D.: Efficient full-field vibration measurements and operational modal analysis using neuromorphic event-based imaging. J. Eng. Mech. **144**(7), 1–12 (2018)

Chapter 11
Full-Field Mode Shape Analysis, Alignment and Averaging Across Measurements

Wesley Scott, Matthew Adams, Yongchao Yang, and David Mascareñas

Abstract Noncontact methods of experimentally acquiring mode shapes and associated natural frequencies eliminate errors induced by mass-weighting of the structure by sensors. Traditional data acquisition methods require costly and delicate sensors such as accelerometers and strain gauges that are time-consuming to setup on each structure needing to be analyzed. Other non-contact data acquisition tools such as Laser Doppler Vibrometers (LDVs) and Digital Image Correlation (DIC) require expensive equipment and placement of speckle patters or high-contrast markers on the structure. Digital video cameras provide a relatively low-cost and portable method to measure a structure with high spatial resolution without needing to modify the structure. Previous work identified a novel variation on Operational Modal Analysis (OMA) to identify full-field mode shapes from video data. This work develops the algorithm's robustness, investigating effects of camera motion, structure excitation type, and background intensity gradients. Camera motion and modal over-specification are shown to cause identification of modes that do not correspond to physical deformations of the structure. Previously, video stabilization algorithms have been used to eliminate camera motion from video data. These algorithms eliminate most camera motion, but residual motion remains and is identified in additional, spurious mode shapes. When the camera motion is oscillatory, these shapes can be correlated in the frequency domain to the spectrum seen by an accelerometer placed on the camera itself. Averaging techniques are implemented to improve mode shape quality and identify structural and camera modes from spurious modes identified from modal over-specification. When robustly understood, identification of full-field mode shapes and properties can cheaply and efficiently advance structural health monitoring, model verification and updating, change detection, load identification, and other fields of structural dynamics.

Keywords Full-field · Blind-source separation · Video · Registration

11.1 Introduction

Full-field, high-resolution, blind-source separation-based methods for structural identification from video measurements have shown significant potential for enabling practical structural health monitoring solutions [1]. These techniques have been shown to be able to detect 3% loss in stiffness in structures using only low-cost video measurements [2]. This class of techniques have been shown to be extended to cases where temporal aliasing may occur [3], thus mitigating the need for the use of high-speed imagers. Techniques have also been developed to allow these techniques to work when the imager is subject to its own motion [4] and these techniques are expected to extend to the case where the structure under consideration is undergoing its own rigid-body motion. These techniques are also imager agnostic and have even been ported to exotic event-based imagers [5]. The fact that these techniques work on the principle of finding statistically independent motion in video suggests they will naturally be resistant to noise caused by atmospheric scintillations. The work completed to date on this class of algorithms coupled with the low-cost associated with imagers suggest their continued development should be pursued to enable a framework that allows their use in the field for a variety of structural dynamics applications [4]. One of the major advantages of imagers is that they make the collection of high-resolution data over long time intervals relatively straightforward and low-cost. Conventional experimental modal analysis practice generally involves averaging across many test to obtain high signal-to-noise ratio estimates of structural mode shapes. The fact that video measurements of structural dynamics could be collected over very long intervals of time suggests it should be possible to obtain high-

W. Scott · M. Adams · D. Mascareñas (✉)
Engineering Institute, Los Alamos National Laboratory, Los Alamos, NM, USA
e-mail: dmascarenas@lanl.gov

Y. Yang
Argonne National Laboratory, Lemont, IL, USA

N. Dervilis (ed.), *Special Topics in Structural Dynamics & Experimental Techniques, Volume 5*, Conference Proceedings of the Society for Experimental Mechanics Series, https://doi.org/10.1007/978-3-030-12243-0_11

resolution, high signal-to-noise ratio measurements of modes from video. However, it must be noted that a technique must be developed to coherently perform the required averaging across the video tests. At least two complications immediately arise. First, the mode shapes extracted by blind source separation do not come out in any particular order and the order can change between measurements. It is necessary to develop methods to identify which modes correspond to one another across multiple measurements in order to average coherently. Second, it is possible that in the case of an imager subject to vibration that the structure under consideration will appear translated slightly across multiple frames. In this work, a method is proposed to deal with these issues. Additional issues exist for averaging across frames with a moving imager such as change in scale, and the issues associated with different numbers of modes appearing in different measurements, but these are beyond the scope of this paper.

11.2 Background

The algorithm for extracting full-field, high resolution structural dynamics information from video of vibrating structures when the imager is vibrating can be summarized as follows [1]:

1. Minimize the effect of the camera vibration by applying a video stabilization algorithm. Consensus-based matching and tracking (CMT) algorithm [6], has thus far been found to be an appropriate algorithm for this purpose as described in [4].
2. Convert the intensity measurements at each pixel into a quantity that represents the displacement at each pixel. This transformation can potentially be accomplished in a variety of ways. For in-plane motion phase-based optical flow [7–9], provides a useful means to perform the conversion from pixel intensity to displacement and was used in this work. Ultimately, this procedure is applied across the time-span of the video and the result is a time series of displacement for every pixel.
3. Perform principle components analysis (PCA) across all of the displacement time series in order to reduce the dimensionality of the data. It is expected that the number of non-trivial eigenvalues calculated from the displacement time series for each pixel generated from a video of a vibrating structure will be of the same order as the number of mode shapes that are observable from the displacement time series. For this reason, it is only necessary to retain about the number of top eigenvectors that correspond to the number of non-trivial singular values.
4. We now take advantage of the observation that the canonical form of the blind source separation problem has exactly the same form as the linear, multi-degree-of-freedom, structural dynamics equations when written in the modal form [10, 11]. If the blind source separation problem is solved using the time series extracted from the principle components analysis above as input, the columns of the mixing matrix provided by a blind source separation solution technique will yield the mode shapes at high-spatial resolution, and the resulting individual signal sources correspond to the modal coordinates for each mode. Thus far, complexity pursuit [12] has been found to be an attractive algorithm for solving the blind-source separation problem for structural dynamics applications.

After applying these steps to the video, the result is high-resolution mode shapes and modal coordinates that can be used to estimate resonant frequencies and damping ratios.

For the purposes of averaging mode shapes across multiple measurements, additional steps must be applied to perform the averaging coherently. First, it is important to note that since the solution to the blind source separation problem does not provide mode shapes in any particular order it is necessary to determine which shapes correspond to one another. The 2-D correlation coefficient provides a measure of similarity between two entities. In structural dynamics, mode shapes are frequently compared using the Modal Assurance Criterion (MAC) which provides a measure of sameness between shapes arranged in 1-D vectors instead of the 2-D arrays of the correlation coefficient. Since the mode shapes measured by an imager are already 2-D, corresponding to x and y pixel locations, the 2-D correlation coefficient reduces the number of steps required to analyze shapes. The 2-D correlation equation for analyzing two 2-D shapes A and B is [13]:

$$corr2\left(\boldsymbol{A},\boldsymbol{B}\right)=\frac{\sum_m\sum_n\left(A_{mn}-\overline{A}\right)\left(B_{mn}-\overline{B}\right)}{\sqrt{\left(\sum_m\sum_n\left(A_{mn}-\overline{A}\right)^2\right)\left(\sum_m\sum_n\left(B_{mn}-\overline{B}\right)^2\right)}} \tag{11.1}$$

Where $\overline{A}$ and $\overline{B}$ refer to the mean of all entries in their respective arrays. The 2-D correlation coefficient takes on values $corr2 \in [-1, 1]$, with absolute values close to one meaning good agreement and values close to zero meaning poor agreement as in the modal assurance criterion (MAC). Scaling of shapes also does not impact this method.

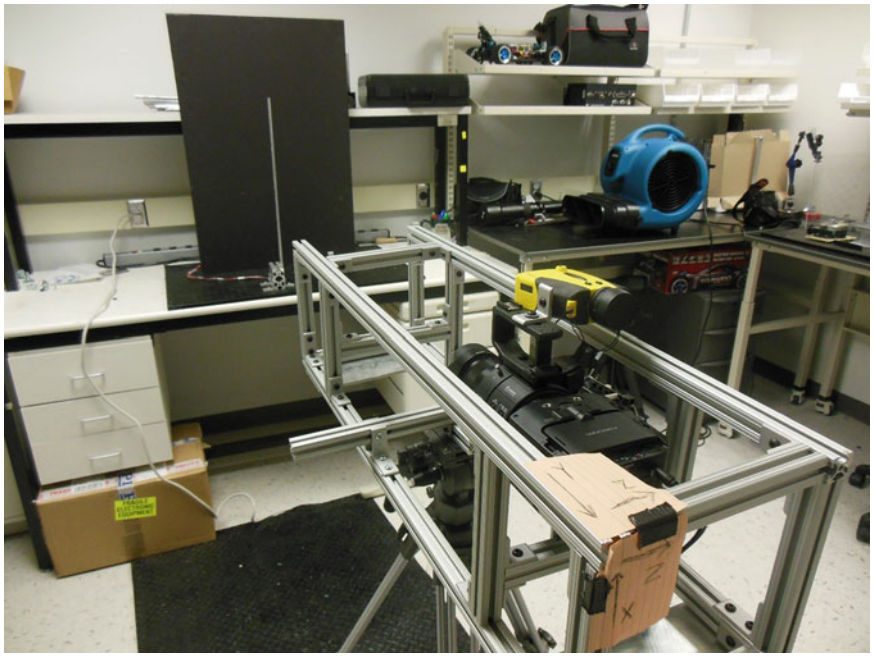

Fig. 11.1 Blue industrial fan is used to excite the cantilever beam

It is also important to note when collecting data from multiple tests, the structure being investigated may not always begin in the same place within the frame. This causes problems identifying shapes for the 2-D correlation coefficient step. In order to align any pixel offsets, the mode shapes are converted to logicals: ones for non-zero pixel entries in the mode shapes, zeros for zero entries. Modifying the (x, y) offset of the pixels sequentially, the 2-D correlation coefficient is checked for all possible offsets. The maximum value of the coefficient corresponds to the pixel offset between the set of shapes.

Once shapes have been identified to a mode, the mode shapes are spatially averaged, and other modal properties such as frequency and damping corresponding to that shape can also be coherently averaged. This effectively removes all spurious computational modes which come from modal over-specification and are not camera motion.

11.3 Analysis

We now consider a demonstration of the technique for performing modal averaging over multiple video measurements. The structure under test in this example is an aluminum cantilever beam as shown in Fig. 11.1. In this case, the beam is excited using an air blower to simulate wind in the laboratory. During these tests, the imager remained static. The analytical solution for the given cantilever beam's suggests the first three resonant frequencies of this beam occur at 7.43, 46.5, and 130.3 Hz. Based on these calculations, video was recorded at 480 frames per second to avoid any aliasing effects. However, techniques do exist to mitigate aliasing phenomena in video data for modal analysis purposes [3].

Figure 11.2 shows the modal coordinates estimated from a single video measurement when using the procedure described in the background section. We find that the wind excitation excites the first two modes enough that a video camera can observe them. The first two resonant frequencies are observed to occur at 7.49 and 46.2 Hz based on this single video measurement. These experimentally estimated values are consistent with the values for the first two resonant frequencies as provided by the analytical solution for a vibrating cantilever beam. Figure 11.3 shows how the two extracted mode shapes appear for the single video measurement case. The first mode is consistent with what would be expected for the first mode of a cantilever beam. However, the second mode exhibits significant variation from the analytical solution for the second mode of a cantilever beam. The estimated second mode has significant, higher spatial frequency content than would be expected. Figure 11.4 shows the estimated mode shapes when three video measurements are combined using the coherent averaging technique described in the background section. The first estimated mode shape continues to be consistent with the first mode shape predicted by the analytical solution for a cantilever beam. More notably, the second mode shape visually displays significantly less variation from the second mode shape predicted by the analytical solution for a vibrating cantilever

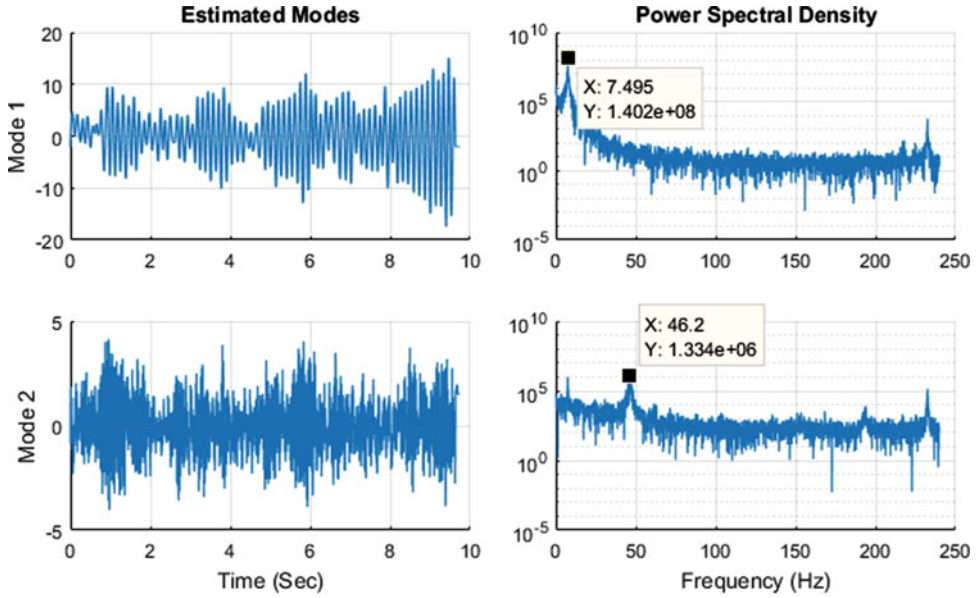

Fig. 11.2 Modal coordinate time response from fan excitation and PSD of random excitation

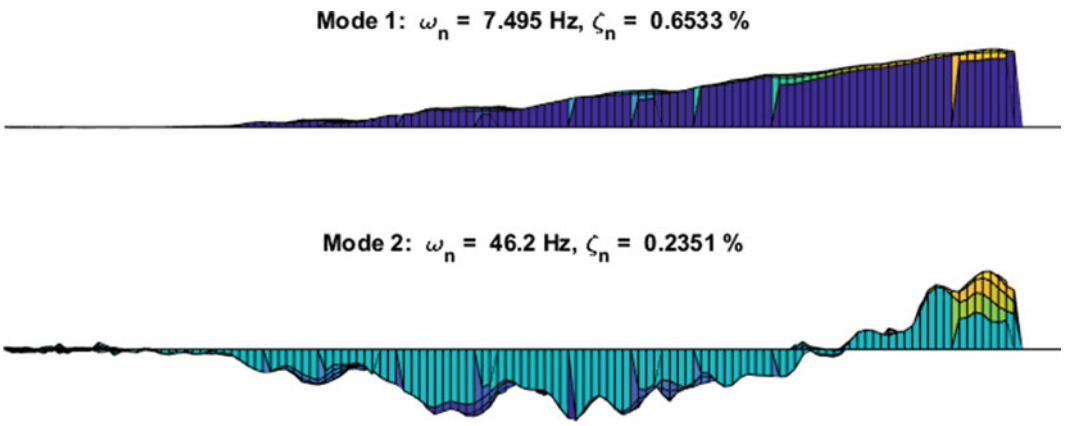

Fig. 11.3 Estimated high-resolution mode shapes of the cantilever beam using a single video measurement

beam. Most of the higher spatial frequency content has been removed. It is interesting to note what a large impact averaging across only three measurements has on the estimate of the second mode. Video measurements are extremely inexpensive to obtain and they highly amenable to automation. In a field application many tens or hundreds of video measurements could potentially be combined to obtain very high-fidelity mode shape estimates that could be used for applications such as detecting damage in the structure under consideration.

Please note that the measured cantilever beam was in a vertical orientation, but the mode shapes shown in Figs. 11.3 and 11.4 are in a horizontal orientation with the clamped end on the left side to facilitate a visual comparison.

11.4 Conclusion

A solution is presented to the problem of performing averaging of high-resolution mode shapes extracted from video of a vibrating structure. The solution technique presented here is capable of operating under common field conditions such as vibration of the imager itself. This work also provides a solution to the problem of determining the number of modes being observed by the camera during a test. As a result, it can help guide the selection of the number of modes that the complexity pursuit algorithm used to solve the blind source separation problem should search for. Future research that

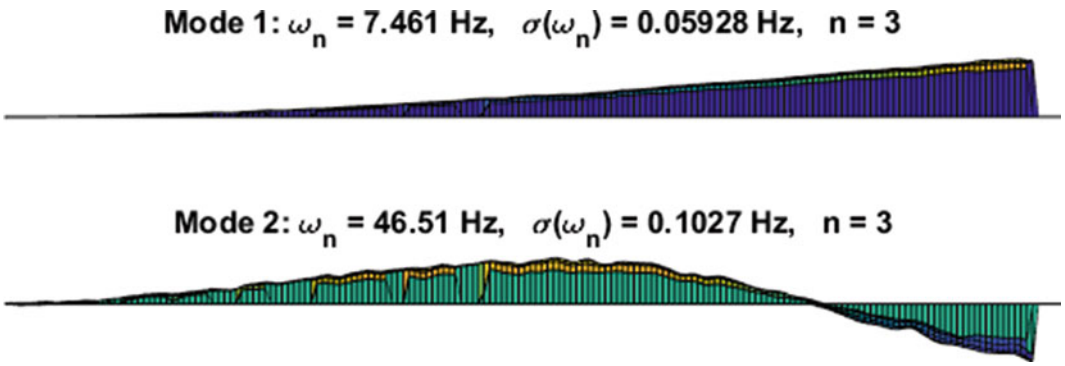

Fig. 11.4 Estimated high-resolution mode shapes of the cantilever beam averaging over n = 3 video measurement

needs to be undertaken to transition this class of techniques to the field includes studying the problem of averaging modal measurements when the scaling of the structure in the image changes. This capability will be important when trying to deploy these techniques using imagers mounted on mobile robotic platforms such as drones. Techniques for quantitatively comparing mode shapes as measured from video still needs further development. It will also be necessary to deal with changes in the contrast between the structure and the background across the spatial dimensions of the structure. Atmospheric turbulence is also a concern with video-based structural dynamics identification. Preliminary results indicate that blind-source separation-based techniques may have some natural robustness against atmospheric turbulence, but a quantitative study of this robustness is still necessary.

Acknowledgments Los Alamos National Laboratory is operated by Los Alamos National Security LLC, for the National Nuclear Security Administration of the U.S. Department of Energy, under DOE Contract DE-AC52-06NA25396.

References

1. Yang, Y., Mancini, C.D.T., Talken, Z., Kenyon, G., Farrar, C., Mascarenas, D.: Blind identification of full-field vibration modes from video measurements with phase-based video motion magnification. Mech. Syst. Signal Process. **85**, 567–590 (2016)
2. Yang, Y., Dorn, C., Mancini, T., Talken, Z., Theiler, J., Kenyon, G., Farrar, C., Mascarenas, D.: Reference-free detection of minute, non-visible, damage using full-field, high-resolution mode shapes output-only identified from digital videos of structures. Struct. Health Monitor. **17**(3), 514–531 (2018)
3. Yang, Y., Dorn, C., Mancini, T., Talken, Z., Nagarajaiah, S., Kenyon, G., Farrar, C., Mascarenas, D.: Blind identification of full-field vibration modes of output-only structures from uniformly-sampled, possibly temporally-aliased (sub-Nyquist), video measurements. Sound Vib. **390**, 232–256 (2017)
4. Dasari, S., Dorn, C., Yang, Y., Larson, A., Mascarenas, D.: A framework for the identification of full-field structural dynamics using sequences of images in the presence of non-ideal operating conditions. Intell. Mater. Syst. Struct. 1–26 (2018)
5. Dorn, C., Dasari, S., Yang, Y., Farrar, C., Kenyon, G., Welch, P., Mascareñas, D.: Efficient full-field vibration measurements and operational modal analysis using neuromorphic event-based imaging. J. Eng. Mech. **144**(7), (2018)
6. Nebehay, G., Pflugfelder, R.: Clustering of static-adaptive correspondences for deformable object tracking. In: IEEE Conference on Computer Vision and Pattern Recognition (CVPR), Boston, MA (2015)
7. Fleet, D.J., Jepson, A.D.: Computation of component image velocity from local phase information. Int. J. Comput. Vision. **5**(1), 77–104 (1990)
8. Wadhwa, N., Rubinstein, M., Durand, F., Freeman, W.T.: Phase-based video motion processing. ACM Trans. Graph. (Proceedings SIGGRAPH). **32**(4), (2013). http://people.csail.mit.edu/nwadhwa/phase-video/
9. Simoncelli, E.P.: matlabPyrTools, 12 2009 (Online)
10. Kerschen, G., Poncelet, F., Golinval, J.-C.: Physical interpretation of independent component analysis in structural dynamics. Mech. Syst. Signal Process. **21**, 1561–1575 (2007)
11. Poncelet, F., Kershen, G., Golinval, D.V.J.-C.: Output-only modal analysis using blind source separation techniques. Mech. Syst. Signal Process. **21**, 2335–2358 (2007)
12. Stone, J.V.: Blind Source Separation Using Temporal Predictability. Neural Comput. **13**(7), (2001)
13. MathWorks, 2-D correlation coefficient, MathWorks. https://www.mathworks.com/help/images/ref/corr2.html (Online). Accessed 10 May 2018

Chapter 12
Investigating Engineering Data by Probabilistic Measures

L. A. Bull, K. Worden, T. J. Rogers, E. J. Cross, and N. Dervilis

Abstract A critical issue for data-based engineering is a lack of descriptive labels for the measured data. For many engineering systems, these labels are costly/impractical to obtain, and as a result, conventional supervised learning is not feasible. This article outlines a probabilistic framework for the investigation and labelling of engineering datasets. Two alternative probabilistic measures are suggested to define the most informative observations to investigate and annotate, in order to maximise the classification performance of a statistical model.

Keywords Active learning · Guided sampling · Semi-supervised learning · Online structural health monitoring

12.1 Introduction

Advanced structural health monitoring (SHM) systems look to provide a framework for the classification and localisation of damage, following preliminary damage detection. This framework requires the categorisation of many data-groups, i.e. classes, relating to different states of structural health—rather than simply classifying data as either normal or novel (outlier analysis) [1]. In an engineering context, a critical issue for the multi-class problem is a lack of comprehensive labelled data, which are required to learn a (standard) supervised classification algorithm. Furthermore, in a online setting, the measured data would arrive as a stream, incrementally, throughout the lifetime of the monitored structure.

Considering these issues, advanced SHM systems should offer three characteristics. Firstly, the system must be adaptive, incorporating any new classes (novel data-groups) as they are discovered—these might relate to damage or various operational conditions. Secondly, a system must be capable of running on-line; that is, the algorithm must be computationally efficient, in order to update and adapt during operation. Finally, the model must be capable of accurate diagnostics (ideally probabilistic) while only requesting descriptive labels for the most informative measured data; this is critical for engineering applications, as the investigation of any abnormal data is both impractical and expensive. This article outlines an approach to address the investigation of engineering data in a semi-supervised, probabilistic framework for online SHM.

12.2 Semi-supervised and Active Learning for Structural Health Monitoring

In pattern-recognition, *supervised* algorithms require fully labelled training-data, $\mathcal{L}$, such that

$$\mathcal{L} = \{(\boldsymbol{x}_i, y_i) | \boldsymbol{x}_i \in X,\ y_i \in Y, i = 1, \ldots, n\}. \tag{12.1}$$

The measured data, $\boldsymbol{x}_i$, are D-dimensional, such that the feature space is $X \in \mathbb{R}^D$. The descriptive labels are categorical, such that $y_i \in Y = \{1, \ldots, K\}$, where K is the number of classes and Y denotes the label space. In contrast, *unsupervised* techniques only require measured data to build a model, i.e.

$$\mathcal{U} = \{\hat{\boldsymbol{x}}_i | \hat{\boldsymbol{x}}_i \in X, i = 1, \ldots, m\}. \tag{12.2}$$

In this case, $\hat{\boldsymbol{x}}_i$ are the *unlabelled* measured data.

L. A. Bull (✉) · K. Worden · T. J. Rogers · E. J. Cross · N. Dervilis
Dynamics Research Group, Department of Mechanical Engineering, University of Sheffield, Sheffield, UK
e-mail: lbull1@sheffield.ac.uk

N. Dervilis (ed.), *Special Topics in Structural Dynamics & Experimental Techniques, Volume 5*, Conference Proceedings of the Society for Experimental Mechanics Series, https://doi.org/10.1007/978-3-030-12243-0_12

In an engineering context, comprehensive labels to describe the observations are rarely available. This fact often forces a dependence on unsupervised techniques in practical applications, specifically, novelty detection. An alternative approach, however, is to apply *semi-supervised* pattern recognition [2]; these algorithms make use of both labelled data, $\mathcal{L}$, and unlabelled data, $\mathcal{U}$, such that dataset used by the algorithm is $\mathcal{D} = \mathcal{L} \cup \mathcal{U}$. Active learning is a variation of semi-supervised learning (or, more generally, partially-supervised learning [3]). As with semi-supervised learning, active algorithms will make use of both $\mathcal{L}$ and $\mathcal{U}$; however, an active learner will query/annotate unlabelled data in $\mathcal{U}$ to automatically extend the labelled dataset ($\mathcal{L}$), in an intelligent and adaptive manner.

In the context of data-based SHM, a pattern-recognition model that is *semi-supervised* and *active* can bring several advantages [4]. Most significantly, these algorithms make use of *limited* labelled data, while requesting further annotations for only the most informative observations; this can significantly reduce the cost associated with investigating abnormal data records from engineering structures. Furthermore, these algorithms can utilise the information in the unlabelled data to improve the diagnostic capabilities of the SHM system. Additionally, active algorithms can be applied offline to a large pool of collected data [5], or online, to drifting data streams [6]. In the online setting, if an algorithm can adapt and update, while only requesting critical labels, this is extremely significant to data-based SHM.

12.3 A Probabilistic Model for Guided Sampling

A probabilistic approach is suggested as the foundation for an active framework with engineering data. The measured data, $\boldsymbol{x}$, are assumed to be sampled from a parametric mixture model; specifically, a mixture of K Gaussian distributions. An small initial sample of labelled data, $\mathcal{L}$, are used to establish the initial number of classes, K, and calculate the Bayes-optimal estimates for the model parameters.

Briefly, the data labels, y_i, are used to group the measurements, $\boldsymbol{x}_i$, according to class, and then calculate the posterior distribution of the parameters that define the categorical distribution, $(\pi_1, \ldots, \pi_K)$; a Dirichlet prior is applied. Similarly, the observations $\boldsymbol{x}_i$ are used to calculate the posterior distribution of the parameter estimates for the Gaussian-distributed features for each class $(\mu_{y,d}, \sigma^2_{y,d})$; in this case, a normal-inverse-chi-squared (hierarchical) prior is used. As the prior distributions are conjugate, the solutions for the posterior distributions over the parameters are tractable; therefore, the *posterior predictive* distributions can be found analytically [7]. The posterior predictive distributions are $p(\boldsymbol{x}|y, \mathcal{L})$ for the Gaussian-distributed observations, and $p(y|\mathcal{L})$ for the Dirichlet-distributed labels. The dependencies of this framework are shown by the graphical model in Fig. 12.1, including any hyperparameters; further details can be found in the references, and the theoretical paper by the authors.

A generative classifier can then be defined using Bayes rule, for the prediction of the label distribution for the unlabelled data in $\mathcal{U}$,

$$p(y|\hat{\boldsymbol{x}}, \mathcal{L}) = \frac{p(\hat{\boldsymbol{x}}|y, \mathcal{L})\ p(y|\mathcal{L})}{p(\hat{\boldsymbol{x}}|\mathcal{L})}\ , \tag{12.3}$$

which assumes independence between each dimension (feature) in X (i.e. naive Bayes), such that

$$p(\hat{\boldsymbol{x}}_i|y, \mathcal{L}) = \prod_{d=1}^{D} p(\hat{x}_{i,d}|y, \mathcal{L}). \tag{12.4}$$

Note, the posterior distribution over the labels, $p(y|\hat{\boldsymbol{x}}, \mathcal{L})$, is a *predictive* likelihood for *each class*, $y \in \{1, \ldots, K\}$. Specifically, the estimate of the probability for each class is combined to give a categorical distribution (when normalised) over the label space. This is not the full posterior, which cannot be found analytically, thus, the classification is not fully Bayesian. The full posterior can be approximated via sampling algorithms (Gibbs sampling); however, this approach is unnecessary, as the full distribution is not required for this example.

Various probabilistic measures can be used to dictate which of the measurements in $\mathcal{U}$ are the most informative when labelled. These observations can be queried, and the cause can be investigated by the engineer/oracle to provide descriptive data labels, y^*. Following the investigation and labelling of data, $\mathcal{L}$ now includes the queried observations, therefore, the model is retrained and new data are queried; this process can then iterate until a label budget is reached, or applied sequentially to streaming data (online).

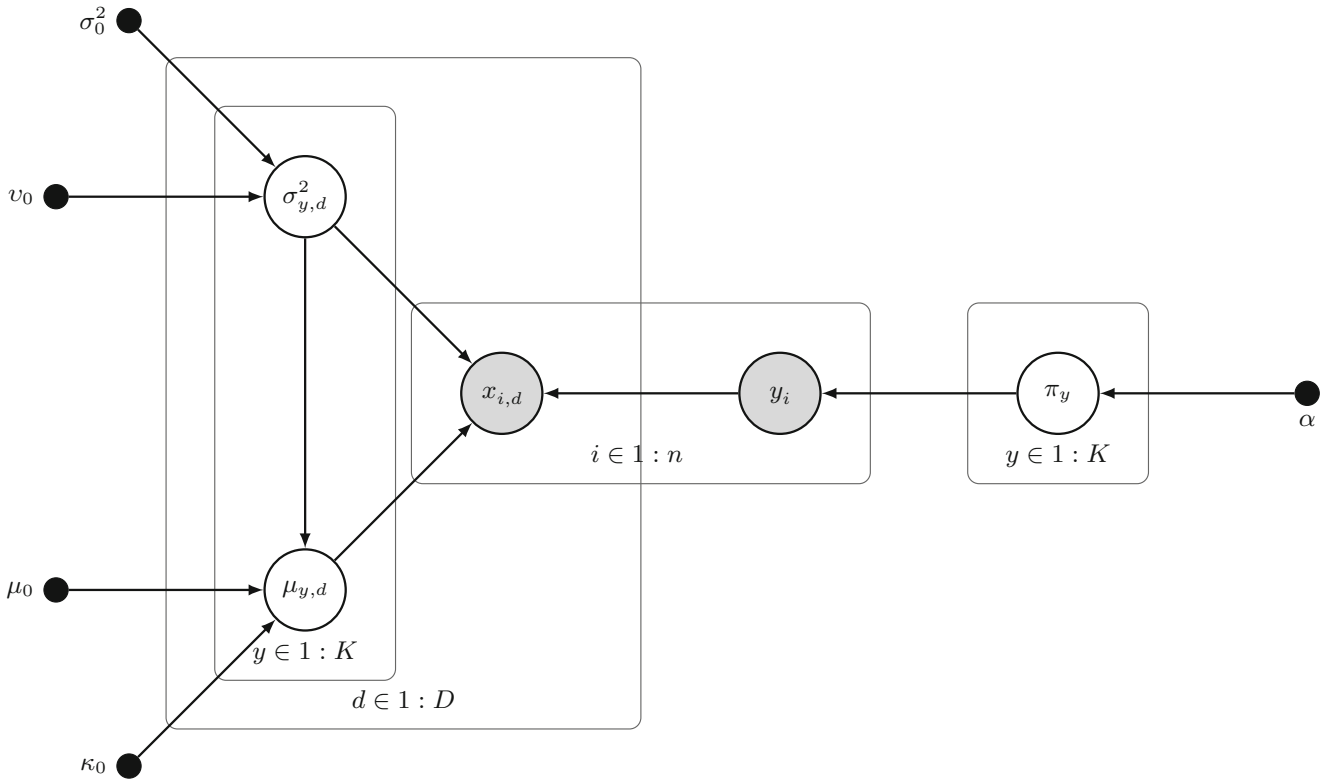

Fig. 12.1 The probabilistic classification model. Shaded and white nodes are the observed and latent variables respectively; arrows represent conditional dependencies; dots represent constants (hyperparameters)

12.4 Data Query Measures

In the active learning literature, there are various approaches to define which of the unlabelled data are the most informative. Generally speaking, if labelled, these data provide the largest increase in the classification performance. However, if queries are too focussed on a specific definition of 'informative', the training-set built by the algorithm can be poorly representative of the underlying distribution of the data; this phenomenon is referred to as *sampling bias* [8]. To combat sampling bias, the query framework should not focus too much on specific regions of the feature-space; this can be achieved by combining several different measures that define *informative* [9]. Usually, these measures correspond to *representative* or *uncertain* observations, according to the current estimate/model of the underlying data distribution. In this article, two probabilistic measures are suggested to direct queries.

Firstly, the *entropy* of the (categorical) label distribution, $p(y|\hat{\boldsymbol{x}}, \mathcal{L})$, can be interpreted a measure of uncertainty,

$$H(Y) = -\sum_{y=1}^{K} p(y|\hat{\boldsymbol{x}}, \mathcal{L}) \log p(y|\hat{\boldsymbol{x}}, \mathcal{L}). \tag{12.5}$$

Therefore, selecting data from $\mathcal{U}$ with a large entropy can be considered uncertainty sampling; that is, selecting data from the unlabelled pool with the most 'mixed' or 'conflicted' label predictions. This criterion will almost always query observations at the boundaries, between two or more classes; for example, queries directed by a large entropy are shown in Fig. 12.2a. Conversely, prioritising low entropy selects records near the centre of the data-groups associated with each cluster (*representative* examples).

Alternatively, observations in $\mathcal{U}$ with the lowest 'maximum-likelihood' (from $p(\hat{\boldsymbol{x}}|y, \mathcal{L}), \forall y \in Y$) can be queried. Again, querying data with a low likelihood can be seen as uncertainty sampling; however, in this case, the corresponding label distribution is not necessarily 'mixed'. Therefore, the queried data can appear in the cluster extremities that are *not* at

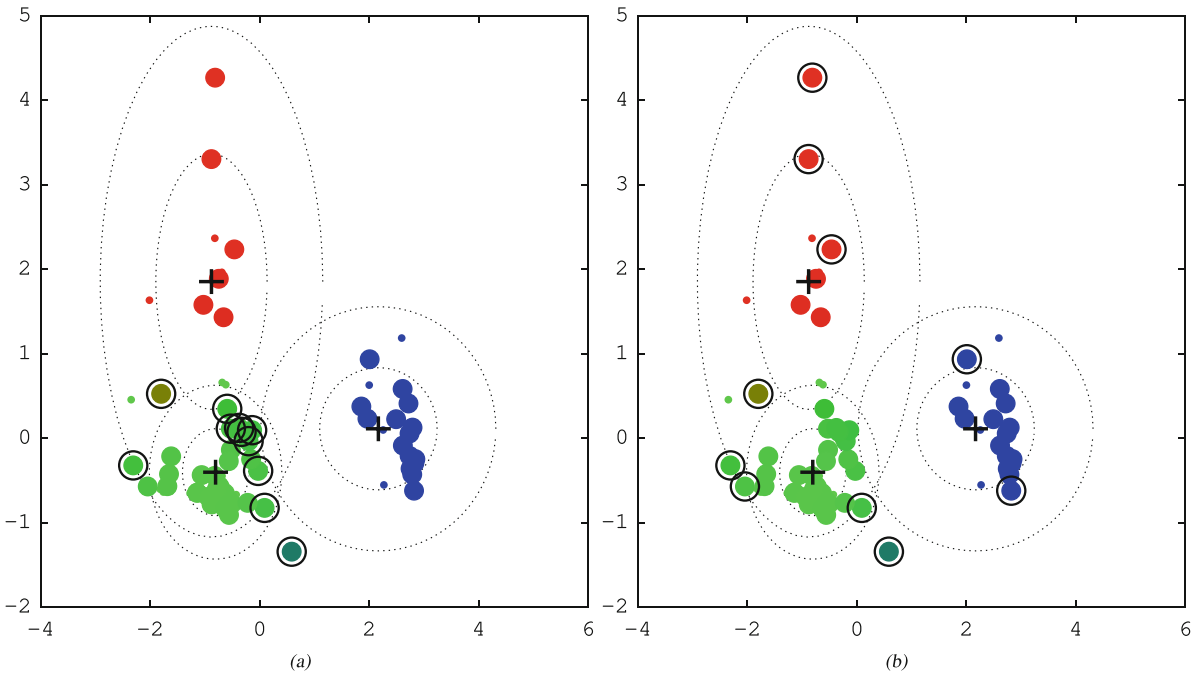

Fig. 12.2 Data for a three-class classification problem, the features are extracted from acoustic emission data. Small markers are the labelled training set, $\mathcal{L}$; large markers are the unlabelled data, $\mathcal{U}$, shaded according to the distribution of the label predictions $p(y|\hat{\boldsymbol{x}}, \mathcal{L})$. The dotted-line and + markers show the maximum *a posteriori* estimates of the standard deviation and cluster locations respectively. The queried data from $\mathcal{U}$ are circled; in (**a**) these data have the *largest entropy*; in (**b**) the data have the *lowest maximum-likelihood*

the boundary between two or more classes; that is, these observations are not necessarily uncertain *in terms of the labels*. Considering these properties, the lowest maximum-likelihood becomes suitable for querying drifting data streams, where novel data are unlikely to appear between the boundaries of existing classes.

12.5 Conclusions

The comprehensive annotation of engineering datasets is costly/infeasible due to practical limitations; therefore, *active* and *semi-supervised* learning techniques are suggested as the framework for the investigation and labelling of the most informative observations. This article suggests a probabilistic model to guide queries, considering a sampling framework to be applied online, to drifting data streams, recorded live from engineering structures. The complete work concerning this project, including theory and applications, will be the subject of further publication.

Acknowledgements The authors gratefully acknowledge the support of the UK Engineering and Physical Sciences Research Council (EPSRC) through Grant reference number EP/R003645/1. Further thanks are extended to Karen Holford and Rhys Pullin at Cardiff University for providing the AE data.

References

1. Farrar, C.R., Worden, K.: Structural Health Monitoring: A Machine Learning Perspective. Wiley, New York (2012)
2. Chapelle, O., Scholkopf, B., Zien, A.: Semi-Supervised Learning. MIT Press,Cambridge (2006)
3. Schwenker, F., Trentin, E.: Pattern classification and clustering: a review of partially supervised learning approaches. Pattern Recogn. Lett. **37**(1), 4–14 (2014)
4. Bull, L., Worden, K., Manson, G., Dervilis, N.: Active learning for semi-supervised structural health monitoring. J. Sound Vib. **437**, 373–388 (2018)
5. Wang, M., Min, F., Zhang, Z.H., Wu, Y.X.: Active learning through density clustering. Expert Syst. Appl. **85**, 305–317 (2017)

6. Zhu, X., Zhang, P., Lin, X., Shi, Y.: Active learning from data streams. Seventh IEEE International Conference on Data Mining (ICDM 2007), pp. 757–762 (2007)
7. Murphy, K.P.: Conjugate bayesian analysis of the Gaussian distribution. Def **1**(7), 1–29 (2007)
8. Dasgupta, S., Hsu, D.: Hierarchical sampling for active learning. In: Proceedings of the 25th International Conference on Machine Learning, pp. 208–215. ACM, New York (2008)
9. Huang, S.J., Jin, R., Zhou, Z.H.: Active learning by querying informative and representative examples. In: Advances in Neural Information Processing Systems, pp. 892–900 (2010)

Chapter 13
Multi-Input Multi-Output Swept Sine Control: A Steepest Descent Solution for a Challenging Problem

Umberto Musella, Bart Peeters, Francesco Marulo, and Patrick Guillaume

Abstract Multiple-Input Multiple-Output (MIMO) swept sine is nowadays acknowledged to be one of the best excitation techniques in applications where testing time is a constraint and high-quality Frequency Response Functions are compulsory. This is the case, for example, of testing large aerospace structures for model validation and updating. The high levels that can be reached during these tests can require a reliable MIMO closed-loop control strategy in order to guarantee that the response spectra will follow safe reference profiles (within defined tolerance limits). The development of a dedicated algorithm for these applications is however very challenging, especially due to the transient nature of the sweeps and the robustness of the MIMO controller. This paper proposes a steepest descent solution for the control of multiple inputs during a continuous sine-sweep, in order to simultaneously match specific response spectra for multiple control channels.

Keywords MIMO · Vibration control · Continuous sweep · Environmental testing · Steepest descent

13.1 Introduction

Nowadays Multiple-Input Multiple-Output (MIMO) swept sine is one of the most popular excitation techniques for the modal testing of large aerospace structures. The success is related to the possibility of characterizing the dynamic response of the unit under test frequency-to-frequency, reaching high excitation levels, high signal to noise ratio and hence high quality FRFs [1–4]. Some of these features were previously obtained running normal modes tests or combining normal modes with broadband or stepped sine excitations at the cost of extremely long testing times (normal modes and stepped sine) or poor excitation levels (broadband random) [5]. Even if these tests are critical, they are scheduled in periods of extreme time pressure, with the full ready-to-use assembly that still needs to undergo additional testing stages, for example acoustic and thermal testing of large satellites [6]. Another example is the Ground Vibration Testing (GVT) of large aircrafts, where the testing, required for flutter prediction analysis, is typically scheduled before the final painting and the maiden flight. Swept sine excitation is, in this sense, the best compromise between testing time and FRFs quality. Other advantages of swept sine testing are related to the deterministic nature of the excitation signals that guarantees high repeatability and the possibility of obtaining preliminar information about potential non-linearities [1–4]. From this perspective, an appealing feature of the swept sine excitation is the possibility of using state-of-the-art feedforward control techniques to define reference levels for specific control channels, e.g. force transducers or accelerometers. This allows the *pre-shaping* of the voltages driving the exciters, by predicting the dynamic behaviour of the unit to be tested. Such prediction relies on a model of the system obtained with a low-level pre-test random system identification. Due to potential non-linear behaviour that can be triggered at the (generally high) test levels reached during the actual sine sweep runs, noise on the measurements and transient effects due to the sweeping itself (for instance beating phenomena [4, 7, 8]), the system can generally differ from the linear model

U. Musella (✉)
Siemens Industry Software NV, Leuven, Belgium
Vrije Universiteit Brussel, Acoustics and Vibration Research Group, Elsene, Belgium
University of Naples "Federico II", Department of Industrial Engineering, Naples, Italy
e-mail: umberto.musella.ext@siemens.com

B. Peeters
Siemens Industry Software NV, Leuven, Belgium

F. Marulo
University of Naples "Federico II", Department of Industrial Engineering, Naples, Italy

P. Guillaume
Vrije Universiteit Brussel, Acoustics and Vibration Research Group, Elsene, Belgium

N. Dervilis (ed.), *Special Topics in Structural Dynamics & Experimental Techniques, Volume 5*, Conference Proceedings of the Society for Experimental Mechanics Series, https://doi.org/10.1007/978-3-030-12243-0_13

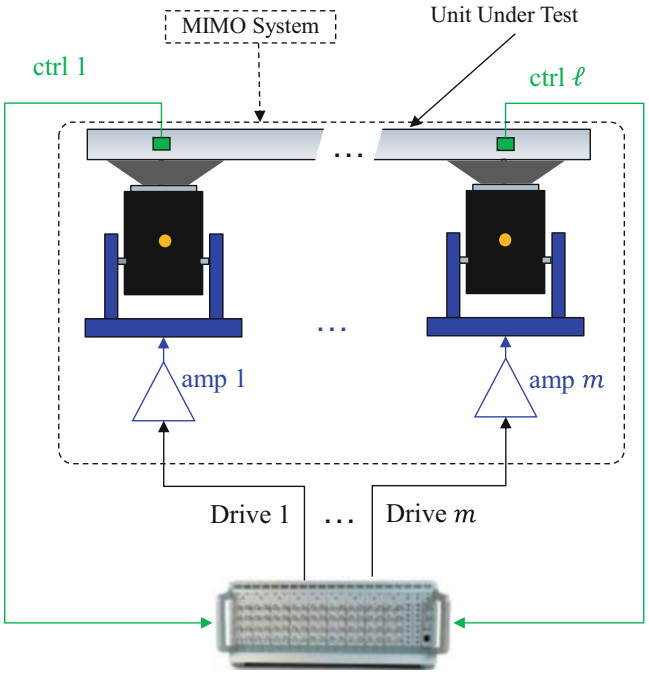

Fig. 13.1 Schematic representation of a MIMO vibration control test

estimated in the pre-test. The spectra of the control channels can therefore deviate from the references and closed loop feedback control strategies are sought to compensate for these differences.

The aim of this paper is to investigate the possibility of combining an amplitude and phase tracking technique to a steepest-descent correction algorithm in the frequency domain in order to simultaneously control the multiple responses to a specific reference amplitude value and guarantee that they will also keep a specific relative phase.

Since in this work most of the derivations are in the frequency domain, all the arrays are functions of the frequency f (in Hz), if not specified otherwise. Vectors are denoted by lower case bold letters, e.g. $\mathbf{a}$, and matrices by upper case bold letters, e.g. $\mathbf{A}$. An over-bar $\overline{\square}$ is used to indicate the complex conjugate operation and the Hermitian superscript $\square^H$ to indicate the complex conjugate transpose of a matrix, e.g. $\overline{\mathbf{a}}$ and $\mathbf{A}^H$. The dagger symbol $\square^\dagger$ is used to indicate the Moore-Penrose pseudo-inverse of a matrix, whereas the hat $\hat{\square}$ is used to emphasize the estimation of a quantity, e.g. $\hat{\mathbf{A}}$ is an estimate of the matrix $\mathbf{A}$. Time domain derivatives are indicated with dots $\dot{\square}$, for example $\dot{a}(t)$ and $\ddot{a}(t)$ are the first and second derivatives of the waveform $a(t)$, respectively.

13.2 MIMO Swept Sine Controlled Excitation

Figure 13.1 is a schematic representation of a general MIMO vibration control test. A set of m voltages is sent to multiple exciters. Typically these signals (the so-called *drives*) drive m independent shakers or, possibly, the multiple degrees of freedom of a multi-axis shaking table [9, 10]. The unit under test responses are recorded in ℓ control channels (the so-called *controls* or *pilots*).

During a MIMO test with swept sine excitation, the unit under test is excited with multiple swept sines over a user-defined frequency band. All the input signals are driven by the same instantaneous frequency.

The reasons to adopt a multi-input excitation for swept sine testing can be different, for example

- the need for testing heavy or slender structures that cannot be accommodated on a single shaker;
- the possibility of setting a defined phase between the responses to better characterize specific mode shapes.
- Multi-axis exciters can be used to perform a *true* single-axis test, by setting as reference very low response spectra in the off-axis directions.

The control target for a MIMO swept sine vibration control test is therefore a set of ℓ reference spectra, characterized by amplitude and phase (relative to the phase of the first control channel). Current excitation techniques make use of a pre-test system identification to pre-shape the drives (feedforward control) in the attempt of matching the reference while continuously sweeping with a specific sweep mode (linear or logarithmic) and sweep rate (in Hz/s or Oct/min).

13.2.1 System Identification

For each frequency, in case the full dynamic system is linear and time invariant, it is possible to write the Input-Output relation

$$\mathbf{y} = \mathbf{H}\mathbf{u} \tag{13.1}$$

where $\mathbf{y} \in \mathbb{C}^{\ell \times 1}$ and $\mathbf{u} \in \mathbb{C}^{m \times 1}$ are the spectra of the controls and the drives, respectively and $\mathbf{H} \in \mathbb{C}^{\ell \times m}$ is the matrix of FRFs. For the sake of simplicity, as most of the derivations are in the frequency domain, the terms drives,controls, responses and references are referred to the drives, controls, responses and reference spectra, respectively, if not specified differently.

In all the vibration control tests, a System Identification pre-test phase is always needed to estimate the system's FRFs. This is usually performed by running a low-level random test and using the so called H_1 estimator [11]

$$\hat{\mathbf{H}} = \hat{\mathbf{S}}_{\mathbf{yu}} \hat{\mathbf{S}}_{\mathbf{uu}}^{-1} \tag{13.2}$$

where $\hat{\mathbf{S}}_{\mathbf{yu}} \in \mathbb{C}^{\ell \times m}$ and $\hat{\mathbf{S}}_{\mathbf{uu}}^{-1} \in \mathbb{C}^{m \times m}$ are spectral density matrices estimated via Welch's averaged periodogram method [12] or other approaches.

Once the FRF is known, the system's *Mechanical Impedance Matrix* $\mathbf{Z}$ can be calculated. Generally an operation of pseudo-inversion is always needed because the number of controls can exceed the number of drives, in what is known in the MIMO control literature as *Rectangular Problem* [13].

13.2.2 Drives Pre-shape

As shown in [14], for each frequency line, independently, the control error

$$\mathbf{e} = \mathbf{r} - \mathbf{y} \tag{13.3}$$

where $\mathbf{r} \in \mathbb{C}^{\ell \times 1}$ are the reference spectra, is minimized in the least square sense by the optimal drives

$$\mathbf{u}_{opt} = (\mathbf{H}^H \mathbf{H})^{-1} \mathbf{H}^H \mathbf{r} \tag{13.4}$$

In order to calculate the drives, since the real plant is unknown, the best solution is to use information obtained from the system identification. To notice that the quantity $(\hat{\mathbf{H}}^H \hat{\mathbf{H}})^{-1} \hat{\mathbf{H}}^H$ is, for the general case of a rectangular problem, the pseudo-inverse of the FRF matrix according to Moore and Penrose $(\hat{\mathbf{H}}^H \hat{\mathbf{H}})^{-1} \hat{\mathbf{H}}^H = \hat{\mathbf{H}}^{\dagger} = \hat{\mathbf{Z}}$. Hence, an *estimate* of the optimal drives can be calculated as

$$\hat{\mathbf{u}}_{opt} = \hat{\mathbf{Z}}\mathbf{r} \tag{13.5}$$

With reference to the active control literature [15], the proposed approach is a traditional feedforward control, also called *drives pre-shape* in environmental testing [7, 8]. Unfortunately, due to the difference in levels between the low level random system identification and the actual test, the transient nature of the sweeps and potential noise in the measurements, the reference and the control spectra will generally differ, and an on-line feedback control is sought to keep the responses as close as possible to the desired spectra.

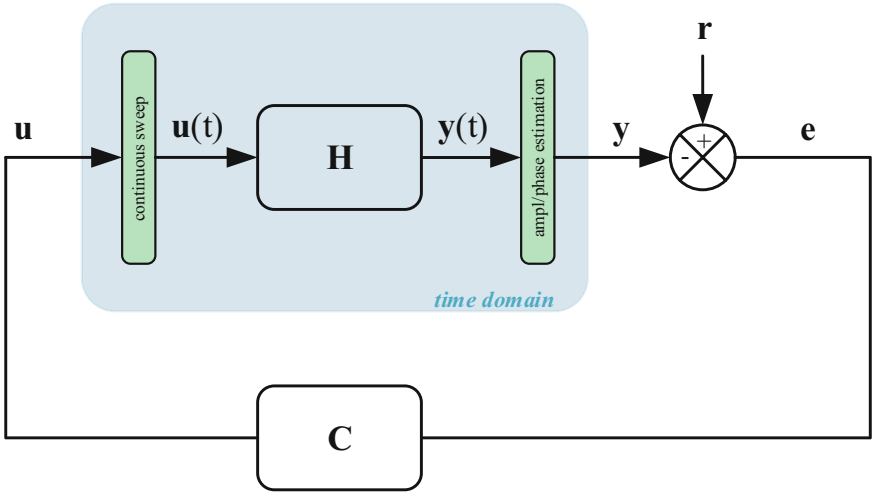

Fig. 13.2 MIMO swept sine feedback control, block scheme. The green blocks highlight the necessary steps of generating a continuous sine sweep from the drives spectra (*continuous sweep* block) and estimating the response amplitude and phase from the time recordings (*ampl/phase estimation* block)

Table 13.1 Different sweep modes and related sine arguments

Sweep mode	Frequency in Hz	Sine argument in rad
Linear up	$f(t) = f_{in} + \mathrm{SR}_{\mathrm{Hz/s}} t$	$\Phi(t) = 2\pi \left(f_{in} t + \frac{\mathrm{SR}_{\mathrm{Hz/s}}}{2} t^2 \right)$
Linear down	$f(t) = f_{end} - \mathrm{SR}_{\mathrm{Hz/s}} t$	$\Phi(t) = 2\pi \left(f_{end} t - \frac{\mathrm{SR}_{\mathrm{Hz/s}}}{2} t^2 \right)$
Log. up	$f_{log,up}(t) = f_{in}\, 2^{\mathrm{SR}_{\mathrm{Oct/min}} t/60}$	$\Phi(t) = 2\pi \left(\frac{60 f_{in}}{\mathrm{SR}_{\mathrm{Oct/min}} \log 2} 2^{\mathrm{SR}_{\mathrm{Oct/min}} t/60} - 1 \right)$
Log. down	$f_{log,up}(t) = f_{end}\, 2^{-\mathrm{SR}_{\mathrm{Oct/min}} t/60}$	$\Phi(t) = 2\pi \left(-\frac{60 f_{end}}{\mathrm{SR}_{\mathrm{Oct/min}} \log 2} 2^{-\mathrm{SR}_{\mathrm{Oct/min}} t/60} - 1 \right)$

13.3 Sweeping and Estimate

Harmonic Estimator The idea of the on-line frequency domain MIMO control for swept sine testing proposed in this paper is closely dependent on the capability of accurately tracking the amplitude and the phase of the response (to be corrected) and the drive (to be updated) waveforms, as shown in Fig. 13.2. The idea of this paper is to use an on-line implementation of a traditional Harmonic Estimator, as currently adopted, for example, in the Siemens Simcenter Testlab Sine Control application [16].

For a general sinusoidal waveform with fundamental natural frequency $2\pi\omega_f$

$$y(t) = |y(t)| \sin[\omega_f t + \phi(t)] = a_c \cos(\omega_f t) + a_s \sin(\omega_f t) \tag{13.6}$$

the amplitude and phase

$$|y(t)| = \sqrt{a_c^2 + a_s^2} \tag{13.7a}$$

$$\phi(t) = \mathrm{atan}\left(\frac{a_c}{a_s}\right) \tag{13.7b}$$

can be calculated assuming that, within p periods, Eq. (13.6) holds, and therefore the parameters a_c and a_s can be estimated in a least square sense using the acquired data (left-hand-side of Eq. (13.6)).

For the on-line estimation during a continuous sine sweep, the frequency of the signals, and therefore the argument $\Phi(t) + \phi(t)$ of the sine wave in Eq. (13.6), continuously varies with a specific sweep mode (linear or logarithmic), as reported in Table 13.1.

Sweeping Output of the frequency domain MIMO control is a set of corrected amplitudes and phases for the drive signals. This set of amplitude and phase can be used to generate the drives during the sweep

$$\mathbf{u}(t) = \mathbf{A}(t) \odot \sin(\omega(t)t + \boldsymbol{\phi}(t)) \tag{13.8}$$

where the $\odot$ represent the element-wise multiplication, ω(t) the instantaneous frequency at the time t, and $\mathbf{A}(t)$ and $\boldsymbol{\phi}(t)$ vectors containing the drives amplitude and phase, update by the controller.

13.4 MIMO Sine Feedback Control

Once the amplitude and the phase of the swept sine waves are accurately estimated, it is the possible to adopt, for each frequency line, the idea is to use a classic feedback control for tonal disturbances in order to correct the potential differences between the reference and the control spectra. The proposed approach follows the theory largely discussed in [15] and is schematically represented in the block diagram of Fig. 13.2.

13.4.1 Drives Update

The cost function associated to the least square error (13.3) is

$$J(\mathbf{u}) = \mathbf{e}^H\mathbf{e} = \mathbf{u}^H\mathbf{H}^H\mathbf{H}\mathbf{u} - \mathbf{u}^H\mathbf{H}^H\mathbf{r} - \mathbf{r}^H\mathbf{H}\mathbf{u} + \mathbf{r}^H\mathbf{r} \tag{13.9}$$

The task of the controller is to iteratively adjust the drives at the nth iteration in order to minimize the cost function (13.9).

$$\mathbf{g}_n = \frac{\partial J_n}{\partial \mathbf{u}_n} = 2(\mathbf{H}^H\mathbf{H}\mathbf{u}_n - \mathbf{H}^H\mathbf{r}) = 2\mathbf{H}^H\mathbf{e}_n \tag{13.10}$$

It is worth to notice that the derivative operation in Eq. (13.10) should not be interpreted in the standard sense, as the real cost function of Eq. (13.9) with respect to the (generally complex) drives fails the Cauchy-Riemann conditions (it is said to be *not analytic* in the space $\mathbb{C}^m$), as analyzed in details in [17] and [18]. Additionally [17, 18] and later [19], propose to tackle the problem considering a representation in *Conjugate Coordinates*. Alternatively, it is possible to consider as different independent variables the real and imaginary part of the drives ($\mathbf{u}_\mathrm{R}$ and $\mathbf{u}_\mathrm{I}$, respectively), so that $\frac{\partial J}{\partial \mathbf{u}} = \frac{\partial J}{\partial \mathbf{u}_\mathrm{R}} + \mathrm{i}\frac{\partial J}{\partial \mathbf{u}_\mathrm{I}}$, where i is the imaginary unit. The drives can then be updated in order to decrease the cost function in the steepest descent direction

$$\mathbf{u}_{n+1} = \mathbf{u}_n + 2\mu\mathbf{H}^H\mathbf{e}_n = \mathbf{u}_n + \alpha\mathbf{H}^H\mathbf{e}_n \tag{13.11}$$

where μ is the *step size* or *convergence factor* and $\alpha = 2\mu$ is often referred to as *convergence coefficient* [15].

The convergence coefficient need to be chosen in order to guarantee the Bounded Input Bounded Output (BIBO) stability of the MIMO closed loop system.

13.4.2 Optimal Convergence Coefficient

To guarantee that the closed loop system is BIBO stable, it is necessary and sufficient to guarantee that the drives will eventually converge to their optimal value (the one that theoretically minimizes the control error), and therefore that for each signal

$$\frac{|u_n - u_{opt}|}{|u_0 - u_{opt}|} < 1 \tag{13.12}$$

Following the theory of [15], two different approaches can be followed to find the optimal convergence coefficient, both leading to the same result. The first approach is quite simple and, for discrete system, reduces to guarantee that the poles of the Closed Loop system (the roots of the so-called *Return Difference Matrix*) need all to lie inside the unit circle. The second approach, discussed here, makes use of a set of a transformed set coordinates and the tools of linear algebra. Decomposing the FRF matrix of the plant with the Singular Values Decomposition (SVD) [20]

$$\mathbf{H} = \mathbf{R}\boldsymbol{\Sigma}\mathbf{Q}^H \tag{13.13}$$

where $\boldsymbol{\Sigma}$ is a diagonal matrix containing the Singular Values (SVs) of $\mathbf{H}$ and $\mathbf{R}$ and $\mathbf{Q}$ are two unitary matrices. The control error at the nth iteration can be transformed pre-multiplying the left and right hand sides of Eq. (13.3) by $\mathbf{R}^H$

$$\boldsymbol{\xi}_n = \mathbf{R}^H\mathbf{e}_n = \mathbf{R}^H\mathbf{r} - \boldsymbol{\Sigma}\mathbf{Q}^H\mathbf{u}_n \tag{13.14}$$

Defining

- *transformed error*, $\boldsymbol{\xi}_n = \mathbf{R}^H\mathbf{e}_n$
- *transformed plant*, $\boldsymbol{\Sigma}$
- *transformed reference*, $\boldsymbol{\rho} = \mathbf{R}^H\mathbf{r}$
- *transformed drives*, $\boldsymbol{\nu}_n = \mathbf{Q}^H\mathbf{u}_n$

Equation (13.3) can be re-written as

$$\boldsymbol{\xi}_n = \boldsymbol{\rho} - \boldsymbol{\Sigma}\boldsymbol{\nu}_n \tag{13.15}$$

From Eq. (13.15) it is possible to see the advantage of moving to a transformed coordinate space: the diagonal nature of $\boldsymbol{\Sigma}$ de-couples the control problem. For this reason, the singular values define a basis for the MIMO system (*principal coordinates*). This means that

- each of the transformed error signals is affected by *only one drive* or *none*. In the principal coordinates the first m signals can therefore be *independently* controlled.
- For each channel, the specific SV represents the optimal step size for the transformed drive. For this reason [15] also refers to the SVs as *Principal Gains*.

In the principal coordinates, the ith independent (transformed) drive update equation can be written as

$$\nu_{i,n+1} = \nu_{i,n} + \alpha\sigma_i\xi_{i,n} \tag{13.16}$$

Following by the definitions of the transformed quantities and the fact that the matrices $\mathbf{R}$ and $\mathbf{Q}$ are unitary, it is worth to notice that the cost function is the same in both the physical and the transformed space $J = \mathbf{e}^H\mathbf{e} = \boldsymbol{\xi}^H\boldsymbol{\xi}$, hence the convergence of the process can be analyzed in the principal coordinates. Specifically for the BIBO stability it needs to be guaranteed that

$$\frac{|\nu_n - \nu_{opt}|}{|\nu_0 - \nu_{opt}|} = |1 - \alpha\sigma_i^2| < 1 \tag{13.17}$$

and hence that

$$0 < \alpha_i < \frac{2}{\sigma_i^2} \tag{13.18}$$

Naturally, to guarantee that all the drives will eventually converge, it is necessary to limit the convergence coefficient with respect to the maximum singular value, obtaining the optimal convergence coefficient

$$\alpha_{opt} = \frac{1}{\sigma_{max}^2} \tag{13.19}$$

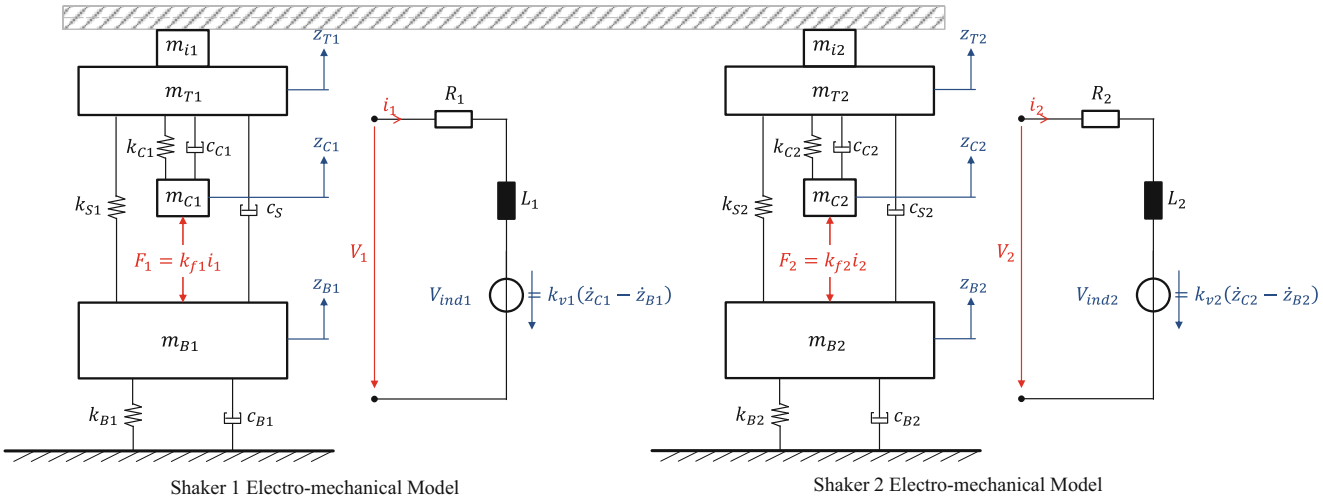

Fig. 13.3 Schematic representation of the two lumped-parameters virtual shakers in twin configuration

13.5 The Challenges of MIMO Swept Sine Control: A Simulated Example Using a Virtual Shaker Model

In this section an explanation of the potential challenges related to a MIMO swept sine controlled test with the proposed algorithm are supported by results obtained from simulations where the algorithm is used to control the responses of two uncoupled lumped mass parameters shakers. The idea is to build the controller in a simulation environment that includes also a full validated virtual model of the amplifiers and the vibration exciters. This approach allows, already in the development stage, to tackle potential issues that can be encountered during an actual test. It is therefore chosen, as excited system, a pair of virtual electro-mechanical lumped-parameters vibration exciters in twin configuration, result of the research [7] and [8] and represented in Fig. 13.3. Even though in the current work, for the sake of simplicity, no coupling structure is considered in the model and hence the two shakers are independently driven, the algorithm is generally developed for both coupled and uncoupled systems. The parameters used to model the shaker 1 are retrieved from the experimental test campaign performed to characterize a 6 kN shaker available at Siemens Industry Software N.V. HQ (Leuven, Belgium). Small differences, with respect to the parameters of the shaker 1, are introduced to obtain the parameters of the twin shaker 2. The selected control channels are the two virtual accelerometers located on the shaker heads (referring to Fig. 13.3, the signals $\ddot{z}_{T1}$ and $\ddot{z}_{T2}$) whereas the drives are the voltages V_1 and V_2 sent to the virtual amplifiers and powering the electrical parts of the shakers. The FRFs from the voltages to the control accelerations of the identified system are represented by the solid blue lines in Fig. 13.4. The dashed red lines represent the FRFs of the system excited during the sine sweep: to introduce a system identification error, the lumped parameters slightly differ from the ones of the system excited during the identification (coil masses and lumped payloads m_i reduced of 1% for the shaker 1 and increased of the same amount for the shaker 2).

13.5.1 Challenges of MIMO Swept Sine Feedback Control

Following the theory of Sect. 13.4, the feedback control of the responses for all the frequencies in a specific band of interest can be obtained considering the drives update (13.11) and the optimal convergence coefficient (13.19). First, the response amplitudes and phases need to be estimated using the procedure illustrated in Sect. 13.3 so that the control error is a known quantity. The update equation and the estimate of the optimal convergence coefficient, require also the knowledge of the real plant, however unknown. To overcome this, the solution is to make use of the system FRFs obtained with a pre-test random system identification. Even though adopting the full drives update (corresponding to the optimal convergence coefficient) would return the fastest convergence rate, it is however a condition at the limit of stability, obtained considering that all the transients have died out and the responses at the control channels have reached their steady-state, which can be a strong assumption for a swept sine test, due to the nature of the sweep. It is hence a practical idea to scale down the convergence including a control gain K between 0 and 1

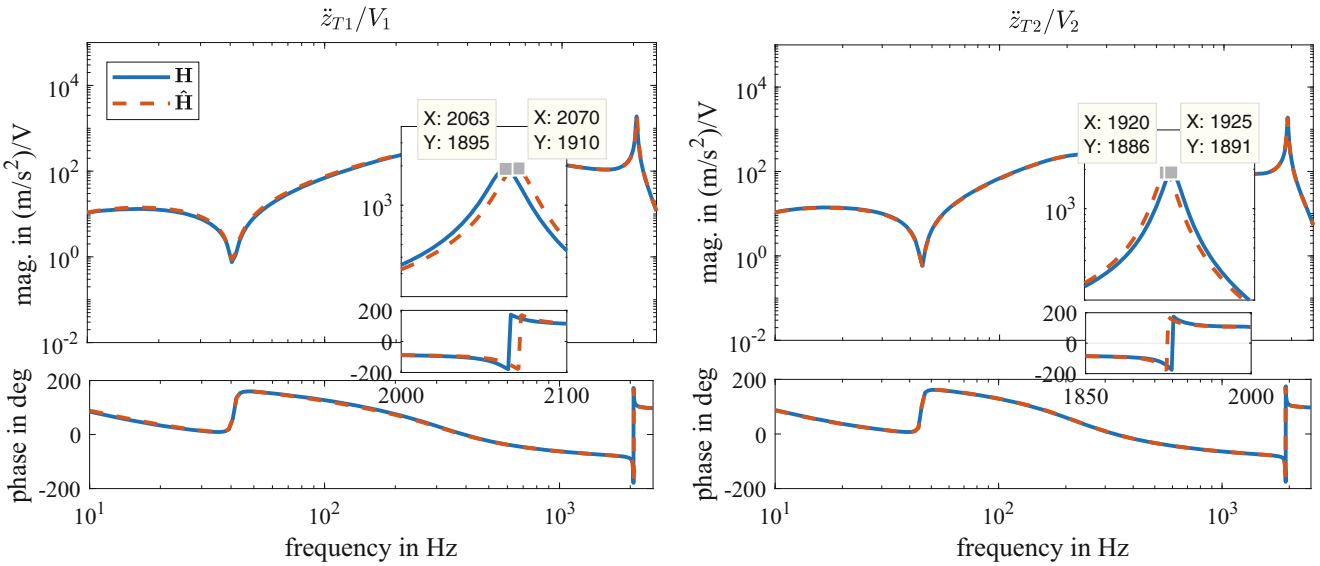

Fig. 13.4 FRFs matrix of the twin shaker. In blue and red the system excited during the MIMO sine control run and the identified system. In the details, it is highlighted the induced system identification error

Table 13.2 Settings adopted for the MIMO swept sine test

Sampling frequency	6400 Hz
Bandwidth	10–2500 Hz
Sweep mode	Linear
Sweep direction	Up
Sweep rate	2 Hz/s
Number of estimation period	1
Control gain	Variable

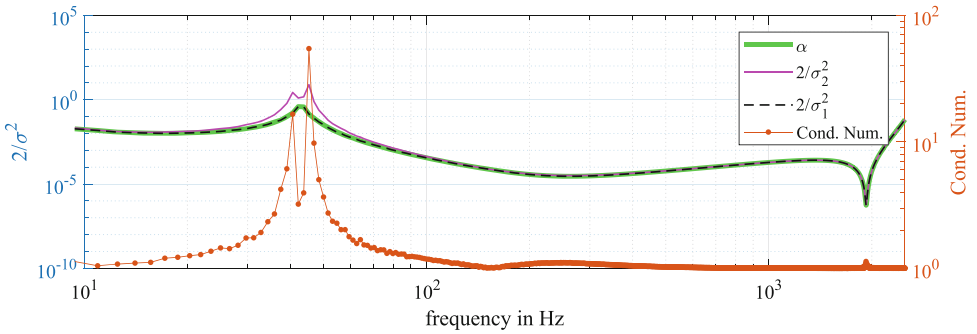

Fig. 13.5 Optimal convergence coefficient in the frequency range of interest is $2/\sigma^2_{max}$. For completeness, in the figure it is also reported the condition number of the system (right y axis)

$$\mathbf{u}_{n+1} = \mathbf{u}_n + K \frac{1}{\hat{\sigma}^2_{max}} \hat{\mathbf{H}}^H \mathbf{e}_n \tag{13.20}$$

The parameters set for the MIMO swept sine control run are shown in Table 13.2.

It is worth to underline that, once the parameters in Table 13.2 are set, the final test duration is automatically defined. For a sine sweep excitation, there is an exact correspondence between each time stamp and the instantaneous swept frequency, known a priori. This is fundamental as it allows to use at each time instant the frequency domain quantities needed for the drives update, i.e. the estimated values of the matrix $\hat{\mathbf{H}}$ and the calculated optimal convergence coefficient. For the simulation example provided in this section, these quantities are illustrated in Figs. 13.4 and 13.5, respectively.

The main issue derived from the combination of the proposed control strategy with a continuous sweep is related to the continuous changes of the cost function resulting from the sweeping and the associated change of the system's FRF

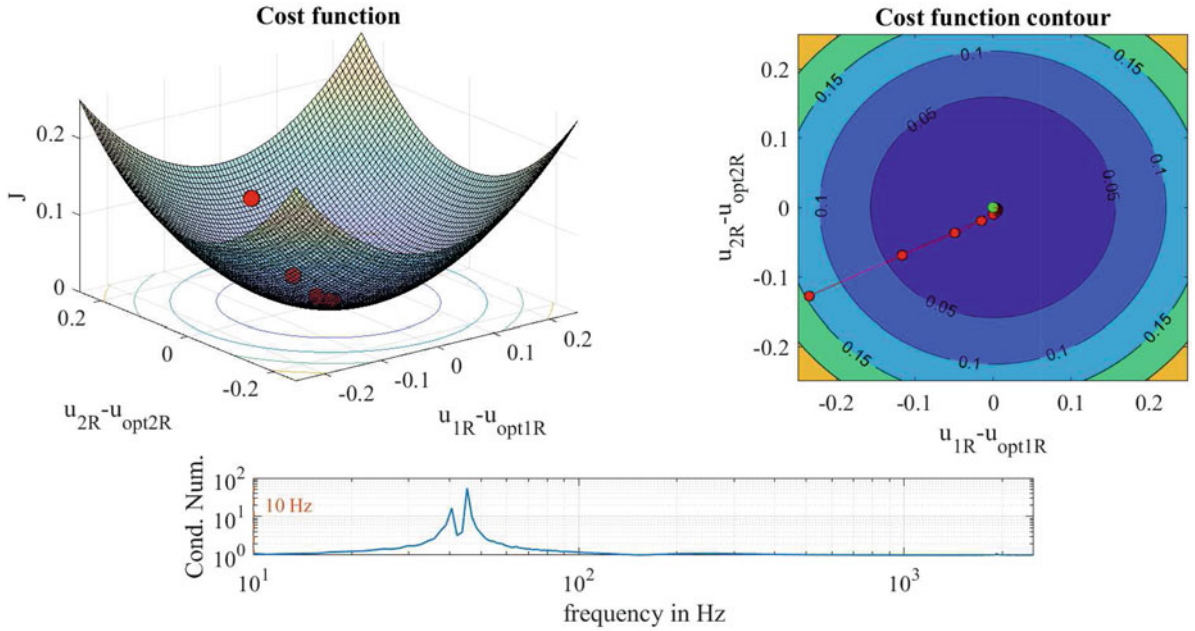

Fig. 13.6 Cost function and cost function's contours in function of the real part of $\mathbf{u} - \mathbf{u}_{opt}$ (drive 1 on the x-axis, drive 2 on the y-axis) at frequency where the condition number of the system FRFs matrix is almost unitary. To notice, from the cost function contours plot, that the convergence occurs almost simultaneously for the two drives

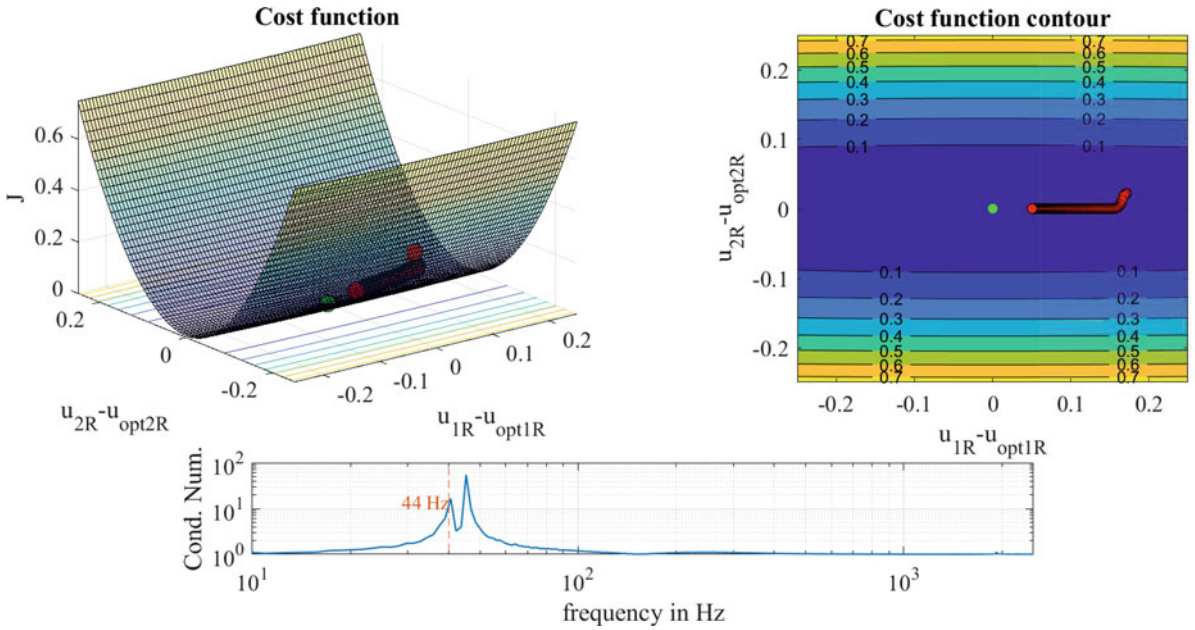

Fig. 13.7 Cost function and cost function's contours in function of the real part of $\mathbf{u} - \mathbf{u}_{opt}$ (drive 1 on the x-axis, drive 2 on the y-axis) at a frequency where the condition number of the system FRFs matrix is relatively high. Because of the shape of cost function, the drive 1 needs more iterations than the drive 2 to converge at this specific frequency

matrix in the Eq. (13.9). For a MIMO system this cost function is a multidimensional complex parabolic surface with as many dimensions as the number of drives and an eccentricity directly related to the condition number of the system. Figures 13.6, 13.7 and 13.8 represent the shape of the cost function, the cost function contours and the condition number at three different frequencies during the sweep. The cost function J and its contours are plotted in function of $\mathbf{u} - \mathbf{u}_{opt}$, where $\mathbf{u}_{opt}$ are the optimal drives that ideally minimize J (known in a simulated scenario). These graphs are therefore centered in zero (the optimum, represented by the green dot in the plots). In the plot only the real part of the drives is considered,

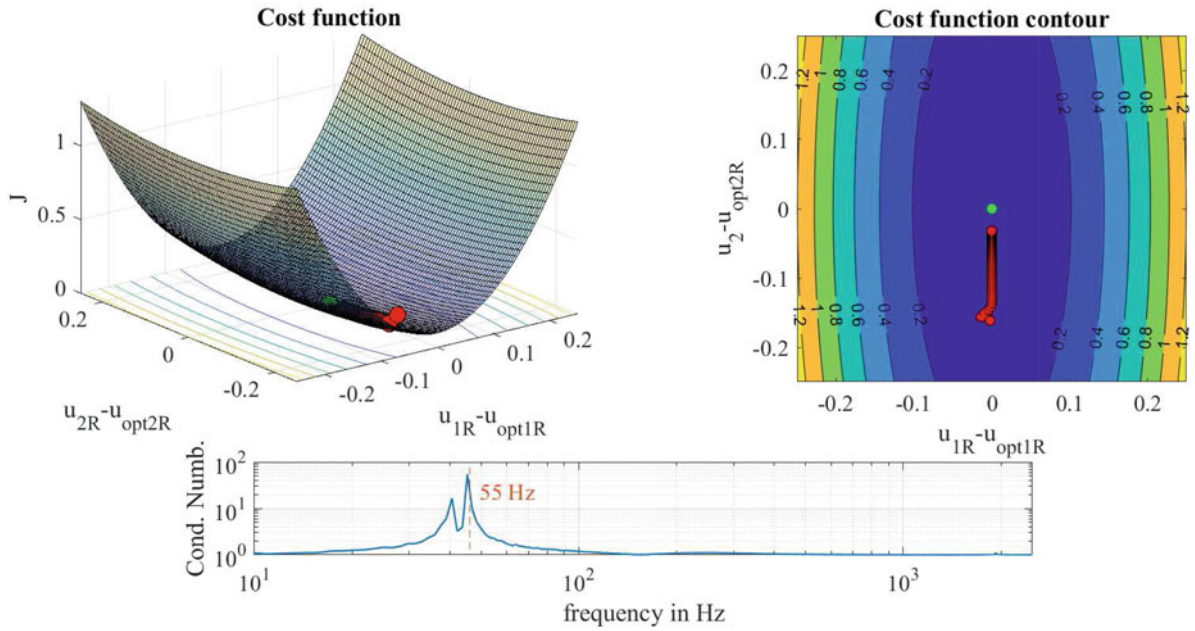

Fig. 13.8 Cost function and cost function's contours in function of the real part of $\mathbf{u} - \mathbf{u}_{opt}$ (drive 1 on the x-axis, drive 2 on the y-axis) at a frequency where the condition number of the system FRFs matrix is relatively high. Because of the shape of cost function, the drive 2 needs more iterations than the drive 1 to converge at this specific frequency

indicated with an additional subscript R, but similar plots can be also obtained considering the imaginary part. The red dots illustrates the drives at each iteration and hence the convergence of the process.

From the figure it is possible to notice that the shape of the cost function, and hence the corrections needed for each drive to reach its optimal value, are strongly influenced by the system's conditioning at a specific frequency. In case of a low condition number (at the limit unitary), the cost function has a regular (at the limit, semi-spherical) shape, indicating that the convergence will most likely occur simultaneously for the two different (transformed) drives, as shown in Fig. 13.6.[1] On the contrary, for the frequency lines where the system has an high condition number, the cost function assumes a stretched shape in the direction of one of the (transformed) drives and hence the convergence for this (transformed) drive would require more iterations than the ones needed by the other. For the specific case of a swept excitation, this might represent a main issue because, during the sweep, the cost function can vary abruptly while the correction algorithm converges, as shown in Fig. 13.9, depending on the system's conditioning and the sweep rate. Even if at the current stage no link has been theoretically made between the convergence and the sweep rate, a scheduling of the control gain K can be used to overcome this potential issue.

A MIMO swept sine control simulation is run to show the applicability of the proposed procedure with twin shaker virtual model and the settings reported in Table 13.2. Figure 13.10 illustrates the comparison from the a classic feedforward approach (drives pre-shape) and the prototype solution of the MIMO swept sine control. Besides the system identification error introduced, as illustrated in Fig. 13.4 also two step disturbances have been introduced on the responses at 400 and 800 Hz for the responses 1 and 2, respectively. From the details in the figure, it is clearly shown the capability of the proposed feedback control strategy of attenuating the differences due to the system identification error and quickly responding to the introduced step disturbances (less than half a second for the response one and approximately one second for the response 2).

[1]For this uncoupled example, the axes of the ellipsoidal cost function's contours are well-aligned with the plane defined by the components of $\mathbf{u} - \mathbf{u}_{opt}$. This simplification, associated to the choice of controlling an uncoupled system, allows to draw considerations on the physical system, but generally these considerations are strictly valid only in the transformed space.

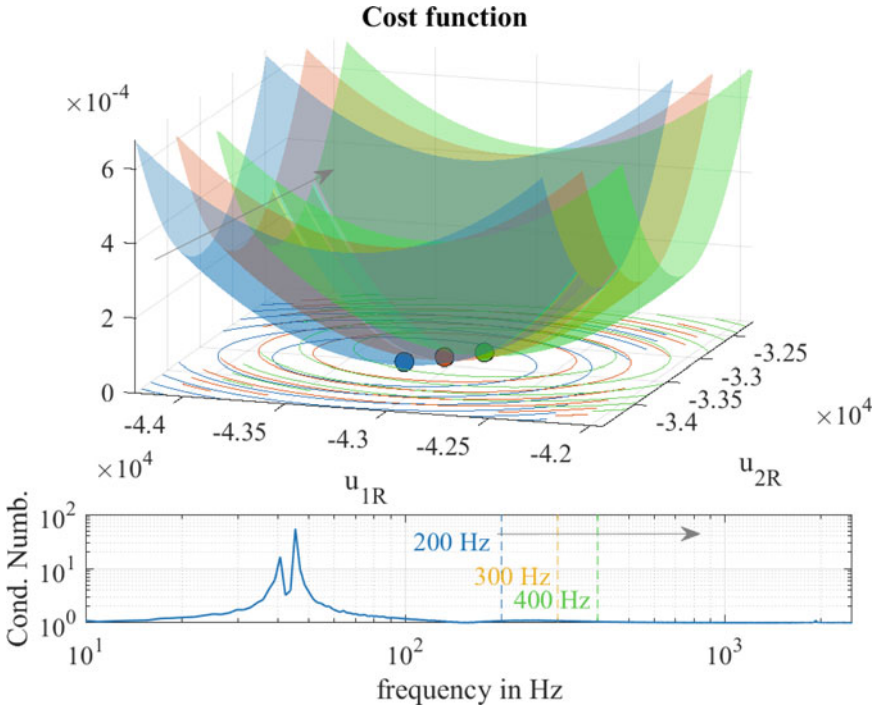

Fig. 13.9 During the sweep the cost function shifts and deforms

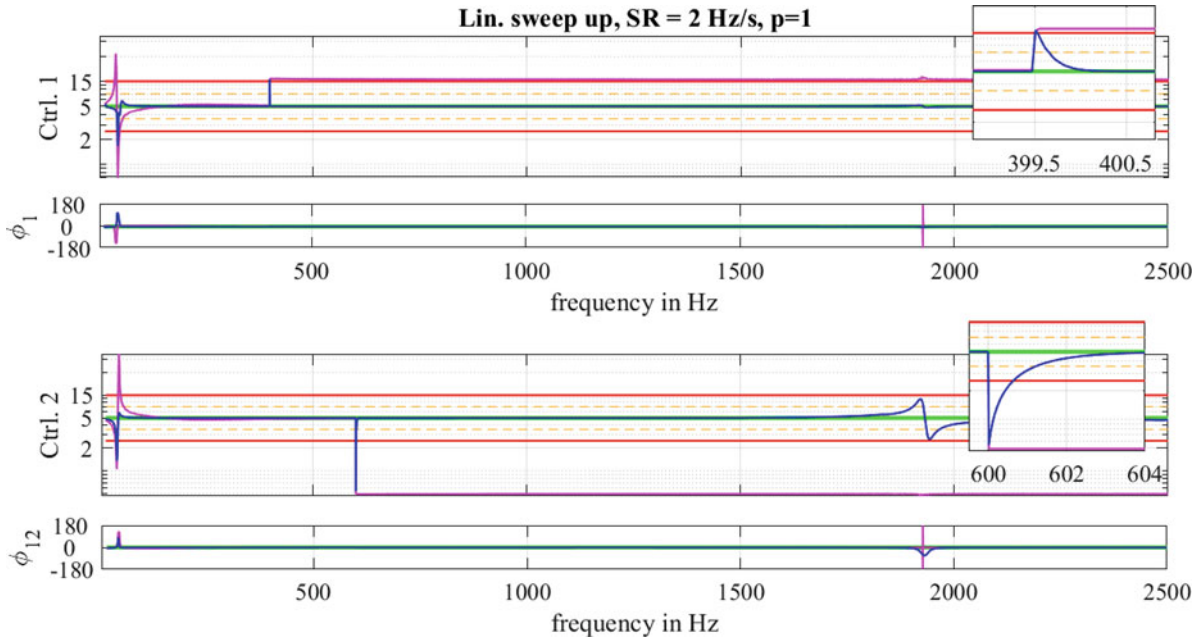

Fig. 13.10 Control results for the simulations run with the pre-shaped drives (solid magenta) and the feedback control (solid blue). The induced errors to be corrected are the system identification error shown in Fig. 13.4 and two step disturbances. The feedback control is able to react to the disturbances and bring back the response on the reference. In the figure the alarm and abort (±3 and ±6 dB) are also reported for completeness

13.6 Conclusions and Future Directions

In this paper the details and the mathematical derivation of a newly developed MIMO swept sine control strategy are discussed. The algorithm makes use of a fast on-line tracking of amplitudes and phases between responses to correct in feedback potential mismatches between the spectra of a user-defined number of control channels and a specific reference,

using a steepest descent algorithm. The details of the convergence challenges associated to the MIMO correction for swept sine excitation and the results of a MIMO closed loop controlled simulation are shown with a virtual model of a setup with shakers in twin configuration, continuously sweeping in a specific band of interest. The promising results motivates further investigations and a real time proof-of-concept, in order to study the feasibility of adopt the proposed methodology for MIMO swept sine environmental testing and acquisition.

Acknowledgements The financial support of VLAIO is gratefully acknowledged (research grant *ADVENT*: ADvanced Vibration ENvironmental Testing).

References

1. Heylen, W., Lammens, S., Sas, P.: Modal Analysis Theory and Testing. K.U. Leuven, Leuven (2016)
2. Pauwels, S., Michel, J., Robijns, M., Peeters, B., Debille, J.: A new MIMO sine technique for accelerated, high quality FRF measurements. In: Proceedings of International Conference on Noise and Vibration Engineering, Leuven (2006)
3. Orlando, S., Peeters, B., Coppotelli, G.: Improved FRF estimators for MIMO sine sweep data. In: Proceedings of International Conference on Noise and Vibration Engineering, Leuven (2008)
4. Gloth, G., Synapius, M.: Analysis of swept-sine runs during modal identification. Mech. Syst. Signal Process. **18**, 1421–1441 (2004)
5. Peeters, B., Hendricx, W., Debille, J.: Modern solutions for ground vibration testing of large aircrafts. Sound Vib. **43**(1) (2009)
6. Fortescue, P., Swinerd, G., Stark, J.: Spacecraft Systems Engineering, 4th edn. Wiley, New York (2011)
7. Waimer, S., Gentile, E., Manzato, S., Peeters, B., Wagner, M., Guillaume, P.: Modelling and experimental validation of a coupled electrodynamic shaker and test structure simulation model. In: Proceedings of International Conference on Noise and Vibration Engineering, Leuven (2016)
8. Waimer, S., Manzato, S., Peeters, B., Wagner, M., Guillaume, P.: Modelling and simulation of a closed-loop electrodynamic shaker and test structure model for spacecraft vibration testing. Adv. Aircr. Spacecr. Sci. **5**, 205–223 (2018)
9. Musella, U., Zanellati, L., Grottoli, M., Celiberti, F., Peeters, B., Marulo, F., Guillaume, P.: Driving a motion platform with a vibration control software for multi-axis environmental testing: challenges and solutions. In: Proceedings of the XXXVI IMAC, Orlando (2018)
10. Musella, U., D'Elia, G., Carrella, A., Peeters, B., Mucchi, E., Marulo, F., Guillaume, P.: A minimum drives automatic target definition procedure for multi-axis random control testing. Mech. Syst. Signal Process. **107**, 452–468 (2018)
11. Pintelon, R., Schoukens, J.: System Identification: A Frequency Domain Approach. Wiley, Hoboken (2012)
12. Bendat, J., Piersol, A.G.: Random Data: Analysis and Measurement Procedures, vol. 729. Wiley, New York (2011)
13. Underwood, M.: Multi-exciter testing applications, theory and practice. In: Proceedings of Institute of Environmental Sciences (2002)
14. Musella, U., Longo, A., Vettori, S., Waimer, S., Di Lorenzo, E., Peeters, B., Marulo, F., Guillaume, P.: Recent advances in swept sine controlled excitation and processing for multi-input multi-output FRFs estimation. In: Proceedings of ISMA 2018 (2018)
15. Elliot, S.: Signal Processing for Active Control. Academic, London (2001)
16. Siemens Industry Software N.V.: LMS Test.Lab Environmental, User Manual (2016)
17. Kreutz-Deglado, K.: The complex gradient operator and the $\mathbb{CR}$-calculus, Preprint, ArXiv (2009)
18. Sorber, L., van Barel, M., de Lathauwer, L.: Unconstrained optimization of real functions in complex variables. SIAM J. Optim. **22**(33), 879–898 (2012)
19. Musella, U., Manzato, S., Peeters, B., Guillaume, P.: $\mathbb{CR}$-calculus and adaptive array theory applied to MIMO random vibration control tests. J. Phys. Conf. Ser. IOP Science **744**(1), 012175 (2016)
20. Meyer, C.D.: Matrix Analysis and Applied Linear Algebra. Society for Industrial and Applied Mathematics, Philadelphia (2000)

Chapter 14
Study on Developing Micro-Scale Artificial Hair Cells

Sheyda Davaria, V. V. N. Sriram Malladi, Lukas Avilovas, Phillip Dobson, Andrea Cammarano, and Pablo A. Tarazaga

Abstract The cochlea, in the mammalian inner ear, transduces acoustic waves into electrical signals that are transmitted to the brain. One of the critical functions of the cochlea is its biological nonlinear behavior that amplifies faint sounds and compresses high sound levels. Previously, authors mimicked the aforementioned nonlinear characteristics in piezoelectric augmented structural cantilevers through nonlinear feedback controllers. The present effort is a continuation of the previous studies in the development of micro-electro-mechanical system (MEMS) scale artificial hair cells (AHCs).

The current research investigates the potential of transforming MEMS scale cantilevers, initially designed for use as scanning thermal microscopy probes, into micro-scale artificial hair cells. These cantilever structures are fabricated by employing electron beam- and photo-lithography, together with Low Pressure Chemical Vapor Deposition (LPCVD), metal evaporation, dry- and wet-etching on n-type silicon wafer substrates. In this work, dynamic characterization of these micro-structures is the focus. A series of dynamic tests are conducted on the MEMS micro-structure as it is subjected to base excitation. The dynamic characteristics of the MEMS system are investigated by varying the excitation levels and evaluating the limits of the structure's linearity. Based on the experimental findings the potential of using these MEMS cantilevers as active artificial hair cells is evaluated.

Keywords Artificial hair cell · MEMS · Nonlinearity · Cochlea · Feedback control

14.1 Introduction

In mammalian auditory system, the acoustic waves passed through the outer and middle ears are transmitted to the cochlea of the inner ear as travelling waves. The tonotopic nature of the basilar membrane in the cochlea, then acts similar to a Fourier analyzer and decomposes the wave into its frequency content. Signals are then amplified or compressed by the outer hair cells (OHCs) of the cochlea based on their amplitude and inner hair cells (IHCs) convert the vibrations of the waves to electrical signals and send them to the brain [1]. The amplification characteristic of the low intensity inputs, and compression characteristic of the high level inputs by the OHCs show a nonlinear behavior [2]. Damage to the OHCs stops these nonlinear processes and causes severe hearing loss [3]. Therefore, these nonlinear characteristics and frequency selectivity of the basilar membrane have been the inspiration for many researchers in developing vibrations and acoustics based sensors and hearing aid prosthesis over the decades [4–7]. Artificial hair cells (AHCs) are among the devices developed for mimicking the nonlinear functions of the OHCs with the ultimate goal of potentially implanting in the mammalian cochlea [8–10].

The authors' previous works showed that the macro active AHCs with a phenomenological nonlinear feedback control law can mimic the OHCs' function [11]. The authors have chosen to investigate the use of SThM (i.e., AFM) cantilever beams as potential AHCs as they offer a ubiquitous, modestly priced MEMS cantilever structure with a wealth of background literature. This makes them ideal as a starting point for subsequent development and modification to achieve micro-scale AHCs. In the present work, to move towards implementing an active AHC at the micro scale, modal characteristics and linearity of a MEMS cantilever developed by Dobson et al. [12] are studied by exciting the structure's base and measuring its response. In the first section, a brief description of the MEMS cantilever and its fabrication process is presented. Then, the test setup and the procedure for high frequency modal testing are described. The first four natural frequencies of the

S. Davaria (✉) · V. V. N. Sriram Malladi · P. A. Tarazaga
Vibrations, Adaptive Structures, and Testing Lab, Department of Mechanical Engineering, Virginia Tech, Blacksburg, VA, USA
e-mail: sheydada@vt.edu

L. Avilovas · P. Dobson · A. Cammarano
School of Engineering, University of Glasgow, Glasgow, UK

N. Dervilis (ed.), *Special Topics in Structural Dynamics & Experimental Techniques, Volume 5*, Conference Proceedings of the Society for Experimental Mechanics Series, https://doi.org/10.1007/978-3-030-12243-0_14

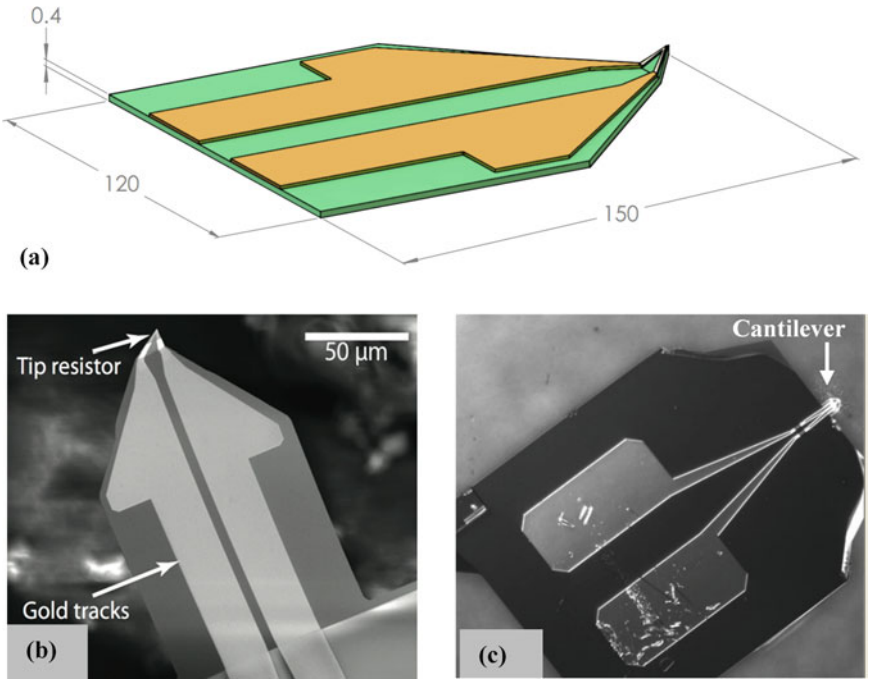

Fig. 14.1 Micro-cantilever, (**a**) schematic with dimensions in µm, (**b**) structure under scanning electron microscope (SEM), and (**c**) Polytec MSA-500 built-in microscope with 20× objective

cantilever structure and its corresponding mode shapes are extracted. Finally, the linearity of the structure is studied by a stepped sine analysis around its fundamental frequency. The results of this study will be used in the future for developing MEMS active AHCs.

14.2 Micro-Cantilever Structure

The cantilever structures consist of 400 nm thick Si_3N_4 beams of dimensions shown on Fig. 14.1, tethered at one end to a silicon substrate. Their original design was intended for use as Scanning Thermal Microscopy (SThM) probes, so they also incorporate a sharp tip, with integrated Palladium (Pd) resistive heater at their free end. Electrical access to the tip heater is achieved through two thin-film Gold (Au) pads and wires that run from the probe body, along the cantilever, to the tip. These gold wires also double as a mirror, providing a strong reflected signal when interrogating the cantilever optically. The complete fabrication process is available elsewhere [12] but in brief, a thin film of Low Pressure Chemical Vapor Deposition (LPCVD) Si_3N_4 on top of a micromachined Si wafer is patterned using ebeam- and photo-lithography followed by anisotropic dry-etching to form the cantilever shape. Wires, pads and resistive heaters are patterned on top of the cantilever using ebeam-lithography followed by lift-off of evaporated thin film metals. Finally, the entire cantilever structure is released from the underlying substrate using a Tetramethylammonium hydroxide (TMAH) wet etch to selectively remove the silicon.

14.3 Experimentation and Analysis

To investigate the possible use of MEMS cantilevers in AHC design, the dynamics of the cantilever are characterized in a high frequency modal test. Therefore, the probe body is mounted on a piezoelectric membrane to provide a base excitation, as shown in Fig. 14.2. Another piezoceramic is attached to the membrane as a sensor to measure input actual excitation of the MEMS structure. The base is excited by a chirp signal with a 0–400 kHz bandwidth and the response of the system is obtained by a Polytec MSA-500 scanning laser vibrometer at various points on the structure.

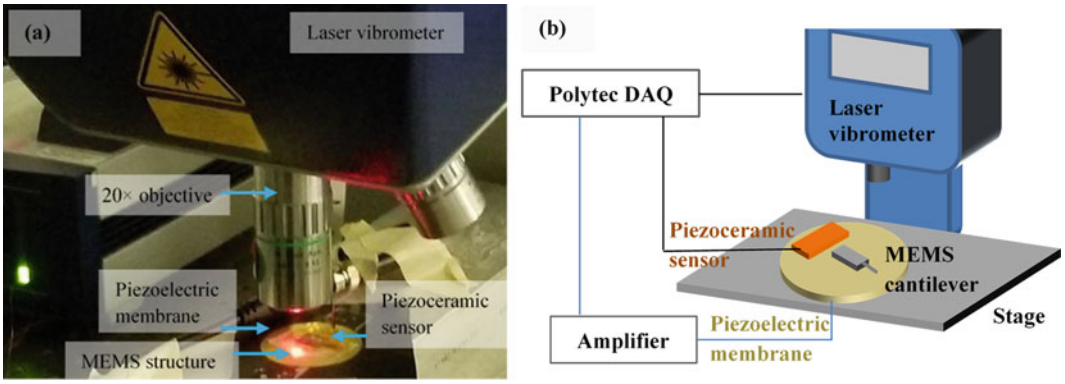

Fig. 14.2 Test setup including the MEMS structure, (**a**) under the Polytec MSA-500 laser vibrometer with a 20× objective, (**b**) shown schematically

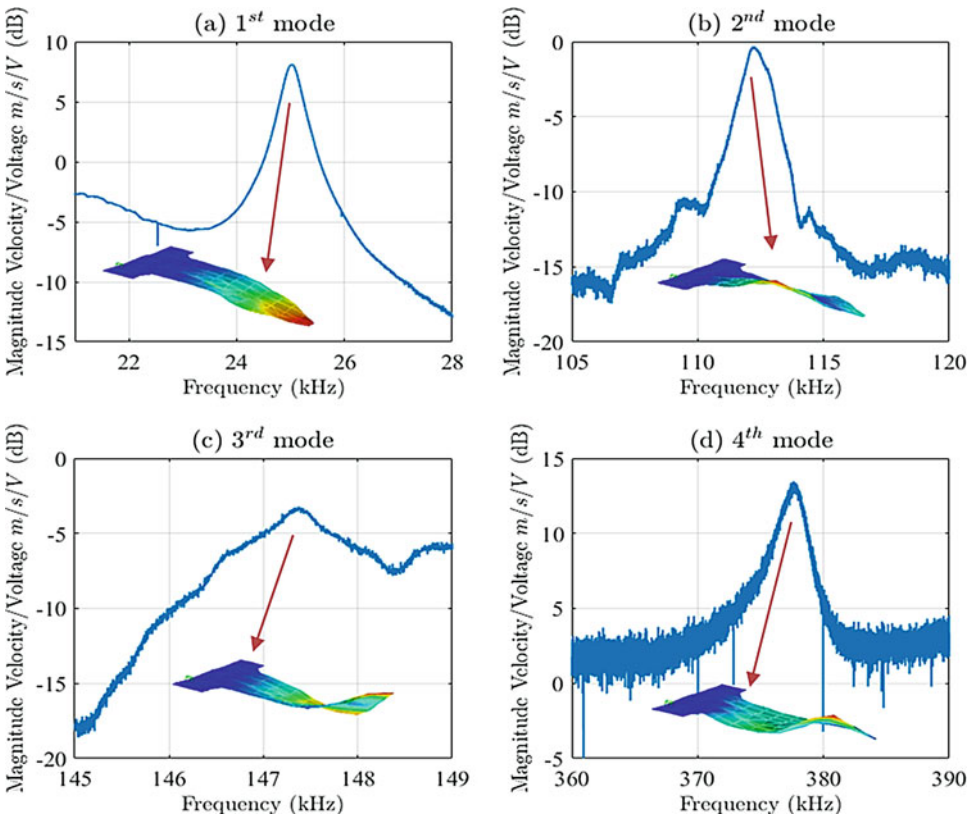

Fig. 14.3 FRFs and mode shapes of the cantilever near the first four natural frequencies

The frequency response functions (FRFs) of the micro structure around the first four natural frequencies of the cantilever along with its corresponding mode shapes are illustrated in Fig. 14.3.

The mode shapes shown in Fig. 14.3 are determined using Siemens LMS Test.Lab PolyMAX modal parameter estimation [13]. The extracted modes are the first bending mode, torsional mode, second bending and third bending mode of the structure, respectively. To demonstrate the quality of the experimental results, the Modal Assurance Criterion (MAC) [14] between the modes are calculated and the MAC chart is displayed in Fig. 14.4.

The MAC chart shows that the correlations between each mode with itself is very high, while its cross-correlations with other modes are very low. As a result, the modes are distinct and easily identifiable. To further characterize the dynamics of the structure near the natural frequencies, the modal damping of the structure corresponding to each mode is tabulated in Table 14.1. PolyMAX's stabilization diagrams constructed from the experimental data are used to extract natural frequencies and damping ratios.

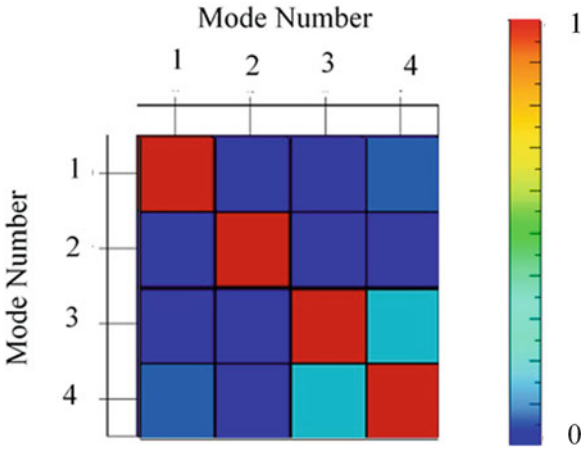

Fig. 14.4 MAC chart comparing the correlation between the experimental modes

Table 14.1 Natural frequencies and modal damping of the cantilever structure

Mode #	Natural frequency (kHz)	Damping ratio (%)
1	25.048	0.79
2	112.211	0.39
3	147.312	0.02
4	377.533	0.07

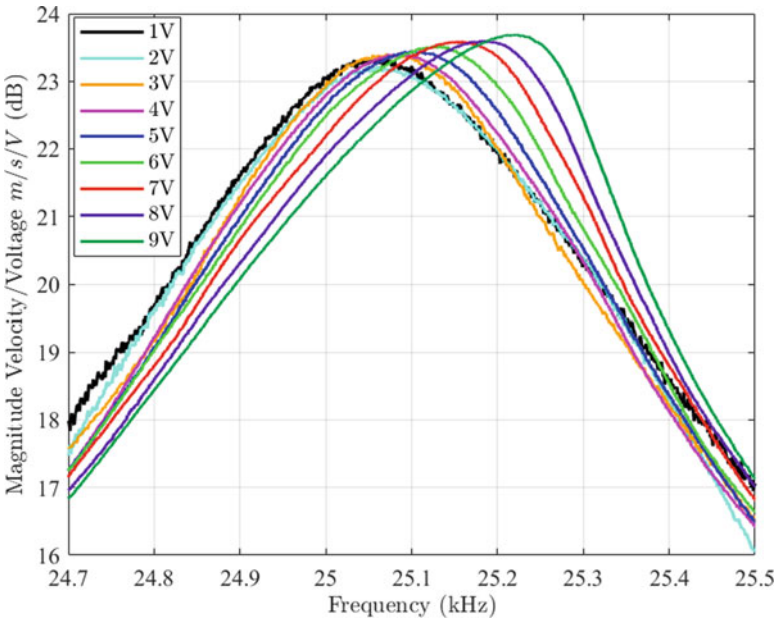

Fig. 14.5 Magnitude tip-velocity/base-voltage experimental FRF for different input levels

To investigate the existence of nonlinearities of the system at voltage inputs of interest, a stepped sine analysis is conducted around the fundamental frequency of the cantilever. Various input voltages, ranging between 1 V to 9 V are supplied to the piezoelectric membrane. The resultant FRFs are shown in Fig. 14.5.

Figure 14.5 shows that as the input level increases, the natural frequency shifts to higher frequencies and the magnitude of the FRF increases. The maximum natural frequency shift and the maximum dB amplitude shift in this input level range are 0.65%–1.45%, respectively. This is a welcomed type of response as strong nonlinearities will be hard to mitigate if an approach to implement a nonlinear feedback controller as in [11] is used to mimic the hair cell behavior.

14.4 Conclusion

In this study, the dynamics of a MEMS cantilever structure initially developed for scanning thermal microscopy is characterized by modal analysis. The first four natural frequencies, mode shapes and modal damping of the structure are obtained by exciting the base of the structure and measuring its velocity response at different locations. Results of the analysis showed that the first natural frequency of the cantilever is about 25 kHz which is not in the bandwidth of the human auditory system. Although this specimen is not in the auditory range, the MEMS cantilever seems to be an ideal candidate for AHC studies specially given its linear behavior. In future studies, the MEMS structures will be designed in the human auditory range (20 Hz to 20 kHz) and a phenomenological control law inspired by the mammalian cochlea will be applied on the cantilevers using feedback actuation. Therefore, the current work is a preliminary study to develop active MEMS AHCs inspired by the function of the mammalian cochlea.

Acknowledgements Authors would like to acknowledge the generous support from the National Science Foundation (NSF) (Grant No.1604360) that provided the funding for this project. Dr. Pablo A. Tarazaga would also like to acknowledge the John R. Jones III Faculty Fellowship.

Any opinions, findings, and conclusions or recommendations expressed in this material are those of the authors and do not necessarily reflect the views of the National Science Foundation.

References

1. Schnupp, J., Nelken, I., King, A.: Auditory Neuroscience: Making Sense of Sound. MIT Press, Cambridge (2011)
2. Hudspeth, A.: Making an effort to listen: mechanical amplification in the ear. Neuron. **59**, 530–545 (2008)
3. Isaacson, B.: Hearing loss. Med. Clin. **94**, 973–988 (2010)
4. Joyce, B.S., Tarazaga, P.A.: A study of active artificial hair cell models inspired by outer hair cell somatic motility. J. Intell. Mater. Syst. Struct. **28**, 811–823 (2017)
5. Park, S., Guan, X., Kim, Y., Creighton, F.X., Wei, E., Kymissis, I., Nakajima, H.H., Olson, E.S.: PVDF-based piezoelectric microphone for sound detection inside the cochlea: toward totally implantable cochlear implants. Trends Hear. **22**, 2331216518774450 (2018)
6. Tsuji, T., Nakayama, A., Yamazaki, H., Kawano, S.: Artificial cochlear sensory epithelium with functions of outer hair cells mimicked using feedback electrical stimuli. Micromachines (Basel). **9**, 273 (2018)
7. Joyce, B.S., Tarazaga, P.A.: Artificial hair cells inspired by active hair bundle motility. J. Intell. Mater. Syst. Struct. **28**, 1816–1831 (2017)
8. Davaria, S., Tarazaga, P.A.: MEMS scale artificial hair cell sensors inspired by the cochlear amplifier effect, Proc. SPIE 10162, Bioinspiration, Biomimetics, and Bioreplication, 101620G (17 April 2017) (2017). https://doi.org/10.1117/12.2260170
9. Joyce, B.S., Tarazaga, P.A.: Mimicking the cochlear amplifier in a cantilever beam using nonlinear velocity feedback control. Smart Mater. Struct. **23**, 075019 (2014)
10. Joyce, B.S., Tarazaga, P.A.: Developing an active artificial hair cell using nonlinear feedback control. Smart Mater. Struct. **24**, 094004 (2015)
11. Davaria, S., Sriram Malladi, V.V.N., Tarazaga, P.A.: Bio-Inspired Nonlinear Control of Artificial Hair Cells, pp. 179–184. Springer International Publishing, Cham (2019)
12. Dobson, P.S., Weaver, J.M., Mills, G.: New methods for calibrated scanning thermal microscopy (SThM). In: Sensors, 2007 IEEE, pp. 708–711. IEEE, New York (2007)
13. Peeters, B., Van der Auweraer, H., Guillaume, P., Leuridan, J.: The PolyMAX frequency-domain method: a new standard for modal parameter estimation? Shock. Vib. **11**, 395–409 (2004)
14. Allemang, R.J.: The modal assurance criterion–twenty years of use and abuse. J. Sound Vib. **37**, 14–23 (2003)

Chapter 15
Dynamic Characteristic Identification

Clay Jordan and Tommy Hazelwood

Abstract This paper introduces a dynamic system parameter extraction approach using experimental data and a known characteristic equation for a single degree of freedom mass-spring-damper system. The efficacy of curve fitting to determine mass, damping, and stiffness for simulated underdamped, critically damped, and overdamped systems is explored. Two methods are investigated to obtain these characteristics for simulated systems; a step response approach in the time domain and a transfer function and dynamic stiffness approach in the frequency domain. Commonly available software, MATLAB, is used for curve fitting. An examination of the effect of inaccurate seeds, or starting values, for mass, damping, and stiffness is included.

Keywords Dynamic stiffness · Step response · Curve fitting · MATLAB · System analysis

15.1 Introduction

This paper investigates a method to identify the mass (m), damping (c), and stiffness (k) of a system by curve fitting a modeled single degree of freedom mass-spring-damper system. Data is computer generated with MATLAB using known values for mass, damping, and stiffness to simulate empirical measurement data that is layered with noise to emulate real data. A step response approach in the time domain and a dynamic stiffness approach in the frequency domain are used to curve fit this data. The step response of the system to an input is curve fit using a MATLAB error minimization algorithm resulting in the identification of the values for the mass, damping, and stiffness coefficients. These parameters are compared to the same values determined using the dynamic stiffness of the modeled system utilizing the same error minimization algorithm. The mass, damping, and stiffness coefficients generated through these two methodologies are compared to the original known values.

15.2 Background

Attempting to understand and control motion in a system—be it a machine tool's linear stage, scientific equipment, or other piece of machinery— is simplified by knowing the basic dynamic characteristics of that system. If the basic dynamic characteristics of mass (m), damping (c), and stiffness (k) are not known, for instance, due to the age of the equipment, an inability to directly access the equipment, or some other gap in knowledge, it is possible to identify these values using minimization/optimization tools. This is accomplished by characterizing the responses of the system to an input or by creating a simple model of the system and using an error minimization function to determine values for the mass, damping, and stiffness coefficients given a reasonable seed.

15.3 Analysis

The efficacy of determining the mass, damping, and stiffness coefficients of a single degree of freedom mass-spring-damper system using MATLAB's *fminsearch* function is investigated by first simulating a system and then separately evaluating the

C. Jordan (✉) · T. Hazelwood
Oak Ridge National Laboratory, Dynamic Systems Analysis Group, Electrical and Electronics Systems Research Division, Oak Ridge, TN, USA
e-mail: jordanca@ornl.gov; hazelwoodtj@ornl.gov

N. Dervilis (ed.), *Special Topics in Structural Dynamics & Experimental Techniques, Volume 5*, Conference Proceedings of the Society for Experimental Mechanics Series, https://doi.org/10.1007/978-3-030-12243-0_15

generated system using a step response in the time domain and the dynamic stiffness in the frequency domain. Ten systems, or test cases, are generated and each test case is evaluated 50 times using MATLAB to generate a population of solutions. Test cases include underdamped, overdamped, and critically damped dynamic systems. This process is presented in Fig. 15.1.

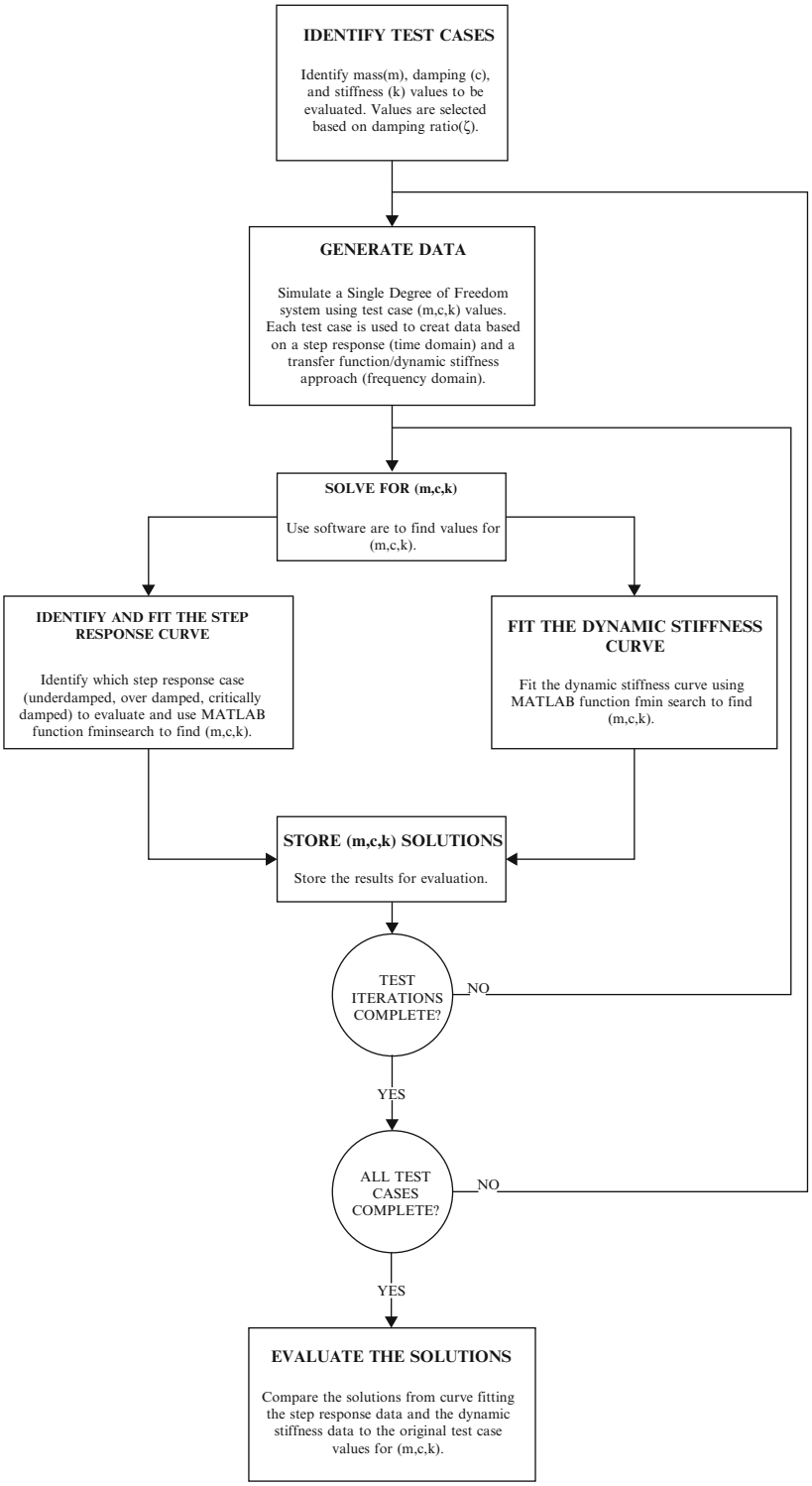

Fig. 15.1 Solver testing process

A single degree of freedom mass-spring-damper system is modeled using a step response method in the time domain and a dynamic stiffness method in the frequency domain. The system may be described by Eq. (15.1).

$$F = \left(-m\omega^2 + ic\omega + k\right) X \tag{15.1}$$

The damping ratio and natural frequency, Eqs. (15.2) and (15.3), are used throughout the following equations.

$$\zeta = \frac{c}{2\sqrt{mk}} \tag{15.2}$$

$$\omega_n = \sqrt{\frac{k}{m}} \tag{15.3}$$

The step responses for the simulated data are presented here. The step response equation used depends on the calculated value of the damping ratio, ζ, and are shown in the equations below from Palm [1].

For underdamped systems where $0 \leq \zeta \leq 1$:

$$x(t) = \frac{1}{k}\left[\frac{1}{\sqrt{1-\zeta^2}} e^{-\zeta\omega_n t} \sin\left(\omega_n\sqrt{1-\zeta^2}t + \varphi\right) + 1\right] \tag{15.4}$$

with

$$\varphi = \tan^{-1}\frac{\sqrt{1-\zeta^2}}{\zeta} + \pi \tag{15.5}$$

And complex roots

$$s = -\zeta\omega_n \pm j\omega_n\sqrt{1-\zeta^2} \tag{15.6}$$

For overdamped systems where $\zeta > 1$:

$$x(t) = \frac{1}{k}\left[\frac{r_2}{r_1 - r_2} e^{-r_1 t} - \frac{r_1}{r_1 - r_2} e^{-r_2 t} + 1\right] \tag{15.7}$$

And real roots $r_1 \neq r_2$ found using

$$-r_1, -r_2 = \frac{-c \pm \sqrt{c^2 - 4mk}}{2m} \tag{15.8}$$

For critically damped systems $\zeta = 1$:

$$x(t) = \frac{1}{k}\left[(-r_1 t - 1)\, e^{-r_1 t} + 1\right] \tag{15.9}$$

And real roots $r_1 = r_2$ using Eq. (15.8).

The dynamic stiffness, Z, is generated from the transfer function

$$Z = \frac{F}{X} = \left(-m\omega^2 + ic\omega + k\right) \tag{15.10}$$

Simulated noise is added to the data by layering random data, generated using MATLAB's *randn* function, over the model data to make the data more representative of a real system. Though known values for the mass, damping, and stiffness coefficients are used in this investigation, these values would not necessarily be known and would need to be estimated. Sample curves generated using test cases for the underdamped, overdamped, and critically damped conditions are shown in Table 15.1.

Table 15.1 Representative generated curves

Underdamped Curves	
Step Response	Dynamic Stiffness
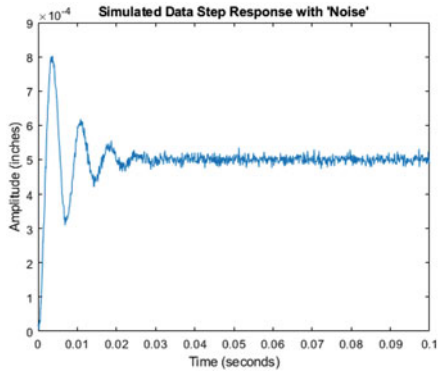	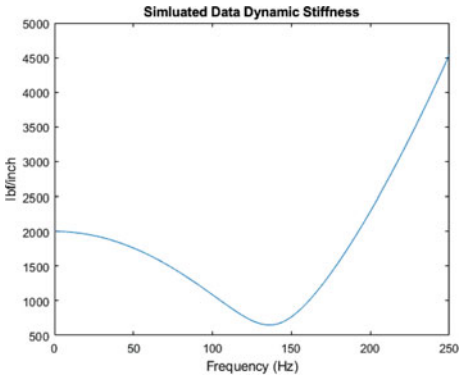
Overdamped Curves	
Step Response	Dynamic Stiffness
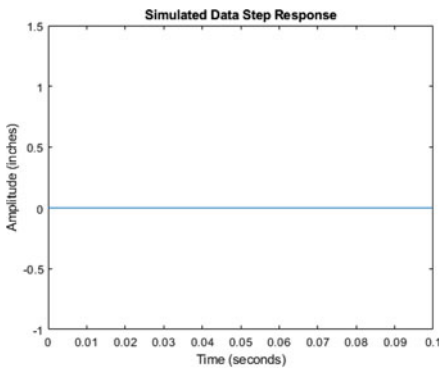	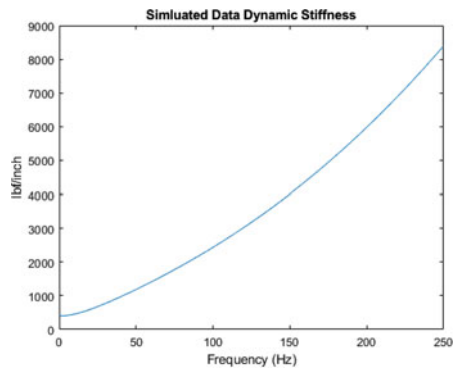
Critically Damped Curves	
Step Response	Dynamic Stiffness
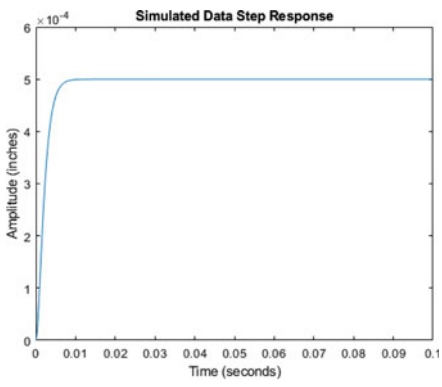	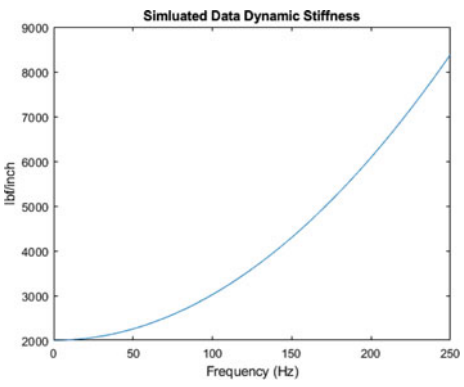

Table 15.2 Test cases for fitting

Test Case	Mass (m)	Damping (c)	Stiffness (k)	Zeta (ζ)
1	0.002588	0.5	1000	0.1554
2	0.002588	0.75	1000	0.2331
3	0.002588	1.25	900	0.4095
4	0.002588	1.75	800	0.6081
5	0.002588	2.25	700	0.8358
6	0.002588	2.75	600	1.103
7	0.002588	3.25	500	1.4285
8	0.002588	3.5	400	1.7110
9	0.002588	3.75	400	1.8428
10	0.002588	4	300	2.2698

Table 15.3 Curve fit percent error results

	Underdamped results		Overdamped results		Critically damped results	
	Dynamic stiffness % error	Step response % error	Transfer function % error	Step response % error	Transfer function % error	Step response % error
Mass avg.	6.72E−09	8.15E+02	1.03E−08	8.44E+20	9.24E−09	7.27E+17
Max.	2.02E−08	1.39E+04	1.07E−08	2.41E+21	9.24E−09	7.27E+17
Min.	6.66E−11	1.71E+02	6.16E−09	4.43E+17	9.24E−09	7.27E+17
Std. deviation	5.27E−09	2.69E+03	3.97E−09	3.53E+20	9.24E−09	7.27E+17
Damping avg.	1.80E−08	1.67E+03	4.03E−09	6.26E+19	9.24E−09	7.27E+17
Max.	5.94E−08	1.03E+04	6.36E−09	3.32E+20	9.24E−09	7.27E+17
Min.	1.12E−09	4.09E+02	4.54E−09	1.10E+16	9.24E−09	7.27E+17
Std. deviation	1.29E−08	3.00E+03	3.15E−09	4.96E+19	9.24E−09	7.27E+17
Stiffness avg.	2.19E−08	1.62E+01	7.47E−08	3.10E+17	9.24E−09	7.27E+17
Max.	4.92E−08	7.94E+01	7.11E−08	6.43E+17	9.24E−09	7.27E+17
Min.	1.67E−09	1.61E+01	1.63E−08	4.47E+15	9.24E−09	7.27E+17
Std. deviation	1.39E−08	3.17E+01	2.81E−08	1.76E+17	9.24E−09	7.27E+17
ζ—Damping ratio avg.	1.82E−08	9.92E+02	4.07E−08	2.86E+03	9.24E−09	7.27E+17
Max.	5.97E−08	1.96E+03	4.09E−08	3.28E+03	9.24E−09	7.27E+17
Min.	2.60E−09	2.31E+02	1.58E−08	3.87E+03	9.24E−09	7.27E+17
Std. deviation	1.42E−08	4.86E+02	1.54E−08	3.13E+03	9.24E−09	7.27E+17

The generated curves are fit in MATLAB using the *fminsearch* function. This is an error minimization solver with user inputs that searches for the minimum of a given function based on user input variables, in this case m, c, and k. The function iterates until values for the mass, damping, and stiffness coefficients are found that minimize the difference between the overall value of the step response function and the modeled data. The test cases investigated are presented in Table 15.2 and present underdamped and overdamped conditions. To create critically damped test cases Eq. (15.2) was solved to force $\zeta = 1$ for each test case. All test cases were solved for 50 iterations to create a population for review. Seeds for these test cases were generated using the *randn* function and a multiplier to increase the magnitude of the seeds.

The percent error between the target values and the curve fit solution are shown in Table 15.3.

The data shows curve fitting to dynamic stiffness yields good results with extremely low error for m, c, and k. ζ is included for completeness. Curve fitting to the step response yields significantly worse results. This error is unexpected and merits investigation that is beyond the scope of this paper, but a possible source of the error is *fminsearch* converging to a local minimum of the curve.

The effect of inaccurate seeds is also investigated. This was accomplished by establishing a single underdamped test case with (m, c, k) = (0.002588, 0.75, 2000). The seeds were then varied as described in Table 15.4.

The curve fitting percent error and iterations to converge to a solution for these cases are presented in Table 15.5. The performance of the dynamic stiffness curve fits exceeds the performance of the step response curve fits. The solutions found by fitting the dynamic stiffness curve are all effectively zero and there is less sensitivity to the proximity of the seeds to the actual values. There is not a clear trend in the number of iterations needed to converge to a solution and the proximity of the seed to the target value. The solutions found by fitting to the step response curve are small for the test cases using seeds up to three times the average damping and stiffness seed values, but errors are large, and the maximum number of iterations

Table 15.4 Seeds for seed accuracy investigation test cases

Test Case	Mass (m)	Damping (c)	Stiffness (k)	Zeta (ζ)
1 (Seed = Target)	0.002588	0.75	2000	0.1648
2 (Avg. c, k)	0.002588	2.375	660	0.9086
3 (2× Avg. c, k)	0.002588	4.75	1320	1.2850
4 (3× Avg. c, k)	0.002588	14.25	3960	2.2256
5 (5× Avg. c, k)	0.002588	71.25	19,800	4.9767
6 (10× Avg. c, k)	0.002588	712.5	198,000	15.7377
7 (Random)	Random	Random	Random	Random

Table 15.5 Seed variation and associated percent errors in solutions

	Dynamic stiffness % errors				Step response % errors			
	m	c	k	Iterations to solution	m	c	k	Iterations to solution
Target = Seed	7.46E−09	1.85E−08	1.09E−08	159.60	2.34E−01	5.99E−01	5.59E−02	197.28
1× Avg	6.69E−09	1.72E−08	8.18E−09	201.96	2.42E+01	2.45E+01	9.26E−01	250.48
2× Avg	5.91E−09	1.84E−08	9.75E−09	187.90	2.70E−01	7.53E−01	6.02E−02	291.40
3× Avg	3.51E−09	3.26E−08	6.93E−09	175.00	1.40E−01	8.26E−02	4.99E−01	303.00
5× Avg	3.61E−09	1.83E−08	1.25E−08	218.00	0.00E+00	9.40E+03	8.90E+02	9000.00
10× Avg	1.18E−09	1.91E−09	3.60E−10	250.00	0.00E+00	9.49E+04	9.80E+03	9000.00
Random seed	9.93E−09	4.30E−08	2.17E−08	275.00	1.92E−01	2.15E+00	6.65E−02	337.00

is reached without converging to a solution for the five times and 10 times average damping and stiffness seed values. It is noteworthy that even when the seeds are the same as the target values a non-zero percent error is still present for the step response fit.

15.4 Conclusion

The efficacy of a MATLAB curve fitting and error minimization function in identifying a single degree of freedom dynamic system's mass, damping, and stiffness coefficients has been investigated. Curve fitting to the dynamic stiffness curve in the frequency domain yields consistently accurate results and appears to do so independent of the quality of the supplied seeds for mass, damping, and stiffness. Curve fitting to a step response curve did not provide consistent results and appears to be more sensitive to the quality of the initial seeds for mass, damping and stiffness than fitting to the dynamic stiffness curve.

Recommended paths for investigation include refinement of the step response curve fitting process to improve consistency, accuracy, and ability to converge to a solution when provided inaccurate seeds.

Reference

1. Palm III, W.J.: System Dynamics, 3rd edn. McGraw-Hill, New York, NY (2014)

Chapter 16
One Year Monitoring of a Wind Turbine Foundations

Marta Berardengo, Stefano Manzoni, Marcello Vanali, and Francescantonio Lucà

Abstract A wind turbine foundation has been monitored for one year in order to assess the effectiveness of a repair work carried out in 2017. A number of displacement transducers have been installed together with strain gauges and accelerometers to understand the turbine dynamic behavior.

One year of data is now available coupled with the machine working parameters (power, wind intensity/direction). These data have been analyzed in order to identify any possible evolution in the turbine behavior and therefore highlight any deterioration in the foundation behavior (stiffness reduction). This paper describes the data analysis taking into account all environmental effects and the associated bias on the measured data. Results show a stable behavior of the turbine foundations through the whole year proving the effectiveness of the performed repairs.

Keywords Wind turbine · Monitoring · Foundations · Vibration monitoring · Structural health assessment

16.1 Introduction

In the first period of 2017 a series of wind turbines experiencing anomalous oscillations of the supporting structures have been the object of meticulous analysis of their foundations resulting in the evidence of cracks and damages. The plant owner commissioned a study to understand the origin of the damage and in parallel planned a series of restoration works on the damaged machines. Restoration was carried out by injecting some resina into the existing foundations, adding also a number of iron reinforcements. The company running the plant decided to start a long term monitoring campaign on one of the repaired machines in order to assess the effectiveness of the resina injection and to assure that the performed restoration was lasting in time.

The proposed monitoring had to be performed measuring the relative oscillations of the turbine with respect to the foundations. An ad hoc measurement system has been designed and installed, and is now working since more than 12 months acquiring data 24 h a day.

The system and the installed measurement set-up will be described in the next paragraph.

16.2 Measurement Set-Up

In order to fulfill the committer requirements, the system had to measure the relative oscillations between the turbine supporting structure and the foundations, as these are the magnitudes on which the health assessment is done according to the machine manufacturer.

M. Berardengo · M. Vanali (✉)
Dipartimento di Ingegneria e Architettura, Università di Parma, Parma, Italy
e-mail: marcello.vanali@unipr.it

S. Manzoni · F. Lucà
Dipartimento di Meccanica, Politecnico di Milano, Milan, Italy

N. Dervilis (ed.), *Special Topics in Structural Dynamics & Experimental Techniques, Volume 5*, Conference Proceedings of the Society for Experimental Mechanics Series, https://doi.org/10.1007/978-3-030-12243-0_16

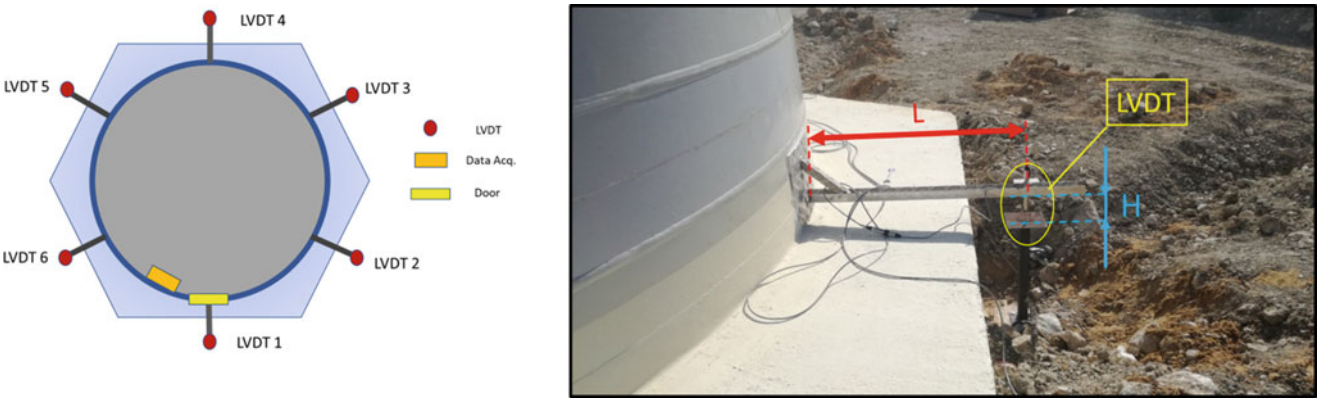

Fig. 16.1 LVDT installation

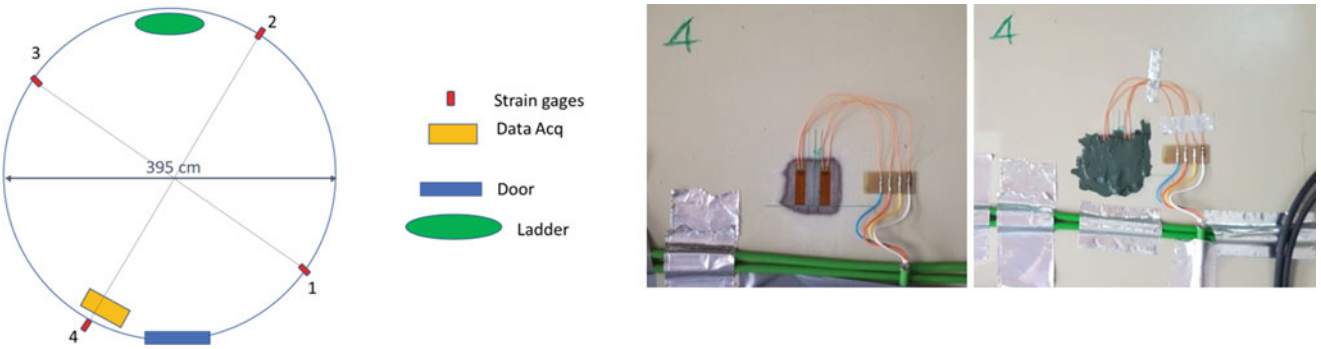

Fig. 16.2 Strain Gages Installation

Fig. 16.3 Data acquisition and accelerometers

As oscillation direction is strictly dependent on the wind direction, 6 LVDT transducers were installed covering all 360° every 60°. In order to measure the oscillation respect to the foundations the transducers were placed at a distance enough to avoid measuring on the first hexagonal concrete collar that is not reinforced and therefore not collaborating with the foundations (Fig. 16.1).

In addition two strain gages bridges were glued directly on the supporting structure configured to measure bending (flexural) moments [1] acting on the steel pipes (Fig. 16.2).

By placing two half bridges on perpendicular axis it is possible to compute the modulus and the direction of the bending moment acting on the structure [1]. The set-up was completed installing 2 accelerometers on the supporting pipes in order to monitor both vibration levels and possibly natural frequency evolution [2] (Fig. 16.3).

The system is working and acquires data 24 h per day. Every month file containing the turbine production/condition every 10 min is provided by the plant keeper in order to correlate the measured oscillation with the turbine working parameters.

16.3 Data-Analysis

At first a check was made to ensure that all data were acquired correctly and that measured magnitudes were consistent. As an example you may see in Fig. 16.4 the correlation between bending moment and wind speed.

Then, particular care had to be taken to identify and remove thermal effects that are in the same order of magnitude of the displacements due to changes in working conditions (Generated Power), Fig. 16.5.

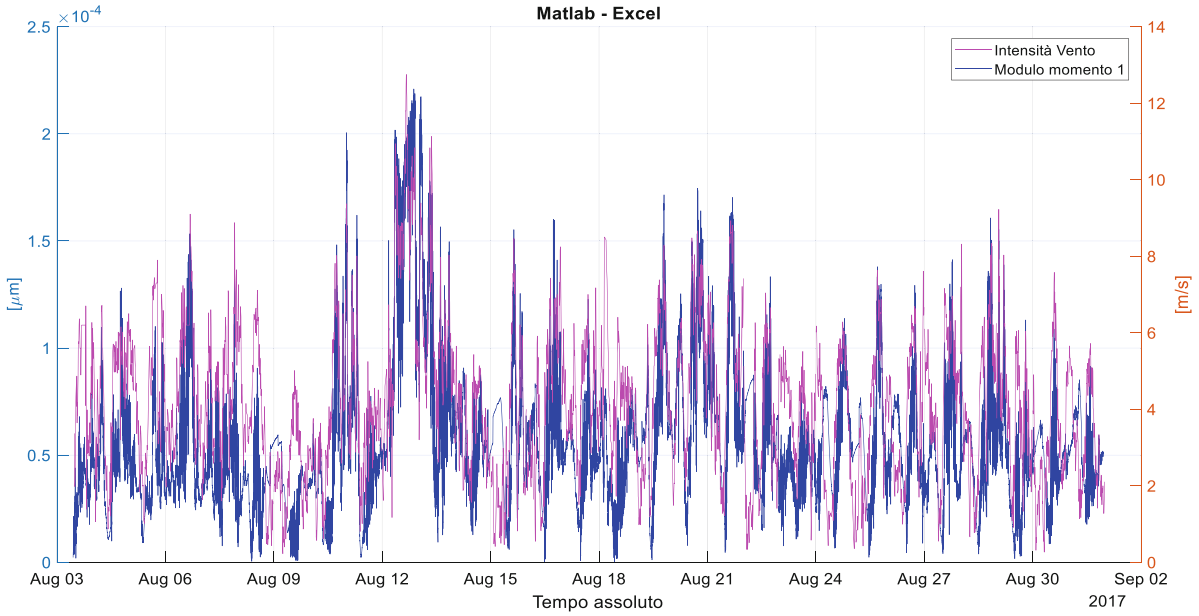

Fig. 16.4 Correlation between measured bending stress (blue line) and wind speed (pink line)

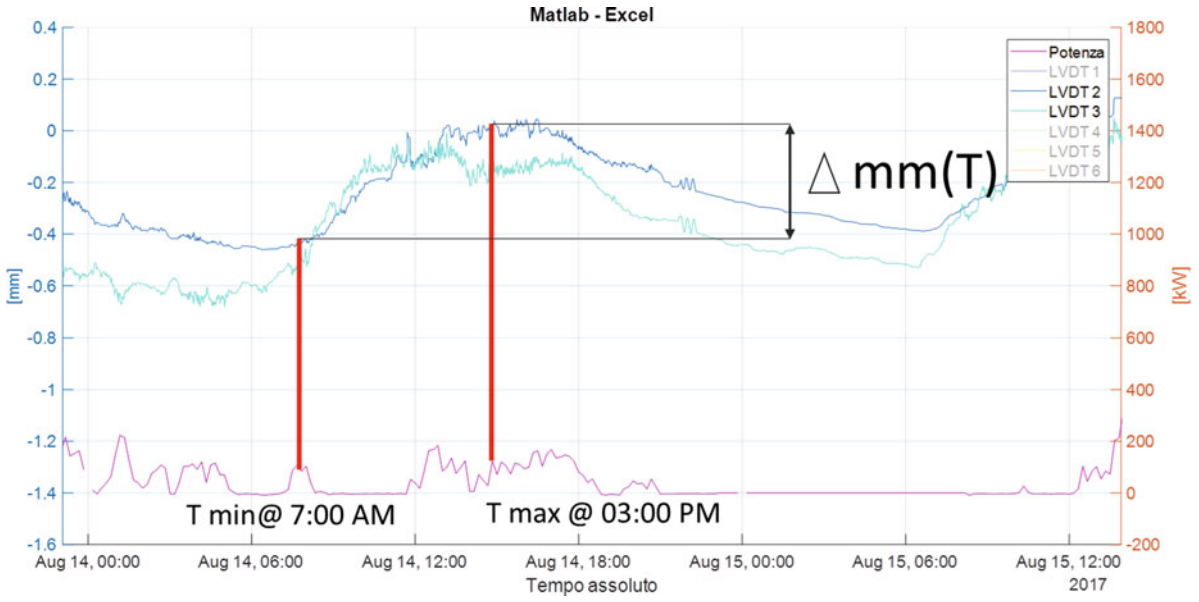

Fig. 16.5 Thermal dilatation and its effects on two LVDT signals

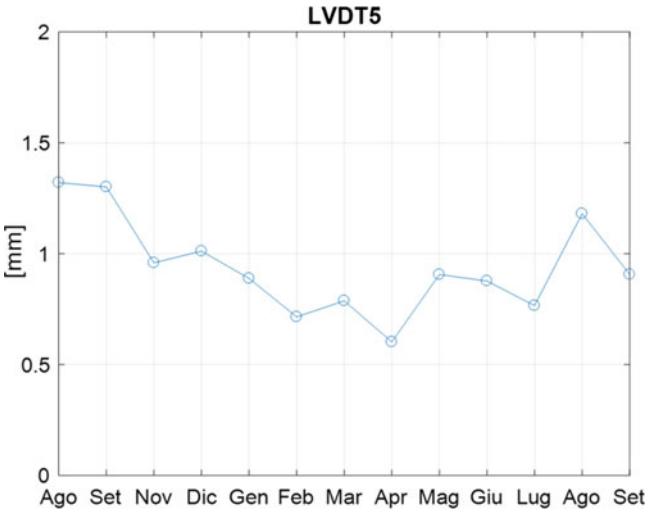

Fig. 16.6 Average Displacements per month, due to production power shifts during one year for LVDT 5

Once the thermal effects have been accounted for, an analysis has been carried out considering the turbine movements due to changes in the electrical power produced.

As can be seen in Fig. 16.6 these changes, averaged per month, do not show any growing trend certifying that the foundations behavior remained constant during the year monitored.

16.4 Conclusion

A permanent monitoring system to assess the turbine foundation behavior has been designed and installed on a plant in the south of Italy. The system is capable to identify the movements between the turbine supporting structure and the foundations during the machine normal operation. A data analysis procedure has been developed and the results show a stable behavior of the machine foundations through the year monitored.

References

1. Doebelin, E.O.: Measurement Systems: Application and Design, 5th edn. McGraw-Hill College, New York (2003). ISBN-10: 007292201X
2. Brandt, A.: Noise and Vibration Analysis: Signal Analysis and Experimental Procedures. Wiley, Hoboken (2011)

Chapter 17
On the Application of Domain Adaptation in SHM

X. Liu and K. Worden

Abstract Machine learning has been widely and successfully used in many Structural Health Monitoring (SHM) applications. However, many machine learning models can only make accurate predictions when the training and test data are measured from the same system; this is because most traditional machine learning methods assume that all the data are drawn from the same distribution. Therefore, to train a robust predictor, it is often required to recollect and label new training data every time when considering a new structure, which can be significantly expensive, and sometimes impossible in the SHM context. In such cases, the idea of transfer learning may be employed, which aims to transfer knowledge between task domains to improve learners. In this paper, a subfield of transfer learning i.e. domain adaptation, is considered, and its utility in SHM applications is briefly investigated.

Keywords Domain adaptation · Transfer learning · Structural health monitoring (SHM)

17.1 Introduction

Machine learning technologies have already achieved significant success in many Structural Health Monitoring (SHM) applications, e.g. [1–5]. Most of these machine learning methods can perform well if the training and test data are drawn from the same distribution, i.e. all the data are measured from the same structure. However, in real-world applications, there are some cases where the training and the test distributions differ, often because damage state data are only available in one case. For example, in the case of a wind farm, suppose there is a sufficient amount of labelled feature data for a specific wind turbine about its normal and damage states (called the *source domain* data) and a large number of unlabelled data of another wind turbine of the same model (called the *target domain* data). As there is a lack of labelled data for the target structure, and supervised learning is thus impossible, one may wish to train a model using the source domain data. However, due to the existence of the inevitable manufacturing and assembling errors for each individual, the data distributions of the two wind turbines may be different, and then the predictions of models trained using traditional machine learning methods can be significantly degraded. The direct solution is to collect and label new training data and rebuild models for each individual, which is expensive or sometimes impossible to implement. In such cases, it is desirable that the knowledge learnt from the related labelled source domain data can be transferred to the target domain.

It will be clear that the context for the discussion here is *population-based* SHM [6], i.e. it is concerned with allowing inferences across populations of structures (even if the number in the population is only two). Furthermore, this paper is concerned with supervised learning; so the required diagnostics are at the higher levels in Rytter's hierarchy [1] and thus directed at inferring damage location, type or severity.

Transfer learning is a research subfield of machine learning which aims to improve a learner from one domain by transferring knowledge from a related domain [7]. *Domain adaption* is one of the branches of transfer learning. The focus of domain adaptation is that the distribution across the source and target domain are different, which matches the issue of the aforementioned damage diagnosis situation, and indicates why the technique is potentially relevant for SHM.

According to [8], the source and target domains of a transfer learning problem can be different in the input feature spaces ($\mathcal{X}_s \neq \mathcal{X}_t$), the label spaces ($\mathcal{Y}_s \neq \mathcal{Y}_t$), the marginal probability distributions of the input data ($P(\mathbf{X}_s) \neq P(\mathbf{X}_t)$) or conditional distributions ($P(\mathbf{Y}_s|\mathbf{X}_s) \neq P(\mathbf{Y}_t|\mathbf{X}_t)$).

X. Liu · K. Worden (✉)
Dynamics Research Group, Department of Mechanical Engineering, University of Sheffield, Sheffield, UK
e-mail: k.worden@sheffield.ac.uk

N. Dervilis (ed.), *Special Topics in Structural Dynamics & Experimental Techniques, Volume 5*, Conference Proceedings of the Society for Experimental Mechanics Series, https://doi.org/10.1007/978-3-030-12243-0_17

Domain adaptation problems can be classified based on the availability of labelled target domain data or the number of source domains available. In this paper, only the unsupervised—i.e. no labelled target domain data—single-source domain adaptation is considered. To the best of the authors' knowledge, this is the first work to investigate the utility of domain adaptation techniques into SHM applications; the main aim of this paper is therefore to provide a general introduction about domain adaptation to readers with expertise in SHM but no familiarity with transfer learning.

It is useful to note that there are similarities between transfer learning and *semi-supervised* and *active* learning, which have also been recently applied in SHM [9], as both techniques make use out of limited labelled data. In the semi-supervised (and to a lesser extent, the active learning) context, one is usually faced with a body of feature data, where only a small subset has labels assigned. Furthermore, it is assumed that any further labelling is expensive. An important technique in active learning and semi-supervised learning is *self-labelling* or *label propagation*, whereby one attempts to learn labels for the unlabelled data from the assignments in the labelled set. If one were to designate the labelled data as one source and task, and the unlabelled data as a second source and task, then the problem is recast as a transfer learning problem. Furthermore, one would have conditions $\mathcal{X}_s = \mathcal{X}_t$ and $P(\mathbf{X}_s) = P(\mathbf{X}_t)$ to work with.

The layout of the paper is as follows: firstly, the definition of domain adaptation is given in Sect. 17.2, alongside a brief discussion about the general strategy. In Sect. 17.3, the three specific domain adaptation techniques considered in this paper are introduced. Next, an artificial damage diagnosis problem based on cantilever beams is simulated to investigate the utility of these example domain adaptation techniques in an SHM scenario. Finally, some conclusions are drawn.

17.2 Domain Adaptation

In transfer learning, there are two essential definitions: 'domain' and 'task' [7].

A domain is defined as $\mathcal{D} = \{\mathcal{X}, P(\mathbf{X})\}$, which consists of two components: a feature space $\mathcal{X}$ and a marginal probability distribution, where a particular learning sample $\mathbf{X} = \{\mathbf{x}_1, \cdots, \mathbf{x}_n\} \in \mathcal{X}$ is specified.

Given a specific domain $\mathcal{D}$, a task is defined as $\mathcal{T} = \{\mathcal{Y}, f(\cdot)\}$, consisting of a label space $\mathcal{Y}$ and an objective predictive function $f(\cdot)$ learned from the training data, i.e. feature vector and label pairs $\{\mathbf{x}_i, y_i\}$, where $f(\cdot)$ could also be seen as a conditional distribution $P(y|\mathbf{x})$ with $y \in \mathcal{Y}$.

Using these two definitions, transfer learning for the case of one source domain and one target domain can be formally defined as:

Definition 17.1 (Transfer Learning) Given a source domain $\mathcal{D}_s$ with a corresponding source task $\mathcal{T}_s$ and a target domain $\mathcal{D}_t$ with a corresponding target task $\mathcal{T}_t$, transfer learning is the process of helping improve the target predictive function $f_t(\cdot)$ in $\mathcal{T}_t$ by using the knowledge learnt from $\mathcal{D}_s$ and $\mathcal{T}_s$, where $\mathcal{D}_s \neq \mathcal{D}_t$ and/or $\mathcal{T}_s \neq \mathcal{T}_t$.

As there exist two essential components in the forms of the domain and task respectively, transfer learning can be further classified based on the consistency of $\mathcal{X}$, $P(\mathbf{X})$, $\mathcal{Y}$ and $P(\mathbf{Y}|\mathbf{X})$ between the source and target learning problem. Domain adaptation is one of the subfields whose formal definition is given as:

Definition 17.2 (Domain Adaptation) Given a source domain $\mathcal{D}_s$ with a corresponding source task $\mathcal{T}_s$ and a target domain $\mathcal{D}_t$ with a corresponding target task $\mathcal{T}_t$, domain adaptation aims to improve the learning of the target predictive function $f_t(\cdot)$ in $\mathcal{T}_t$ by using the knowledge learnt from $\mathcal{D}_s$ and $\mathcal{T}_s$, where $\mathcal{X}_s = \mathcal{X}_t$, $\mathcal{Y}_s = \mathcal{Y}_t$, but $P(\mathbf{X}_s) \neq P(\mathbf{X}_t)$ and $P_s(\mathbf{Y}_s|\mathbf{X}_s) \neq P_t(\mathbf{Y}_t|\mathbf{X}_t)$.

As defined, domain adaption is mainly applicable to the SHM of *homogeneous* populations, i.e. populations of nominally identical structures. In those circumstances, the feature spaces will match naturally, and the tasks will match in the sense that location, type and severity labels will make sense for each individual in the population.

From the definition of domain adaptation, it will be clear that any performance deterioration of the classifier learnt from the source labelled data applied to the target data will mainly be because of the distribution differences. Therefore, an intuitive solution may simply be reducing the differences. To do this, a criterion to quantify the differences between domains is required. In the transfer learning field, *Kullback-Leibler divergence* [10], *Jensen-Shannon divergence* [11], *Hellinger distance* [12] and *Maximum Mean Discrepancy* (MMD) [13] are widely used as the transferring criterion for measuring the distance between distributions. Once the criterion is specified, the distribution adaptation can be performed. In the next section, the mechanisms of three specific techniques will be introduced to demonstrate how to realise the domain adaptation.

17.3 Three Examples of Domain Adaptation Techniques

Before introducing the domain adaptation techniques, it is worth beginning with the definitions and terminology; Table 17.1 summaries the frequently-used notation and terms.

17.3.1 Transfer Component Analysis (TCA)

TCA was introduced in [14]. The main idea of this method is based on the assumption that there exists a nonlinear transformation from the domain feature space into a *Reproducing Kernel Hilbert Space* (RKHS), i.e. $\phi : \mathcal{X} \rightarrow \mathcal{H}$, which makes $P(\phi(\mathbf{X}_s)) \approx P(\phi(\mathbf{X}_t))$ where $P(\mathbf{Y}_s|\phi(\mathbf{X}_s)) = P(\mathbf{Y}_t|\phi(\mathbf{X}_t))$. Therefore, the target distance between domains may be expressed as,

$$\text{Dist}(\mathcal{D}_s, \mathcal{D}_t) \approx \text{Dist}(P(\mathbf{X}_s), P(\mathbf{X}_t)) \tag{17.1}$$

TCA uses the maximum mean discrepancy (MMD) as the distance criteria, computed as,

$$\text{Dist}(P(\tilde{\mathbf{X}}_s), P(\tilde{\mathbf{X}}_t)) = \left\| \frac{1}{n_s} \sum_{i=1}^{n_s} \phi(\mathbf{x}_{s,i}) - \frac{1}{n_t} \sum_{j=1}^{n_t} \phi(\mathbf{x}_{t,j}) \right\|_{\mathcal{H}}^2 \tag{17.2}$$

where $\tilde{\mathbf{X}}$ represents the transformed feature matrix.

Using the 'kernel trick', $k(\mathbf{x}_i, \mathbf{x}_j) = \phi(\mathbf{x}_i)^\intercal \phi(\mathbf{x}_j)$, Eq. (17.1) may be written as,

$$\text{Dist}_K(P(\mathbf{X}_s), P(\mathbf{X}_t)) = \text{tr}(\mathbf{KM}), \tag{17.3}$$

where $\text{tr}(\cdot)$ denotes the trace of a matrix, $\mathbf{K} = \phi(\mathbf{X})^\intercal \phi(\mathbf{X}) \in \mathbb{R}^{(n_s+n_t)\times(n_s+n_t)}$ is the kernel matrix defined on the combined input feature space, $\mathbf{X} = \mathbf{X}_s \cup \mathbf{X}_t \in \mathbb{R}^{(n_s+n_t)\times m}$, m is the number of features, and $\mathbf{M} \in \mathbb{R}^{(n_s+n_t)\times(n_s+n_t)}$ is the *MMD* matrix, defined by,

$$M_{ij} = \begin{cases} \dfrac{1}{n_s^2}, & x_i, x_j \in X_s \\ \dfrac{1}{n_t^2}, & x_i, x_j \in X_t \\ \dfrac{-1}{n_s n_t}, & \text{otherwise} \end{cases} \tag{17.4}$$

Instead of learning the kernel $k(\cdot, \cdot)$, the problem can be solved via considering the kernel matrix $\mathbf{K}$. In [15], a semi-definite programming (SDP) approach is formulated to directly learn the kernel matrix. However, there are several issues with doing this, e.g. the SDP solution is very computationally expensive. For this reason, TCA utilises an explicit low-rank representation of the kernel matrix, i.e.

Table 17.1 Summary of notation and descriptions of terms

Notation	Description	Notation	Description
$\mathcal{X}$	Input feature space	n	Number of input feature instances
$\mathcal{Y}$	Label space	$P(\mathbf{X})$	Marginal distribution
$\mathcal{D}$	Domain	$P(\mathbf{Y})$	Label distribution
$\mathcal{T}$	Predictive learning task	$P(\mathbf{Y}\|\mathbf{X})$	Conditional distribution
Subscript s	Denotes source	$P(\mathbf{X}\|\mathbf{Y})$	Class-conditional distribution
Subscript t	Denotes target	$\phi(\cdot)$	Mapping function
$\mathbf{x}$	Input feature vector	$f(\cdot)$	Objective predictive function
$\mathbf{X}$	Input feature matrix	$\text{Dist}(\cdot, \cdot)$	Distance in distributions

$$\tilde{\mathbf{K}} = \mathbf{K}\mathbf{V}\mathbf{V}^{\intercal}\mathbf{K} \tag{17.5}$$

where $\mathbf{V} \in \mathbb{R}^{(n_s+n_t)\times k}$ is a reduction transformation matrix where $k \ll (n_s + n_t)$. Using the definition of $\tilde{\mathbf{K}}$, the distance between domains becomes,

$$\begin{aligned} \text{Dist}_K(P(\mathbf{X}_s), P(\mathbf{X}_t)) &= \text{tr}((\mathbf{K}\mathbf{V}\mathbf{V}^{\intercal}\mathbf{K})\mathbf{M}) \\ &= \text{tr}(\mathbf{V}^{\intercal}\mathbf{K}\mathbf{M}\mathbf{K}\mathbf{V}) \end{aligned} \tag{17.6}$$

on using the cyclic property of the trace. Now the problem becomes one of finding $\mathbf{V}$ from,

$$\min_{\mathbf{V}^{\intercal}\mathbf{K}\mathbf{H}\mathbf{K}\mathbf{V}=\mathbf{I}} \quad \text{tr}(\mathbf{V}^{\intercal}\mathbf{K}\mathbf{M}\mathbf{K}\mathbf{V}) + \mu\ \text{tr}(\mathbf{V}^{\intercal}\mathbf{V}) \tag{17.7}$$

where $\mu > 0$ is a tradeoff parameter to control the complexity of $\mathbf{V}$, $\mathbf{I}$ is the identity matrix, $\mathbf{H} = \mathbf{I} - \frac{1}{n_s+n_t}\mathbf{1} \in \mathbb{R}^{(n_s+n_t)\times(n_s+n_t)}$, and $\mathbf{1}$ is the matrix of ones. Equation (17.7) can then be reformulated as,

$$\max_{\mathbf{V}} \quad \text{tr}\left((\mathbf{V}^{\intercal}(\mathbf{K}\mathbf{M}\mathbf{K} + \mu\mathbf{I})\mathbf{V})^{-1}\mathbf{V}^{\intercal}\mathbf{K}\mathbf{H}\mathbf{K}\mathbf{V}\right) \tag{17.8}$$

whose solution is provided by the k leading eigenvectors of $(\mathbf{K}\mathbf{M}\mathbf{K} + \mu\mathbf{I})^{-1}\mathbf{K}\mathbf{H}\mathbf{K}$.

Once the adaptation matrix $\mathbf{V}$ is obtained, the new k-dimensional combined feature representation can be computed, i.e. $\mathbf{Z} = \mathbf{K}\mathbf{V} \in \mathbb{R}^{(n_s+n_t)\times k}$. Then a standard supervised learning algorithm, e.g. SVM, can be trained on the labelled transformed source domain data, and reused on the target domain data.

17.3.2 Joint Domain Adaptation (JDA)

It is noteworthy that TCA only reduces the differences in the marginal distribution but not those of the conditional distribution which is assumed to be identical for the source and target domains in the new representation space. However, this assumption does not always hold. As a result, the authors of [16] have proposed the JDA framework, with the ability to reduce the differences in both distributions simultaneously. The target distance of JDA may be described as,

$$\text{Dist}(\mathcal{D}_s, \mathcal{D}_t) \approx \text{Dist}(P(\mathbf{X}_s), P(\mathbf{X}_t)) + \text{Dist}(P(\mathbf{Y}_s|\mathbf{X}_s), P(\mathbf{Y}_s|\mathbf{X}_t)) \tag{17.9}$$

Similarly to TCA, the JDA framework also assumes that in a transformed feature space, the domain distance can be significantly reduced. In [16], the authors chose dimensionality reduction methods to learn the transformed feature representation and MMD to measure the differences in distributions, thus

$$\begin{aligned} \text{Dist}(P(\tilde{\mathbf{X}}_s), P(\tilde{\mathbf{X}}_t)) &= \left\| \frac{1}{n_s}\sum_{i=1}^{n_s} \mathbf{A}^{\intercal}\mathbf{x}_{s,i} - \frac{1}{n_t}\sum_{j=1}^{n_t} \mathbf{A}^{\intercal}\mathbf{x}_{t,j} \right\|^2 \\ &= \text{tr}(\mathbf{A}^{\intercal}\mathbf{X}\mathbf{M}_0\mathbf{X}^{\intercal}\mathbf{A}) \end{aligned} \tag{17.10}$$

where $\mathbf{A} \in \mathbb{R}^{m\times k}$ is an orthogonal transformation matrix derived from PCA (Principal Component Analysis), and $\mathbf{M}_0$ is the MMD matrix computed as in Eq. (17.4).

As for the conditional distribution; because the target domain data is unlabelled, $P(y_t|\mathbf{x}_t)$ cannot be directly modelled. In JDA, the pseudo labels of the target domain data, predicted from some base classifiers trained on the labelled source data, are used. Furthermore, instead of matching $P(y_s|\mathbf{x}_s)$ and $P(y_t|\mathbf{x}_t)$, the class-conditional distributions $P(\mathbf{x}_s|y_s)$ and $P(\mathbf{x}_t|y_t)$ are matched via,

$$\begin{aligned}\text{Dist}(P(\mathbf{Y}_s|\tilde{\mathbf{X}}_s),\, P(\mathbf{Y}_s|\tilde{\mathbf{X}}_t)) &\approx \sum_{c=1}^{C}\left\| \frac{1}{n_s^{(c)}} \sum_{\mathbf{x}_i \in \mathcal{D}_s^{(c)}} \mathbf{A}^\intercal \mathbf{x}_i - \frac{1}{n_t^{(c)}} \sum_{\mathbf{x}_j \in \mathcal{D}_t^{(c)}} \mathbf{A}^\intercal \mathbf{x}_j \right\|^2 \\ &= \sum_{c=1}^{C} \text{tr}(\mathbf{A}^\intercal \mathbf{X} \mathbf{M}_c \mathbf{X}^\intercal \mathbf{A})\end{aligned} \tag{17.11}$$

where $\mathcal{D}_s^{(c)} = \{\mathbf{x}_i : \mathbf{x}_i \in \mathcal{D}_s \wedge y(\mathbf{x}_i) = c\}$ is the set of instances belonging to class c in the source data, $y(\mathbf{x}_i)$ is the true label of $\mathbf{x}_i$, and $n_s^{(c)} = |\mathcal{D}_s^{(c)}|$. Correspondingly, $\mathcal{D}_t^{(c)} = \left\{\mathbf{x}_i : \mathbf{x}_i \in \mathcal{D}_t \wedge \hat{y}(\mathbf{x}_i) = c\right\}$ is the set of the instances belonging to class c in the target data, $\hat{y}(\mathbf{x}_j)$ is the pseudo-predicted label of $\mathbf{x}_j$, and $n_t^{(c)} = |\mathcal{D}_t^{(c)}|$. Thus the MMD matrices $\mathbf{M}_c$ involving class labels are computed as follows,

$$(M_c)_{ij} = \begin{cases} \dfrac{1}{n_s^{(c)} n_s^{(c)}}, & \mathbf{x}_i, \mathbf{x}_j \in \mathcal{D}_s^{(c)} \\ \dfrac{1}{n_t^{(c)} n_t^{(c)}}, & \mathbf{x}_i, \mathbf{x}_j \in \mathcal{D}_t^{(c)} \\ \dfrac{-1}{n_s^{(c)} n_t^{(c)}}, & \begin{cases} \mathbf{x}_i \in \mathcal{D}_s^{(c)}, \mathbf{x}_j \in \mathcal{D}_t^{(c)} \\ \mathbf{x}_i \in \mathcal{D}_t^{(c)}, \mathbf{x}_j \in \mathcal{D}_s^{(c)}, \end{cases} \\ 0 & \text{otherwise} \end{cases} \tag{17.12}$$

Minimising Eqs. (17.10) and (17.11) results in the objective function of JDA, written as,

$$\min_{\mathbf{A}^\intercal \mathbf{X} \mathbf{H} \mathbf{X}^\intercal \mathbf{A} = \mathbf{I}} \sum_{c=0}^{C} \text{tr}(\mathbf{A}^\intercal \mathbf{X} \mathbf{M}_c \mathbf{X}^\intercal \mathbf{A}) + \mu \|\mathbf{A}\|^2 \tag{17.13}$$

where μ is the trade-off parameter. The optimal adaptation matrix $\mathbf{A}$ is the k leading eigenvectors of,

$$\left(\mathbf{X} \sum_{c=0}^{C} \mathbf{M}_c \mathbf{X}^\intercal + \mu \mathbf{I}\right)^{-1} \mathbf{X} \mathbf{H} \mathbf{X}^\intercal \tag{17.14}$$

Then, $\mathbf{Z} = \mathbf{X}\mathbf{A} \in \mathbb{R}^{(n_s+n_t)\times k}$ is the new feature representation for learning the objective function $f(\cdot)$. It is worth noting that the idea of kernel mapping can also be applied to the JDA framework. For example, using the kernel matrix, Eq. (17.13) becomes,

$$\min_{\mathbf{A}^\intercal \mathbf{K} \mathbf{H} \mathbf{K}^\intercal \mathbf{A} = \mathbf{I}} \sum_{c=0}^{C} \text{tr}(\mathbf{A}^\intercal \mathbf{K} \mathbf{M}_c \mathbf{K}^\intercal \mathbf{A}) + \mu \|\mathbf{A}\|^2 \tag{17.15}$$

and the new feature representation becomes $\mathbf{Z} = \mathbf{K}\mathbf{A}$. Also, note that the implement of JDA usually involves an iterative pseudo-label refinement procedure for obtaining a more accurate prediction.

17.3.3 Adaptation Regularisation-Based Transfer Learning (ARTL)

Although the JDA framework can minimise the differences in both marginal and conditional distributions between domains, the result could be unsatisfactory for some scenarios. This issue is because the discriminative directions of the source and target domains may still be different. Considering this issue, the authors of [17], have proposed the ARTL framework, which can not only adapt the distribution differences but also match the discriminative directions (aka *manifold regularisation*)

between domains. Compared with JDA and TCA, another improvement of ARTL is that the classifier is trained with the distribution adaptation and manifold regularisation simultaneously, which can boost the final classification performance.

The overall objective prediction function of the ARTL framework is formulated as,

$$f = \arg\min_{f \in \mathcal{H}} \sum_{i=1}^{n_s} \ell(f(\mathbf{x}_{s,i}), y_{s,i}) + \mu \|f\|_K^2 + \lambda \text{Dist}_{f,K}(\mathcal{D}_s, \mathcal{D}_t) + \gamma \text{MR}_{f,K}(P_s, P_t) \tag{17.16}$$

where $f = \mathbf{w}^\intercal \phi(\mathbf{x})$ is the prediction function, $\mathbf{w}$ is the vector of classifier parameters and μ, λ, γ are positive regularisation parameters.

The first two terms in Eq. (17.16), i.e.

$$f = \arg\min_{f \in \mathcal{H}} \sum_{i=1}^{n} \ell(f(\mathbf{x}_{s,i}), y_{s,i}) + \mu \|f\|_K^2 \tag{17.17}$$

are for minimising the structural risk functional on the labelled source domain, where $\ell(\cdot, \cdot)$ is the loss function. The third term in Eq. (17.16) is for the joint distribution adaptation,

$$\text{Dist}_{f,K}(\mathcal{D}_s, \mathcal{D}_t) = \text{Dist}_{f,K}(P(\mathbf{X}_s), P(\mathbf{X}_t)) + \sum_{c=1}^{C} \text{Dist}_{f,K}^{(c)}(P(\mathbf{Y}_s|\mathbf{X}_s), P(\mathbf{Y}_t|\mathbf{X}_t)) \tag{17.18}$$

where,

$$\text{Dist}_{f,K}(P(\mathbf{X}_s), P(\mathbf{X}_t)) = \left\| \frac{1}{n_s} \sum_{i=1}^{n_s} f(\mathbf{x}_{s,i}) - \frac{1}{n_t} \sum_{j=1}^{n_t} f(\mathbf{x}_{t,j}) \right\|_{\mathcal{H}}^2 \tag{17.19}$$

and,

$$\text{Dist}_{f,K}(P(\mathbf{Y}_s|\mathbf{X}_s), P(\mathbf{Y}_t|\mathbf{X}_t)) = \left\| \frac{1}{n_s^{(c)}} \sum_{\mathbf{x}_i \in \mathcal{D}_s^{(c)}} f(\mathbf{x}_i) - \frac{1}{n_t^{(c)}} \sum_{\mathbf{x}_j \in \mathcal{D}_t^{(c)}} f(\mathbf{x}_j) \right\|_{\mathcal{H}}^2 \tag{17.20}$$

Note that Eqs. (17.19) and (17.20) are the classifier versions of Eqs. (17.10) and (17.11), denoting the MMD on the marginal distribution and the conditional distribution between domains respectively. The last term in the objective function is for manifold regularisation, computed as,

$$\begin{aligned} M_{f,K}(P_s, P_t) &= \sum_{i,j=1}^{n_s+n_t} (f(x_i) - f(x_j))^2 W_{ij} \\ &= \sum_{i,j=1}^{n_s+n_t} f(x_i) L_{ij} f(x_j) \end{aligned} \tag{17.21}$$

where $\mathbf{W} \in \mathbb{R}^{(n_s+n_t)\times(n_s+n_t)}$ is the *graph affinity matrix*, defined as,

$$W_{ij} = \begin{cases} \cos(\mathbf{x}_i, \mathbf{x}_j), & \text{if } \mathbf{x}_i \in \mathcal{N}_p(\mathbf{x}_j) \vee \mathbf{x}_j \in \mathcal{N}_p(\mathbf{x}_i) \\ 0, & \text{otherwise} \end{cases} \tag{17.22}$$

$\mathcal{N}_p(\mathbf{x}_i)$ is the set of p-nearest neighbours of point $\mathbf{x}_i$, $\mathbf{L} \in \mathbb{R}^{(n_s+n_t)\times(n_s+n_t)}$ is the normalised *graph Laplacian matrix*, computed as,

$$\mathbf{L} = \mathbf{I} - \mathbf{D}^{-1/2} \mathbf{W} \mathbf{D}^{-1/2}, \tag{17.23}$$

where $\mathbf{D} \in \mathbb{R}^{(n_s+n_t)\times(n_s+n_t)}$ is a diagonal matrix with each item $D_{ii} = \sum_{j=1}^{n_s+n_t} W_{ij}$. The manifold regularisation applied here is based on the manifold assumption that the conditional distribution of two geometrically close points should be similar [18].

Now, traditional machine learning algorithms can be extended based on the ARTL framework via substituting a specific loss function ℓ into Eq. (17.16) to learn an adaptive prediction function $f(\cdot)$. The authors of [17] proposed two applications of this framework to RLS (Regularised Least Squares) and SVMs (Support Vector Machines). In this paper, the AR-SVM is employed for the following example application.

17.4 Application: A Cantilever Beam Problem

This section considers the application of the domain adaptation techniques in a highly-idealised SHM scenario; Fig. 17.1 shows a schematic of the class of cantilever beams considered.

Each of two beams will be subject to a static mechanical load, F, on their free ends. Furthermore, a time-varying thermal load with different temperatures on the beam top and bottom surfaces is applied, described by,

$$\begin{aligned} T_t &= 10 \times \left[\sin(12\pi t) + \sin(4\pi t) + 3t \times 10^{-3}\right] \\ T_b &= 8 \times \left[\sin(12\pi t - 0.5\pi) + \sin(4\pi t) + 3t \times 10^{-3} - 2\right] \end{aligned} \tag{17.24}$$

It is assumed that measurements of the angle of rotation of the beam are made; these will consists of two parts: mechanical and thermal rotations, defined by,

$$\begin{aligned} \theta_T &= \frac{\alpha(T_s - T_t)x}{d} \\ \theta_M &= \frac{F(-lx + 0.5x^2)}{EI} \\ \theta &= \theta_T + \theta_M \end{aligned} \tag{17.25}$$

where θ_T, θ_M and θ are the thermal, mechanical and total rotations respectively, α is the thermal expansion coefficient, and x is the distance of the point on the beam from the fixed-end, $I = \frac{1}{12}bh^3$ is the moment of inertia and l, b and h are the beam length, width and height respectively. For the purposes of this illustration, the Young's modulus of each beam is assumed to be linearly correlated with the temperature, so that,

$$E = E_0 + \lambda T \tag{17.26}$$

where $T = (T_t + T_s)/2$ is the mean temperature between the top and bottom surfaces and E_0 is the Young's Modulus of the beam at 0 °C and λ is an expansion coefficient.

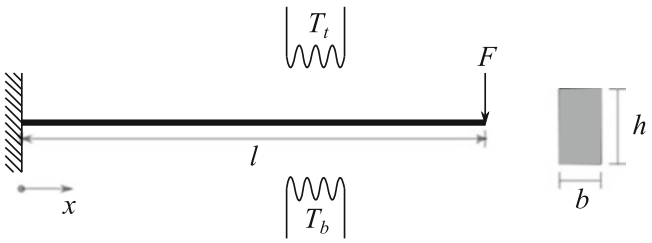

Fig. 17.1 A schematic of a cantilever beam subjected to a load at the tip

17.4.1 Data Acquisition

To simulate an experimental situation, an amplitude-dependent Gaussian noise is added to the theoretical results of rotation angles, i.e.

$$\hat{\theta} = \theta + \theta \times \varepsilon \tag{17.27}$$

where $\hat{\theta}$ is the measured rotation angle and ε is Gaussian noise with $\varepsilon \sim N(0, 1)$.

Two specific beams are considered here, with their properties summarised in Table 17.2. For each beam, 10,000 time points were simulated using Eq. (17.25) for four positions: $x_1 = 0.25l$, $x_2 = 0.5l$, $x_3 = 0.75l$ and $x_4 = l$, in every individual simulation, and 500 pairs of independent simulations were conducted in total. The damage is simulated by a reduction of the stiffness (Young's modulus) of the beam after data point 5000. Figure 17.2 shows a representation of the simulated data, from which, the point of introduction of the damage cannot be distinguished as the temperature and noise variations are dominant.

The rotation angle data from all four positions on both beams, for both normal and damage states, are then used to formulate a linear regression model relating their values to the instantaneous average temperature,

$$\hat{\theta}_i = \alpha_i T + \beta_i, \tag{17.28}$$

to obtain a pair of parameter estimates α_i and β_i for the normal and damaged conditions. The regression parameters are used as the input features to learn the classifiers; because there are four locations, the feature vector is eight-dimensional. The problem formulated here is a little unusual; the dynamics of the beam are generated by time-varying temperature, rather than by direct dynamic forcing; also, the features are rather non-standard. However, as a data-based SHM problem, the situation presents the usual difficulties.

Table 17.2 The properties of the beams considered

Beam	Length l	Height h	Width b	E_N/E_D
1	10	1	0.5	200/150
2	9	0.9	0.55	200/180

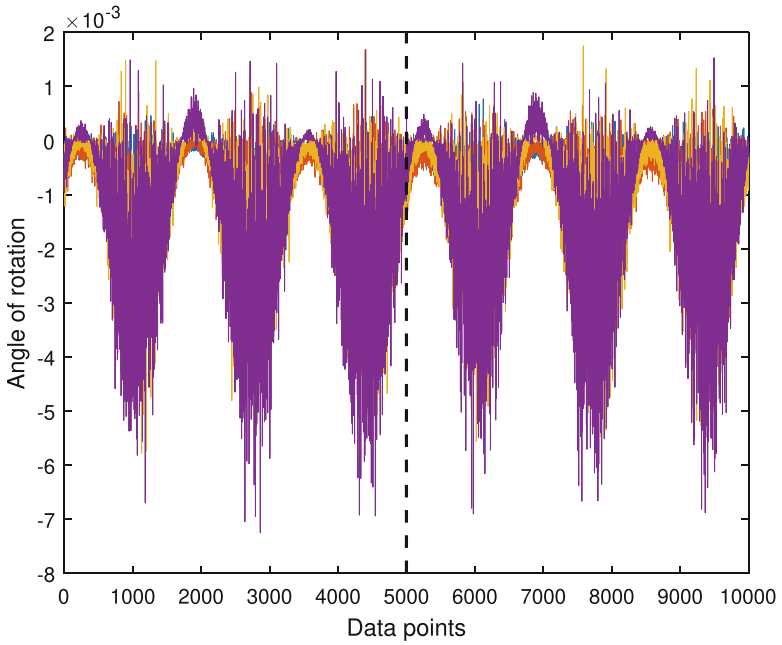

Fig. 17.2 A representation of the measured rotation angles of the four positions ($0.25l$, $0.5l$, $0.75l$ and l) on Beam 1

17.4.2 Results

The data acquisition step produced 500 normal and 500 damage feature instances with 8 features for each beam. Because of the material property differences between the beams, the feature distributions corresponding to the two example beams are quite different—see Fig. 17.3. As a result, a classifier trained on the data of either beam would be unlikely to perform well on the other. For this situation, domain adaptation will be applied.

The data of beam 1 and beam 2 are considered here as the labelled source and unlabelled target data, respectively. The data allocation is summarised as:

- Training set: 800 points of labelled beam 1 data (randomly chosen) + 200 unlabelled points of beam 2 data (randomly chosen).
- Cross-validation set: the remaining 200 points of labelled beam 1 data.
- Test set: the remaining 800 points of beam 2 data.

Note that as the target data is assumed to be unlabelled, the cross-validation can only be performed on the labelled source data to tune the optimal parameters.

To demonstrate the performance of the domain adaptation techniques, a support vector machine (SVM) is employed as a baseline method which is trained on the labelled training data to predict the unlabelled test data. TCA and JDA were run on all data as a transforming step, then an SVM classifier was trained on the transformed labelled training data. ARTL was trained on all the training data to directly induce a domain-adaptive classifier. The classification accuracy on the test data was used as the evaluation metric, as defined by,

$$\text{Accuracy} = \frac{|\mathbf{x} : \mathbf{x} \in D_{\text{test}} \vee f(\mathbf{x}) = y(\mathbf{x})|}{|\mathbf{x} : \mathbf{x} \in D_{\text{test}}|} \tag{17.29}$$

Table 17.3 presents the accuracy results of the classifier using no transfer learning, and with TCA, JDA and ARTL. The poor result of the baseline method proves that the distribution differences will cause a significant prediction degradation. All the three domain adaptation techniques achieve much better classification accuracy than the traditional learning method, where TCA and JDA achieve the same performance with an error reduction of 44.6% and ARTL boosts the performance even more with a further 2.1% error reduction. This performance implies that (a) the assumption that $P(\mathbf{Y}_s|\phi(\mathbf{X}_s)) = P(\mathbf{Y}_t|\phi(\mathbf{X}_t))$ can be valid for this case and (b) the manifold regularisation can further improve the performance of the classifier.

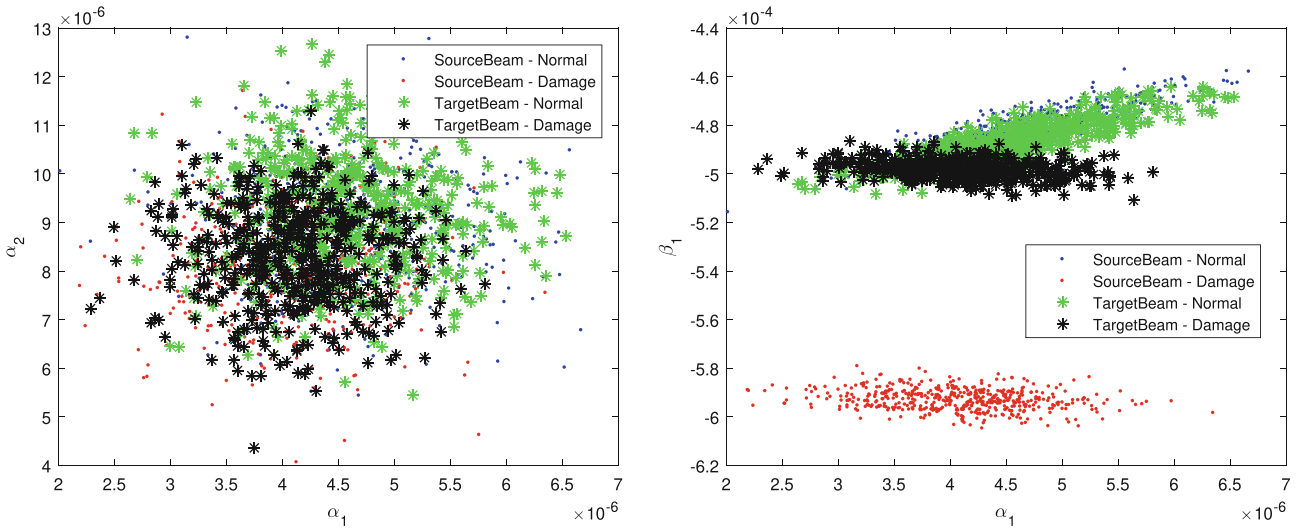

Fig. 17.3 A representation of the feature distributions of beams 1 and 2

Table 17.3 Accuracy of the different learners

	SVM	TCA	JDA	ARTL
Accuracy	50.0%	94.6%	94.6%	96.7%

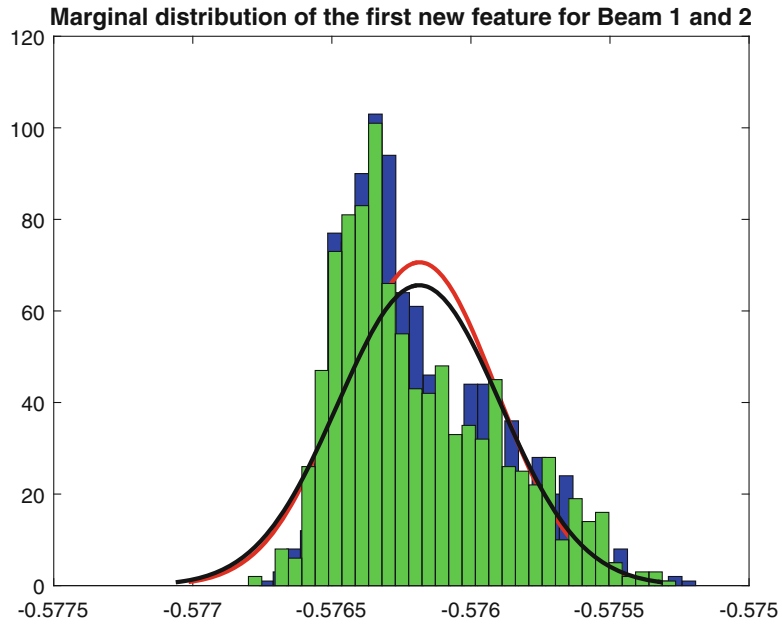

Fig. 17.4 The histogram plot of the first principal transferred feature: beam 1 (blue) and beam 2 (green)

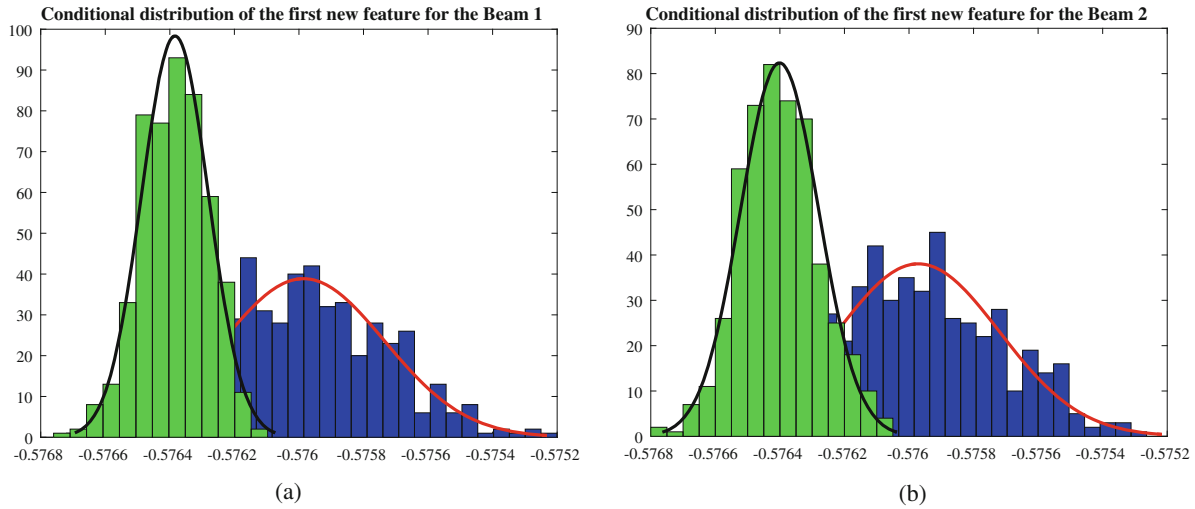

Fig. 17.5 The histogram plots of the first principal transferred features of the beams; normal condition (blue) and damage condition (green): (**a**) beam 1 and (**b**) beam 2

To visually demonstrate that the transfer learning technique has reduced the feature distribution differences between domains, the distributions of the new feature representation transformed from JDA are shown as a representation. Figures 17.4 and 17.5 show the marginal distributions and conditional distributions of the first principal transferred features of beam 1 and 2, respectively. It can be seen that both distributions have been matched via the transformation.

17.5 Conclusions

This paper has investigated the utility of a specific transfer learning method, i.e. domain adaptation, on an SHM application. The main benefit of the transfer learning algorithms is that they can utilise traditional supervised machine learning methods to learn a robust classifier on the unlabelled data of a target problem by transferring knowledge learnt from a labelled dataset of a different, but related, source problem. Domain adaptation mainly targets the situation where the differences between the source and target domains only exist in the data distributions, including the input feature marginal distribution and output label conditional distribution.

This paper has specifically considered three domain adaptation methods: TCA, JDA and ARTL, which can progressively perform the marginal distribution adaptation, the conditional distribution adaptation and manifold regularisation. The utility of these methods was investigated via their applications to an artificially simulated damage detection problem. The normal and damage state data of two cantilever beams of different geometrical and material properties were considered; one was considered as the labelled source data while the other played the role of the unlabelled target data. Compared with the performance of a traditional machine learning method, it has been demonstrated that all the domain adaptation methods employed can significantly improve the classification accuracy on the target data.

In discussing the applicability of transfer learning to population-based SHM generally, it will be necessary to distinguish between *homogeneous* and *heterogeneous* populations of structures. A homogeneous population is a set of nominally-identical structures, e.g. a set of wind turbines of the same make and model, situated in a wind farm. In this case, it will make complete sense that the same features will be used for monitoring of each individual structures. Suppose for the sake of argument that the feature vector is composed of the first five natural frequencies (without wishing to suggest that natural frequencies are *good* features for SHM). Further suppose that the objective is to locate damage to within a single blade of the three present. In this case, considering one turbine as the source domain/task and another as the target domain/task, the feature spaces are identical $\mathcal{X}_s = \mathcal{X}_t$ and the classifier labels are also identical $\mathcal{Y}_s = \mathcal{Y}_t$. However, because of inevitable differences in manufactured parts and structural assembly, the distributions on the feature space and label space will be different: $P(\mathbf{X}_s) \neq P(\mathbf{X}_t)$ and $P_s(\mathbf{Y}_s|\mathbf{X}_s) \neq P_t(\mathbf{Y}_t|\mathbf{X}_t)$. One would hope that the distributions were close to each other in some appropriate metric. In any case, it is clear that the conditions for the applicability of domain adaptation apply here.

In contrast, a heterogeneous population could be composed of quite different structures (e.g. turbines, bridges, aircraft). In this case, the feature *spaces* could correspond e.g. one might decide to monitor the first five natural frequencies for each structure; however, the label spaces will not match, as it will not generally be possible to put locations (for example) on the different structures into correspondence. This fact means that the conditions for domain adaptation are not present and a more general transfer learning methodology would be needed for heterogeneous populations.

Acknowledgements The authors would like to gratefully acknowledge the support of the UK Engineering and Physical Sciences Research Council via grants EP/J016942/1 and EP/K003836/2. KW would also like to thank Lawrence Bull of the University of Sheffield for discussions on the nature of active learning and for commenting on the manuscript.

References

1. Farrar, C.R., Worden, K.: Structural Health Monitoring: a Machine Learning Perspective. Wiley, New York (2012)
2. Worden, K., Dulieu-Barton, J.M.: An overview of intelligent fault detection in systems and structures. Struct. Health Monit. **3**, 85–98 (2004)
3. Worden, K., Manson, G.: The application of machine learning to structural health monitoring. Philos. Trans. R. Soc. Lond. A **365**, 515–537 (2007)
4. Figueiredo, E., Park, G., Farrar, C.R., Worden, K., Figueiras, J.: Machine learning algorithms for damage detection under operational and environmental variability. Struct. Health Monit. **10**, 559–572 (2011)
5. Dervilis, N., Choi, M., Taylor, S.G., Barthorpe, R.J., Park, G., Farrar, C.R., Worden, K.: On damage diagnosis for a wind turbine blade using pattern recognition. J. Sound Vib. **333**, 1833–1850 (2014)
6. Papatheou, E., Dervilis, N., Maguire, E.A., Antoniadou, I., Worden, K.: Population-based SHM: a case study on an offshore wind farm. In: Proceedings of 10th International Workshop on Structural Health Monitoring, Palo Alto, CA (2015)
7. Pan, S.J., Yang, Q.: A survey on transfer learning. IEEE Trans. Knowl. Data Eng. **22**, 1345–1359 (2010)
8. Zhang, J., Li, W., Ogunbona, P.: Transfer learning for cross-dataset recognition: a survey (2017). arXiv:1705.04396v2 [cs.CV]
9. Bull, L., Worden, K., Manson, G., Dervilis, N.: Active learning for semi-supervised structural health monitoring. J. Sound Vib. **437**, 373–388 (2018)
10. Sugiyama, M., Nakajima, S., Kashima, H., Buenau, P.V., Kawanabe, M.: Direct importance estimation with model selection and its application to covariate shift adaptation. In: Advances in Neural Information Processing Systems, pp. 1433–1440 (2008)
11. Quanz, B., Huan, J., Mishra, M.: Knowledge transfer with low-quality data: a feature extraction issue. IEEE Trans. Knowl. Data Eng. **24**, 1789–1802 (2012)
12. Baktashmotlagh, M., Harandi, M.T., Lovell, B.C., Salzmann, M.: Domain adaptation on the statistical manifold. In: Proceedings of IEEE Conference on Computer Vision and Pattern Recognition, pp. 2481–2488 (2014)
13. Borgwardt, K.M., Gretton, A., Rasch, M.J., Kriegel, H.-P., Schölkopf, B., Smola, A.J.: Integrating structured biological data by kernel maximum mean discrepancy. Bioinformatics **22**, e49–e57 (2006)
14. Pan, S.J., Tsang, I.W., Kwok, J.T., Yang, Q.: Domain adaptation via transfer component analysis. IEEE Trans. Neural Netw. **22**, 199–210 (2011)
15. Pan, S.J., Kwok, J.T., Yang, Q.: Transfer learning via dimensionality reduction. In: AAAI, vol. 8, pp. 677–682 (2008)
16. Long, M., Wang, J., Ding, G., Sun, J., Yu, P.S.: Transfer feature learning with joint distribution adaptation. In: IEEE International Conference on Computer Vision (ICCV), pp. 2200–2207 (2013)

17. Long, M., Wang, J., Ding, G., Pan, S.J., Yu, P.S.: Adaptation regularization: A general framework for transfer learning. IEEE Trans. Knowl. Data Eng. **26**, 1076–1089 (2014)
18. Belkin, M., Niyogi, P., Sindhwani, V.: Manifold regularization: a geometric framework for learning from labeled and unlabeled examples. J. Mach. Learn. Res. **7**, 2399–2434 (2006)